

Modeling and Analysis of Chemical Kinetics for Hypersonic Flows in Air

**A DISSERTATION
SUBMITTED TO THE FACULTY OF THE GRADUATE SCHOOL
OF THE UNIVERSITY OF MINNESOTA
BY**

Ross S. Chaudhry

**IN PARTIAL FULFILLMENT OF THE REQUIREMENTS
FOR THE DEGREE OF
DOCTOR OF PHILOSOPHY**

Adviser: Graham V. Candler

November 2018

© Ross S. Chaudhry 2018
ALL RIGHTS RESERVED

Acknowledgements

There are many people I wish to thank for their instruction, support, and friendship. I have enjoyed my time in Minnesota because of you.

Thanks first to my adviser, Professor Graham Candler, who provided a wealth of knowledge and experience. The research environment he fosters is one of experimentation and discovery; I have always been afforded the freedom to try new things, even if they may fail. My work has been more inquisitive and productive as a result. Thanks also to Professor Tom Schwartzenruber, who was always willing to listen and provided much-needed advice and grounding. And thanks to Professor Don Truhlar; his perspective and expertise was always welcome. Working with such a well-qualified team of academics has been an inspiring experience. I also sincerely appreciate my various instructors throughout the years, especially professors Longmire and Mahesh.

I am grateful to Dr. Jason Bender for his attention to detail, enabling me to more easily pick up where he left off. I also appreciate discussions and contributions to my thesis work from Narendra Singh and Drs. Ioannis Nompelis, Paolo Valentini, Maninder Grover, Erik Torres, Zoltan Varga, and Yuliya Paukku. Thank you to my friends and colleagues in the Candler group, current and former, who were always willing to be dragged to the whiteboard: Anand, Anthony, Anubhav, Charlie, Chiara, Derek, Durgesh, Eric Stern, Erik Tylczak, Heath, Honest, Jeff, Joe, Joey, John Reinert, John Thome, Justin, Loretta, Michael Koenig, Nick, Olivia, Prakash, Pramod, Sidharth, Tyler, and Vlad. Thanks also to my friends in AEM outside the Candler group, who often provided a different perspective: Nate, Mary, Michael Kroells, Eric Geistfeld, Praveen, Wyatt, Karim, Mark, and Jacob.

I am grateful for the mentorship of Dr. Michael Barnhardt, and to my other colleagues at NASA Ames: Aaron, Brett, David Hash, David Saunders, Suman, Todd, and Mike Wright. I appreciate the hard work of Ray Muno and the rest of the enet staff. The staff of the Beacon, especially Alex, were also helpful; many productive discussions have occurred there. Thanks also to my friends Alex and Colin, who often provided a necessary reprieve from aerospace engineering. I would not be here today without my family, Anita, Lisa, Janet, and Sunil. My wife Lyndsay was always supportive, and thanks also to her family for treating me as one of their own.

This work was sponsored by the Air Force Office of Scientific Research under grants FA9550-16-1-0161 and FA9550-17-0250. The views and conclusions contained herein are those of the authors and should not be interpreted as necessarily representing the official policies or endorsements, either expressed or implied, of the funding agencies or the U.S. Government.

for Lyndsay

Abstract

Gas-phase chemical kinetics are relevant for hypersonic flows, but they are currently modeled in CFD using empirical assumptions and decades-old experimental data. Recent advances in quantum chemistry have enabled the construction of accurate potential energy surfaces (PESs) for diatom-diatom interactions in air. Using these PESs, a database of simulated interactions is generated and analyzed; $\text{N}_2 + \text{N}_2$, $\text{N}_2 + \text{N}$, $\text{N}_2 + \text{O}_2$, $\text{O}_2 + \text{O}_2$, and $\text{O}_2 + \text{O}$ reactions are considered. The conditions studied range from 4000 K to 30,000 K and include thermal equilibrium and nonequilibrium test sets.

The nitrogen dissociation rate is found to be similar for collision partners N_2 , N , and O_2 . The oxygen dissociation rate, in contrast, is moderately dependent on partner species; O_2 is approximately 2 to 3 times more effective than partner N_2 . Oxygen dissociation with partner N_2 is therefore found to be substantially overpredicted by current CFD models, which is consistent with the limited experimental data available for this reaction. The presence of N is known from experiments to promote nitrogen dissociation; this augmentation is found to be due to increased vibrational relaxation, rather than an increased dissociation rate as described by current CFD models. Similar observations are made for oxygen dissociation with partner O , due to a combination of vibrational and electronic energy relaxation. Using only the shock tube data that informed popular CFD models, it was impossible to isolate the effect of increased relaxation from increased dissociation.

The change in vibrational energy per dissociation, a necessary input to CFD, is found to be very sensitive to the degree of thermal nonequilibrium. This dependence is not well predicted by any existing chemical kinetics models; correctly describing this term fundamentally changes the thermal evolution of a gas in CFD. The mechanics of dissociation are similar for all reactions studied, so a series of aggregate analyses on all dissociation reactions is performed. Vibration is found to have a more pronounced effect on dissociation than rotation, due to rotation increasing the centrifugal barrier. The classic Marrone-Treanor [1] preferential dissociation model is found to accurately describe all data in the nonequilibrium test sets, but it neglects the effect of rotational energy on dissociation. A modified model is proposed that describes rates to within 22 % and vibrational energy changes to within 4 % of the dissociation energy, for all dissociation reactions and conditions.

For this work, we have considered Boltzmann or approximately Boltzmann distributions, but the population of high-energy molecules is known to be depleted in a dissociating gas ensemble. Various kinetics models based on Boltzmann distributions are implemented in US3D, a production CFD solver designed for hypersonic flows. As expected, the dissociation rate is overpredicted compared to the benchmark data. Work remains, therefore, to account for the non-Boltzmann distributions that exist in reality. These data and insights about dissociation can form the basis for next-generation chemical kinetics models for CFD.

Contents

Acknowledgements	i
Dedication	iii
Abstract	iv
List of Figures	viii
List of Tables	xi
1 Introduction	1
1.1 Motivation	1
1.2 Measurements of Oxygen Dissociation	5
1.2.1 Interferometry	5
1.2.2 Absorption Spectroscopy	6
1.2.3 Two-Temperature Absorption Spectroscopy	8
1.2.4 Reviews of Experimental Data	8
1.3 Chemical Kinetics Models for CFD	13
1.4 Potential Energy Surfaces	14
1.4.1 Electronic Energy	15
1.4.2 System Spin and Degenerate Interaction States	16
1.5 Quasiclassical Trajectory Literature Review	18
1.5.1 State-to-State and Master Equation	18
1.5.2 Sampling from Fixed Distributions	19
1.5.3 Direct Molecular Simulation	21
2 QCT Methodology	23
2.1 Preparation of Particles	24
2.1.1 Enumeration of Rovibrational Levels	24
2.1.2 Separation of Energies	25

2.1.3	Distribution of States	28
2.1.4	Conditions Studied	30
2.2	Time Integration	32
2.3	Processing of Final States	33
2.3.1	Possible Reactions and Rate Expressions	33
2.3.2	Stratified Sampling	34
2.3.3	Raw Probability	36
2.3.4	Derived Statistics	37
2.3.5	Expected Values	38
2.3.6	Uncertainty in Moments	39
2.3.7	Uncertainty in Relative Contribution from Trajectory Subsets	42
2.4	The REAQCT Code and the QCT Database	45
2.4.1	The REAQCT Code	45
2.4.2	REAQCT Scaling	47
2.5	The QCT Database	48
3	QCT Results	51
3.1	Nitrogen Dissociation	51
3.1.1	Dissociation Rate	51
3.1.2	Internal Energy Exchange in $\text{N}_2 + \text{N}$	53
3.1.3	Vibrational Energy Change during Dissociation	56
3.2	$\text{O}_2 + \text{O}_2$ Results	59
3.3	$\text{O}_2 + \text{O}$ Results	64
3.3.1	Dissociation in $\text{O}_2 + \text{O}$	64
3.3.2	Vibrational Energy Transfer in $\text{O}_2 + \text{O}$	68
3.4	Oxygen Dissociation in $\text{O}_2 + \text{N}_2$, and Aggregate Oxygen Dissociation	73
3.5	Effect of Reactant States	79
3.5.1	The Support Factor	79
3.5.2	Simple Dissociation	82
3.5.3	Thermal Nonequilibrium and Non-Simple Dissociations	86
3.5.4	Comparison of Energy Separation Methodologies	89
3.5.5	Why Vibration?	90
3.6	Fitting QCT Data	94
3.6.1	Equilibrium Dissociation Rate	94
3.6.2	Nonequilibrium Dissociation Rate	97
3.6.3	Nonequilibrium Vibrational Energy Change per Dissociation	99
3.6.4	Equilibrium Vibrational Energy Change Per Dissociation	105
3.6.5	Fitting All Data in the QCT Database	108

3.7	Miscellaneous QCT Results	114
3.7.1	All Reactions for $\text{N}_2 + \text{O}_2$	114
3.7.2	Degeneracy Error	117
3.7.3	Atom-Diatom Interaction Times	118
3.7.4	Transition Probabilities	120
4	CFD Methodology and Results	124
4.1	Methodology	124
4.1.1	Conservation Equations	124
4.1.2	Park Model	126
4.1.3	Park with New Parameters	127
4.1.4	<i>ab-Initio</i> Model: Boltzmann	128
4.1.5	Consistency with DMS	131
4.2	Zero-Dimensional Isothermal Results	133
4.2.1	Individual Comparisons	133
4.2.2	Comparison Between Models	135
4.3	Other Conditions	139
4.3.1	Adiabatic Single-Cell	139
5	Conclusions	143
Bibliography		147
Appendix A Glossary		160
A.1	Nomenclature	160
A.2	Acronyms	162
Appendix B Tables of QCT Data		163
Appendix C Miscellaneous		172
C.1	PES Source Wishlist	172
C.1.1	Problem	172
C.1.2	Proposed Solution	173
C.1.3	Other Changes	174
C.2	Sample Results File	176
C.3	Physical Constants	180
C.4	Enthalpy Fits	181
C.5	Evaluating Near $\delta = 0$	181

List of Figures

1.1	Literature rates for oxygen dissociation at thermal equilibrium	10
2.1	Schematic for internal energy separation frameworks	27
2.2	Difference between internal energy separation frameworks	27
2.3	Dependence of PDF moment on bin spacing	41
2.4	Dependence of PDF moment error on bin spacing	41
2.5	Assessment of weak scaling	49
2.6	Assessment of strong scaling	49
3.1	Nitrogen dissociation rate	52
3.2	Exchange and dissociation rates in $\text{N}_2 + \text{N}$	55
3.3	Vibrational energy change in $\text{N}_2 + \text{N}$	55
3.4	PDFs for nitrogen dissociation	58
3.5	Vibrational energy change per nitrogen dissociation	58
3.6	Reaction rates for $\text{O}_2 + \text{O}_2$	61
3.7	Relative contribution for $\text{O}_2 + \text{O}_2$	61
3.8	PDF of dissociating molecule v and j for $\text{O}_2 + \text{O}_2$	62
3.9	Change in energy per dissociation for $\text{O}_2 + \text{O}_2$	62
3.10	$\text{O}_2 + \text{O}_2$ dissociation rate compared to literature	63
3.11	Reaction rates for $\text{O}_2 + \text{O}$	65
3.12	PDF of dissociating molecule v and j for $\text{O}_2 + \text{O}$	65
3.13	Change in energy per dissociation for $\text{O}_2 + \text{O}$	67
3.14	$\text{O}_2 + \text{O}$ dissociation rate compared to literature	67
3.15	Probability of exchange in $\text{O}_2 + \text{O}$	71
3.16	PDF of vibrational energy change in $\text{O}_2 + \text{O}$	71
3.17	Average vibrational energy change in $\text{O}_2 + \text{O}$	72
3.18	Exchange and change in energy at $T_{\text{tr}} = 10,000 \text{ K}$, $T_v = 4000 \text{ K}$	72
3.19	Oxygen dissociation with all partners	74
3.20	Change in energy per oxygen dissociation for all partners	75

3.21 PDF of dissociating molecule v and j for oxygen dissociation with partner N ₂	75
3.22 Average change in vibrational energy for all dissociation reactions	77
3.23 Normalized average change in vibrational energy for all dissociation reactions	77
3.24 Oxygen dissociation rate with partner N ₂ compared to literature	78
3.25 Probabilities and PDFs for oxygen dissociation with partner N ₂	81
3.26 Support for oxygen dissociation with partner N ₂	81
3.27 Support for simple dissociation by reactant internal energies	84
3.28 Support for simple dissociation by reactant relative translational energy . .	84
3.29 Support for simple dissociation by energies of the dissociating molecule . .	85
3.30 Effect of partner internal energy for the nonequilibrium test set	88
3.31 Support for swap dissociation by reactant internal energies	88
3.32 Effect of energy separation methodology on conclusions with support factor	89
3.33 Probability of dissociation from each rovibrational level	90
3.34 Joint probability of dissociation as a function of energy components	92
3.35 Joint probability of dissociation as a function of internal energy	92
3.36 Effective diatomic potential for two rovibrational states	93
3.37 Probability of dissociation from remainder energy	93
3.38 Nonequilibrium fits for oxygen dissociation	101
3.39 Support for oxygen dissociation compared to Marrone-Treanor	104
3.40 Change in vibrational energy per oxygen dissociation, equilibrium test set .	106
3.41 PDF of dissociating molecule v	108
3.42 Dependence of Marrone-Treanor U on temperature	109
3.43 New model for nitrogen dissociation	111
3.44 New model for oxygen dissociation	112
3.45 All rates for N ₂ + O ₂	115
3.46 PDF of impact parameter for N ₂ + O ₂ events	116
3.47 Energies of product NO	116
3.48 Effect of degeneracy error	117
3.49 PDF of interaction time	121
3.50 Time history for long interactions	121
3.51 PDF of initial and final v	123
3.52 Probability of component energy change	123
4.1 Electronically-excluded fits of C_p for N ₂ and N	133
4.2 Standard Park compared to DMS, $T_{v,0} = T_{tr,0}$	136
4.3 Effect of initial T_v , with standard Park	136
4.4 Effect of using preferential change in vibrational energy per dissociation .	137
4.5 Effect of electronic energy, Park original model	137

4.6	Comparison between original Park and ‘Park with new parameters’	138
4.7	All models	138
4.8	Adiabatic results	141
4.9	Vibrational energy source term for adiabatic simulations, $T_{v,0} = T_{tr,0}$	142
C.1	Relative error magnitude when computing expressions near $\delta = 0$	184

List of Tables

1.1	O ₂ dissociation shock tube experiments	11
1.2	O ₂ dissociation shock tube fits	12
1.3	Interaction states for O ₂ + O ₂ and O ₂ + O	18
2.1	Diatomeric potentials	25
2.2	Number of trajectories for nitrogen dissociation	31
2.3	Number of trajectories for oxygen dissociation	31
3.1	Fit to equilibrium nitrogen dissociation rate	96
3.2	Fit to equilibrium oxygen dissociation rate	96
3.3	New model for nitrogen dissociation	113
3.4	New model for oxygen dissociation	113
4.1	Initial conditions for adiabatic simulations	139
B.1	Data tables for N ₂ + N ₂ , T _{tr} = T _v	164
B.2	Data tables for N ₂ + N ₂ , T _{tr} = 20,000 K	164
B.3	Data tables for N ₂ + N ₂ , all conditions	165
B.4	Data tables for N ₂ + N, T _{tr} = T _v	166
B.5	Data tables for N ₂ + N, T _{tr} = 20,000 K	166
B.6	Data tables for N ₂ + O ₂ , T _{tr} = T _v	167
B.7	Data tables for N ₂ + O ₂ , T _{tr} = 10,000 K	167
B.8	Data tables for N ₂ + O ₂ , T _{tr} = 20,000 K	167
B.9	Data tables for O ₂ + O ₂ system, T _{tr} = T _v	168
B.10	Data tables for O ₂ + O ₂ system, T _{tr} = 10,000 K	168
B.11	Data tables for O ₂ + O ₂ , all surfaces, T _{tr} = T _v = 10,000 K	169
B.12	Data tables for O ₂ + O ₂ , all surfaces, T _{tr} = T _v = 5000 K	169
B.13	Data tables for O ₂ + O ₂ , all surfaces, T _{tr} = 10,000 K, T _v = 4000 K	169
B.14	Data tables for O ₂ + O system, T _{tr} = T _v	170
B.15	Data tables for O ₂ + O system, T _{tr} = T _v	170

B.16 Data tables for O ₂ + O, all surfaces, $T = 10,000\text{ K}$	170
B.17 Data tables for O ₂ + O, all surfaces, $T = 5000\text{ K}$	171
B.18 Data tables for O ₂ + O, all surfaces, $T_{\text{tr}} = 10,000\text{ K}$, $T_{\text{v}} = 4000\text{ K}$	171
C.1 Physical constants	180
C.2 N ₂ Dissociation Temperatures	180
C.3 O ₂ Dissociation Temperatures	180

Chapter 1

Introduction

1.1 Motivation

Chemical reactions occur in the gas flow around vehicles traveling at hypersonic speeds, which is typically defined as at least five times faster than the speed of sound. The rate of these reactions is often comparable to the time scales of the flow and other relevant processes. Therefore, predictions of the chemical evolution of the flow must consider the finite rate at which chemical kinetics occur [2, 3]. Accurately predicting these rates is important; for example, the concentration of atomic oxygen at the vehicle surface affects the material decomposition rate [4]. Unfortunately, the extreme nature of these phenomena, with small time scales and high temperatures, means that there is considerable uncertainty in current predictions. The goal of this work is to study the finite-rate chemistry that occurs in air at conditions relevant for hypersonic flight.

A key aspect of the chemical nonequilibrium we describe is its two-way coupling to thermal nonequilibrium, as follows. Consider the behavior of air passing through a strong shock. The shock rapidly converts bulk motion into random thermal motion. Rotational energy typically relaxes relatively quickly, followed by vibrational energy which is relatively slow. As the gas is relaxing, its internal energy state may not be characterized by a single temperature; it is described as being in a state of thermal nonequilibrium. Throughout this relaxation process, there is less energy in internal energy modes, especially vibration, than there would be at thermal equilibrium. This nonequilibrium is important for chemical kinetics because molecules with substantial internal energy, especially in the vibrational mode, are more likely to dissociate. This means that, behind a strong shock, there is a delay before dissociation begins to meaningfully occur. In the literature, this delay is known as the incubation period, and its existence motivated the development of thermochemical nonequilibrium models [5, 6]. This dependence of the dissociation rate on the degree of thermal equilibrium is one direction of the two-way coupling. The early Hammerling *et al.* [7]

model, in fact, only considered this single mechanism of coupling.

The internal energy distribution of molecules is also affected by chemical reactions, as those molecules are formed or destroyed. The population of molecules removed by dissociation is biased to include excited molecules, because they are more likely to dissociate. Therefore, dissociation promotes thermal nonequilibrium. Traditionally, the nonequilibrium that is produced is described as being *between modes*, i.e. by removing more energy from vibration than other modes [1, 8, 9]. Recently, however, it has become clear that nonequilibrium is also promoted *within modes*, i.e. the vibrational energy distribution is non-Boltzmann because the population of vibrationally-excited molecules is depleted [10, 11]. If a gas is dissociating, this mechanism causes thermal nonequilibrium, regardless of how many characteristic internal energy relaxation times have elapsed since the initial shock. This promotion of thermal nonequilibrium is balanced by relaxation processes, yielding a quasi-steady state (QSS) distribution of internal energy levels, which is different than an equilibrium distribution especially in vibration. Due to dissociation's dependence on the thermodynamic state, the dissociation rate at QSS is lower than it would be at equilibrium. Therefore, predicting the chemical evolution of a hypersonic flow requires an understanding of the thermochemical kinetics.

Many experiments have measured the rate of oxygen and nitrogen dissociation, especially in the late 1950's and 1960's. In these shock tube studies, the test gas is subjected to a strong shock, and the resulting density is measured by some optical diagnostic system. A detailed review of experiments that measured oxygen dissociation is provided in Section 1.2. In the older, non-Russian literature that still informs the popular models today, two crucial assumptions are made: thermal nonequilibrium is neglected; and a form for the rate expression is assumed, with either one or two model parameters. These assumptions provide a relationship between the rate expression model parameters and the measured dissociation profile; parameters that best fit all the data are selected.

When available, the estimated uncertainty due to measurement error (typically dominated by the measurement of initial shock speed) is usually about 30 % [12–15]. More importantly, there is systematic error due to neglecting the effect of thermal nonequilibrium. This can disproportionately affect quantities of interest for specific reactions, because the degree of thermal nonequilibrium may depend on the gas species present as relaxation occurs. These errors are compounding, especially for measurements of dissociation with the corresponding atomic partner (e.g. O₂ + O), for reasons that are discussed in Section 1.2. Ultimately, these experimental studies should be interpreted as measuring the dissociation rate at QSS, rather than at thermal equilibrium.

In the late 1980s and early 1990s, Park [9, 16–20] reinterpreted those experimental data using a two-temperature model, with the goal of accounting for the effect of vibrational

nonequilibrium. The specifics of his model form, and details of other models designed for CFD, are described in Section 1.3. Using several assumptions, Park proposed a chemical kinetics model except for the reaction rate constants. Then, for a large body of shock tube dissociation experiments, each experimental condition was simulated, and reaction rate expressions that best matched the experimental data were determined. Those reaction rates, along with the aforementioned inputs, form the Park two-temperature model. Because all data were reinterpreted within the same framework, the Park model as developed is self-consistent, which is required to capture the coupled nature of the dissociation process. The CFD tools designed for hypersonic flows that the authors are aware of all implement the Park model, including US3D, DPLR, and LAURA [21–23].

Recent advances in computational chemistry have enabled accurate calculations of the electronic structure of four-atom systems that are relevant to hypersonic applications. As detailed in Section 1.4, a potential energy surface (PES) may be constructed, which describes the force on each atom during a molecular interaction. The time-evolution of an atomic system, such as an $\text{N}_2 + \text{O}_2$ interaction, may therefore be simulated using the classical equations of motion. Molecules in the system are initialized using atomic positions and velocities corresponding to quantized rovibrational states. Such an interaction is called a quasiclassical trajectory (QCT), because the initial condition is quantized but the motion is computed classically [24].

Analyses based on QCTs are able to provide detailed information about dissociation and relaxation, beyond what may be identified in an experiment. Broadly, there are several different ways QCTs are used in the literature; they are differentiated by how initial conditions are selected and how the final states are used. For each of these, the actual trajectory calculation is the same. In the implementation of the present work, initial conditions are sampled from fixed distributions; quantities of interest, such as the reaction probability or average energy change, are determined by averaging over many trajectories [25]. Alternatively, choosing a particular initial rovibrational state yields state-specific reaction rates and transition probabilities; the ‘master equation’ may then be solved to determine the time-evolution of each state’s population [26]. Finally, in direct molecular simulation (DMS), the final trajectory state is used as an input for a subsequent collision; the distribution of states therefore evolves in a time-accurate manner [27]. Both master equation analysis and DMS are able to represent the non-Boltzmann distributions that exist as a recently-shocked gas relaxes and dissociates. The analysis method we use, in contrast, samples each batch of trajectories from a fixed distribution that is approximately Boltzmann, so that particular condition may be studied in detail. A review of QCT-based works in the literature is given in Section 1.5; the community has primarily focused on nitrogen so far.

In this work, we use recently-published PESs to simulate interactions corresponding to

5 different interactions that occur in air. A range of conditions chosen to be relevant for hypersonic flight are considered for each reaction, including those at thermal nonequilibrium, which we approximate by using a different vibrational temperature. A database of QCT interactions is the key result, and it comprises approximately 13 billion trajectories computed on 14 different PESs. The simulations due to Bender *et al.* [25], whose effort led directly to the present work, are also included. This QCT database is systematically analyzed in several ways. First, for each dissociation reaction, we describe quantities of interest for chemical kinetics models in CFD. For the case of oxygen dissociation in $O_2 + O_2$ and $O_2 + O$, multiple PESs are required per reaction, and we compare results between these surfaces. Next, we define a framework to aggregate data for all computed dissociation reactions, and use this paradigm to study the effect that each reactant state has on dissociation. By better understanding the causes of dissociation, we construct a self-consistent model that describes all quantities of interest in the database. Finally, several new chemical kinetics models are implemented in a production CFD code designed for hypersonic applications.

Key outcomes of this work are as follows. A paper published in the *Journal of Thermophysics and Heat Transfer* [28] describes nitrogen dissociation with collision partners N_2 , N, and O_2 , and it attempts to motivate how QCT data may help improve CFD models. That nitrogen dissociation data and discussion are also present, in some form, in two AIAA conference papers [29, 30]. Preliminary data for $N_2 + O_2$ interactions [31] and oxygen dissociation with collision partners O_2 , O, and N_2 [30] are also described in conference papers. A variety of CFD models based on Boltzmann distributions were implemented in a production CFD code, and the effect of each type of input was also analyzed [32]. Work to publish the oxygen dissociation data in a journal is ongoing. A final conference paper, scheduled for January 2019, concerns aggregate statistical analyses of the database [33]. Components of these papers are adapted, or sometimes copied verbatim, for sections of this Thesis¹. The database of QCT results, along with the software package used to create and analyze it, is also a deliverable of this work; we describe it further in Section 2.4.1.

¹This is consistent with the AIAA policy, which is available at <https://www.aiaa.org/publicationpolicies>, accessed October 4, 2018.

1.2 Measurements of Oxygen Dissociation

All experimental measurements of oxygen dissociation that we are aware of, with one exception², use shock tubes. In this Section, we review experiments that measured the dissociation rate of oxygen with collision partners O₂, O, or N₂. These partners are the major contributors to oxygen dissociation in air, and they are also the partners we have simulated with QCT. We focus on the sources of random and systematic uncertainty, and also provide perspective on these experiments in the context of our current understanding of chemical kinetics. Almost all measurements fit their rates to the generalized Arrhenius form, (e.g., p. 130, Ref. [35]),

$$k_d = CT^n \exp\left(-\frac{T_D}{T}\right) \quad (1.1)$$

Tables and plots for the literature described herein are collected at the end of this Section.

In a shock tube, a high-pressure driver gas, typically hydrogen or helium, is separated from a low-pressure test gas by a plastic or metal membrane. In some cases, they are separated by two membranes, with a buffer gas between the membranes. As the pressure in the driver gas increases, often due to pumping but sometimes combustion [36], the diaphragm bursts, which causes a strong shock to propagate into the test gas. In the recently-shocked region, the molecular oxygen in the test gas begins to dissociate, and the degree of dissociation is measured in the test section by some procedure that we will discuss shortly.

At this stage, the most important source of uncertainty is the shock speed. The shock speed is measured by recording the the shock's passage at a number of stations through the test gas chamber: Matthews [12] used thin-film resistance thermometers, and Ibraguimova *et al.* [36] used pressure transducers, for example. The shock is assumed to propagate at a constant speed. A commonly-quoted uncertainty for the shock speed is near 1% [12, 36, 37]. Relative uncertainty in the shock speed is magnified in quantities of interest by approximately a factor of 20 to 30 [37], and so uncertainty in the shock speed is a substantial contributor to random uncertainty in the reported reaction rates. Once the shock has reached the test section, several different methodologies are used to determine the rate constants.

1.2.1 Interferometry

Matthews [12] and Byron [13] both used interferometry to measure the total density behind the shock. In their techniques, light from a white source is split in two, and each beam passes through a different section of the shock tube, spaced 9 inches apart for Byron's experiment.

²The exception is Eckerman [34], which we describe at the end of this Section.

Each beam experiences an optical path length that depends on the total density of the gas at the corresponding test section. The beams are then combined, and any differences in optical path length are detected and recorded as a fringe shift. In this fashion, the difference in density between these two test stations is recorded in time.

Using the measured density and the conservation equations, the degree of dissociation is determined behind the shock. The dissociation rate is then determined from a series of these profiles determined from many runs of the shock tube. For the work of Byron [13], the time to reach halfway between no dissociation and chemical equilibrium was used. (He notes that measuring the initial slope consistently yields a dissociation rate that is too low, which we now recognize as the incubation period.) Due to the limited data available, a form for the rate expression must be assumed: both studies prescribed a generalized Arrhenius rate with a fixed temperature exponent that was different for each partner and each study.

Interferometric measurements are unique from other methods in several aspects. The fringe shift measurement, which is central to the technique, yields a density error between 1 and 2.5% according to Byron [13]. Because total density is the measured quantity, a substantial amount of the test gas must dissociate to yield a good measurement. This precludes the possibility of using a test gas with very dilute quantities of O₂, which is used in absorption-based studies (discussed next) to isolate the effect of a single collision partner. Matthews [12] therefore only reported rates with collision partner O₂. Byron [13] did report rates with partners O₂, O, and Ar, by first using pure oxygen and neglecting the O₂ + O rate to yield the O₂ + O₂ rate. The rate with partner Ar was determined next by using a test gas with 3.46% O₂, and the partner O rate was finally determined from a 15% mixture. At each step, the dissociation rates with known partners are used to discount the effect of those partners, leaving only the unknown partner's rate. This means that the rate computed for partner O is particularly sensitive to amplification of error.

1.2.2 Absorption Spectroscopy

The most prevalent technique to measure the oxygen dissociation rate is single-wavelength absorption spectroscopy, which was used by Camac and Vaughan [37], Rink *et al.* [14], Schexnayder and Evans [38], Generalov and Losev [39], and Jerig *et al.* [15]. In this method, laser light passes through the test section, and the transmitted intensity is measured. The measured signal has been attenuated due to absorption by the test gas, in an amount that depends on the density of the absorbing species. Most often, molecular oxygen is the sole absorbing species and the chosen frequency is in the UV band. The two exceptions to this, in the literature we discuss here, is Jerig *et al.* [15] who used UV absorption of atomic oxygen, and Rink *et al.* [14] who used x-ray absorption of molecular oxygen.

As described by Schexnayder and Evans [38], there are three effects that contribute to

the measured intensity following the passage of the shock. First, the concentration of oxygen molecules decreases due to dissociation; this is the effect that the experiment is designed to capture. Second, the vibrational temperature of the gas is decreasing because dissociation is progressing, which affects the absorption coefficient of molecular oxygen. Third, the total density is increasing because atomic species are being formed. These three effects combine to yield the measured intensity. It is furthermore necessary to describe the electronic states of O₂ present in the shocked region, because they also influence the amount of absorption. Schexnayder and Evans [38] assumed that all electronic states were excited when the test gas was pure oxygen, but that only the ground state was populated when the test gas was a mixture of oxygen and argon. Camac and Vaughan [37] assumed that all electronic states were in equilibrium³. These details illustrate that measurements of dissociation were not made in isolation: the coupling that exists in thermochemical nonequilibrium was modeled, with significant assumptions, in order to yield a result.

One feature of using absorption spectroscopy compared to density interferometry is a sensitivity to the sole absorbing species (typically O₂). Therefore, the effect of a specific collision partner, typically Ar, may be isolated by using a test gas with dilute concentrations of O₂. For example, the rate with partner Ar was determined by Camac and Vaughan [37] using a test gas with either 0.25 % or 1 % O₂. Therefore, the rate of oxygen dissociation with partner Ar is relatively well characterized, compared to other partners [40]. Subsequent measurements using test gasses with other mixture fractions may accurately discount the effect of partner Ar. However, separating the effect of partner O and O₂ is still challenging; Camac and Vaughan [37], for example, only determined the rate with partner O₂ as an upper bound.

The experiments performed using interferometry and single-wavelength absorption spectroscopy do not attempt to account for thermal nonequilibrium⁴ [12–15, 37–39]. For their conditions, the dissociation time is much larger than vibrational relaxation time (at least 50× for Byron [41]). Therefore, the logic at the time went, vibrational relaxation has completed and thermal equilibrium is achieved before any meaningful amount of dissociation has occurred. Thus the measured rates are described as equilibrium rates. We now recognize this to be false: thermal nonequilibrium is also caused by dissociation, because dissociation occurs disproportionately from excited molecules. A dissociating gas ensemble, even after many characteristic vibrational relaxation times have elapsed, does not have internal energy characterized by a Boltzmann distribution at one temperature. Thus, measurements of ‘equilibrium’ dissociation rates in literature should be interpreted as at QSS, rather than

³The electronic states must also be described for interferometric measurements, but only to define the specific heat, which has a relatively small effect. Byron [13] assumed that the first two levels were fully-excited.

⁴At the time, this was commonly referred to as ‘vibration–dissociation coupling’

Boltzmann distributions characterized by one temperature.

1.2.3 Two-Temperature Absorption Spectroscopy

Absorption spectroscopy can also be performed using two different light wavelengths simultaneously, to measure both density and vibrational temperature. Shatalov [42] and Ibraguimova *et al.* [36] both used this technique, which is more popular in the Russian literature. Density is obtained in a manner similar to the single-wavelength case. Then, because the absorption cross section for each wavelength is different, and because this difference depends on the population of low-lying vibrational levels, the vibrational temperature may also be determined. The uncertainty associated with measuring T_v in this manner is described by Ibraguimova *et al.* [36] to be between 10 and 25 %, depending on the condition and location of measurement. The estimated uncertainty in rate reported by Ibraguimova *et al.* is a factor of 2. The population of low-lying vibrational energy levels is assumed to be Boltzmann.

These experiments were performed for relatively high temperatures: up to 10,000 K for Shatalov [42] and up to 11,000 K for Ibraguimova *et al.* [36]. At these conditions, dissociation occurs rapidly, before many characteristic vibrational relaxation times have elapsed. Therefore, rate constants are measured as a function of T_{tr} and T_v , which are, in general, different. Then, using an assumed (for Shatalov) or inferred (for Ibraguimova *et al.*) form of the rate expression, the final rate parameters are determined.

Because the measured rate is specific to both T_{tr} and T_v , these experiments account for thermal nonequilibrium between vibration and translation-rotation. However, the distribution of vibrational energies is still non-Boltzmann. We also note that Ibraguimova *et al.* [36] only measured the rate with partner O₂; for their analysis, the rate with partner O was assumed to be 3.5 times the rate with partner O₂. As with the single-wavelength case, there are a number of assumptions necessary to close the system of equations required to yield a reaction rate.

1.2.4 Reviews of Experimental Data

An early review of the oxygen shock tube data was performed by Johnston in 1968 [40], which includes a detailed tabulation of individual rate measurements. His review focused on data with collision partner argon because those results followed theory relatively well, compared to the results with oxygen as a collision partner. Bortner [43] also collected a variety of dissociation data for all air reactions, focusing on high temperature dynamics. Both of these reviews include measurements of dissociation for a single temperature value, which we have neglected for the present review. They also present recommended equilibrium rates, which typically include larger uncertainties than referenced individual experiments.

According to Wray [44], who also collected and fitted rates, Byron [13] found that oxygen dissociation with a N_2 collision partner is approximately 4 times less effective than with a O_2 collision partner. Byron did briefly examine partner N_2 , but no specific rates, or ratios of rates, are provided in his paper or his thesis [13, 41]. In fact, Byron specifically cautions against using his data to determine rates with partner N_2 [41, p. 64]. Wray's review occurred before Generalov and Losev [39] measured the rate with partner N_2 , so Wray fit only to Byron's apparent data. Therefore, we believe that Wray's recommendation for oxygen dissociation with partner N_2 should be considered invalid. The available data for oxygen dissociation with partner N_2 is still extremely limited; we discuss this more in Section 3.4.

We also comment on the novel technique used by Eckerman [34] to measure the dissociation rate of oxygen in 1958 using a ballistic range. Nylon spheres were shot into a test pure O_2 test gas, and the shock standoff distance and projectile velocity were measured. Using a potential flow approximation, the relationship between reaction rate and shock standoff was determined and a reaction rate was fit to the standard Arrhenius form. Unfortunately, the Ph.D thesis we have access to offers few details on the methodology, and the work is seldom cited in the modern literature. No uncertainty estimate is provided.

All equilibrium rates we have discussed, for partners O_2 , O , and N_2 , are shown in Figure 1.1 and Tables 1.1 and 1.2. Data for Ibraguimova's [45] recommended rates, based on the Russian literature, is included too. The rates of Park [16, 18] are shown; they are described further in the next Section.

We finally note that, by focusing on oxygen dissociation with partners O_2 , O , and N_2 , a variety of studies have been neglected. Many experimental measurements of nitrogen dissociation have been performed [46–50]; Bender *et al.* [25] compares $N_2 + N_2$ results to experiment. Owen *et al.* [51] has recently measured oxygen dissociation with partner Ar, using modern absorption spectroscopy techniques; their results have lower scatter and are analyzed in a similar manner to the historical shock tube literature.

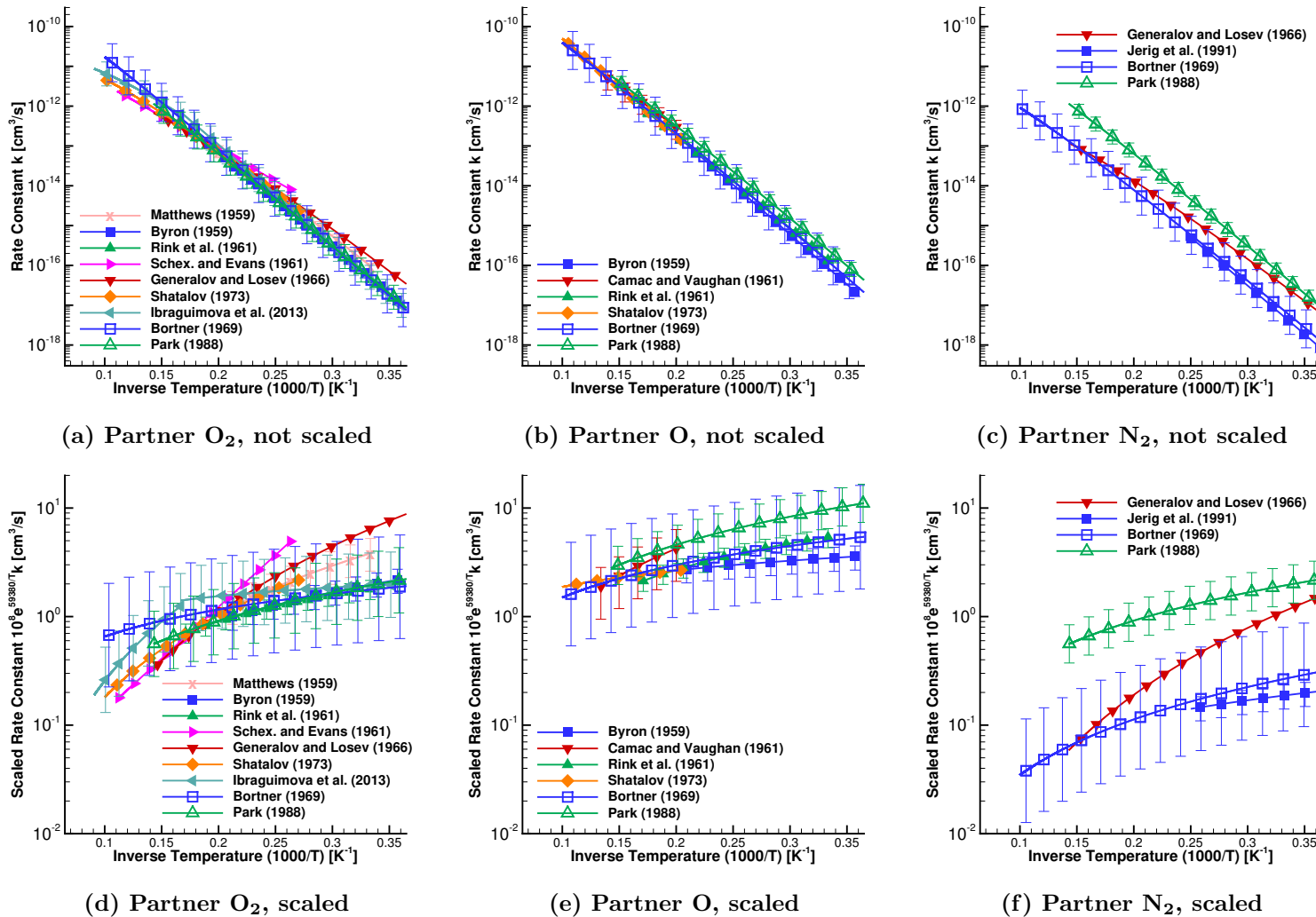


Figure 1.1: Equilibrium oxygen dissociation rate constants from experiments and fits to experiments; lower plots are scaled by $10^8 \exp(59,380 K/T)$ to better visualize the data. Filled symbols: experiment; hollow symbols: fit.

Table 1.1: Summary of oxygen dissociation shock tube experiments with partners O₂, O, and N₂. Equilibrium dissociation rate fit to Arrhenius form, Equation (1.1), is shown. For this table, 5 significant figures are provided for C and T_D regardless of estimated uncertainty.

Reference	Year	Method	M	Rate Parameters			Uncertainty [%]		Temp. Range [K]
				C [cm ³ s ⁻¹ K ⁻ⁿ]	n	T _D [K]	lower	upper	
Eckerman [34]	1958	Ballistics Range	O ₂	2.6782×10^{-3}	-1.5	59,396	-	-	4000 to 7000
Matthews [12]	1959	Interferometry	O ₂	1.8857×10^1	-2.5	59,380	37	32	3000 to 5000
Byron [13]	1959	Interferometry	O ₂	3.1948×10^{-3}	-1.5	59,350	25	25	2800 to 5000
			O	1.8905×10^{-6}	-0.5		-	-	
Camac and Vaughan [37]	1961	UV absorption	O ₂	1.7745×10^{-5}	-1	59,369	99	0	6000 to 7000
			O	1.0535	-2		50	50	
Rink <i>et al.</i> [14] [*]	1961	x-ray absorption	O ₂	5.3030×10^{-5}	-1	59,578	20	20	3000 to 6000
			O	1.5909×10^{-4}	-		-	-	
Schexnayder and Evans [38]	1961	UV absorption	O ₂	1.5073×10^{-10}	0	37,378	-	-	3800 to 9000
Generalov and Losev [39] [†]	1966	UV absorption	O ₂	9.4965×10^4	-	59,380	-	-	2600 to 7000
			N ₂	1.6800×10^4	-3.5		-	-	
Shatalov [42]	1973	2-T UV absorption	O ₂	1.8079×10^1	-2.5	59,369 [‡]	-	-	3700 to 10,000
			O	1.8735×10^{-6}	-0.5		-	-	
Jerig <i>et al.</i> [15]	1991	UV absorption (O)	N ₂	5.6458×10^{-5}	-1	59,380	25	25	2463 to 3999
Ibraguimova <i>et al.</i> [36]	2013	2-T UV absorption	O ₂	6.4263×10^3	-3.1	59,380	50	100	6000 to 11,000 [§]

^{*} Rink *et al.* [14] reports recombination rates, so the equilibrium constant is required to determine the dissociation rate. For the data shown, we have used the two-parameter fit of Johnston [40], which is based on the contemporary JANAF tables [52].

[†] Based on information in the translated abstract and Ref. [43]; no complete translation is available.

[‡] Dissociation energy is not given directly, so the value from Generalov and Losev [39] is used.

[§] For low temperatures (2000 K to 6000 K), the fit by Ibraguimova *et al.* [45] (summarized in Table 1.2) was found to describe the data.

Table 1.2: Summary of fits and reinterpretations of oxygen dissociation shock tube data with partners O₂, O, and N₂. Equilibrium dissociation rate fit to Arrhenius form, Equation (1.1), is shown. For this table, 5 significant figures are provided for C and T_D regardless of estimated uncertainty.

Reference	Year	Method	M	Rate Parameters			Uncertainty [%]		Temp. Range [K]
				C [cm ³ s ⁻¹ K ⁻ⁿ]	n	T _D [K]	lower	upper	
Wray [44]	1962	Fit to Refs [12–14, 37]	O ₂	5.4062×10^{-5}					3000 to 8000
		Fit to Refs [13, 14, 37]	O	1.5017×10^{-4}	-1	59,380	-	-	
		Fit to Refs [13] [*]	N ₂	1.2014×10^{-5}					
Johnston [40]	1968	Fit to Refs [12, 14, 38]	O ₂	4.5709×10^{-5}	-1	59,752	50	100	1000 to 8000
Bortner [43]	1969	Fit to Refs [12–14, 37–39]	O ₂	1.3700×10^{-5}	-0.83				100 to 10,000
		Fit to Refs [13, 14, 37]	O	1.5000×10^{-4}	-1	59,400	67	200	
		Fit to Ref [39]	N ₂	2.2000×10^{-3}	-1.7				
Park [16]	1988	2-T fit to Refs [12–14, 37–39]	O ₂	3.3211×10^{-3}			50	100	Up to 7000
		2-T fit to Refs [13, 14, 37]	O	1.6605×10^{-2}	-1.5	59,500	33	50	
		2-T fit to Ref [39]	N ₂	3.3211×10^{-3}			33	50 [†]	
Ibraguimova et al. [45] [‡]	1999	Fit to various Refs [§]	O ₂	3.3211×10^{-9}			50	100	300 to 40,000
			O	1.1790×10^{-8}	0.3	59,380	50	100	
			N ₂	3.3211×10^{-9}			60	150	

^{*} As described on Page 9, we believe that this fit is invalid.

[†] Park notes a particularly large discrepancy for the case of partner N₂, but does not provide a correspondingly-high uncertainty estimate.

[‡] For this work, the Arrhenius form is multiplied by [1 – exp(–2238 K/T)].

[§] The cited literature is exclusively from the Russian community, and many works are unavailable in English.

^{||} The stated uncertainty is for 3000 K to 5000 K; other temperatures have slightly higher uncertainty.

1.3 Chemical Kinetics Models for CFD

As described in Section 1.1, thermal nonequilibrium is coupled to chemical nonequilibrium. This must be reflected in chemical kinetics models for CFD. In 1959, Hammerling *et al.* [7] proposed the coupled vibration–dissociation (CVD) model: vibrational relaxation times were taken from Blackman [53], and the dissociation rate was modeled to depend on the translational-rotational temperature T_{tr} and the vibrational temperature T_v . Vibrational energy was treated separately from rotational and translational energy because it relaxes relatively slowly. Thus, in this model, the chemical evolution of a gas depends on the degree of thermal nonequilibrium. Treanor and Marrone [1, 8] expanded on the CVD model, incorporating the effect that dissociation has on thermal nonequilibrium. Molecules that dissociate tend to have more vibrational energy than the average molecule, and therefore dissociation results in a decrease in the average vibrational energy of the gas. These developments form the basis of a two-temperature chemical kinetics model for CFD, which has three inputs: reaction rates, vibrational relaxation rates, and vibrational energy changes due to dissociation. These three inputs are coupled: increasing the dissociation rate causes more dissociation, for example, but so does increasing the vibrational relaxation rate or depleting less vibrational energy per dissociation.

Although the CFD models were designed to account for the effect of thermal nonequilibrium, dissociation rate measurements from the Apollo era did not. Simply applying the experimentally-measured equilibrium rate to a two-temperature model’s equilibrium rate neglects that dissociation occurs from QSS. Park [9, 16–20] attempted to rectify this by constructing a self-consistent chemical kinetics model based on two temperatures. He began by making two key assumptions. First, the controlling temperature for dissociation was assumed to be the geometric mean of both temperatures, $\sqrt{T_{\text{tr}}T_v}$, which emphasizes the importance of vibrational energy for the dissociation rate. Second, the vibrational energy decrease due to dissociation was assumed to be the dissociation energy minus a translational energy term, $(D_0 - k_B T_{\text{tr}})$. The net dissociation rate was therefore reduced substantially by vibrational energy decrease due to dissociation [16]. Park also used vibrational relaxation times available in the literature, primarily from Millikan and White’s empirical correlation [54], which is itself based on shock tube measurements of vibrational relaxation from the 1950s and early 1960s.

With these assumptions, Park had an entire thermochemical kinetics model except for the reaction rates. Then, for many of the shock tube experiments available at the time, the data were reinterpreted using this two-temperature framework, instead of the single-temperature framework used in the original works. The rate parameters that best fit the experimental data were determined, and those parameters are Park’s rates. Together with the assumptions used to derive them, they form the Park model. The specific manner of his

rate determination, such as the weighting given to each experiment, or the specific input data used, is unclear, but a 1988 conference paper [16] discusses some methodology that we have not found elsewhere.

Because all data were reinterpreted using the same inputs, the Park model as developed is self-consistent. However, the Park model as implemented uses a different vibrational energy change per dissociation. Following his reinterpretation, Park published a different model for this term [55], and the CFD tools that we are aware of all use nonpreferential dissociation instead⁵. This modification is made because both models considered by Park are ill-suited for implementation in CFD. We discuss why this occurs, and compare to QCT data, in Section 3.1.3.

A variety of models based on kinetic theory have also been proposed. Jaffe [56] attempted to account for the effect of rotation on dissociation by considering a molecule's effective bond energy, which is reduced by rotation. Assuming that vibrational energy relaxes through a series of Boltzmann distributions characterized by T_v , Olynick and Hassan [57] analytically determined the effect of vibrational nonequilibrium on the dissociation rate. The preferential dissociation model of Marrone and Treanor [1] was extended to exchange reactions by Knab *et al.* [58], which led to the coupled vibration–chemistry–vibration model. Based on the minimum translational energy required to induce dissociation, Macheret and Rich [59] predicted that dissociation occurs via two different mechanisms: from low vibrational levels at thermal nonequilibrium and from a range of vibrational levels at thermal equilibrium. This model has been recently reexamined and corrected by Luo *et al.* [60]. Finally, state-specific rates were determined by Macheret and Adamovich [61] using a modified forced harmonic oscillator model. Section 3.6 discusses some of these models further, and compares them to QCT data.

1.4 Potential Energy Surfaces

A potential energy surface (PES) describes the force on each atom during a specific interaction, for example $\text{N}_2 + \text{O}_2$. An *ab-initio* PES is constructed in two steps. First, the potential energy of a particular atomic arrangement is computed; this is known as the electronic structure calculation. In this step, the Schrödinger equation is solved using the Born-Oppenheimer approximation, which decouples the motion of electrons from the motion of nuclei. The electronic structure, which determines the potential energy, is therefore computed using quantum mechanics. This allows for an accurate representation of the multi-atomic systems that exist as bonds are broken and formed. Each electronic structure

⁵For US3D and DPLR, this information is based on first-hand knowledge of the code, by either Chaudhry or Dr. Ioannis Nompelis. For LAURA and FUN3D, this information is based on personal communication with Dr. Peter Gnoffo, January 18, 2017.

calculation has uncertainty which depends on the atomic system and the method used to solve the approximate Schrödinger equation. In order to construct the PES, many electronic structure calculations are performed for a variety of nuclear positions.

The second step is to fit the potential energy at each electronic structure point to a multi-dimensional surface, the PES. A global, high-order polynomial with terms tailored to physical features of the atomic system is typically used. A local moving least-squares method was explored by Bender *et al.* [62]; it was found to be more accurate but less computationally efficient than the global fit. Fitting uncertainty is often measured using mean unsigned error (MUE), which is the average absolute difference in energy between electronic structure points and the PES. The accuracy of the fitting method should be at least comparable to the accuracy of the underlying electronic structure method. Otherwise, there is no basis to claim that QCT calculations meaningfully leverage the electronic structure dataset.

For the present work, we use *ab-initio* PESs from the Truhlar group: $\text{N}_2 + \text{N}_2$ and $\text{N}_2 + \text{N}$ interactions use the N_4 surface due to Paukku *et al.* [25, 63, 64], $\text{N}_2 + \text{O}_2$ interactions use the N_2O_2 surface due to Varga *et al.* [65], $\text{O}_2 + \text{O}_2$ interactions use the O_4 surfaces due to Paukku *et al.* [66, 67], and $\text{O}_2 + \text{O}$ interactions use the O_3 surfaces due to Varga *et al.* [68]. All of these surfaces are freely available online [69, 70]. These surfaces were created specifically to study reaction rates and energy transfer mechanisms at hypersonic conditions. Their electronic structure calculations use the complete active space second-order perturbation theory (CASPT2) method, which is designed to treat fully and partially-broken bonds [71, 72]. The PESs are fit using permutationally-invariant polynomials, which ensures the surface yields the same energy when two homogeneous atoms are swapped. Uncertainties associated with the electronic structure calculation and the fitting procedure are discussed in detail in the cited papers. For the PESs used for nitrogen dissociation, for example, the MUE for points below 10 eV (approximately the dissociation energy of N_2) is below 0.1 eV [25, 65].

1.4.1 Electronic Energy

We assume that each reactant begins at and remains in the ground electronic state throughout the trajectory. The QCT calculation, therefore, neglects electronic energy. This assumption is particularly relevant for O_2 , which has two relatively low-lying electronic energy levels. In a real relaxing and dissociating gas ensemble, these levels will become populated to some extent, and they have a higher dissociation rate than the ground electronic state. The precise effect of electronically-excited molecules on dissociation, for the conditions we are interested in, remains unknown. Perhaps, similar to vibrational energy, some non-Boltzmann distribution of electronic energy levels is formed as electronic energy relaxation balances with depletion due to dissociation.

An approximation for the effect of electronic energy on the oxygen dissociation rate was initially proposed by Nikitin [73] and is also described by Andrienko and Boyd [74] and Grover [75]. First, the population distribution of all bound electronic levels is assumed to be Boltzmann. Second, dissociation from each electronically-excited state is assumed to be more likely than the ground electronic state, by an amount equal to the Boltzmann factor $\exp\left(\frac{\varepsilon}{k_B T}\right)$, where the energy ε is the difference in well depth between the ground and excited state. Therefore, the population of each electronically-excited state is less than the ground state *by the same factor* that it is more likely to dissociate. These factors cancel, and so each electronic state, including the ground state, contributes an amount to the final dissociation rate equal to its degeneracy. The ground-state degeneracy is 3, the two low-lying levels have degeneracies 2 and 1, and the remaining 3 bound states (all within 1 eV of dissociation) have a combined degeneracy of 10. Combining all bound states yields the multisurface correction factor, $\eta = \frac{16}{3}$. In order to account for the effect of electronic energy, the dissociation rate is simply multiplied by this factor for all temperatures. This method is very approximate, and Nikitin notes a particularly low certainty associated with states near the bound limit, which contribute $\frac{10}{3}$ to the factor. Nevertheless, it has been used by several other researchers, sometimes to achieve a reasonable match with experiment, as we discuss in the next Section. Unless stated otherwise, we do not multiply by this factor. In our view, the uncertainty in reaction rate associated with electronic energy is approximately bounded by using or not using the multisurface correction factor.

1.4.2 System Spin and Degenerate Interaction States

All trajectories we consider are assumed to be *spin-conserving*, which means that the system's quantum spin is invariant. This is a reasonable assumption for the interactions we consider, because nitrogen and oxygen are relatively heavy. The initial spin state for each reactant corresponds to its ground electronic state, and the reactants' spins combine to yield the system spin. System spin is a necessary input to an electronic structure calculation. Therefore, each PES is constructed for a particular system spin, which corresponds to the interaction of interest. For example, N₂ is a singlet and O₂ is a triplet, which combine to yield a triplet system, and so the N₂O₂ surface designed to simulate N₂ + O₂ interactions is a triplet PES.

Therefore, simply having the correct atomic constituents is an insufficient condition for a PES to be valid for a given interaction. For example, the N₂O₂ surface with one oxygen atom far away is invalid for N₂ + O interactions, because the spin state of the subsystem is neither correct nor invariant. For N₂ + O interactions, a separate N₂O PES has been developed [76]. The N₄ surface, in contrast, may be used to simulate N₂ + N interactions

when one atom is far away. N_2 is a singlet and N is a quartet⁶, and so the system of an $\text{N}_2 + \text{N}$ interaction is a quartet. For the N_4 PES, the whole system is a singlet (designed for $\text{N}_2 + \text{N}_2$), and spin state of the non-interacting N is a quartet, which means that the remaining N_3 system is a quartet as required. Furthermore, for a variety of interacting $\text{N}_2 + \text{N}$ atomic arrangements, this N_3 subsystem remains a quartet⁷. Only when the subsystem has the correct system spin *and* remains invariant during interaction may a PES be used to perform QCT calculations with one atom placed far away.

For both $\text{O}_2 + \text{O}_2$ and $\text{O}_2 + \text{O}$ interactions, more than one interaction state is possible, even though all reactants are in their ground electronic state. O_2 is a triplet, and two triplets combine to yield either a singlet, triplet, or quintet system. When two oxygen molecules combine, the spin state of the interacting system is randomly selected from these three possibilities. The probability of each state is 1, 3, and 5 for the singlet, triplet, and quintet system respectively. Atomic oxygen is also a triplet, and so $\text{O}_2 + \text{O}$ interactions occur at one of three spin states, as with $\text{O}_2 + \text{O}_2$. Furthermore, three colliding atoms form a plane of interaction that is invariant, which results in a threefold spatial degeneracy for each spin state. For each spin state, the $1\text{A}'$, $1\text{A}''$, and $2\text{A}'$ states are equally possible. The spin multiplicity (e.g., 1 for singlet) is denoted in superscript, so there are 9 total interaction states that may occur for ground-state $\text{O}_2 + \text{O}$ interactions: $1^1\text{A}'$, $1^1\text{A}''$, $2^1\text{A}'$, $1^3\text{A}'$, $1^3\text{A}''$, $2^3\text{A}'$, $1^5\text{A}'$, $1^5\text{A}''$ and $2^5\text{A}'$. These states, and their degeneracies, are summarized in Table 1.3. The table also includes the equilibrium fraction, which is used in Section 2.3.2.

PESs for all three spin states for $\text{O}_2 + \text{O}_2$ were constructed by Paukku *et al.* [66, 67], and for all nine interaction states for $\text{O}_2 + \text{O}$ by Varga *et al.* [68]. One of the primary goals of our work with oxygen dissociation is to assess the difference between these surfaces. Along with the complementary PES and DMS analysis by Grover *et al.* [78, 79], this is the first comparison between degenerate interaction states for oxygen reactions that we are aware of. As described in Section 2.3.2, trajectories are computed for each PES separately, and then combined in postprocessing. We refer to results for the weighted average over all interaction states as the ‘system’, or ‘SYS’. Unless otherwise stated, results are for the system, rather than any single interaction state. We reiterate that our $\text{O}_2 + \text{O}_2$ and $\text{O}_2 + \text{O}$ trajectories are still spin-conserving and electronically adiabatic, but they consider the multiple ground-electronic-state degenerate states.

The Varandas and Pais [80] O_3 PES was constructed using a combination of *ab-initio* calculations and experimental data for ozone. The PES is of the the $1^1\text{A}'$ interaction state, which is the only one that admits ozone. This PES was originally designed to study ozone at relatively low temperatures, but it has been used by several researchers to study $\text{O}_2 + \text{O}$ at

⁶A good resource for the spin states discussed here is the Computational Chemistry Comparison and Benchmark DataBase (CCCBDB) [77]

⁷Personal communication with Dr. Yuliya Paukku, November 16, 2018.

Table 1.3: Ground-electronic-state interaction states for $O_2 + O_2$ and $O_2 + O$, with the corresponding degeneracy and equilibrium fraction.

Reactants	Interaction State	Degeneracy	Equilibrium Fraction
$O_2 + O_2$	singlet	1	1/9
	triplet	3	3/9
	quintet	5	5/9
$O_2 + O$	$1^1A'$	1	1/27
	$1^1A''$	1	1/27
	$2^1A'$	1	1/27
	$1^3A'$	3	3/27
	$1^3A''$	3	3/27
	$2^3A'$	3	3/27
	$1^5A'$	5	5/27
	$1^5A''$	5	5/27
	$2^5A'$	5	5/27

hypersonic conditions, which we discuss in the next Section. The Varandas and Pais [81] O_4 surface was also constructed using data from ozone. We discuss this further in Section 3.3.2.

1.5 Quasiclassical Trajectory Literature Review

As we described briefly in Section 1.1, quasiclassical trajectories are used in a variety of ways to study thermochemical kinetics. In all cases, the core concept is similar; the time-evolution of an atomic system, corresponding to an interaction of interest, is computed classically using a PES. What differentiates these methods is the manner of particle initialization and the use of the QCT result. In this Section, we describe some of the QCT literature for chemical reactions in air.

1.5.1 State-to-State and Master Equation

At the most detailed level, QCT calculations may be used to compute integral cross sections $\sigma_{if}(E_r)$. This cross section reflects the probability of initial state i transitioning to final state f , given relative translational energy E_r . The cross section for a specific transition may be integrated in translational energy, by assuming an equilibrium distribution of translational energy at some translational temperature, to yield a state-to-state rate. Then, the population of each rovibrational level, in a dissociating and relaxing gas ensemble, may be computed in time; this is known as master equation analysis. A good description is given by Jaffe *et al.* [26].

A database of state-to-state rates were computed for $\text{N}_2 + \text{N}$ interactions by Jaffe *et al.* [82–84]. Nitrogen has approximately 10,000 rovibrational levels, so there are a total of approximately 10^8 transition rates: from each level to each level. Using this database, the dynamics of the N_3 system was studied by Kim and Boyd [85] and Panesi *et al.* [84, 86]. They found that exchange reactions in $\text{N}_2 + \text{N}$ substantially enhance the rate of vibrational relaxation of nitrogen in the presence of atomic nitrogen. Andrienko and Boyd [74, 87–90] have analyzed $\text{O}_2 + \text{O}$, including using the master equation, and found that exchange reactions in oxygen play a similar role. These calculations for an atom-diatom system required a large amount of QCT data, but they were feasible.

A similar effort for diatom-diatom interactions, however, is computationally infeasible. A total of approximately 10^{15} transitions would be required [27, 91]: from each initial diatom-diatom combination to each final diatom-diatom combination. Therefore, the full rovibrational state-to-state approach must be modified to treat diatom-diatom interactions, which are of course critically important for air chemistry. Instead of resolving the population of each rovibrational level, and computing state-to-state rates for all of them, states are typically grouped in some fashion. In the vibrational state-to-state approach, which was used recently by Andrienko and Boyd [92] to study $\text{O}_2 + \text{O}_2$, rotation is assumed to be at thermal equilibrium at the translational temperature. States with similar energy may be grouped instead; Torres and Magin [93] used energy bins with variable width to study $\text{N}_2 + \text{N}$ for DSMC.

Grouping by any strategy is an approximation that states in the same group behave similarly and may be therefore described in aggregate. Macdonald *et al.* [91] developed and compared two coarse-grained grouping models for $\text{N}_2 + \text{N}_2$ interactions; the results are qualitatively and quantitatively dependent on the grouping model. The relaxation process was found to be best captured by grouping each vibrational level separately. The dissociation process, however, was found to be best captured by grouping based on internal energy. This means that rotational energy contributes meaningfully to the dissociation process. Sahai *et al.* [94] explored adaptive grouping strategies that combine rovibrational states connected by highly-probable transitions.

1.5.2 Sampling from Fixed Distributions

Trajectories may alternatively be initialized by sampling from Boltzmann or approximately-Boltzmann distributions characterized by one or more temperatures. When the rotational and vibrational temperature is the same, a Boltzmann distribution at T_{rv} is used. When the rotational and vibrational temperatures are different, an exactly Boltzmann distribution is impossible, due to rovibrational coupling [25]. Instead, the distribution of rotational energies is nearly Boltzmann at T_r , and the distribution of vibrational energies is nearly Boltzmann

at T_v . As we have discussed, the population of a relaxing and dissociating gas ensemble is non-Boltzmann because of depletion of the high-energy tail. Therefore, any combination of T_r and T_v is not an accurate representation of the true distribution that exists in reality.

Nevertheless, this method has several advantages. Aggregate quantities of interest, such as reaction rates or average energy change per reaction, may be relatively rapidly converged using Monte-Carlo sampling [24]. In contrast to state-resolved calculations, the dissociation rate from each state does not need to be captured. Rigorous uncertainty estimates due to statistical error may also be computed and propagated to derived quantities. Additionally, analysis is flexible and relatively simple; one simply averages over a batch of trajectories sampled from the condition of interest. We use this technique for our present work.

Bose and Candler studied the first [95, 96] and second [97] Zeldovich reactions using trajectories sampled from three generally-distinct temperatures. They found that NO formed at nonequilibrium conditions is relatively rotationally and vibrationally excited. Building on simulations of Boyd *et al.* [98], CFD calculations incorporating using this result [99] were found to match the bow-shock ultra-violet (BSUV) experiments [100–103].

Bender *et al.* [25] simulated $N_2 + N_2$ interactions using trajectories sampled from T_{tr} and T_v , using the PES due to Paukku *et al.* [25, 63, 64]. When conditions were sampled with $T_{tr} = T_v$, molecules that dissociate were found to be primarily vibrationally-excited. When vibrational temperature was substantially below translational-rotational temperature, rotation was found to compensate. Therefore, for all conditions simulated, the average internal energy decrease per dissociation is near the dissociation energy. Many of Bender's results and methods are incorporated into the present work.

If the initial distribution of molecules is known, stratified sampling can be used to accelerate statistical convergence. The initial distribution is modified to yield more events of interest; impact parameter is typically the only altered reactant quantity. This modification must be corrected for in postprocessing. It's also possible to discard trajectories which do not have sufficient energy to yield events of interest; this technique was used by Voelkel *et al.* [104] to capture dissociation for a wide range of conditions, including low temperatures that are difficult to converge otherwise. Andrienko and Boyd [92] also skipped trajectories which do not have sufficient energy for the case of $O_2 + O_2$ at 3000 K. This exclusion technique may be thought of as extreme stratified sampling in total collision energy, and it has the potential to substantially reduce the number of trajectories computed for low temperatures. However, only retaining trajectories with energy above the dissociation energy means that events requiring less than the dissociation energy, such as exchange reactions, are not captured correctly.

1.5.3 Direct Molecular Simulation

The Direct Molecular Simulation (DMS) method has been developed within the last decade by the Schwartzentruber group. In this technique, the outcome of each trajectory calculation is retained, to be used as an input for a subsequent trajectory calculation. Colliding particles are selected using a DSMC framework. The population distribution therefore evolves in time, and this distribution, along with other aggregate quantities of interest, are a result of the simulation. For studying chemical kinetics, the transient behavior of a zero-dimensional reactor is often considered, but spatial variation is also possible. Schwartzentruber *et al.* [27] has recently reviewed and summarized the method.

Koura [105, 106] combined classical trajectory calculations with DSMC, calling it CTC-DSMC, to study rotational relaxation through a shock. Norman *et al.* [107] validated the method using molecular dynamics simulations, and explored speedup using GPUs. Valentini *et al.* [108] first extended the method to study vibrational relaxation. Next, the *ab-initio* N₄ PES due to Paukku *et al.* [25, 63, 64] was implemented, enabling dissociation to be simulated. Valentini *et al.* then studied relaxing and dissociating nitrogen with only N₂ + N₂ interactions [10], and with both N₂ + N₂ and N₂ + N interactions [11]. The dissociation rate for a nitrogen ensemble with only N₂ + N₂ interactions was found to be lower than the corresponding Boltzmann rate by a factor of between 4 and 5, due to depletion of the high-energy tail during QSS. Enabling N₂ + N interactions was found to increase the dissociation rate by approximately a factor of 2, due to exchange reactions promoting vibrational relaxation. This effect is discussed further in Section 3.1.2.

Master equation analysis and DMS are both designed to capture the dynamics of the non-Boltzmann distributions that exist in a relaxing and dissociating gas ensemble. Unlike fully-resolved state-to-state, however, DMS remains tractable for diatom-diatom interactions because it relies on Monte Carlo sampling. Results from master equation and DMS have recently been compared by Macdonald *et al.* for both N₂ + N [109] and N₂ + N₂ [110] interactions. Jaffe *et al.* [111] also compared results of N₂ + N₂ interactions for two different N₄ surfaces. Grover *et al.* has studied O₂ + O₂ [112] and O₂ + O [78, 79] interactions using multiple PESs from the Truhlar group [66–68]. We compare to some of those results in Section 3.3.

The DMS method is relatively expensive, because a trajectory is simulated for every diatom-diatom or diatom-atom interaction. However, it is able to simulate a gas that includes diatom-diatom interactions, using only PESs as an input. As a result, DMS has revealed insights about the dissociation process, especially QSS. The QCT technique chosen for the present work, which uses fixed distributions characterized by T_{tr} and T_{v} , is complemented well by DMS. Fixed distributions enable rigorously-quantified statistical uncertainty, and the in-depth analysis of a single, invariant state. Throughout this work,

we will often reference the corresponding DMS result, and our QCT analyses have been performed in close cooperation with DMS authors, especially Grover.

Chapter 2

QCT Methodology

In this project, we rely heavily on the work by Bender *et al.* [25, 113]. In particular, he was the primary developer of the Rovibrational Energetics and Analysis of QuasiClassical Trajectories (REAQCT) code package, which was used to run a suite of trajectory calculations on $\text{N}_2 + \text{N}_2$. A small portion of the REAQCT code is based on the Adiabatic and Nonadiabatic Trajectories (ANT) code developed by the Truhlar group [114]. We also use REAQCT, and focus here on the extensions and modifications made to the preexisting methodology and tools. As we will discuss in this Chapter, these extensions include stratified sampling in more than one dimension, postprocessing joint probability distribution functions (PDFs), and uncertainties for more quantities of interest. Therefore, only the basics of our underlying QCT methodology are described here, and the interested reader is directed to Bender's excellent methodology section [113, p. 62 to 90] and the supporting literature cited therein.

Our QCT analysis consists of three primary steps. First, the initial atomic positions and velocities are determined by sampling from distributions defined by the condition of interest. Second, using atomic forces described by the PES, the simulation progresses forward in time until the interaction is complete. Many such interactions are simulated, yielding a set of initial and final states for molecular interactions at the given condition. Third, aggregate quantities such as the dissociation probability are determined by postprocessing this set of interactions. Most of the methodological progress made in the present work applies to the third step.

2.1 Preparation of Particles

2.1.1 Enumeration of Rovibrational Levels

For each reactant diatom, we first construct a list of every possible rovibrational state, along with that state's energy. This process depends on the diatomic potential $V_D(r)$ which describes the energy of a diatom as a function of the interatomic spacing. Each of the multi-atom PESs used also contains a diatomic potential for each possible combination of atoms; this diatomic potential is evaluated separately when possible to reduce computational cost. The effective diatomic potential is the diatomic potential plus a centrifugal term,

$$V_{D,\text{eff}}(r, j) = V_D(r) + \frac{j(j+1)\hbar^2}{2\mu_D r^2} \quad (2.1)$$

where j is the rotational quantum number, \hbar is the reduced Planck's constant and μ_D is the reduced mass for the diatom. For each integer value of j , all possible vibrational levels are computed by solving the vibrational Schrödinger equation using the semiclassical Wentzel-Kramers-Brillouin approximation [24, 113]. This procedure yields N_{rv} total rovibrational levels, and the corresponding energies ε_{int} and rotational and vibrational quantum numbers.

At this point, we identify several quantities based on the enumerated rovibrational levels that we will use elsewhere. The energy of the ground rovibrational state ($v=0, j=0$), relative to the minimum in the diatomic potential, is known as the ground-state energy,

$$\varepsilon_{\text{GS}} = \varepsilon_{\text{int}}(v=0, j=0) - V_{D,\text{min}} \quad (2.2)$$

This energy is often denoted as $\frac{1}{2}\hbar\nu$ (eg. Boyd and Schwartzentruber [35, p. 66]), and it is also related to the characteristic vibrational temperature,

$$\Theta_v = \frac{2\varepsilon_{\text{GS}}}{k_B} \quad (2.3)$$

In this work, we represent molecular energies relative to the ground state, rather than the minimum of the diatomic potential as was previously done by Bender [25]. This choice was made for consistency with CFD, and it is also the recommendation of Vincenti and Kruger [115, p. 137]. Only the postprocessing is affected, but some quantities of interest, such as the vibrational energy change per dissociation, will be offset by ε_{GS} compared to previous results.

The dissociation energy, measured relative to the ground state, is

$$D_0 = \lim_{r \rightarrow \infty} V_D(r) - \varepsilon_{\text{int}}(v=0, j=0) \quad (2.4)$$

Table 2.1: Statistics about various diatomic potentials used in the present work. Dissociation energy is also shown in Tables C.2 and C.3

Diatomc Potential	r_{eq} [\AA]	Dissociation Energy		Ground State			v_{max}	j_{max}	\mathcal{N}_{rv}
		D_0 [eV]	T_D [K]	ε_{GS} [eV]	Θ_v [K]				
N ₂ in N ₄ [25, 63, 64]*	1.098	9.7704	113,381	0.1470	3411	54	278	9198	
N ₂ in N ₂ O ₂ [65]	1.098	9.7572	113,228	0.1471	3415	54	278	9181	
NO in N ₂ O ₂ [65]	1.152	6.5002	75,431	0.1173	2722	45	245	6809	
O ₂ in O ₄ , O ₃ [66–68]	1.208	5.1130	59,334	0.0982	2280	44	241	6115	
O ₂ in N ₂ O ₂ [65]	1.207	5.1167	59,377	0.0975	2263	36	252	5900	

* The N₄ surface is used for both N₂ + N₂ and N₂ + N interactions.

This energy corresponds to the dissociation temperature T_D and the formation enthalpy h_s . Rovibrational levels with energy greater than the dissociation energy exist; these states are *quasibound*. The equilibrium bond length r_{eq} is the separation distance at which the diatomic potential is minimized. Table 2.1 shows summary values for all diatomic potentials considered for the present work.

2.1.2 Separation of Energies

As we will describe in Section 2.1.3, we choose to sample initial conditions from distributions characterized by two temperatures: rotational T_r and vibrational T_v . In order to construct a distribution when these two temperatures are different, we must define a methodology to separate the internal energy of a state into rotational and vibrational components. This separation is ambiguously defined, because rotation and vibration are coupled, especially at high v and j combinations. Two separation frameworks are considered for the present work [116]; each involves defining one component of energy in terms of its corresponding quantum number only, and then assigning the remaining energy to the other component.

In a vibration-prioritized framework, the vibrational energy of a given v -level is defined using the $j=0$ state,

$$\varepsilon_{\text{vib}}(v, j) = \varepsilon_{\text{vib}}(v) \equiv \varepsilon_{\text{int}}(v, j=0) \quad (2.5)$$

$$\varepsilon_{\text{rot}}(v, j) = \varepsilon_{\text{int}}(v, j) - \varepsilon_{\text{vib}}(v) \quad (2.6)$$

This strategy is commonly employed by researchers at the University of Minnesota and elsewhere [25, 74, 78, 79, 84, 86], and we use it for the present work also.

For the purposes of comparison, we also consider the rotation-prioritized framework,

$$\varepsilon_{\text{rot}}(v, j) = \varepsilon_{\text{rot}}(j) \equiv \min[V_{\text{D,eff}}(j)] \quad (2.7)$$

$$\varepsilon_{\text{vib}}(v, j) = \varepsilon_{\text{int}}(v, j) - \varepsilon_{\text{rot}}(j) \quad (2.8)$$

These two frameworks are illustrated in Figure 2.1, which shows how a particular rovibrational level is calculated using each framework. The state ($v=30, j=150$) is chosen as an example because it yields a relatively large difference in component energies computed both ways. We quantify this difference using the following metric,

$$\mathcal{D}_{\text{rot-vib}}(v, j) = \frac{\varepsilon_{\text{vib}}^{(\text{vib-prio})}(v, j) - \varepsilon_{\text{vib}}^{(\text{rot-prio})}(v, j)}{\varepsilon_{\text{int}}(v, j)} 100\% \quad (2.9)$$

which is plotted for two of the diatomic potentials we use in Figure 2.2. The difference between these frameworks, which may be interpreted as the rovibrational coupling we neglect by choosing to separate in the first place, is largest when both v and j are large. For all diatomic potentials we consider, the largest difference is slightly less than 20% for a single rovibrational state. We also examine the effect of separation methodology briefly in Section 3.5.4; we should remain aware of the issues surrounding separating rotational and vibrational energy.

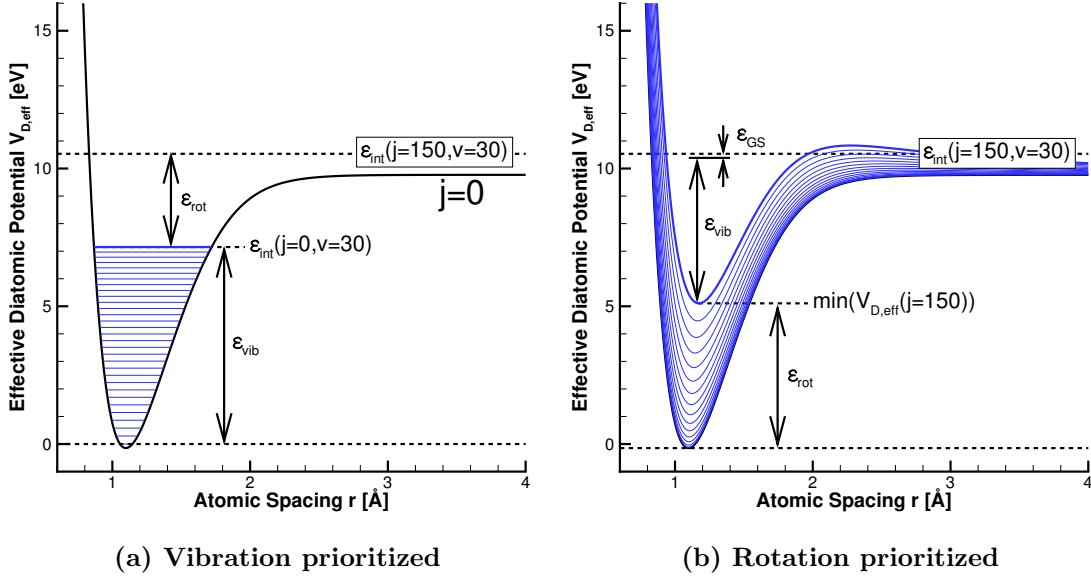
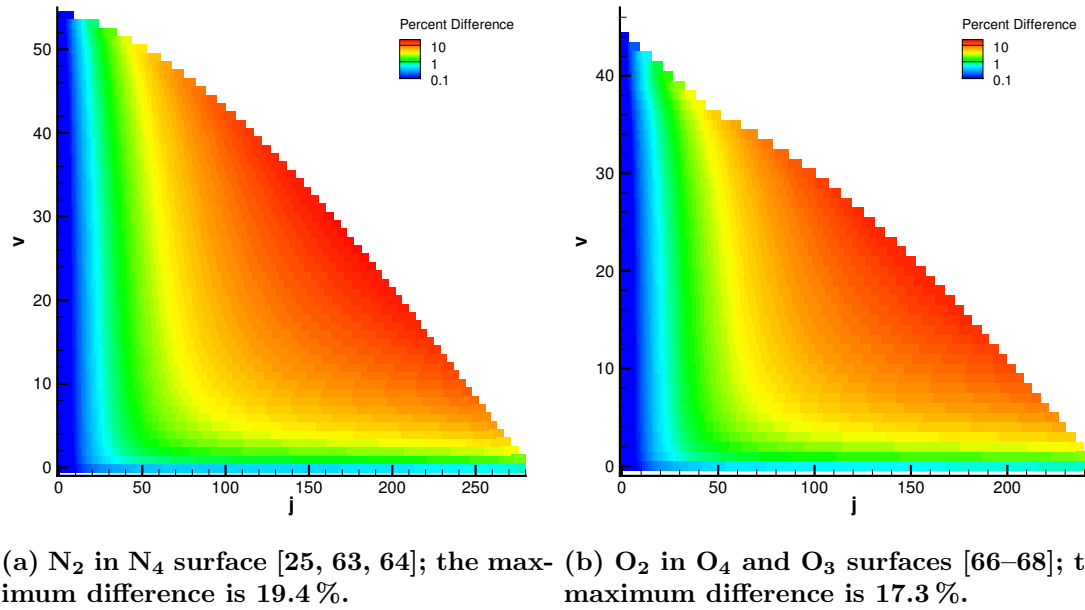


Figure 2.1: Schematic for how internal energy is separated into vibrational and rotational components, for the two frameworks considered in this work.



(a) N_2 in N_4 surface [25, 63, 64]; the maximum difference is 19.4 %. (b) O_2 in O_4 and O_3 surfaces [66–68]; the maximum difference is 17.3 %.

Figure 2.2: Difference between vibration-prioritized and rotation-prioritized energy separation frameworks, for two of the diatomic potentials used in this work. Difference is defined in Equation (2.9).

2.1.3 Distribution of States

Now that we have determined all possible rovibrational states, we must determine the probability of each level occurring in the ensemble we wish to study. A Boltzmann distribution of states characterized by a single rovibrational temperature T_{rv} is,

$$f(v, j) = \frac{1}{Q_{\text{rv}}(T_{\text{rv}})} (2j + 1) \exp\left(-\frac{\varepsilon_{\text{int}}(v, j)}{k_B T_{\text{rv}}}\right) \quad (2.10)$$

$$Q_{\text{rv}}(T_{\text{rv}}) = \sum_{v,j} (2j + 1) \exp\left(-\frac{\varepsilon_{\text{int}}(v, j)}{k_B T_{\text{rv}}}\right) \quad (2.11)$$

where the factor of $(2j + 1)$ is the degeneracy and Q_{rv} is the rovibrational partition function. We neglect the nuclear spin degeneracy.

The dynamics of a gas ensemble with rotation and vibration characterized by the same temperature is useful and forms a major component of the present work. However, we are also interested in studying the behavior of a gas in conditions similar to those encountered in hypersonic flows. As outlined in the introduction, and as we address in Section 3.5.2, vibrational energy distributions are often not described by the same temperature that describes rotation. We therefore generate distributions with rotational energy distributions characterized by T_r and vibrational energy distributions characterized by a different T_v . Following the multi-temperature model outlined by Bender *et al.* [25], we first define the distribution of vibrational quantum numbers using the vibrational temperature,¹

$$f(v) = \frac{1}{Q_v(T_v)} \exp\left(-\frac{\varepsilon_{\text{vib}}(v)}{k_B T_v}\right) \quad (2.12)$$

$$Q_v(T_v) = \sum_v \exp\left(-\frac{\varepsilon_{\text{vib}}(v)}{k_B T_v}\right) \quad (2.13)$$

where Q_v is the vibrational partition function. Then, the distribution of j -levels for a specific v is defined using the distribution of rovibrational levels that exist at the rotational temperature. This yields the following two-temperature distribution of rovibrational

¹Note that this procedure relies on vibrational energy being independent of j , which is satisfied for the vibration-prioritized separation framework but not the rotation-prioritized framework. A different procedure is required to generate distributions with $T_r \neq T_v$ and a rotation-prioritized separation of internal energy.

levels [25],

$$f(v, j) = \frac{1}{\eta} \frac{\exp\left(-\frac{\varepsilon_{\text{vib}}(v)}{k_B T_v}\right)}{Q_v(T_v)} \frac{\left(\frac{(2j+1) \exp\left(-\frac{\varepsilon_{\text{int}}(v,j)}{k_B T_r}\right)}{Q_{\text{rv}}(T_r)}\right)}{\left(\frac{\exp\left(-\frac{\varepsilon_{\text{vib}}(v)}{k_B T_r}\right)}{Q_v(T_r)}\right)} \quad (2.14)$$

in which η is a normalization factor that is near 1. Equation (2.14) reduces to a standard Boltzmann distribution, Equation (2.11), when $T_r = T_v$. When the temperatures are not equal, this expression yields a distribution of vibrational levels that resembles a Boltzmann at T_v , and the distribution of rotational levels resembles a Boltzmann at T_r . However, the match is not exact, and this expression should be recognized as only approximately Boltzmann. Nevertheless, Equation (2.14) is a reasonable model for a rovibrational distribution defined by T_r and T_v . The initial rovibrational state of each diatom is therefore determined by sampling from this distribution.

Other aspects of the initial trajectory are also determined, which is again described in more detail by Bender [113] and Truhlar and Muckerman [24]. The relative translation energy is sampled using the translational temperature via,

$$f(E_r) = \frac{E_r}{k_B T_t} \exp\left(-\frac{E_r}{k_B T_t}\right) \quad (2.15)$$

Impact parameter, b , is the initial distance between reactant centers-of-mass in the direction normal to their relative velocity. (A small impact parameter is a head-on collision, whereas a large impact parameter is a glancing collision.) The impact parameter is sampled from

$$f(b) = \frac{2b}{b_{\max}^2} \quad (2.16)$$

in which b_{\max} is the maximum impact parameter; this is dependent on the *sub-run* due to stratified sampling, which we discuss in Section 2.3.2. The direction of each molecule's angular momentum, and the phase within the rotation period, is also determined. Each molecule's vibrational phase is randomized by allowing the diatom to 'drift' for a random amount of time up to half its vibrational period, beginning from either the inner or outer turning point. Finally, each reactant is then placed a conservatively-large distance, 15 Å, apart. In this fashion, a single trajectory is prepared based on randomly sampling from the condition, defined by T_t , T_r , and T_v . Many trajectories are generated for each condition; the chosen conditions are discussed next.

2.1.4 Conditions Studied

For the present work, we study interactions between the following reactants: $\text{N}_2 + \text{N}_2$, $\text{N}_2 + \text{N}$, $\text{N}_2 + \text{O}_2$, $\text{O}_2 + \text{O}_2$, and $\text{O}_2 + \text{O}$. These interactions occur on the PESs described in Section 1.4. We are particularly interested in nitrogen and oxygen dissociation; these reactants yield each dissociation reaction with 3 different collision partners. For each dissociating molecule, we choose a temperature range of interest. Temperatures are then chosen within this range to be roughly evenly spaced in inverse temperature space. We are interested in conditions similar to those encountered in hypersonic flows, and so we consider two test sets. For the equilibrium test set, all temperatures are equal and take values within the temperature range. For the nonequilibrium test set, the translational-rotational temperature is set to a single, relatively high value, and the vibrational temperature varies within the temperature range. This strategy is chosen based on the results of Bender *et al.* [25], who simulated many combinations of T_{tr} and T_{v} and observed behavior primarily restricted to these two test sets.

Therefore, the conditions we consider are defined by T_{tr} and T_{v} . This allows us to directly compare to various vibrational-nonequilibrium chemical kinetic models designed for CFD, which is done in Section 3.6.5. Additionally, because QCT allows us to access detailed statistics for each collision, we can examine the effect of any reactant state, which is done in Section 3.5.

The temperature range chosen for studying nitrogen dissociation is 8000 K to 30,000 K, because the bond in N_2 is relatively strong. The fixed value of T_{tr} for the nitrogen nonequilibrium test set is 20,000 K. For oxygen dissociation, 4000 K to 13,000 K is chosen instead; the bond energy of O_2 is approximately half the bond energy of N_2 . The fixed value of T_{tr} for the oxygen nonequilibrium test set is 10,000 K. The specific temperatures studied are shown in Tables 2.2 and 2.3.

For each condition, the number of trajectories simulated is chosen to yield an estimated uncertainty of 5% or less, for each quantity of interest² The quantities of interest are the effective dissociation rate and average change in vibrational energy per dissociation. (Uncertainties, change in component energy, and rates are all defined later in this Chapter.) REAQCT easily allows for extra simulations to improve statistical convergence, and any combination of previous runs (typically at the same condition) may be analyzed together. Conditions in which we examine statistical cross-sections typically have extra trajectories. The number of trajectories computed for each condition is shown also in Tables 2.2 and 2.3.

²By November of 2018, this was achieved for all conditions in the database except for $\text{N}_2 + \text{O}_2$ at 4000 K. Additional trajectory calculations to reduce uncertainty for this condition are ongoing.

Table 2.2: Number of trajectories in the QCT database, for the purposes of studying nitrogen dissociation, in millions. For the equilibrium test set, $T_{\text{tr}} = T_v$; for the nonequilibrium test set, $T_{\text{tr}} = 20,000 \text{ K}$.

Reactants	Test Set	Vibrational Temperature T_v				
		8000 K	10,000 K	13,000 K	20,000 K	30,000 K
$\text{N}_2 + \text{N}_2^*$	Equilibrium	400	256	56	40 [†]	16
	Nonequilibrium	240	96	70	40 [†]	16
$\text{N}_2 + \text{N}^\ddagger$	Equilibrium	240	150	60	18 [†]	18
	Nonequilibrium	90	60	60	18 [†]	60
$\text{N}_2 + \text{O}_2$	Equilibrium	343 [§]	240 [§]	12 [§]	120 [†]	60
	Nonequilibrium	120	120	18	120 [†]	6

* The $\text{N}_2 + \text{N}_2$ trajectories were run almost entirely by Bender *et al.* [25].

† The condition with $T_{\text{tr}} = T_v = 20,000 \text{ K}$ is included in both the equilibrium and nonequilibrium test set.

‡ Some of the $\text{N}_2 + \text{N}$ results were first described in Valentini *et al.* [11].

§ These conditions are used to study both nitrogen dissociation and oxygen dissociation and are duplicated in Table 2.3

Table 2.3: Number of trajectories in the QCT database, for the purposes of studying oxygen dissociation, in millions. For the equilibrium test set, $T_{\text{tr}} = T_v$; for the nonequilibrium test set, $T_{\text{tr}} = 10,000 \text{ K}$.

Reactants	Test Set	Vibrational Temperature T_v					
		4000 K	5000 K	6500 K	8000 K	10,000 K	13,000 K
$\text{O}_2 + \text{O}_2^*$	Equilibrium	360	360	180	90	180 [*]	18
	Nonequilibrium	180	90	54	18	180 [*]	18
$\text{O}_2 + \text{O}^\ddagger$	Equilibrium	1080	540	270	54	540 [*]	54
	Nonequilibrium	540	270	54	54	540 [*]	54
$\text{N}_2 + \text{O}_2$	Equilibrium	360 [†]	1440	660	343 [‡]	240 ^{*,‡}	12 [‡]
	Nonequilibrium	30	600	120	120	240 ^{*,‡}	120

* The condition with $T_{\text{tr}} = T_v = 10,000 \text{ K}$ is included in both the equilibrium and nonequilibrium test set.

† Quantities of interest for $T_{\text{tr}} = T_v = 4000 \text{ K}$ have relative uncertainty above 5 %; trajectory runs are ongoing for this condition.

‡ These conditions are used to study both nitrogen dissociation and oxygen dissociation and are duplicated in Table 2.2.

2.2 Time Integration

Once the trajectory is initialized, the simulation steps forward in time. Each atom is treated separately, and they move classically according to $\vec{F} = m\vec{a}$. Throughout the trajectory, the force on each atom is described by the PES, via $\vec{F} = -\frac{\partial V}{\partial \vec{x}}$. A velocity Verlet integrator is used for time integration, which is second-order accurate. The timestep is fixed at 0.05 fs, based on an energy conservation and rate convergence analysis performed by Bender [113] for the N₂ + N₂ system at 30,000 K. The inter-molecular cutoff distance for terminating a trajectory is 15 Å and, for the purposes of terminating a trajectory due to dissociation, the threshold to define a molecular bond as broken is 10 Å.

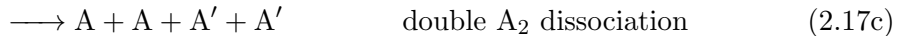
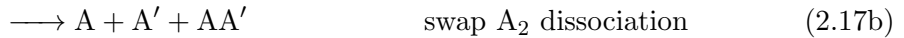
The time integration step of the QCT process is by far the most computationally expensive, primarily due to the cost of evaluating the multibody PES. A variety of other time integration methods are used by other QCT practitioners in the literature. Andrienko and Boyd [74] used an 11th-order accurate accurate Adams-Bashforth-Moulton scheme with a variable timestep between 100 fs and 0.1 μs for the O₂ + O system. In the QCT analysis of N₂ + O by Lin *et al.* [117], a Bulirsch-Stoer integrator was used, which also has a variable time step. A good overview of time step methods for QCT is provided by Truhlar and Muckerman [24]. In the future, these other methods should at least be tested; a variable time step has the potential to provide substantial computational savings because the force acting on each atom is highly variable throughout a trajectory calculation³. Other tunable constants, such as the initial trajectory spacing and trajectory termination thresholds, could also be analyzed. We chose not to focus on such analyses in the present work, however, and simply retained the values determined by Bender [113].

³ Any savings that does occur would likely provide more payoff for DMS than QCT, due to the relatively large number of high-*b* trajectories computed in DMS because stratified sampling is not available.

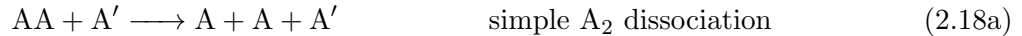
2.3 Processing of Final States

2.3.1 Possible Reactions and Rate Expressions

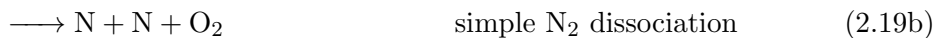
When the interaction is complete, the final state is analyzed as described by Bender [113] and Grover [75]. Based on the final arrangement of atoms and diatoms, the following events are possible. A prime is used to distinguish between atoms when necessary. For an $N_2 + N_2$ or $O_2 + O_2$ interaction, which we denote as $A_2 + A_2$,



For an $N_2 + N$ or $O_2 + O$ interaction, which we denote as $A_2 + A$,



Finally, for an $N_2 + O_2$ interaction,



In a simple dissociation, one reactant's atomic constituents are unchanged, and the other reactant dissociates. In a swap dissociation, both reactant bonds break and one new bond is formed; this event is termed ‘dissociation and exchange’ in $N_2 + O_2$ because a new molecule is formed. In a double dissociation, both reactant bonds break and no new bonds are formed. For all trajectories at a given condition, each of these events has a probability of occurring, P_e , which we will describe in Section 2.3.3. This probability is used to compute

a reaction rate for each event,

$$k_e = \frac{1}{\mathcal{S}} \pi b_{\max}^2 \sqrt{\frac{8k_B T_t}{\pi \mu_C}} P_e \quad (2.20)$$

in which μ_C is the reduced mass of the collision partners. The symmetry factor, \mathcal{S} , is 2 if the reactants are identical and 1 otherwise, and is used to address the “double-counting” issue [115, p. 52].

Different reactions may have identical effects on species concentrations. For example, both simple and swap dissociations in $N_2 + N_2$ result in the destruction of one nitrogen molecule and the formation of two nitrogen atoms. A double dissociation, too, has the same effect on species concentration as two subsequent simple dissociations. From the macroscopic perspective of either CFD or shock tube experiments, these reactions are indistinguishable. Existing experimental data and CFD models aggregate the effect of reactions with the same result into a single rate. In the Park [18] model, for example, reactions Equations (2.17a) to (2.17c) are combined into a single rate of A_2 dissociation via A_2 partner. In QCT, we can distinguish between all reactions; Bender *et al.* [25] found that swap dissociations are moderately prevalent in high temperature $N_2 + N_2$ collisions. Therefore, for the purposes of comparing with existing data and between collision partners, we also define aggregated rates. For each set of reactants, the effective dissociation rate is

$$k_{d,\text{eff}}^{(A_2+A_2)} = k_{d,\text{simple}} + 2 k_{d,\text{double}} + k_{d,\text{swap}} \quad (2.21)$$

$$k_{d,\text{eff}}^{(A_2+A)} = k_{d,\text{simple}} \quad (2.22)$$

$$k_{d,\text{eff}}^{(A_2+B_2)} = k_{d,\text{simple}} + k_{d,\text{double}} \quad (2.23)$$

We will often refer to the effective dissociation rate simply as k_d . Because a ‘dissociation and exchange’ reaction produces NO, it is not included in the effective rate constant. We find that reactions combined into the same effective rate are different from a microscopic perspective, which may have consequences for modeling, see Section 3.5.3.

2.3.2 Stratified Sampling

Stratified sampling is the practice of modifying the initial distribution of some reactant state, in order to achieve more rapid statistical convergence for some quantity of interest. This modification is then corrected for in postprocessing. The first variable we perform stratified sampling in, impact parameter b , is used to describe and motivate the process.

To capture almost all events, the maximum impact parameter, b_{\max} , must be relatively large; most of our data use $b_{\max} = 6 \text{ \AA}$. However, events of interest, including dissociation and energy exchange, are more probable when the impact parameter is low. Recall that

the distribution of impact parameters, which was shown in (2.16), is proportional to the impact parameter. Thus, without modification, the majority of trajectories computed would be uninteresting, and statistics of interest would be more difficult to converge. Thus, we modify the initial distribution of impact parameters to select more low- b collisions, resulting in a better-converged reaction rate. We choose to sample trajectories for a given condition in batches, each with a different b_{\max} from 1 Å to 6 Å, spaced 1 Å apart. The number of strata in impact parameter, K_b , is therefore 6⁴.

The k_b -th stratum has minimum impact parameter b_k^- and maximum impact parameter b_k^+ . Each strata contributes a fraction $\mathcal{V}_{b,k}$ to the final statistics, such that the true distribution, Equation (2.16), is satisfied,

$$\mathcal{V}_{b,k} = \frac{(b_k^-)^2 - (b_k^+)^2}{b_{\max}^2} \quad (2.24)$$

where the strata are assumed to be sorted in ascending order in b . Stratified sampling in impact parameter is relatively common, and is also described by Truhlar and Muckerman [24] and Bender *et al.* [25]. In the case of $b_{\max} = 6$ Å with 1 Å spacing, approximately 25 % of all collisions are below 1 Å, compared to 2.8 % with no stratified sampling.

We also perform stratified sampling in the ground-electronic-state degenerate state s . As discussed in Section 1.4, O₂ + O₂ interactions may occur on one of three ground-electronic-state spin states: singlet, triplet and quintet. O₂ + O interactions may occur on one of nine states: three spin states and either 1 A', 1 A'', or 2 A'. Each of these interaction states has a corresponding PES, which must be randomly selected in a manner similar to how the initial rovibrational state is selected. When all surfaces are considered together, we refer to the condition as the O₂ + O₂ ‘system’, ‘SYS’, or simply O₂ + O₂. However, we are also interested in statistics, such as the distribution of v -levels among dissociating trajectories, for each surface. Therefore, we often compute the same number (or an arbitrary number) of trajectories for each PES, and the correctly-averaged result must be computed using stratified sampling. Each degenerate state is one stratum, and has a weight equal to its equilibrium fraction shown in Table 1.3.

We could also perform stratified sampling in other variables, such as relative translational energy E_r . The total number of variables to perform stratified sampling in is N_k , or the ‘number of dimensions’ of stratified sampling. For our current work, N_k is 2 for O₂ + O₂ and O₂ + O interactions, and 1 for all other interactions. Our analysis is valid for any

⁴Most of the N₂ + N₂ trajectories computed by Bender [25] use a maximum impact parameter of 8 Å instead; Tables B.1 to B.3 shows all conditions in the QCT database that do not use $b_{\max} = 6$ Å.

number of stratified sampling variables, however. We define a vector of stratum indexes,

$$\bar{k} = (k_1, \dots, k_{N_k}) \quad (2.25)$$

For example, in $O_2 + O_2$ interactions, this vector contains the index of impact parameter stratum and ground-electronic-state interaction state stratum, $\bar{k} = (k_b, k_s)$. The volume of a specific stratum in all stratified sampling dimensions is the product of each dimension's volume,

$$\mathcal{V}_{\bar{k}} = \prod_{d=1}^{N_k} \mathcal{V}_{d,\bar{k}_d} \quad (2.26)$$

By construction, the volume of any one stratified sampling dimension must sum to one,

$$\sum_{k_d=1}^{K_d} \mathcal{V}_{d,k_d} = 1 \quad (2.27)$$

and all strata in the entire stratified sampling space must also sum to one,

$$\sum_{\bar{k} \in \bar{K}} \mathcal{V}_{\bar{k}} = 1 \quad (2.28)$$

The values of \mathcal{V} will be used in the next section. We also note here that this is equivalent to weighting each trajectory in the \bar{k} -th stratum with weight w ,

$$w_{\bar{k}} = \frac{\mathcal{V}_{\bar{k}}}{\mathcal{N}_{\bar{k}}} \quad (2.29)$$

where $\mathcal{N}_{\bar{k}}$ is the number of trajectories in stratum \bar{k} . The total of all weights, across all trajectories, is therefore also one,

$$\sum_i^{\mathcal{N}} w_i = 1 \quad (2.30)$$

2.3.3 Raw Probability

For a given reaction at some initial condition (T_{tr} and T_v), we wish to compute the probability of some outcome $P(\bar{o})$. This outcome \bar{o} is a combination of an event e and/or any number of conditions \bar{c} , as follows. An event is a dichotomous (yes/no) variable indicating whether the trajectory has resulted in a particular reaction, for example, a dissociation event or an exchange event. A condition c is whether a continuous variable (such as relative translational energy E_r) or integer variable (such as reactant vibrational quantum number

v) lies within a certain range. An arbitrary number of conditions may be combined, denoted as \bar{c} , for example that the reactant molecule has vibrational energy and rotational energy each in some range. In summary, we define,

$$\bar{c} = c_1 \cap c_2 \cdots c_n \quad (2.31)$$

$$\bar{o} = e \cap \bar{c} \quad (2.32)$$

For an arbitrary number of stratified sampling variables as discussed in the previous section, the probability of some outcome is,

$$P(\bar{o}) = \sum_{\bar{k} \in \bar{K}} \mathcal{V}_{\bar{k}} \frac{\mathcal{N}_{\bar{k}}(\bar{o})}{\mathcal{N}_{\bar{k}}} \quad (2.33)$$

where $\mathcal{N}_{\bar{k}}$ is the total number of trajectories in stratum \bar{k} , and $\mathcal{N}_{\bar{k}}(\bar{o})$ is the number of trajectories in stratum \bar{k} satisfying outcome \bar{o} . The estimated one-sigma statistical error is [24],

$$\delta P(\bar{o}) = \sqrt{\sum_{\bar{k} \in \bar{K}} \mathcal{V}_{\bar{k}}^2 \frac{\mathcal{N}_{\bar{k}}(\bar{o}) [\mathcal{N}_{\bar{k}} - \mathcal{N}_{\bar{k}}(\bar{o})]}{\mathcal{N}_{\bar{k}}^3}} \quad (2.34)$$

This probability and its corresponding uncertainty is used to compute reaction rates as described in Section 2.3.1

2.3.4 Derived Statistics

The raw probabilities discussed above are used to compute specific derived statistics that are used to interpret QCT data. In the previous work of Bender *et al.* [25], these derived statistics were restricted to one variable at a time, for example the distribution of v -levels among molecules that dissociate. This work extends that result to any number of variables simultaneously.

The unconditional PDF is simply the probability of any number of conditions \bar{c} , normalized by the spacing of each condition $\Delta \bar{c}$. For example, if the condition is that the reactant molecule has ε_{vib} and ε_{rot} in some range, $\Delta \bar{c} = \Delta \varepsilon_{\text{vib}} \Delta \varepsilon_{\text{rot}}$. (The term unconditional means the statistic is not associated with any event.) The ranges themselves have no estimated uncertainty, so the uncertainty in the unconditional PDF is trivial.

$$f(\bar{c}) = \frac{P(\bar{c})}{\Delta \bar{c}} \quad (2.35)$$

$$\delta f(\bar{c}) = \frac{\delta P(\bar{c})}{\Delta \bar{c}} \quad (2.36)$$

Conditional PDFs are the same as unconditional PDFs except they are also dependent on an event e , and are normalized by the total probability of that event,

$$f_e(\bar{c}) = \frac{P(e \cap \bar{c})}{P(e) \Delta \bar{c}} \quad (2.37)$$

$f_e(\bar{c})$ is equivalent to $f(\bar{c} | e)$. The estimated uncertainty of f_e is computed using standard uncertainty propagation techniques, assuming independent errors [118, p. 73],

$$\delta f_e(\bar{c}) = f_e(\bar{c}) \sqrt{\left(\frac{\delta P(e \cap \bar{c})}{P(e \cap \bar{c})} \right)^2 + \left(\frac{\delta P(\bar{c})}{P(\bar{c})} \right)^2} \quad (2.38)$$

The conditional probability of some event e , which we denote $P_e(\bar{c})$ but may also be denoted $P(e | \bar{c})$, is,

$$P_e(\bar{c}) = \frac{P(e \cap \bar{c})}{P(\bar{c})} \quad (2.39)$$

$$\delta P_e(\bar{c}) = P_e(\bar{c}) \sqrt{\left(\frac{\delta P(e \cap \bar{c})}{P(e \cap \bar{c})} \right)^2 + \left(\frac{\delta P(\bar{c})}{P(\bar{c})} \right)^2} \quad (2.40)$$

and the support factor, which we describe and motivate in Section 3.5, is

$$S_e(\bar{c}) = \frac{P(e \cap \bar{c})}{P(e) P(\bar{c})} \quad (2.41)$$

$$\delta S_e(\bar{c}) = S_e(\bar{c}) \sqrt{\left(\frac{\delta P(e \cap \bar{c})}{P(e \cap \bar{c})} \right)^2 + \left(\frac{\delta P(e)}{P(e)} \right)^2 + \left(\frac{\delta P(\bar{c})}{P(\bar{c})} \right)^2} \quad (2.42)$$

Each of these quantities is used when interpreting and reporting QCT data.

2.3.5 Expected Values

An expected value is simply the average of some value given a restriction, or set of restrictions. In our terminology, the quantity q , given the outcome \bar{o} , has an expected value of,

$$E_{\bar{o}}(q) = \frac{\sum_i q w_i}{\sum_i w_i \text{ given } \bar{o}} \quad (2.43)$$

Note that the weights w must be computed unconditionally, from Equation (2.30), regardless of the expected value's outcome. This formulation of expected value is very flexible because

there are a variety of meaningful outcomes and quantities. A simple use case is to compute exact moments of distribution functions. For example, the expected value of the change in the system's vibrational energy, given an outcome of dissociation d , is

$$\langle \varepsilon_{\text{vib}} \rangle_d = E_d(\Delta\varepsilon_{\text{vib}}) \quad (2.44)$$

Moments computed using a PDF are compared to their expected values in Section 2.3.6.

We also compute expected values using the same outcomes used to generate conditional and unconditional PDFs. This yields, for each point in an arbitrarily-dimension PDF, the correctly-weighted average of any quantity q . This capability was instrumental in exploring the mechanics of dissociation in Section 3.5.5, and we provide examples there. We believe that expected values associated with PDF points will be useful for a variety of analyses that are currently unknown, and its implementation in REAQCT was designed to allow for easy prototyping.

Note that, for a given set of completed trajectories, evaluating the numerator of Equation (2.43) directly is unfeasible because the weights w are not known until all trajectories have been looped through. Rather than looping first to compute weights and then again to compute the expected value, we reformulate Equation (2.43),

$$E_{\bar{o}}(q) = \sum_{\bar{k} \in \bar{K}} \left(w_{\bar{k}} \sum_{\substack{i \in \bar{k} \\ \text{given } \bar{o}}} q \right) \quad (2.45)$$

The inner sum may be computed while looping over all trajectories in postprocessing, without knowing the weights in advance. The outer sum is computed after the loop is complete. Thus, with this formulation, the RAM requirements for computing an expected value for each PDF point is similar to the requirements for computing the PDF itself: storing values for each outcome, for each strata.

2.3.6 Uncertainty in Moments

In addition to the expected value method described in the previous section, a PDF itself may be used to compute moments. The n -th moment of some condition c (such as change in the system's vibrational energy $\Delta\varepsilon_{\text{vib}}$), conditional on some event e , computed using the PDF defined in Equation (2.37), is

$$M_e^{(n)}(c) = \sum_i f_e(c_i) (c_i)^n \Delta c \quad (2.46)$$

where $f_e(c_i)$ is PDF, conditional on event e , at the i -th point it is defined. The midpoint value of the condition at this point is c_i . We have restricted ourselves to a single condition variable, which has spacing Δc . This formula is also valid for unconditional moments; simply remove the e subscript.

This definition of the moment is dependent on the spacing chosen for each bin. Especially for relatively coarse spacings (perhaps by necessity because there are few total dissociation events), the central value for each bin c_i deviates from the true average of c for trajectories within that range. As the bin spacing becomes smaller, the moment value computed from the PDF converges to the moment value computed via the expected value method described in the previous Section. This is shown in Figure 2.3, which plots PDFs⁵ for the same trajectory data computed with a variety of spacings in the PDF variable. The first conditional moment, computed with both methods, is also shown. For all reported moments, we use the expected value method. This is a slight improvement over the previous method used by Bender *et al.* [25], where only the PDF-based method was available.

The main benefit of computing moments using the PDF is to estimate the statistical uncertainty in a moment. We are not aware of a method to compute the uncertainty of a moment using an expected value. Assuming independent errors for each point in the PDF⁶, and applying standard error propagation to Equation (2.46) yields,

$$\delta M^{(n)}(c) = \sqrt{\sum_i [\delta f_e(c_i)]^2 [(c_i)^n \Delta c]^2} \quad (2.47)$$

Of course, this form is dependent on the bin spacing, and we observe good convergence as the bin spacing decreases, which is shown in Figure 2.4 For all moment quantities reported in this work, the uncertainty is computed using this method. In some cases, distributions exhibit irregular shapes; the case of vibrational energy change due to a no-reaction interaction, for example, has a strong peak at 0. In these cases, PDF convergence is more difficult, and care should be taken to ensure the uncertainty is mostly independent of the spacing.

⁵The data is from single O₂ + O₂ interactions with $T_{\text{tr}} = 10,000$ K, $T_v = 5000$ K, and the chosen PDF is in change in energy per dissociation, $\Delta\varepsilon_{\text{vib}}$. Complete results will be shown later.

⁶This assumption is likely slightly incorrect; see the brief discussion on page 44.

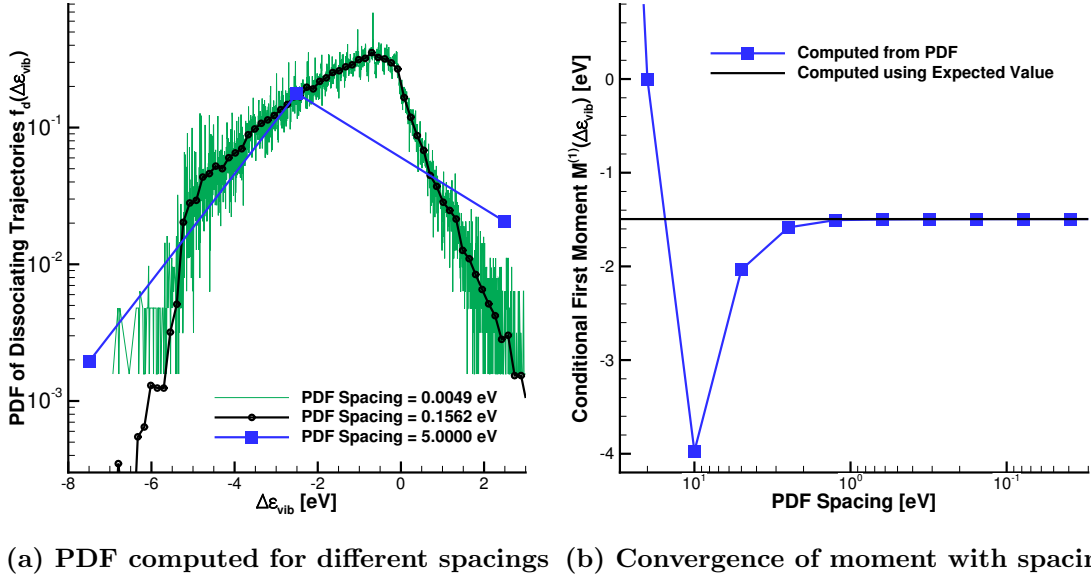


Figure 2.3: PDF of change in vibrational energy due to dissociation, showing the moment calculation's dependence on bin spacing. The condition is chosen to be the $O_2 + O_2$ singlet surface at $T_{tr} = 10,000$ K, $T_v = 5000$ K.

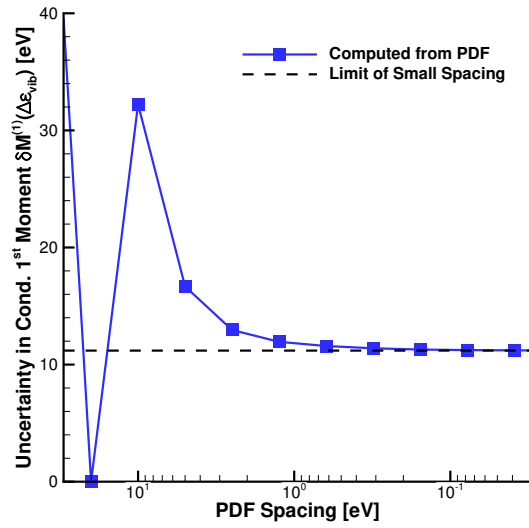


Figure 2.4: Dependence of moment uncertainty on bin spacing, for vibrational energy due to dissociation on the $O_2 + O_2$ singlet surface at $T_{tr} = 10,000$ K, $T_v = 5000$ K.

2.3.7 Uncertainty in Relative Contribution from Trajectory Subsets

Often, a reaction rate may be described as the weighted sum of several intermediate rates. For example, the effective oxygen dissociation rate for $O_2 + O_2$ collisions is⁷,

$$k_d^{(eff)} = k_d^{(simple)} + k_d^{(swap)} + 2k_d^{(double)} \quad (2.48)$$

In this Section, we define the uncertainty associated with each relative contribution, given the uncertainty in each component rate. Throughout this work, we compute the relative contribution of four trajectory subsets:

1. Contributions from different dissociation types: simple, swap, and double. Section 2.3.1 describes which dissociation types are possible for each reaction.
2. Contributions from different reactant types: bound and quasibound. This analysis has not been a focus of the present work, but the results are available in the processed QCT database.
3. Contributions from different impact parameter strata. This is primarily used for determining a suitable maximum impact parameter.
4. Contributions from different ground-electronic-state degenerate interaction states.

Consider the effective dissociation rate as a weighted sum of N component rates $k_d^{(i)}$ with coefficients c_i ,

$$k_d^{(eff)} = \sum_{i=1}^N c_i k_d^{(i)} \quad (2.49)$$

The relative contribution of subset i , which we denoted here as g_i , is

$$g_i = \frac{c_i k_d^{(i)}}{k_d^{(eff)}} \quad (2.50)$$

The statistical uncertainty of the effective rate is not independent of the component rates, because they are explicitly related. However, each component rate is approximately uncorrelated with each other, so we cast the relative contribution only in terms of the component rates, and then propagate uncertainty as usual. The partial derivatives of g_i

⁷For this Section, the notation has been modified slightly, because we believe our typical notation adds unnecessary clutter.

with respect to each uncertain quantity is,

$$g_i = \frac{c_i k_d^{(i)}}{\sum_{m=1}^N c_m k_d^{(m)}} \quad (2.51)$$

$$\frac{\partial g_i}{\partial k_d^{(j)}} = \delta_{i,j} \frac{c_i}{\sum_{m=1}^N c_m k_d^{(m)}} - \frac{c_i k_d^{(i)}}{\sum_{m=1}^N c_m k_d^{(m)}} c_j \quad (2.52)$$

where $\delta_{i,j}$ is the Dirac delta function. The estimated statistical uncertainty in g_i is,

$$(\delta g_i)^2 = \sum_{j=1}^N \left(\frac{\partial g_i}{\partial k_d^{(j)}} \right)^2 (\delta k_d^{(j)})^2 \quad (2.53)$$

$$(\delta g_i)^2 = \left[\frac{c_i}{k_d^{(eff)}} - \frac{c_i^2 k_d^{(i)}}{\left(k_d^{(eff)} \right)^2} \right]^2 (\delta k_d^{(i)})^2 + \sum_{\substack{j=1 \\ j \neq i}}^N \left[\frac{c_i c_j k_d^{(i)}}{\left(k_d^{(eff)} \right)^2} \right]^2 (\delta k_d^{(j)})^2 \quad (2.54)$$

Using the example of oxygen dissociation in $O_2 + O_2$ as before, the estimated uncertainty for the relative contribution of simple dissociation is,

$$\begin{aligned} \left[\delta \left(\frac{k_d^{(simple)}}{k_d^{(eff)}} \right) \right]^2 &= \left[\frac{1}{k_d^{(eff)}} - \frac{k_d^{(simple)}}{\left(k_d^{(eff)} \right)^2} \right]^2 (\delta k_d^{(simple)})^2 \\ &\quad + \left[\frac{k_d^{(simple)}}{\left(k_d^{(eff)} \right)^2} \right]^2 (\delta k_d^{(swap)})^2 + \left[\frac{k_d^{(simple)}}{\left(k_d^{(eff)} \right)^2} \right]^2 (\delta k_d^{(double)})^2 \end{aligned} \quad (2.55)$$

It can be seen that, if the simple dissociation rate is much larger than the swap and double dissociation rates, then the estimated uncertainty in relative contribution becomes low. This is the expected result: if simple dissociations are the only relevant reaction, they comprise nearly 100% of the effective rate, even if the simple dissociation rate is uncertain. This analysis illustrates the need for correctly propagating uncertainty, as we have done here.

For convenience, we may cast Equation 2.54 into a different form as follows. The uncertainty of the effective rate, $\delta k_d^{(eff)}$, is often already computed, and it typically satisfies,

$$(\delta k_d^{(eff)})^2 = \sum_{j=1}^N c_j^2 (k_d^{(j)})^2 \quad (2.56)$$

For any valid component i , we can isolate its error,

$$\left(\delta k_d^{(eff)}\right)^2 = c_i^2 \left(k_d^{(i)}\right)^2 + \sum_{\substack{j=1 \\ j \neq i}}^N c_j^2 \left(k_d^{(j)}\right)^2 \quad (2.57)$$

where the sum over all j except i also appears in Equation (2.54). Substituting yields,

$$(\delta g_i)^2 = \left[\frac{c_i^2}{\left(k_d^{(eff)}\right)^2} - \frac{2c_i^3 k_d^{(i)}}{\left(k_d^{(eff)}\right)^3} \right] \left(\delta k_d^{(i)}\right)^2 + \left[\frac{c_i^2 \left(k_d^{(i)}\right)^2}{\left(k_d^{(eff)}\right)^4} \right] \left(\delta k_d^{(eff)}\right)^2 \quad (2.58)$$

Equations (2.54) and (2.58) are typically equivalent. The first form is more useful for understanding the effect of each component error, and the second is more convenient for calculation. Conceptually, this analysis could be applied extended to more than one subset simultaneously, for example the uncertainty of the triplet surface swap dissociation rate to the effective dissociation rate in $O_2 + O_2$. However, for this work, we have only applied it to one subset at a time. Also, this technique could be applied to generated PDFs, but in that case there are many subsets (points in the PDF) and the overall decrease in uncertainty would be negligible.

We note one minor issue with the preceding analysis. When the trajectory subsets are drawn from different stratified sampling strata, as is the case for impact parameter or ground-state degenerate state, Equation (2.56) is exact. However, in the case of dissociation types and reactant types, counts for the total contribution are also maintained. For example, when postprocessing an $O_2 + O$ case, counts are maintained for the number of all dissociations, and the number of all dissociations from either bound or quasibound states. This means that the uncertainty estimate of the effective dissociation rate is *slightly* lower than the propagated uncertainty from each subset. (This behavior is desirable, because distinguishing between bound and quasibound should not make the final rate more uncertain.) As a result, Equation (2.56) is not exactly correct for non-strata subsets. However, the difference between the two methods are within 5% for all cases in the database, and the larger uncertainty estimate is chosen for these subsets.

2.4 The REAQCT Code and the QCT Database

2.4.1 The REAQCT Code

The Rovibrational Energetics and Analysis of QuasiClassical Trajectories (REAQCT) code package implements all stages of the QCT analysis process that we have described in this Chapter. Bender led its development until approximately February of 2016, and development by Chaudhry has continued for the present work. The code features that existed before the present work are well described by Bender [113, p. 82 to 90], and none of the core functionality described there have been removed. Here, we describe some key features that have been developed since then.

All PESs for $O_2 + O_2$ and $O_2 + O$ interactions have been implemented [66–68]. The calling interface for PESs has also been modified to accommodate modern Fortran best practices; we coordinated with the University of Minnesota Department of Chemistry to update their PES wrapper structure also. This modification allowed for multiple PESs to be compiled into the program simultaneously, and also improved the performance and accessibility of diatomic potentials embedded in the multi-body PES. Section C.1 shows the whitepaper used to motivate this process.

The postprocessor, which reads all trajectories' reactant and product rovibrational levels and energies, has been substantially reworked. As described in Section 2.3, this component of the code now supports an arbitrary number of stratified sampling variables and joint PDFs in any number of variables. Trajectory runs for all ground-state interaction states in $O_2 + O$ or $O_2 + O_2$ may therefore be combined.

The code package now includes a limited suite of self tests, which may be automatically run. Regression testing is also implemented: for most PESs, a ‘Control’ run folder is maintained that contains the expected result for a given random seed. When the code is updated, the run may be repeated and checked. The source code is archived regularly using the git version control software. REAQCT has been run using Intel, GCC, and PGI compilers, and it has used Open MPI and Intel MPI.

L^AT_EX tables may now be auto-generated from QCT data; this capability was used to write all data tables in Appendix B. This functions as a separate utility to be executed in each run directory following all other analysis. One key feature of this utility is the automatic parsing of a value-uncertainty pair: the number of reported significant figures depends on the uncertainty. Each value-uncertainty pair may be output to either plain L^AT_EX or handled by the `siunitx` package⁸, which is designed to display numbers and units. The value-uncertainty parsing component was designed separately and uploaded to

⁸ Available in standard T_EX distributions or at <https://ctan.org/pkg/siunitx?lang=en>, accessed September 26, 2018

the author’s personal github⁹. This feature has been rigorously tested, as there are several edge cases with behavior that may not be immediately obvious.

In this project, we are sometimes interested in aggregate quantities, such as a fit to the dissociation rate, averaged over all O₃ surfaces, as a function of temperature. We are also interested in specific quantities, such as the difference in population of vibrational energies that dissociate between different O₃ surfaces at a single temperature. Particular attention was paid in this project to enabling analysis throughout this range of specific to aggregate. A driving philosophy here is that, if data are quickly and automatically made available, more of it will get meaningfully used and analyzed. The workflow of REAQCT therefore incorporates processing at multiple levels, which we briefly outline. Various scripts that automate the process are also described; they are all included in the REAQCT package. Many of the scripts call the REAQCT code in various modes.

1. First, a series of trajectories are computed for a single surface at a single condition; a single ‘run’ in a single folder. Here, trajectories are sampled from their corresponding distributions, integrated forward in time, and their final state parsed into rovibrational states and energies. This is the only computationally expensive step, and it is typically performed on a high-performance cluster using the `My_reaqct_main.sh` submit script. Aggregate quantities associated with this run, such as the dissociation rate and contributions from impact parameter strata, are recorded in the `results.dat` file; a sample results file is provided in Section C.2. All PDFs that may be generated for this reaction are also computed. This step is input/output intensive, and may be performed on either a cluster or a local machine, typically using the `My_reaqct_allbin.sh` script.
2. If more trajectories are required at the same condition, step 1 is repeated for a new folder, sometimes multiple times. Then, for all of these folders, the files describing the final rovibrational states and energies are linked to a folder that aggregates all data at this condition. This linking is performed using the `Symlink_States.sh` script. Then, in this ‘Stats’ folder, all data may be analyzed together using the `My_reaqct_allbin.sh` script, similar to the single-run case.
3. When the reaction of interest occurs on multiple ground-electronic-state interaction states, data at the same condition for each surface of a given reactant set (eg. singlet, triplet and quintet for O₂ + O₂) are linked to the same folder. This linking is again performed using the `Symlink_States.sh` script, and then aggregate quantities and PDFs are generated using the `My_reaqct_allbin.sh` script.

⁹Publicly accessible at <https://github.com/ross-chaudhry>, last updated August 2018. The parse value-uncertainty code is not specific to REAQCT and no other portions of code are publicly available.

4. Next, we aggregate data across different conditions. In each run folder described by steps 1 to 3, a single-row text file has been generated that contains all aggregate quantities of interest. For example, in the case of $O_2 + O$ reactions, this row contains: number of trajectories, surface, temperatures, rate constant for dissociation and exchange, average change in each component of energy per each reaction, and other quantities. Uncertainties are also included when applicable. In a ‘collector’ folder, lines from individual runs are combined together for a range of temperatures, using the `Collect_Lines.sh` script. The result is a single file describing the dependence of each quantity of interest on temperature, typically for either the equilibrium or nonequilibrium test set.
5. Multiple ‘collected’ files may be plotted together, for example to compare the behavior for different collision partners. Fitting is also performed on all ‘collected’ files, as described in Section 3.6.

Almost all of the files produced by REAQCT for the purposes of visualization are designed to work with Tecplot. They also contain metadata, such as the dissociation energy and the simulation parameters, to normalize plots as necessary.

2.4.2 REAQCT Scaling

The CPU-intensive components of a trajectory calculation are: the drift operation when preparing initial molecules, the main time integration, and the determination of rovibrational states and energies from final positions and velocities. Of these, the main time integration is the most expensive, because it calls the full multi-body PES. All of these operations involve relatively little communication, and so they are implemented in a manager-worker scheme written by Dr. Ioannis Nompelis. We expect this scheme to scale well with problem size and number of processes, and in this Section we briefly assess the scaling performance of these 3 operations in REAQCT. MSI’s high-performance Mesabi cluster¹⁰ was used for this test, and similar results are expected for other systems. The chosen test condition is $N_2 + O_2$ at 4000 K, because that case was relatively difficult to converge.

Two test sets are considered. The first test set fixes the number of trajectories per process, evaluating what is known as weak scaling. We choose 600 trajectories per process, and the number of processes is between 2 and 960. The total time taken per process, per trajectory, is shown in Figure 2.5. Overall, the code scales well, as expected. At very low processor count (less than about 10), the performance is worse because the manager does not perform any expensive tasks. At high process count (higher than about 500), the pre-

¹⁰Information about the system is available at <https://www.msi.umn.edu/content/mesabi>, accessed October 28, 2018.

and post-processing components begin to scale poorly. Because of their relatively low cost compared to the main run, this has less than a 10% impact on the total runtime even at 960 processes. Three total sweeps were computed, and the results were found to be repeatable.

The second test set fixes the total number of trajectories, which evaluates strong scaling. Here we choose 192,000 trajectories, and the number of processes is between 16 and 960. These numbers were chosen to be large enough to assess scaling in a meaningful way, but small enough to not waste resources. The strong scaling results are similar to the weak scaling results; good overall performance with minor slowdown at 960 processes. We therefore conclude that REAQCT scales well for the large problem sizes considered in the present work. We also note that, if scaling did become an issue, one may simply run multiple smaller runs simultaneously and combine their results in postprocessing, as described in the previous Section.

2.5 The QCT Database

Most of the trajectories presented in the present work, including all of the trajectories described in the Conditions section (2.1.4), have been collected in what we call the QCT database. The database includes all run files and postprocessing output, for each condition. As of November 2018, the database takes up approximately 7.2 TB. The database is hosted in two primary locations. First, the Aerospace Engineering and Mechanics (AEM) high-performance lustre file system, `abyss`, contains all rovibrational levels and energies files. These data are all that is required to postprocess PDFs and quantities of interest. Second, the entire database is archived to MSI’s second-tier storage¹¹. From there, it may be accessed via Amazon S3 or Globus, which are both capable of dealing with scientific data on this scale. Either of those platforms is suitable for sharing data between institutions, and the database was designed with this in mind. Alternatively, users with access to the AEM computing systems may also access the data directly on `abyss`; several collaborators have access to portions of the database already. A variety of management utilities and scripts accompany the database, and they can repostprocess and backup portions of the QCT database en masse.

Having easy access to a large collection of QCT data, for a variety of conditions and reactions, has proven beneficial for the present project in several aspects. All reactions and conditions, even those run approximately 5 years ago by Bender *et al.* [25], are updated to work with the latest version of REAQCT. Therefore, all run folders provide a uniform output format with the same postprocessing methods. Comparing aggregate data, or even cross-sectional statistics such as PDFs of dissociating molecule quantum number, is therefore

¹¹For further information, see <https://www.msi.umn.edu/content/second-tier-storage>, accessed October 28, 2018.

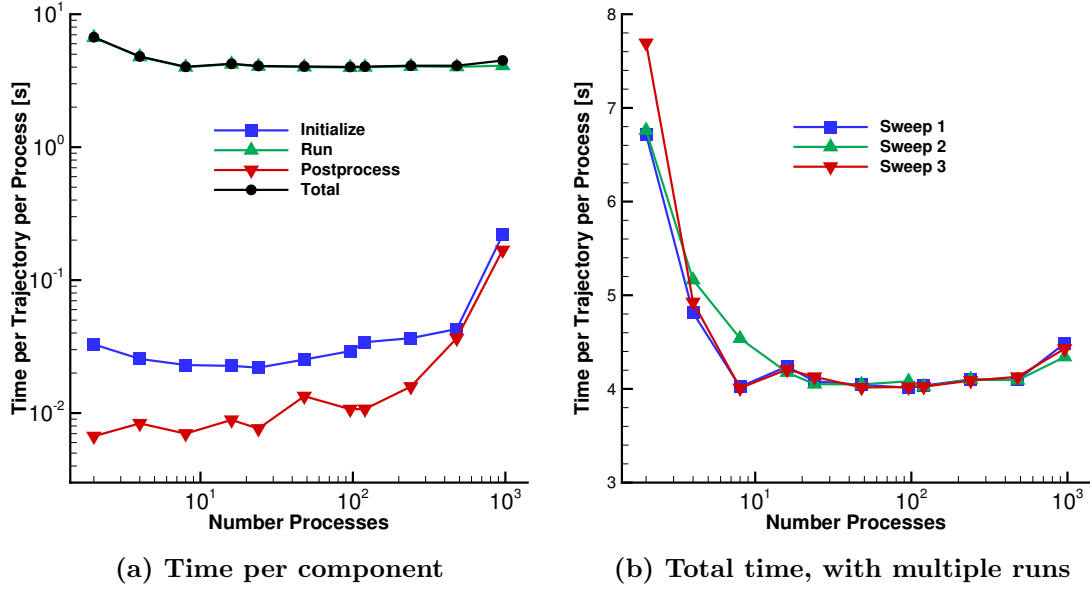


Figure 2.5: Weak scaling performance of REAQCT; 600 trajectories computed per process for each run.

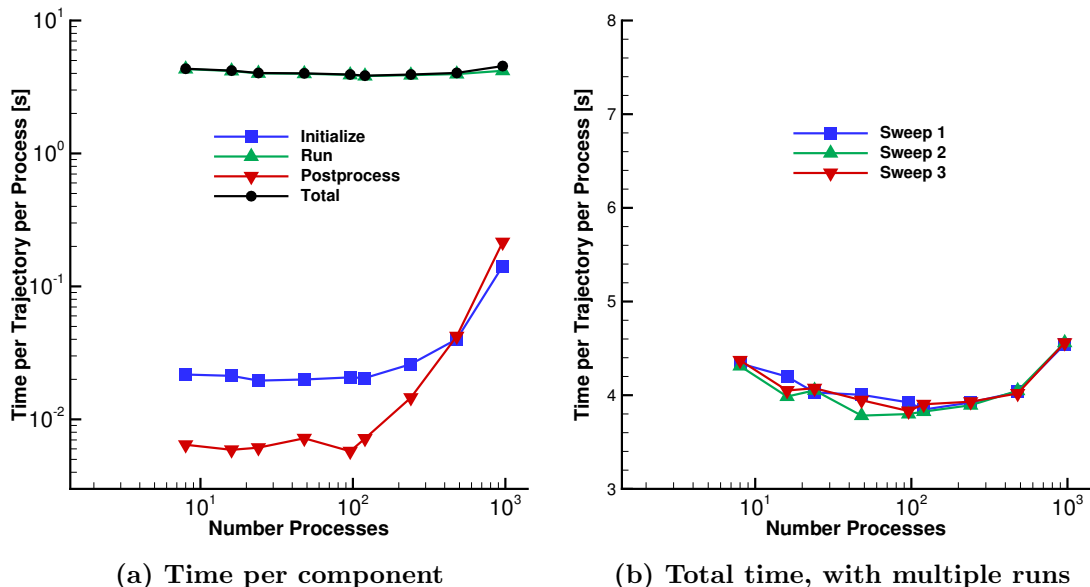


Figure 2.6: Strong scaling performance of REAQCT; 192,000 trajectories computed for each run.

easy. If one adds a new PDF or expected value to the REAQCT code, scripts are available to easily repostprocess the entire database. This type of postprocessing, where rovibrational states and energies are read from a file, is computationally cheap. We believe the QCT database is a rich source of information, and hope that others may use it in the future.

Chapter 3

QCT Results

In this Chapter, we present the results of all quasiclassical trajectory (QCT) simulations performed for this work. We first discuss nitrogen dissociation with all collision partners. Next, we describe oxygen dissociation, focusing on each collision partner in turn: O₂, O, and N₂. We then aggregate data for all collision partners and investigate the common mechanisms behind dissociation. Finally, we fit all quantities of interest to functional forms found in the literature, and present a new form that consistently describes all data at once. Most of the information here is presented as figures; tabulated data may be found in Appendix B.

3.1 Nitrogen Dissociation

In this Section, we discuss nitrogen dissociation in the context of a traditional chemical kinetics framework by comparing to Park's two-temperature model [18]. We present results for collision partners N₂, N, and O₂; the N₂ + N₂ results are also discussed by Bender *et al.* [25], and some N₂ + N rates were presented by Valentini *et al.* [11]. Three types of input are required for a kinetics model: reaction rates, internal energy relaxation, and energy change due to dissociation. Each are discussed in turn.

3.1.1 Dissociation Rate

Figure 3.1 shows the effective dissociation rate constant for nitrogen, for conditions sampled from thermal equilibrium and nonequilibrium. Rate constants from Park, for either a diatomic or monatomic collision partner, are also shown. We find that all collision partners have similar dissociation rates for a given thermal environment. The largest difference between partners occurs at extreme thermal nonequilibrium, where the rate constant for a partner N is approximately 50% higher than for partners N₂ or O₂. The similarity between

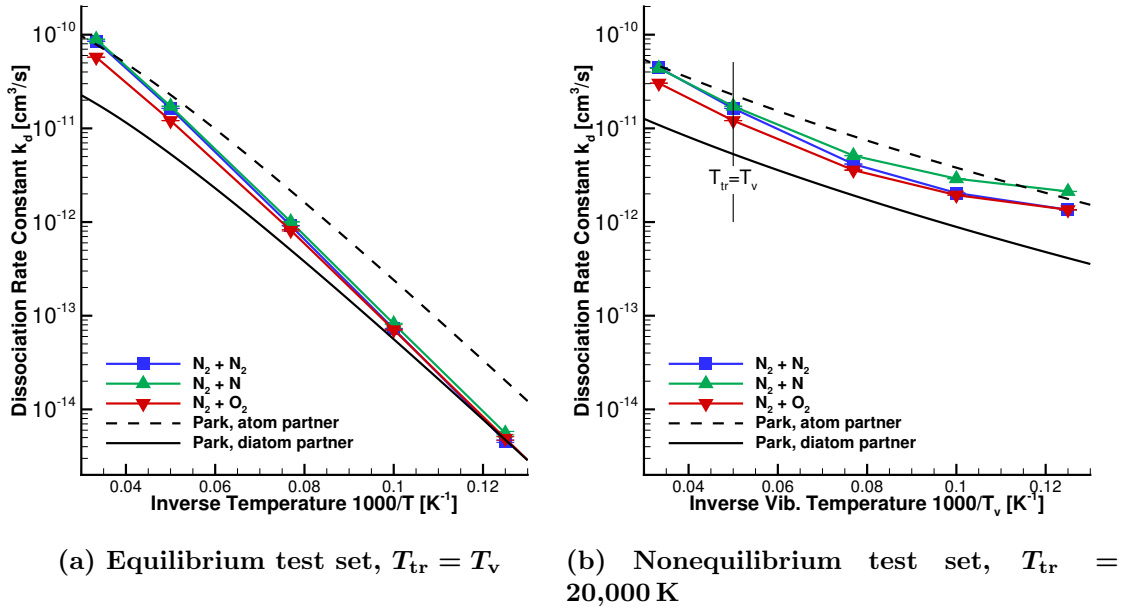


Figure 3.1: Effective dissociation rate constants for nitrogen with different collision partners, compared to Park [18].

$\text{N}_2 + \text{N}_2$ and $\text{N}_2 + \text{N}$ rates is particularly striking; their rate constants are within 15% for all conditions sampled from thermal equilibrium. These differences are all relatively small in the context of a chemical kinetics model, where reaction rates vary by several orders of magnitude.

In previous work by Bender *et al.* [25], QCT-computed nitrogen dissociation rates for $\text{N}_2 + \text{N}_2$ were compared to those available in the shock tube literature [47–49]. The results were found to be in reasonable agreement with the experimental data. However, a rigorous comparison was impossible, especially at relatively high temperatures, because vibrational relaxation was neglected when deriving rates from experimental data. Therefore, in this Section, we compare only to the work of Park [18], which includes the effect of vibrational relaxation.

Here, we compare to trends and physical mechanisms observed in the shock tube data. Most of those experiments in nitrogen found that N_2 dissociates much more readily in the presence of N [47–49]. Park’s two-temperature model, therefore, recommends a larger rate constant for $\text{N}_2 + \text{N}$ collisions, by a factor of 4.3 at all conditions. However, this large difference is clearly not supported by our QCT data. Instead of efficiently dissociating N_2 , the presence of N promotes the vibrational relaxation of N_2 via exchange reactions, resulting in more dissociation. This is discussed next.

3.1.2 Internal Energy Exchange in $\text{N}_2 + \text{N}$

Atomic nitrogen is particularly efficient at vibrationally relaxing diatomic nitrogen due to exchange processes, which are very common and often yield a large difference in vibrational energy between products and reactants. The role of exchange reactions in the $\text{N}_2 + \text{N}$ system has been discussed previously [11, 84, 85]; this Section presents the relevant QCT data. An exchange reaction occurs when reactant N replaces one of the atoms in reactant N_2 , and it was defined previously in Equation (2.18b).

Exchange reactions occur at a range of conditions in both the equilibrium and nonequilibrium test set. Figure 3.2 compares the reaction rates for nitrogen dissociation to the rates for exchange. Exchange reactions are at least 10 times more likely than dissociation, and this trend is stronger for conditions with $T_v < T_{\text{tr}}$ and low temperature equilibrium. They are even a substantial fraction of the total collision rate. For example, defining a head-on collision to have an impact parameter between 0 and 1 Å (comparable to the equilibrium bond length of N_2), an exchange occurs in 35% of all head-on collisions for $T_{\text{tr}} = 20000$ K, $T_v = 8000$ K. Note that exchange reactions also occur in $\text{N}_2 + \text{N}_2$, but they are at least 5 times less likely than dissociation [25].

Mechanisms of vibrational relaxation can be investigated using QCT by examining the change in vibrational energy due to a collision. Probability density functions (PDFs) of change in vibrational energy are shown in Figure 3.3, for a condition sampled from thermal equilibrium or nonequilibrium with $T_{\text{tr}} = 20,000$ K, $T_v = 8000$ K. We first discuss trajectories where no dissociation or exchange occurs, but the collision is nearly head-on ($0 < b < 1$ Å), labeled ‘no reaction’. For all conditions, these trajectories almost always produce a very small change in vibrational energy, as evidenced by the sharp peak at 0 eV. This is an expected result; vibrational energy does not strongly couple to translational or rotational energy for low to moderately excited particles. At thermal nonequilibrium, the PDF is slightly skewed towards positive vibrational energy change because collisions relax toward equilibrium. However, this effect is relatively small; the average change in vibrational energy for the thermal nonequilibrium condition shown is 0.18 eV. This is a microscopic description of a well-known macroscopic phenomenon: vibrational relaxation is relatively slow.

In contrast, trajectories which undergo an exchange reaction yield a large change in vibrational energy relatively often. The PDF of vibrational energy change still peaks at 0 eV for all conditions, but the tail is much broader. Furthermore, conditions sampled from thermal nonequilibrium yield a large positive vibrational energy change more frequently. The average vibrational energy change for exchange reactions at the thermal nonequilibrium condition shown is 0.91 eV, approximately 5 times larger than a head-on ‘no reaction’ collision. Exchange reactions are effective at promoting vibrational relaxation because they

form a new molecule. Restrictions on vibrational energy coupling, which prevent ‘no reaction’ collisions from imparting much vibrational energy, do not apply [84].

Vibrational relaxation has a profound impact on the net dissociation rate. Data obtained from QCT may be used to qualitatively assess mechanisms of vibrational relaxation, as discussed above. However, quantifying the rate of vibrational relaxation and its effect on net dissociation rate is difficult with our method, because we choose to sample initial conditions from a given, fixed distribution (approximately Boltzmann). DMS [27], where trajectory results are used to update the distribution of initial conditions, is able to study these effects. For a nitrogen ensemble with only $\text{N}_2 + \text{N}_2$ reactions, the DMS net dissociation rate is lower than the QCT thermal equilibrium dissociation rate by a factor of approximately 5, due to depletion of the high-energy tail of the vibrational energy distribution [10]. However, when $\text{N}_2 + \text{N}$ reactions are allowed in addition to $\text{N}_2 + \text{N}_2$ reactions, exchange reactions efficiently replenish the populations of vibrationally-excited molecules. This results in an increase in the net dissociation rate by a factor of 2 – 3, compared to the rate when only $\text{N}_2 + \text{N}_2$ reactions are allowed [11]. Along with the QCT results showing a similar effective dissociation rate constant for $\text{N}_2 + \text{N}_2$ and $\text{N}_2 + \text{N}$ across a range of conditions at equilibrium and nonequilibrium (Figure 3.1), we reach an important conclusion. The increased dissociation of N_2 in the presence of N observed by shock tube experiments [47–49] is due primarily to increased vibrational relaxation via $\text{N}_2 + \text{N}$ exchange reactions. We conclude that Park’s interpretation of these data - that $\text{N}_2 + \text{N}$ has a substantially higher dissociation rate than $\text{N}_2 + \text{N}_2$ for the same thermal environment - is incorrect. Using the limited data provided by the shock tube experiments, it was impossible to distinguish increased vibrational relaxation from a larger dissociation rate constant¹.

These conclusions are a reminder that all parameters used to model gas-phase chemical kinetics are tightly coupled. They must all be studied and modeled together, as a complete package. Using new data for only a few parameters may actually reduce predictive capability, even if the new data are more correct. For example, updating the nitrogen dissociation rate constant for $\text{N}_2 + \text{N}_2$ and $\text{N}_2 + \text{N}$ with QCT data without also accounting for the vibrational relaxation provided by exchange reactions in $\text{N}_2 + \text{N}$ would entirely neglect the role that N plays in promoting nitrogen dissociation.

¹This conclusion is also described in Section 4.2.1.

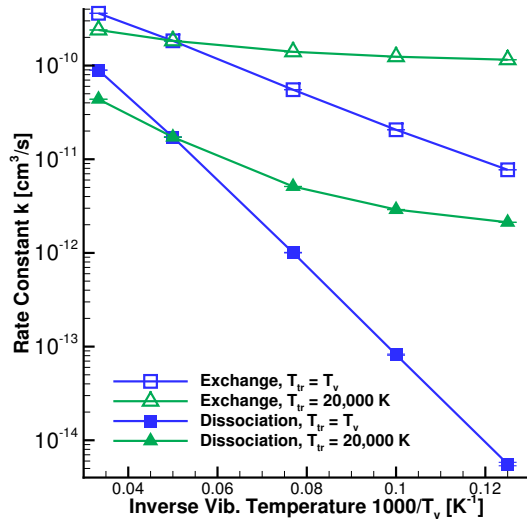


Figure 3.2: Reaction rate constants for exchange and dissociation in $\text{N}_2 + \text{N}$, for the equilibrium and nonequilibrium test set.

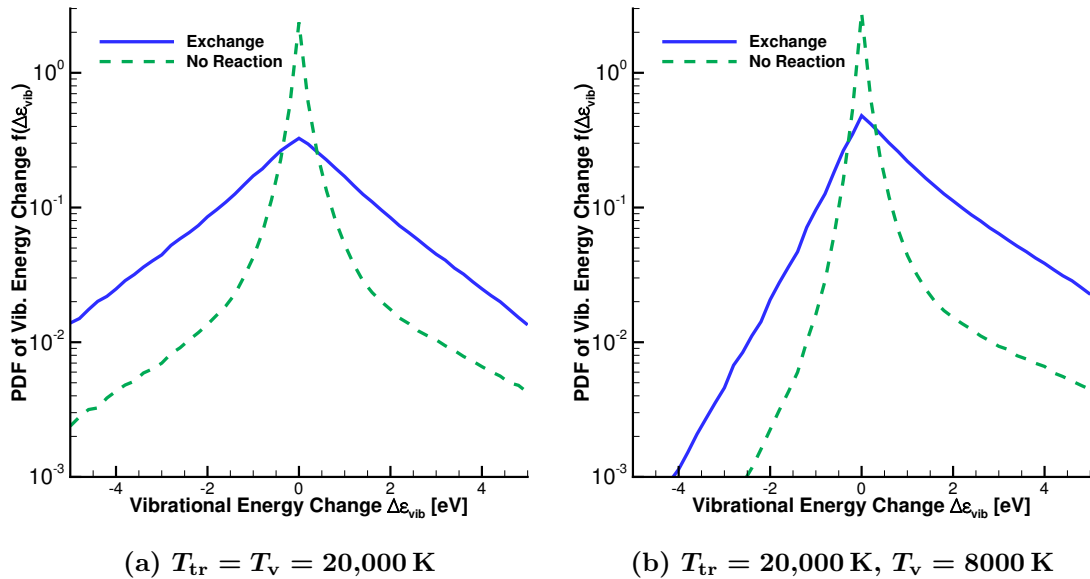


Figure 3.3: PDF of change in vibrational energy for $\text{N}_2 + \text{N}$ trajectories, for a condition sampled from thermal equilibrium and nonequilibrium.

3.1.3 Vibrational Energy Change during Dissociation

A multi-temperature chemical kinetics model for CFD also requires the energy change due to reaction. In a collision in which a diatomic bond breaks or forms, the system's energy ($E_r + \varepsilon_{\text{rot}} + \varepsilon_{\text{vib}}$) decreases or increases by the ground-state dissociation energy D_0 . In a CFD framework, this is kept track of using the enthalpy of formation. When components of energy are treated separately, such as by a two-temperature model, we must determine how much energy comes from each component. For the nitrogen dissociation data, we discuss the decrease in vibrational energy due to nitrogen dissociation. This quantity is necessary to predict the evolution of vibrational temperature as a gas dissociates, and it may be intuitively understood as the average amount of vibrational energy contributed to each dissociation. In this Section, we focus on data for simple dissociations only, because identifying a dissociating molecule and collision partner helps to explain the observed physical behavior. Incorporating swap and double dissociations does not meaningfully alter the results.

We must first understand which molecules tend to dissociate, because the dissociating molecule loses all internal energy upon dissociation. The dissociating molecule's initial vibrational energy is therefore the dominant contributor to the decrease in vibrational energy due to dissociation. The collision partner's change in vibrational energy also contributes, but the basic trends are due to the dissociating molecule's reactive state only. PDFs of initial quantum numbers and change in system energies, for the trajectories which result in a simple nitrogen dissociation, are shown in Figure 3.4. At conditions sampled from thermal equilibrium, the particles which dissociate tend to be vibrationally excited and only slightly rotationally excited. The system's vibrational energy therefore decreases substantially due to dissociation, by an amount close to the dissociation energy of 9.8 eV. When the vibrational temperature is less than the translational-rotational temperature, in contrast, vibrationally-excited molecules are less common than rotationally-excited ones, and so rotation compensates for vibration. Molecules which dissociate are now rotationally excited and rotational energy decreases by a large amount. The difference in behavior at conditions sampled from equilibrium and nonequilibrium is stark, and is discussed further by Bender *et al.* [25]. We now aggregate the data for each condition and collision partner by taking the first moment of $f_d(\Delta\varepsilon_{\text{vib}})$ (shown in Figure 3.4): this is the average decrease in vibrational energy due to dissociation.

Figure 3.5 shows the average decrease in vibrational energy due to simple nitrogen dissociation at thermal equilibrium and nonequilibrium, and it compares QCT data for 3 collision partners to theory. First, let us discuss the QCT data at conditions sampled from thermal equilibrium. Here, for all collision partners, vibrational energy is the dominant contributor of energy for dissociation. This bias is particularly strong at relatively low

temperatures, where dissociation occurs almost exclusively from high- v molecules. When $T \leq 10,000\text{ K}$, more than 75% of the dissociation energy comes from vibration, for all collision partners studied. As temperature increases, rotational and translational energies are more able to induce dissociation from lower- v molecules, and so less energy comes from vibration. Nevertheless, more than 55% of dissociation energy comes from vibration even at 30,000 K.

The behavior observed by QCT is very different when conditions are sampled from thermal nonequilibrium. Once again, all collision partners behave similarly. As T_v decreases while T_{tr} is held fixed, vibrational energy contributes less toward dissociation. For $T_{tr} = 20,000\text{ K}$, $T_v = 8000\text{ K}$, less than 15% of the dissociation energy comes from vibration for all collision partners studied. In the limit of extreme nonequilibrium, the decrease in vibrational energy due to dissociation goes to zero. It must: a gas with no vibrational energy cannot draw from vibration in order to dissociate. (Note that this requirement becomes meaningless in the limit of low-temperature thermal equilibrium, because the dissociation rate goes to zero in that case.) The difference in dissociation mechanisms at equilibrium and nonequilibrium is reflected by the difference in trend of the QCT data between Figures 3.5a and 3.5b.

Figure 3.5 also shows the model used by Park's reinterpretation of shock tube data [16]², the theory due to Sharma *et al.* [55] which was later recommended by Park [18], and the theory of non-preferential dissociation; none of these capture the observed difference between equilibrium and nonequilibrium. The first two curves are theoretical models of preferential dissociation, in which vibrationally-excited molecules are more likely to dissociate. However, neither go to zero when the vibrational temperature is substantially less than the translational-rotational temperature. They are both, therefore, ill-conditioned for implementation in CFD because, with such a model, vibrational energy can become negative behind a strong shock. Consequently, typical implementations of the Park model in CFD use non-preferential dissociation, in which the average vibrational energy is removed by dissociation. This results in the desired behavior in the limit of extreme thermal nonequilibrium, but means that dissociation does not result in a decrease in the average vibrational energy of the gas. Thus, dissociation in current CFD models does not directly decrease the vibrational temperature of the gas, an outcome which is inconsistent with both the development of Park's rates and our current understanding of chemical kinetics. This is a known issue, but it has remained unresolved because the vibrational energy decrease due to dissociation is impossible to determine directly from shock tube data.

²As we discuss in Section 3.6.3, this is also the Losev [119] model with $\beta = 1$.

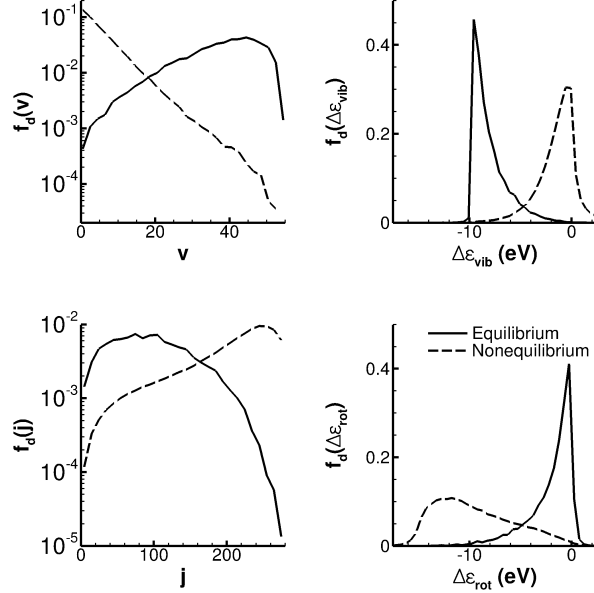


Figure 3.4: PDFs for simple nitrogen dissociation at equilibrium ($T_{\text{tr}} = T_{\text{v}} = 10,000 \text{ K}$) and nonequilibrium ($T_{\text{tr}} = 20,000 \text{ K}$, $T_{\text{v}} = 8000 \text{ K}$) in $\text{N}_2 + \text{N}_2$.

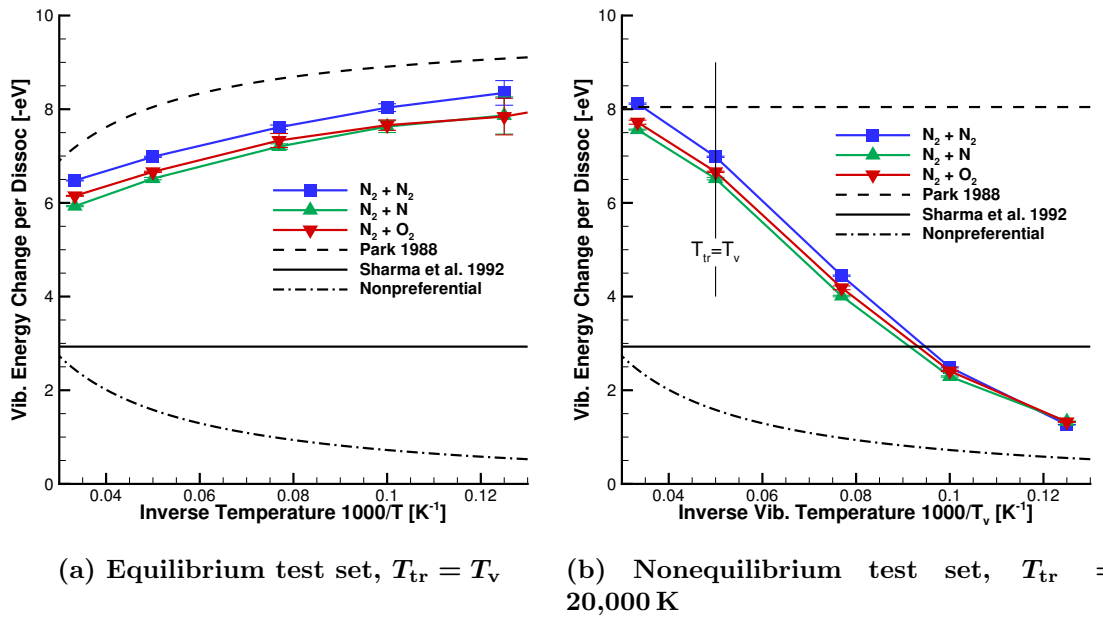


Figure 3.5: Average vibrational energy decrease due to nitrogen dissociation, compared to theory [16, 55].

3.2 O₂ + O₂ Results

In this Section, we describe the CFD quantities of interest and some of the related microscopic behavior for O₂ + O₂ interactions. Electronically ground-state O₂ + O₂ interactions may occur at one of three system spin states: singlet, triplet, and quintet. We are therefore also interested in studying the differences between these surfaces, as well as examining their degeneracy-weighted average (denoted ‘SYS’ in plots).

The reaction rates for effective dissociation and metathesis, for conditions sampled from the equilibrium and nonequilibrium test set, are shown in Figure 3.6. Both rates have a roughly Arrhenius-like form, and the metathesis rate is between 1 and 2 orders of magnitude less than the effective dissociation rate. This means that, as was the case with N₂ + N₂, we do not expect the relaxation rate due to O₂ + O₂ collisions to be affected by metathesis reactions. The contributors to the effective dissociation rate are shown in Figure 3.7. Simple dissociation is the dominant contributor, but swap dissociations are non-negligible for all conditions. Even at the coldest equilibrium condition, more than 10 % of effective dissociations are due to swap dissociation. This is different than for N₂ + N₂, where the relative contribution of swap dissociation fell off rapidly at low temperatures: at 8000 K, less than 1 % came from swap dissociations. The relative contribution of swap dissociation for the nonequilibrium test set is roughly constant near 20 % for both N₂ + N₂ and O₂ + O₂.

Figure 3.8 shows the distribution of dissociating molecule v and j for two conditions: relatively cold equilibrium (5000 K) and nonequilibrium ($T_{\text{tr}} = 10,000 \text{ K}$, $T_v = 4000 \text{ K}$). These conditions are chosen to be qualitatively similar to the PDFs shown for dissociation in N₂ + N₂ in Figure 3.4. When conditions are sampled from thermal equilibrium, especially relatively cold equilibrium, the population of molecules that dissociate are highly vibrationally excited and only moderately rotationally excited. When vibrational energy is suppressed, as in the nonequilibrium condition shown, rotation compensates for vibration and the molecules that dissociate are rotationally excited instead. This microscopic behavior yields the vibrational energy change per dissociation shown in Figure 3.9. The change in rotational and internal energy components is also shown. The rotational energy change per dissociation increases as the equilibrium temperature increases, and as the vibrational temperature decreases in the nonequilibrium test set. This yields a roughly constant change in internal energy per dissociation, which is again consistent with the results of Bender *et al.* [25] and Panesi *et al.* [84] for nitrogen dissociation.

We observe moderate dependence of these results on the interaction’s spin state. The triplet surface results in approximately 60 % more dissociation than the other surfaces for all conditions considered. Also, the PDF of dissociating molecule j is favored toward high- j molecules for the quintet surface in the nonequilibrium conditions, which result in a different

rotational energy decrease per dissociation. The reason for these differences is unclear, but there is no reason that these surfaces should be identical. Based on the O₂ + O₂ results, it is necessary to include the effect of ground-electronic-state interaction spin; neglecting the triplet surface at 5000 K, for example, yields a dissociation rate that is approximately 25 % less.

Figure 3.10 compares the present results with a variety of dissociation rates from the literature, including the shock-tube dissociation results discussed in Section 1.2 [12–14, 36, 38, 39, 42], fits and reinterpretations of experimental results [9, 43], and the QCT analysis of Andrienko and Boyd [92]. The reader is cautioned that this comparison is not self-consistent, for several reasons. First, most of the shock tube experiments entirely neglect vibrational relaxation when determining their rates. Second, we sample from Boltzmann distributions for our QCT results, and the distribution of internal and vibrational energies in a dissociating gas ensemble are non-Boltzmann [10, 11]. Finally, the role of electronic energy has been neglected for our results. Overall, the results are found to be roughly similar to the experimental data, although there are substantial uncertainty estimates and scatter within the literature. Multiplying by the multisurface correction factor $\eta = \frac{16}{3}$ factor [73] clearly does not match any other data, so we do not do it here. It is difficult to draw further conclusions when comparing to the experimental data.

The most rigorous comparison is to the QCT results of Andrienko and Boyd [92], because we are comparing to their Boltzmann-sampled data and they also do not employ the multisurface correction factor for this case. We observe a lower dissociation rate by approximately a factor of 2, which we attribute to differences in the PES. In their work, the almost 30-year-old Varandas and Pais O₄ surface [81] is used, which is based on the previous O₃ surface [80]. As described by Grover *et al.* [78, 79], this O₃ surface exhibited substantial error when compared to modern *ab-initio* electronic structure calculations and the PES due to Varga *et al.* [68].

We finally remark on the visualization technique used for Figure 3.10b, where we pre-multiply out the exponential term in the Arrhenius rate equation and normalize to near 1. (This scaling was also used in Section 1.2.) By removing this strong trend that exists in all of the data, the range in the ordinate is reduced to only 3 orders of magnitude, compared with 9 orders of magnitude for Figure 3.10a. Differences between these data may be more clearly seen as a result. This technique is also used when comparing to data in the literature in future Sections.

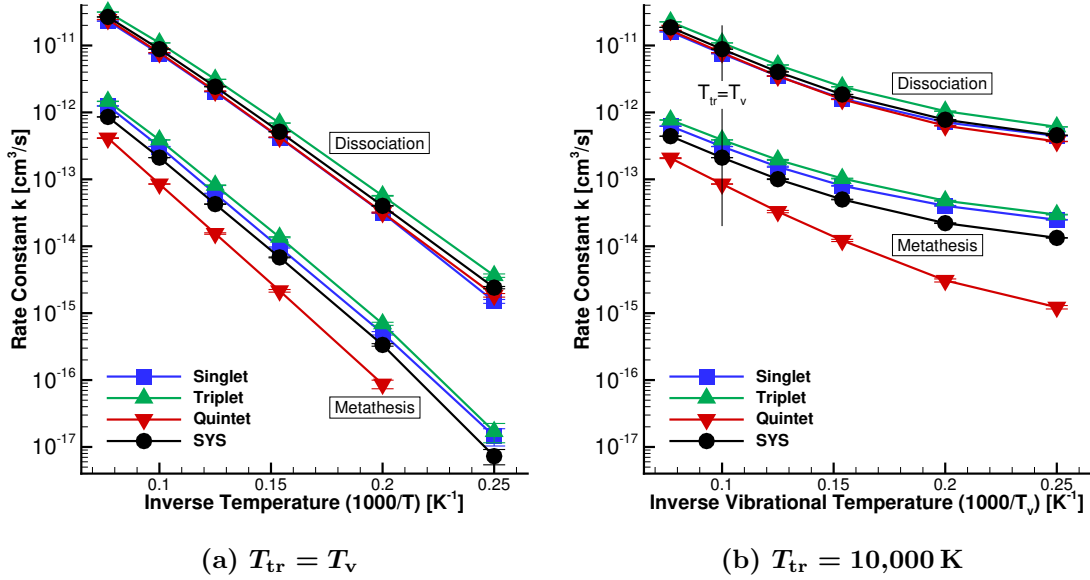


Figure 3.6: Reaction rates for effective dissociation and metathesis for O₂ + O₂, for the equilibrium and nonequilibrium test set.

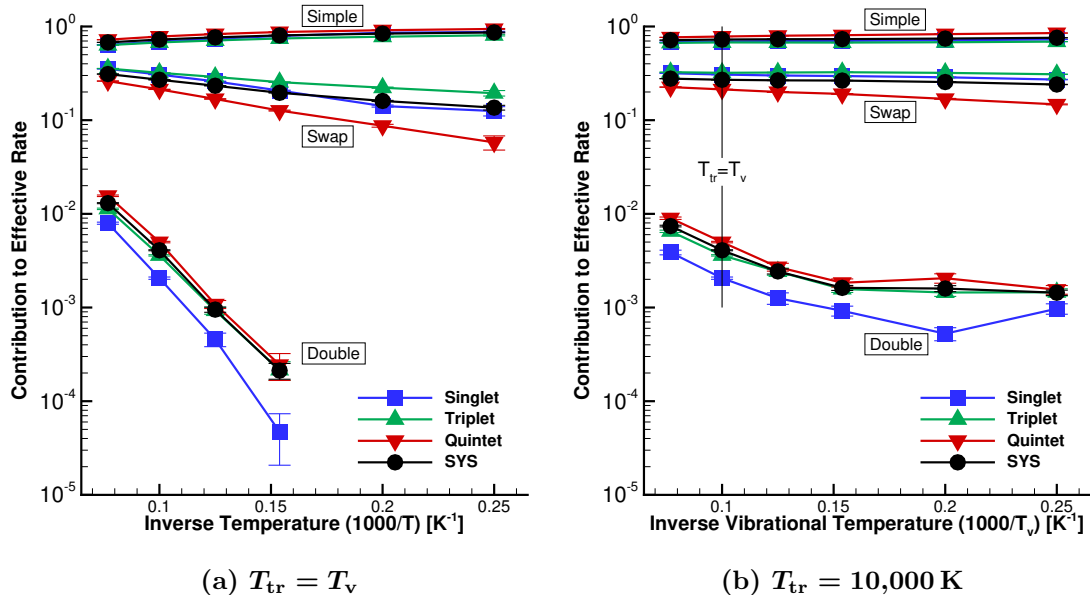


Figure 3.7: Relative contribution to the effective dissociation rate for O₂ + O₂, for the equilibrium and nonequilibrium test set.

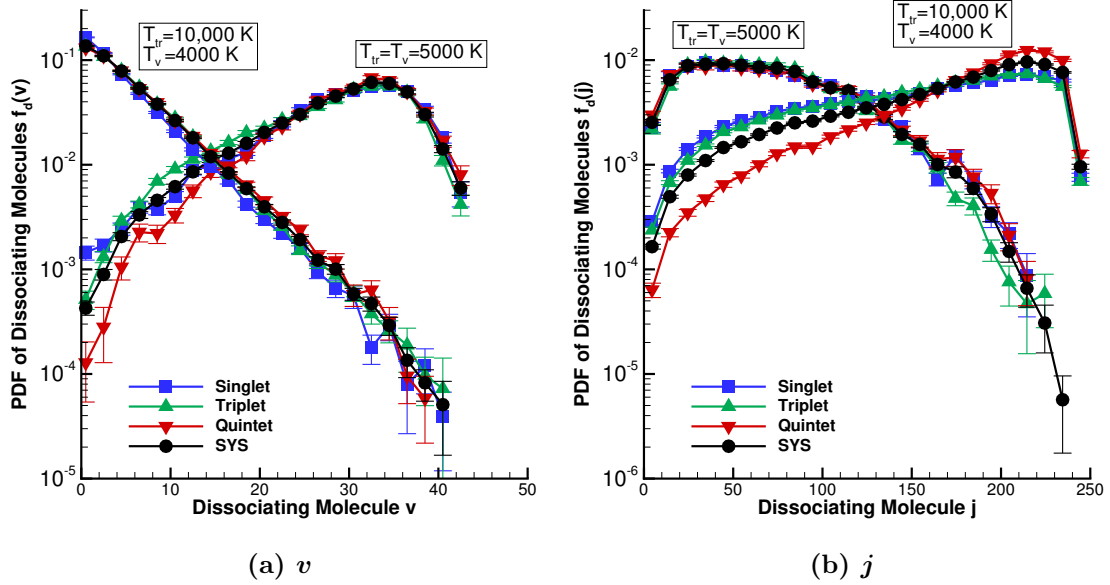


Figure 3.8: PDF of v and j for the population of molecules that undergo simple dissociation in $\text{O}_2 + \text{O}_2$, for an equilibrium and nonequilibrium condition.

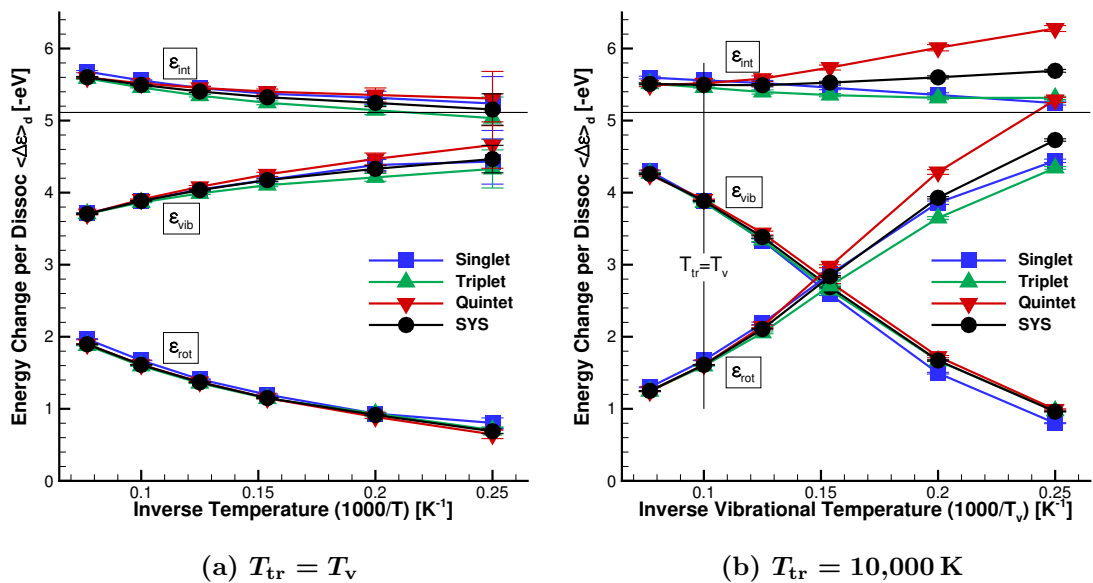


Figure 3.9: Change in system energy per dissociation for $\text{O}_2 + \text{O}_2$, for the equilibrium and nonequilibrium test set.

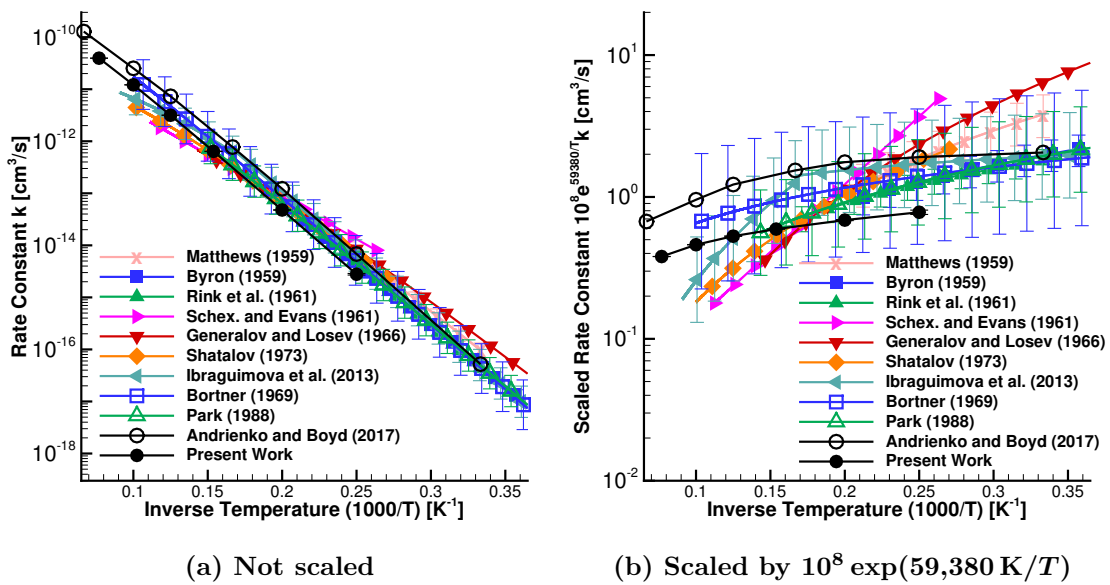


Figure 3.10: Equilibrium effective dissociation rate for O₂ + O₂ system, compared to literature.

3.3 O₂ + O Results

For O₂ + O interactions, as in the previous Section, we are interested in quantities of interest for CFD and the related microscopic behavior. Electronically-ground-state O₂ + O interactions may occur on one of three spin states and one of 3 spatially-degenerate states for each spin state, so results are presented for 9 PESs and their degeneracy-weighted average (denoted ‘SYS’ in plots)³. As described in Section 3.1.2, exchange reactions in N₂ + N is found by our work and others [11, 84, 85] to substantially promote vibrational relaxation; we are interested in investigating this in O₂ + O. We note here the recent work of Grover *et al.* [78, 79], who performed DMS with O₂ + O reactions on these surfaces: he found that vibrational relaxation is promoted by exchange reactions in O₂ + O. We use this result for our analysis herein and also provide the QCT perspective on these findings in Section 3.3.2.

3.3.1 Dissociation in O₂ + O

Rates of dissociation and exchange are shown for each surface, for the equilibrium and nonequilibrium test set, in Figure 3.11. The dissociation rate for all surfaces is found to be similar when conditions are sampled from thermal equilibrium: the maximum difference is 30 % at 5000 K. In the nonequilibrium test set, the difference in dissociation rate is found to be reasonably large: the dissociation rate for the triplet 1 A' and 1 A'' surfaces is approximately 4 times greater than the quintet 1 A'' surface for the condition T_{tr} = 10,000 K, T_v = 4000 K. The exchange rate is described in the next Section.

As we did for O₂ + O₂, PDFs of dissociating molecule quantum number, for a selected nonequilibrium and equilibrium condition, is shown in Figure 3.12. The corresponding energy change per dissociation, for each component, is shown next, in Figure 3.13. The character of molecules that dissociate in O₂ + O reactions, for all PESs, is found to be similar to previous conclusions for nitrogen dissociation and O₂ + O₂. There exist statistically-significant differences between interaction states for O₂ + O, but no clear trends are observed. As a result, the average vibrational energy per dissociation is similar between PESs and with previously-shown reactions. We do note, however, that the average internal energy decrease per dissociation is below the dissociation energy for cases with T_v < T_{tr}. This was also observed for N₂ + N, shown in Table B.5; we attribute it to the more pronounced effect translational energy has on atom-diatom reactions compared to diatom-diatom reactions.

³9 different PESs makes visualization challenging, but we are typically not interested in isolating the behavior of any single surface, so visualizing trends and scatter in the data are often enough. Unfortunately, there is no meaningful grouping or reduction strategy that seems to make interpreting the results easier without substantially increasing the number of plots required. The reader is reminded that tables of these data are available in the Appendix: system statistics are shown for each temperature in Tables B.14 and B.15, and results for each PES are shown for fixed conditions in Tables B.16 to B.18.

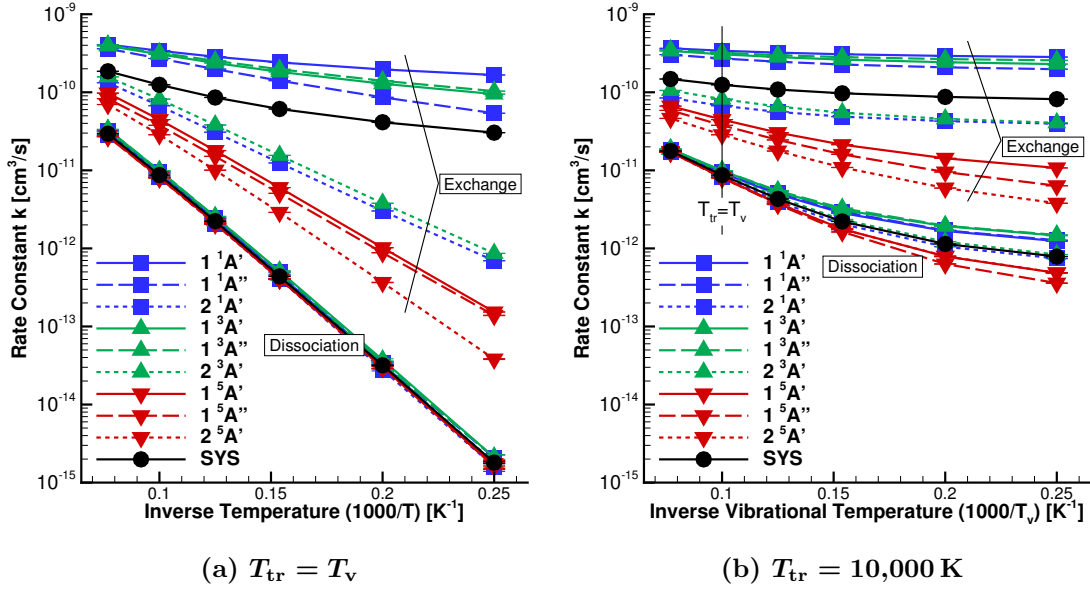


Figure 3.11: Reaction rates for dissociation and exchange for O₂ + O, for the equilibrium and nonequilibrium test set.

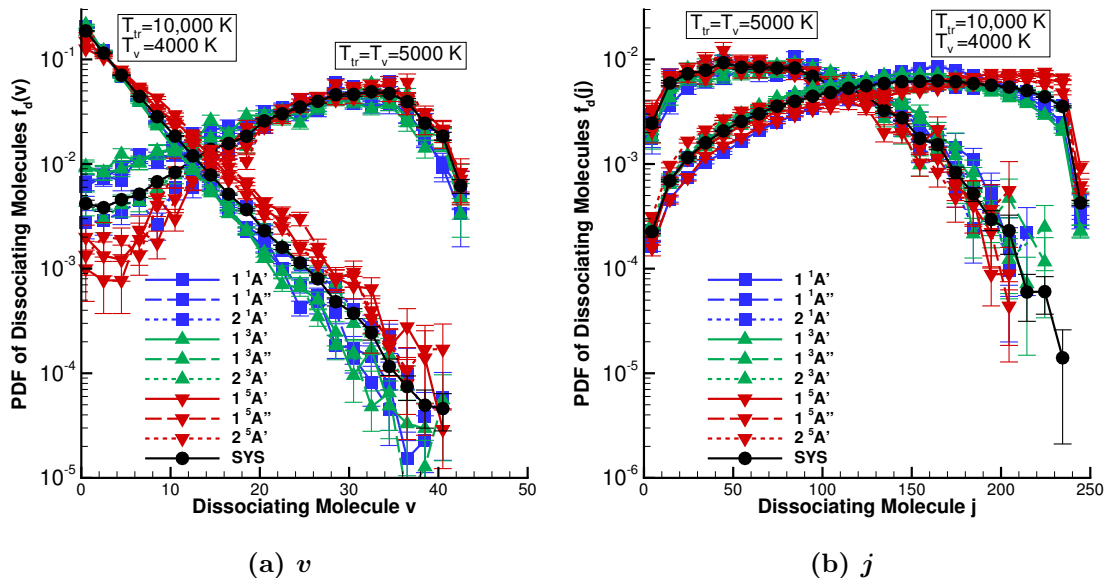


Figure 3.12: PDF of v and j for the population of molecules that undergo dissociation in O₂ + O, for an equilibrium and nonequilibrium condition.

In Figure 3.14, we show a comparison of the dissociation rate with various data from the literature, including shock tube experiments [13, 14, 37, 42], fits and reinterpretations of shock tube data [9, 43], and modern QCT analyses [74, 120]. The present data is shown twice: either multiplied by the multisurface correction factor, $\eta = \frac{16}{3}$ [73], or not⁴. We first describe the comparison with QCT data; Refs. [74, 120] both multiply by η so we compare to our data with the factor also. The present results are found to be reasonably similar to those of Mankodi *et al.* [120] at low temperatures, but they diverge near 6500 K. At 13,000 K, their result is 50 % greater than the present work. The reason for this difference is unknown, but we cannot ascribe it to a difference between interaction states because all present PESs give similar results for the condition where the differences occur. Mankodi *et al.* [120] use an *ab-initio* PES generated in the same work that performed the QCT analysis. The results of Andrienko and Boyd [74] are found to be 50 % to 70 % higher than the present results. We attribute this difference to the PES; they use the Varandas and Pais O₃ surface [80], which has been found by Grover *et al.* [78, 79] to contain spurious features.

When comparing to the experimental data, we find that the multisurface correction factor is necessary to achieve a reasonable match, which is what motivated previous QCT-based results to incorporate the factor [74, 78, 79, 120]. We describe two interpretations of this result. The first interpretation is that, for a system with O₂ + O reactions, electronic energy relaxation is relatively fast. Therefore, the multisurface correction factor, which assumes that all bound electronically-excited states are fully excited [73, 74], is a reasonable way to account for electronic energy. In their work on O₂ + O₂, Andrienko and Boyd [92] argue that this should be the case for O₂ + O but not O₂ + O₂ interactions, based on intuition about the O₃ interaction.

However, recall that a similar position was encountered for nitrogen: the dissociation rate in N₂ + N was found to be lower than experimental results by approximately a factor of 4 (we described this in Section 3.1.2, and it is also addressed by Valentini *et al.* [11]). Electronic energy is not expected to play a major role in nitrogen dissociation at the temperatures considered. Instead, exchange reactions in N₂ + N were found to substantially promote vibrational relaxation, resulting in a higher dissociation rate in the presence of atomic nitrogen. Similar observations are made for oxygen: O₂ + O is found to promote vibrational relaxation (quantified by Grover *et al.* [78, 79] and also described next). Therefore, the difference between the present QCT results and those in the shock tube dissociation literature could also be due to the increased role of vibrational relaxation in O₂ + O. Complicating the issue is that the vibrational relaxation rate of O₂ with partner O was known to be faster than with partner O₂ based on the 1967 results of Kiefer and Lutz [121]. The difference between O₂ + O and O₂ + O₂ relaxation was included in Park's reinterpretation [16,

⁴This is the only time in the entire work we multiply our results by η .

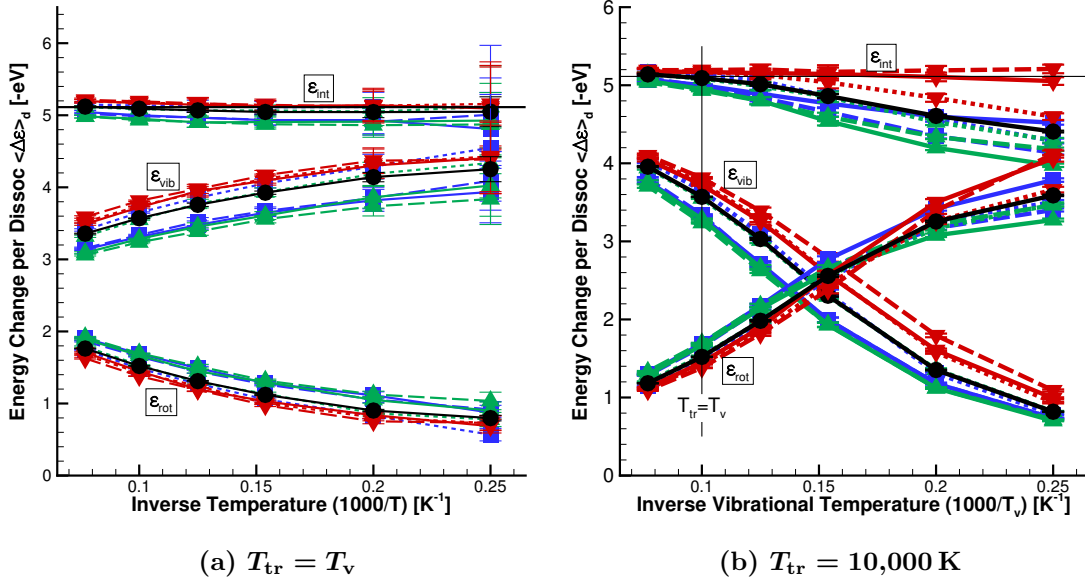


Figure 3.13: Change in system energy per dissociation for O₂ + O, for the equilibrium and nonequilibrium test set.

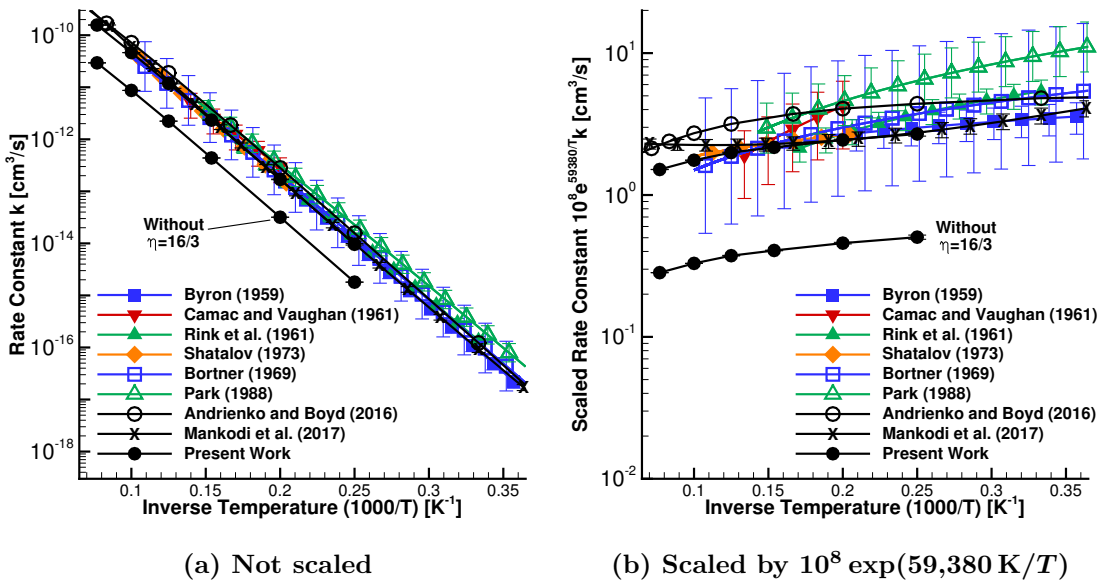


Figure 3.14: Equilibrium dissociation rate for O₂ + O system, compared to literature. Includes present work with and without the multisurface correction factor $\eta = 16/3$; all other data do not include this factor.

p. 5] and his recommendations for relaxation times in air [19]. Oxygen and nitrogen are different in this respect, because the nitrogen relaxation rate with partner N₂ was thought to be approximately the same as with partner N at the time of Park's reinterpretation [54].

The reason for the difference between QCT results and the observed experimental data is likely some combination of these two factors, in addition to our QCT method assuming Boltzmann distributions. This is consistent with the results from DMS due to Grover *et al.* [78, 79], who was able to match the experimental results of Shatalov [42] by using the multisurface correction factor. DMS inherently accounts for the effect of non-Boltzmann distributions and internal energy relaxation.

3.3.2 Vibrational Energy Transfer in O₂ + O

As shown in Figure 3.11, the exchange rate in O₂ + O is found to be extremely dependent on the interaction state. For all conditions, the 1¹A' PES yields the highest rate and the 2⁵A' PES yields the lowest; their difference varies between an order of magnitude and more than three orders of magnitude. In all cases, the exchange rate is larger than the dissociation rate, and so we expect exchange reactions to contribute to vibrational relaxation, similar to previous observations from N₂ + N [11, 84, 85]. We therefore focus our analysis of exchange reactions to a single condition in the nonequilibrium test set, $T_{\text{tr}} = 10,000\text{ K}$, $T_{\text{v}} = 4000\text{ K}$, where the mechanisms of vibrational relaxation may be analyzed.

Figure 3.15a shows the probability of exchange from a specific impact parameter, for each PES. We see that most surfaces exhibit similar shapes, but are offset by a large factor corresponding to their average probability of exchange. The 1¹A' PES is an exception here: the shape is much broader, and the probability of exchange on this surface is roughly the same for all impact parameters from 0 Å to 1.5 Å. Nevertheless, the rough shape similarity means that the large difference in exchange rate is not explained by a dependence on impact parameter.

Figure 3.15b shows the probability of exchange from a specific total collision energy, ($E_{\text{r}} + \varepsilon_{\text{int}}$). We observe a clear stratification when visualizing the data in this manner. An O₂ + O interaction occurring at the 2⁵A' state may only result in an exchange if the total collision energy is above approximately 65 % of the dissociation energy, which means there is an energy barrier for exchange. Based on the data shown, this barrier is surface-dependent; the singlet and triplet 2 A' surfaces require approximately 40 % of the dissociation energy, for example. In the most striking case, there is no energy barrier for the 1¹A' state; we will summarize results for this specific interaction state at the end of this Section. This energy barrier is a direct result of the electronic structure of O₃, and it is discussed in more detail by Grover *et al.* [78, 79] and Varga *et al.* [68]. As expected, the energy barrier correlates well with the rate of exchange: surfaces with a low energy barrier exhibit a higher rate of

exchange, and vice versa. The probability of exchange for the case of N₂ + N is also shown; results for N₂ + N lie within the range of O₂ + O interaction states.

Based on previous N₂ + N results, we may expect that surfaces with a higher exchange rate exhibit more vibrational relaxation. However, there are other physical mechanisms present, and some of them compete with each other, as follows. Exchange reactions are effective at promoting vibrational relaxation in N₂ + N because a new molecule is formed, and it has no ‘memory’ of the previous state, an effect that is well described by Panesi *et al.* [84]. Therefore, the new molecule can form at a wide range of rovibrational states, which may yield a large vibrational energy change from a single interaction. In O₂ + O, though, some interaction states may experience exchange reactions with very little total energy; in that case, substantial vibrational relaxation cannot occur because there is almost no energy in the entire collision system. Only when the interaction occurs with substantial total energy can an exchange reaction augment the vibrational relaxation rate. Because the exchange rate is correlated with the energy barrier, surfaces with a high exchange rate result in less vibrational energy increase per exchange reaction. The distribution of vibrational energy change per exchange reaction is shown in Figure 3.16a, and the behavior of the quintet curves in particular illustrates the point. We therefore have two competing effects.

A third difference between surfaces is also observed regarding vibrational relaxation, and it is shown in Figure 3.16b. The vibrational energy change per no-reaction, where neither a dissociation nor exchange event occurs, is also found to be dependent on the interaction state. For example, due to a no-reaction event, the 2⁵A' surface yields a 2 eV increase in vibrational energy approximately 100 times less often than the 1¹A' surface does. This trend is observed to be somewhat correlated with the energy barrier, because surfaces with a large exchange rate tend to have a broader change in vibrational energy PDF during a no-reaction event. We hypothesize that surfaces with a high energy barrier tend to yield more simple scattering collisions, in which vibrational energy transfer is rare. In contrast, surfaces with a low energy barrier may admit more complex, long-lived interactions that, although no reaction occurs, are more able to transfer vibrational energy⁵.

Another way to quantify these effects is to compute the average vibrational energy change per event: the first moment of Figure 3.16. We plot this quantity, for each surface, for both exchange and no-reaction events, at all conditions in the nonequilibrium test set, in Figure 3.17. This figure describes the trend as T_v varies: the behavior is approximately monotonic toward the equilibrium case, at which point the average vibrational energy change is 0. An alternative visualization is provided in Figure 3.18, which shows a single condition. The relationship between exchange rate and average energy change per exchange and no-reaction, for each PES, is most easily seen in this representation of the data. The shape

⁵Interaction times are discussed briefly in Section 3.7.3.

of exchange rate is essentially inverted to yield the shape of average vibrational energy change per exchange; this reflects their strong negative correlation. The shape of average vibrational energy change per no-reaction is roughly similar to the shape of exchange rate, reflecting their moderate positive correlation.

Based on these results, it is clear that differences between the ground-electronic-state interaction states of an O₂ + O interaction have a profound effect on vibrational relaxation. The description of these multiple competing mechanisms, as far as we are aware, is novel. Quantifying their effect on the vibrational relaxation time is difficult using our QCT data alone, however, because conditions are sampled from a fixed initial state. The corresponding DMS analysis, which is able to quantify reaction times, has recently been performed by Grover *et al.* [78, 79]. His conclusions match well with data are qualitatively consistent with our conclusions; we find that our QCT technique and the DMS method are complementary.

We finally note the behavior of the 1¹A' degenerate state. Ozone exists only at this state, and the Varandas and Pais O₃ surface [80] was developed nearly 30 years ago to study ozone at relatively low temperatures. In the absence of a better option, this surface has been used to study the dynamics, for both dissociation and relaxation, of oxygen dissociation at hypersonic conditions [74, 122–124]. However, it only accounts for 1/27 of all O₂ + O interactions, and interactions on this degenerate state are found by our work to be substantially different than on other degenerate states. For an interaction angle near the bond angle of ozone (approximately 117°), the barrier to exchange is extremely limited due to the potential well of ozone [68]. This is why exchange can occur from all total collision energies for the 1¹A' surface, and it also explains the relatively broad impact parameter dependence shown in Figure 3.15a. Quantitatively, this surface exhibits the largest exchange rate, the smallest vibrational energy increase per exchange⁶, and the largest vibrational energy increase per no-reaction. Therefore, the 1¹A' state is different *because* it admits ozone, and it is not representative of the O₃ ground-state interaction system as a whole. Besides the uniqueness of the 1¹A' interaction state when it is described accurately by the Varga *et al.* [68] surface, the Varandas and Pais surface also has spurious features that are described by Grover *et al.* [78, 79]. These results demonstrate that, for the case of O₂ + O, it is necessary to study the dynamics of all 9 interaction states.

⁶Tied within uncertainty with the 1³A' surface.

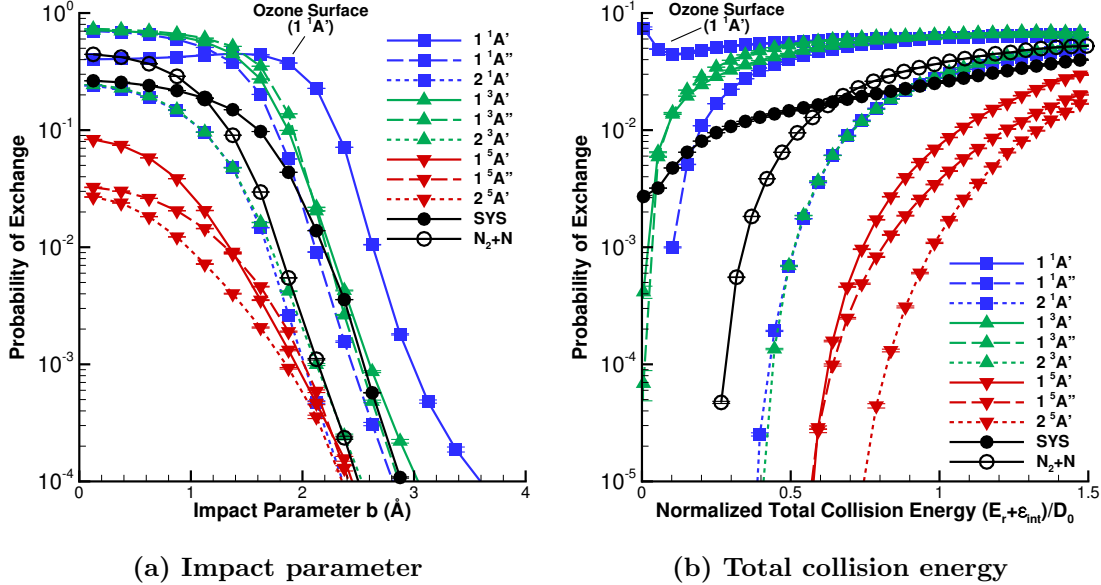


Figure 3.15: Probability of exchange in O₂ + O as a function of two reactive states, for $T_{tr} = 10,000$ K, $T_v = 4000$ K. N₂ + N data is included for comparison, at $T_{tr} = 20,000$ K, $T_v = 8000$ K.

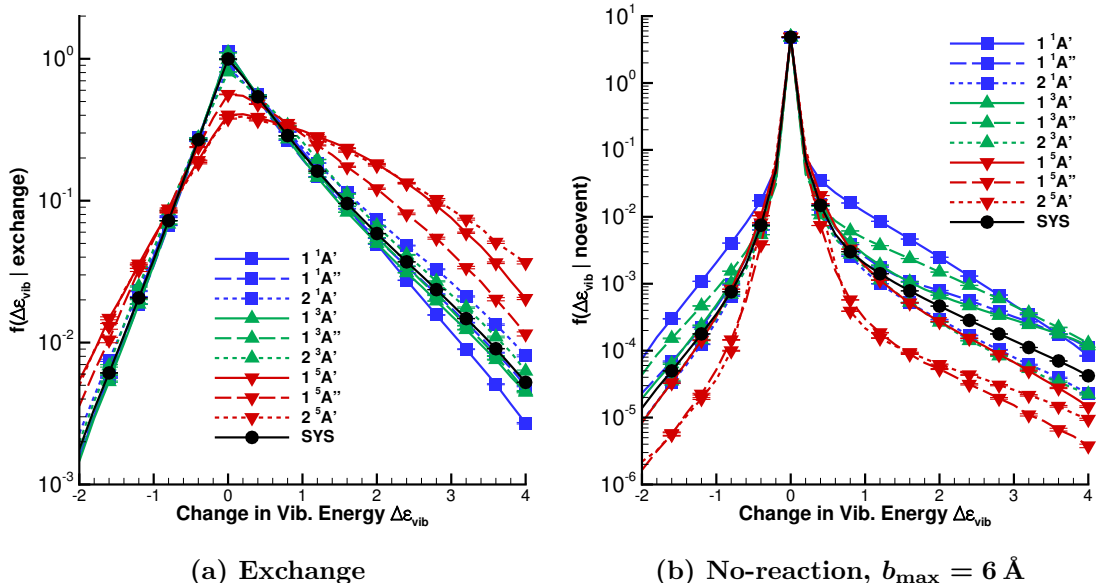


Figure 3.16: PDF of vibrational energy change per event, either exchange or no-reaction for $T_{tr} = 10,000$ K, $T_v = 4000$ K.

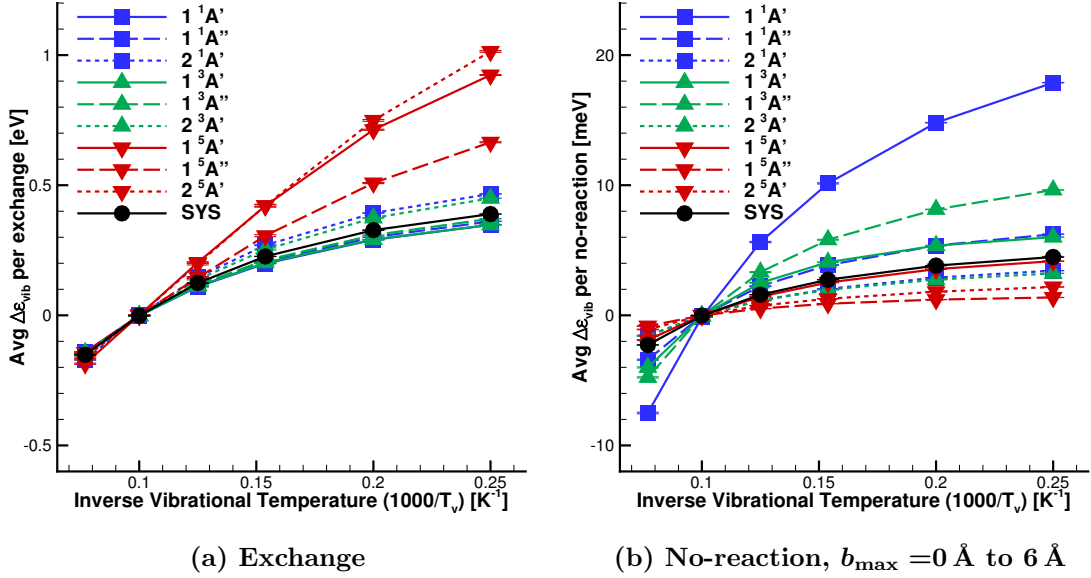


Figure 3.17: Average vibrational energy change per event, either exchange or no-reaction, for the nonequilibrium test set ($T_{tr} = 10,000 \text{ K}$).

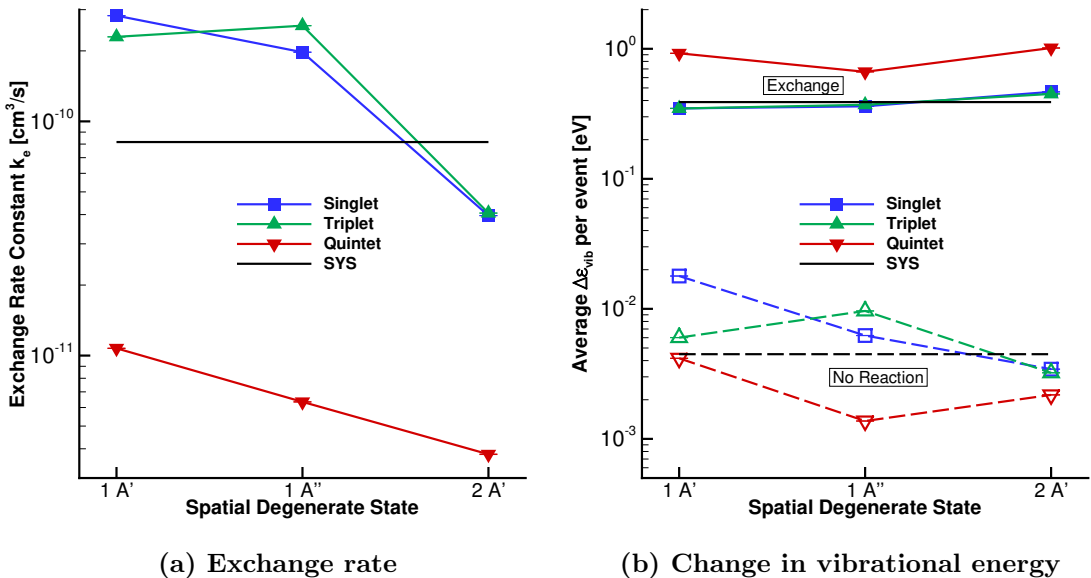


Figure 3.18: Exchange rate and average vibrational energy change per exchange and no-reaction for $T_{tr} = 10,000 \text{ K}$, $T_v = 4000 \text{ K}$.

3.4 Oxygen Dissociation in $O_2 + N_2$, and Aggregate Oxygen Dissociation

Only one PES is required to capture the ground-state interaction of $N_2 + O_2$. Therefore, in this Section, results are presented for oxygen dissociation with partner N_2 , often plotted with results for partners O_2 and O for comparison. As before, we are interested in the reaction rate and vibrational energy change per dissociation, along with any associated microscopic behavior.

The oxygen dissociation rate with partners N_2 , O_2 , and O , for the equilibrium and nonequilibrium test set, is shown in Figure 3.19. The rate with partner O_2 is found to be considerably higher than for partner N_2 . The largest deviation is in the equilibrium test set at 4000 K, in which the partner N_2 rate is 3.25 times less than the partner O_2 rate⁷. For the majority of cases, including in the nonequilibrium test set, the difference is approximately a factor of 2. We also observe a difference between partners O_2 and O . At conditions sampled from equilibrium, the dissociation rate with partner O is approximately 50 % lower than with partner O_2 . For conditions sampled with $T_v < T_{tr}$, the rate with partner O becomes higher than with partner O_2 . A similar observation was made with $N_2 + N$: as T_v is lowered in the nonequilibrium test set, the rate with atomic collision partners decrease less than they do with diatomic collision partners. In Section 3.5.2, we show that this is due to the increased effect translational energy has on $A_2 + A$ type collisions.

For the nitrogen dissociation cases described in Section 3.1, the reaction rate was nearly independent of collision partner species, especially at conditions sampled from low temperature equilibrium. In this respect, oxygen dissociation is substantially different. Many cross-sectional statistics are compared, for all collision partners, in Section 3.5.2, and none of them provide a definitive reason why this difference occurs. The dissociation rate with nitrogen collision partner is compared to data in the literature soon; the Park [18] fits are included here for convenience and consistency with Figure 3.1.

The average energy change per dissociation, for all three collision partners, for the equilibrium and nonequilibrium test set, is shown in Figure 3.20. The vibrational energy change is relatively similar between collision partners in both test sets; the maximum difference is approximately 0.3 eV, which is similar to observations made for nitrogen dissociation from Figure 3.5. In the equilibrium test set, the average change in internal energy varies from 5.0 eV to 5.9 eV for all collision partners, which near or slightly above the dissociation energy; this is also similar to the findings from $N_2 + N_2$ [25]. In contrast, the cases with $T_v < T_{tr}$ exhibit substantial variation in rotational energy change per dissociation, which in turn modifies the internal energy. For the $T_{tr} = 10,000$ K, $T_v = 4000$ K case, the rotational

⁷This value is based on 360 million trajectories which yields an estimated 7.5% relative error; further statistical convergence is ongoing.

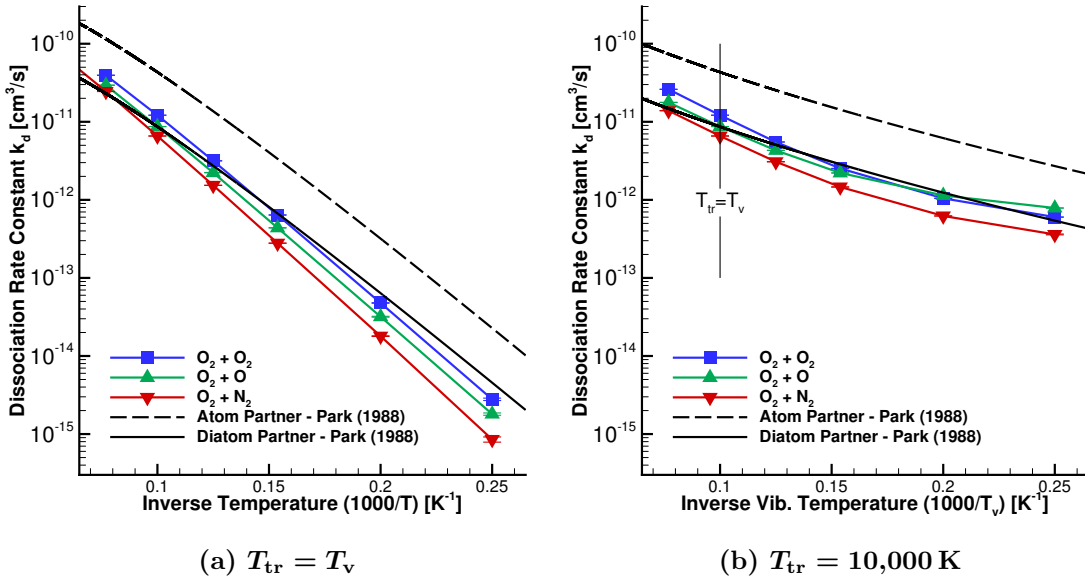


Figure 3.19: Oxygen dissociation rate with collision partners O_2 , O , and N_2 for the equilibrium and nonequilibrium test set.

energy decrease per dissociation exceeds the dissociation energy, and the internal energy decrease is almost 2 eV higher for N_2 partner than O partner. We do not fully understand the behavior of the rotational energy for this strongly nonequilibrium case, therefore. Nevertheless, the vibrational energy change per dissociation, which is a primary quantity of interest, is similar for all collision partners.

The corresponding PDFs of dissociating molecule v and j are shown in Figure 3.21⁸. The character of dissociating molecules is found, as expected, to be primarily vibrationally-excited when conditions are sampled from thermal equilibrium, and rotation compensates for vibration when T_v is suppressed.

At this point, we also show the average vibrational energy change per dissociation for all 6 dissociation reactions in the QCT database, adding nitrogen dissociation with partners N_2 , N , and O_2 . Recall that the temperature range of interest for nitrogen and oxygen dissociation is different, and that the nonequilibrium test set uses a different T_{tr} ; the conditions are described in Section 2.1.4. We first show, in Figure 3.22, results for all reactions on the typical scale: inverse temperature compared to average energy change. Although the curves for nitrogen and oxygen dissociation are similarly shaped, the temperature and energy scales are different. We therefore normalize the change in vibrational energy per dissociation by the corresponding dissociation energy, and the temperature by the corre-

⁸Rovibrational levels may not be consistently compared between the results with partner N_2 and partners O_2 and O , because the oxygen diatomic potentials are different; see Table 2.1. Quantities related to these PDFs are described and compared between collision partners in Section 3.5.2.

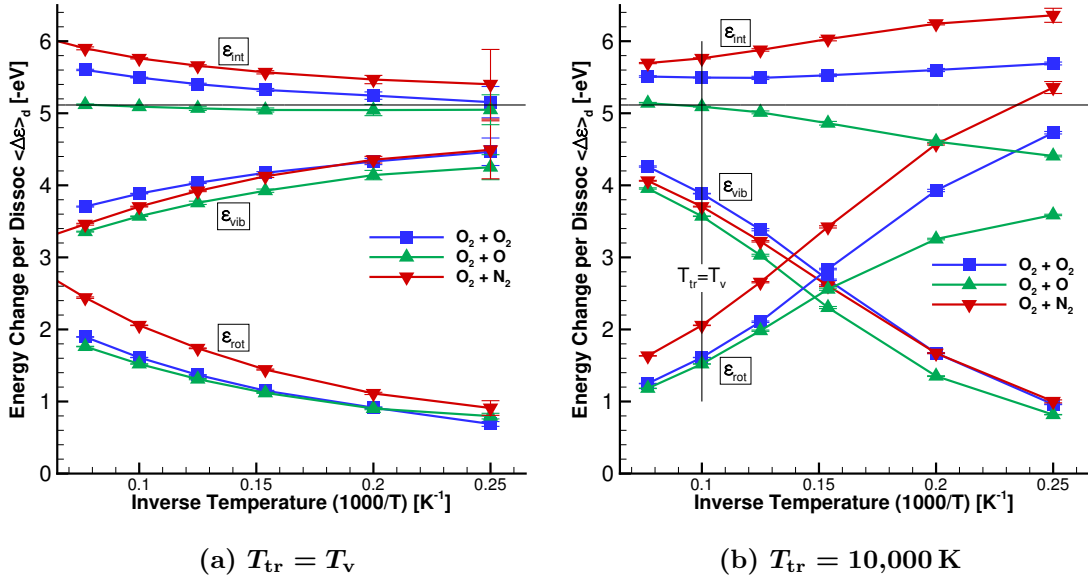


Figure 3.20: Change in system energy per oxygen dissociation for collision partners O_2 , O , and N_2 , for the equilibrium and nonequilibrium test set.

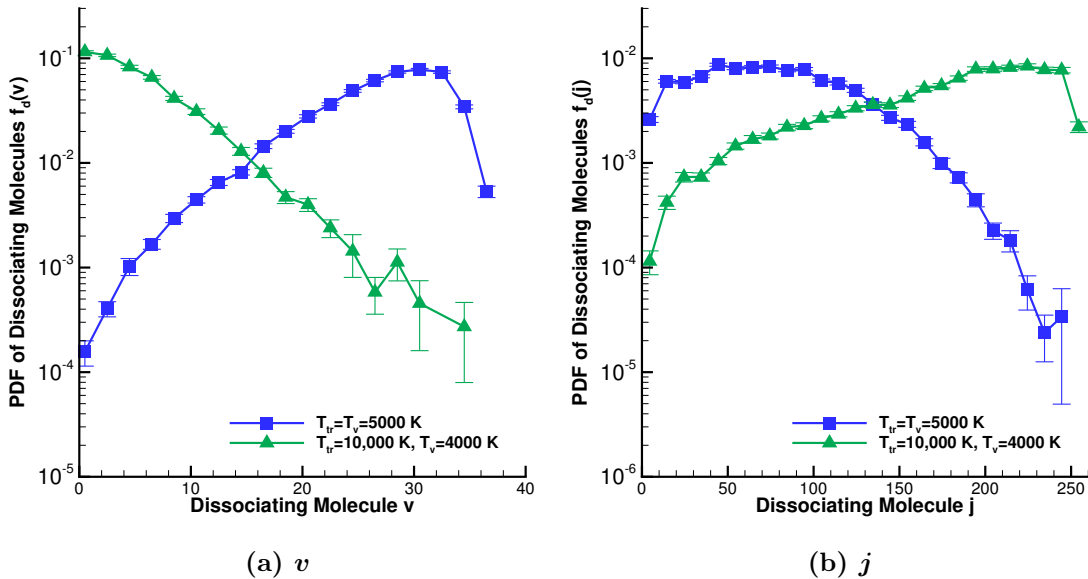


Figure 3.21: PDF of v and j for the population of molecules that undergo oxygen dissociation with N_2 partner, for an equilibrium and nonequilibrium condition.

sponding dissociation temperature. This yields Figure 3.23. Now, we can clearly see that all curves roughly collapse, to within about 10 % of the dissociation energy. These curves indicate the character of molecules that dissociate. As described by Bender [25] for the case of $N_2 + N_2$, when conditions are sampled from thermal equilibrium, molecules that dissociate are primarily vibrationally excited. This specificity weakens as temperature increases, because other modes of energy are more able to make up for a lack of vibrational energy. When conditions are sampled with $T_v < T_{tr}$, rotation compensates for vibration and molecules that dissociate are rotationally excited instead. The present results demonstrate that those findings apply in general for both nitrogen and oxygen dissociation, for the variety of collision partners studied. We also perform aggregate analyses in Sections 3.5 and 3.6.

Finally, Figure 3.24 compares the available data in the literature to our results for oxygen dissociation with partner N_2 . Based on the reviews of oxygen dissociation shock tube data performed in the 1960s [40, 43, 44], the available data for partner N_2 was extremely limited at the time. This conclusion still holds today: we are only aware of two experimental measurements [15, 39] of this reaction. The fits of Bortner [43] and the reinterpretation of Park [9], which we show, are based only on the work of Generalov and Losev [39]. Other reviews and fits that we have examined [40, 45] also do not include other sources of data for this reaction. Therefore, Park [9] based his rate for partner N_2 , at least in part, on the better-characterized rate for partner O_2 ; the two rates are equal in his model. In fact, Park's rate for partner N_2 is too large compared to the experimental result of Generalov and Losev [39], which is specifically noted in one of his works [16, p. 9]. Furthermore, the experimental data of Jerig *et al.* [15], which was performed after Park's reinterpretation and had a primary goal of measuring this rate, found a rate that was much lower than the one described by Park. In this context, it seems reasonable that Park's recommendation for oxygen dissociation with partner N_2 may be too high.

Our present results are consistent with this hypothesis. At 4000 K, the present result is within a factor of 2 of both experimental measurements [15, 39], which are themselves approximately a factor of 3 apart. At this condition, the Park rate is a factor of 5 higher than the present work. The differences are somewhat dependent on temperature, but our result is at least two times lower than the Park rate for the entire temperature range that the Park rates were initially quoted to be accurate (up to 7000 K). Our results are also similar to those of Andrienko and Boyd [90], who also used the Varga *et al.* [65] N_2O_2 PES. The temperature range of the present work is wider than that reported for Andrienko and Boyd [90].

As we noted in the previous Sections, a self-consistent comparison of our Boltzmann-sampled data with experimental data is difficult. The primary reason for this is the thermal

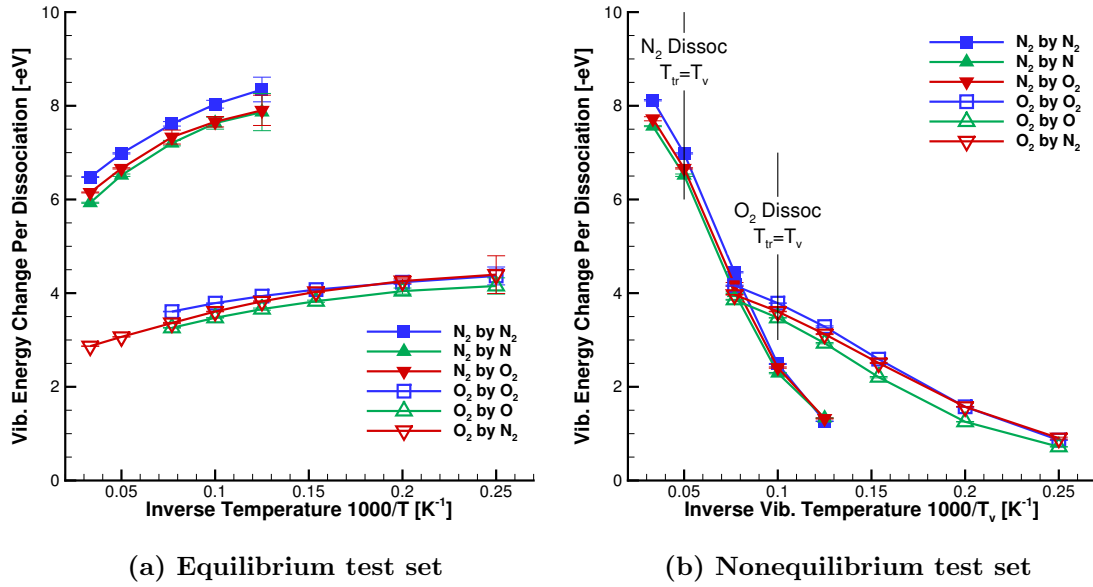


Figure 3.22: Average change in vibrational energy per dissociation for all 6 dissociation reactions, for their corresponding equilibrium and nonequilibrium test set.

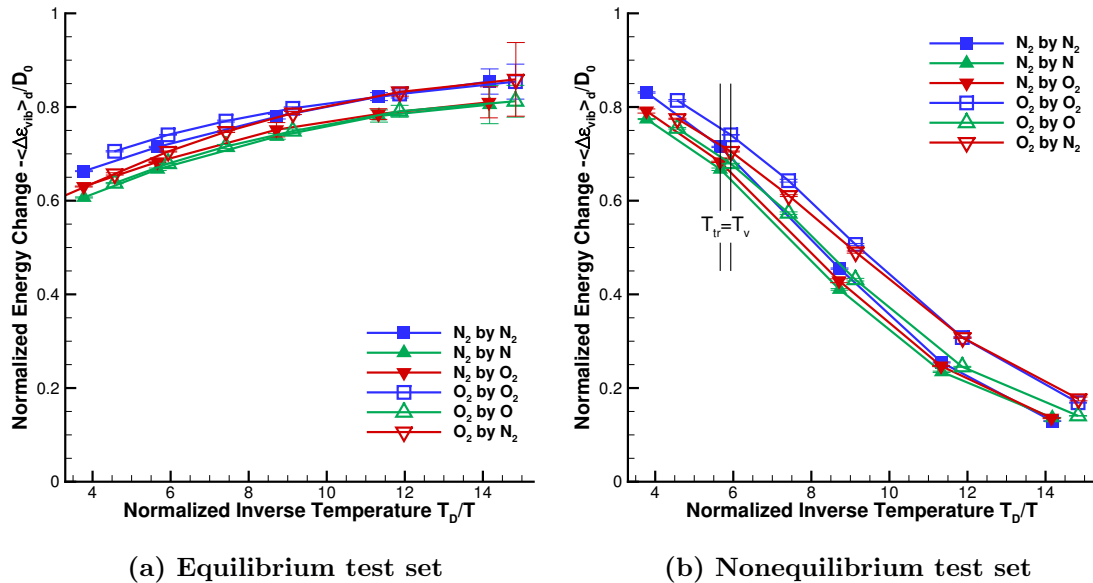


Figure 3.23: Average change in vibrational energy per dissociation for all 6 dissociation reactions, for their corresponding equilibrium and nonequilibrium test set. Temperature is normalized by dissociation temperature T_D and vibrational energy change per dissociation by dissociation energy D_0 .

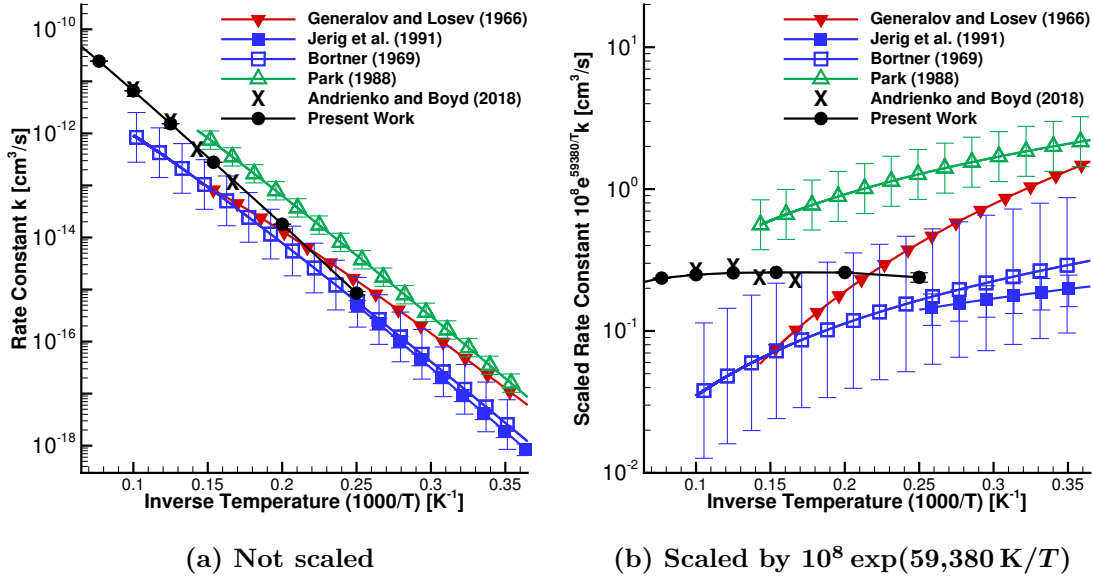
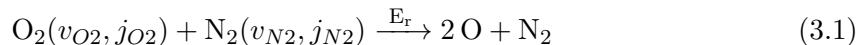


Figure 3.24: Equilibrium oxygen dissociation rate with partner N_2 , compared to literature.

nonequilibrium that exists in a real dissociating gas, resulting in a lower dissociation rate during QSS. We do not account for QSS here, but such a correction would lower the dissociation rate, bringing it further from the Park rate. We are also not aware of any mechanism that could substantially promote vibrational or electronic relaxation in an $N_2 + O_2$ system. Therefore, we find that the widely-used Park rate for oxygen dissociation with partner nitrogen is too high. Because we do not account for QSS, we cannot quantify a new rate at this point. Further investigation, ideally with DMS or other tools that can account for the role of vibrational relaxation and nonequilibrium, is warranted. The initial decomposition of air is dominated by oxygen dissociation with partner N_2 , and so a variety of quantities of interest are expected to be sensitive to this rate.

3.5 Effect of Reactant States

QCT and other similar methods can provide a wealth of data and detailed information about mechanisms and outcomes. In order to develop reduced-order models for CFD, we must investigate which effects are important and which may be neglected. Consider the case of oxygen dissociation by nitrogen. The probability of dissociation may depend on the rovibrational state of all reactants and the relative translational energy,



There are many reactant degrees of freedom for this reaction; N_2 and O_2 have around 9000 and 6000 possible rovibrational states (v, j combinations) respectively, and translational energy is continuous. Which of these reactant states are important for the dissociation rate, and to what extent do they influence the outcome? In this Section, we quantify the effect that each reactive state has on whether dissociation will occur.

We first determine a framework to assess this question, and define the support factor S to aggregate data across multiple conditions and reactions. Data are shown for all 6 simple dissociations in the QCT database: nitrogen dissociation via collision partners N_2 , N and O_2 , and oxygen dissociation via collision partners O_2 , O , and N_2 .

3.5.1 The Support Factor

Consider, for example, the effect of oxygen's vibrational quantum number v on whether that oxygen molecule will dissociate. Figure 3.25a shows the average probability of dissociation P_d and the probability of dissociation from a specific v -level $P_d(v)$. We see that vibrationally-excited (high- v) oxygen molecules are much more likely to dissociate than non-excited molecules. Furthermore, v is an initial condition and dissociation is an outcome, and so this relationship is causal. The range of probabilities in Figure 3.25a is large: for this condition, a high- v molecule is approximately ten thousand times more likely to dissociate than a low- v molecule. From this information, we conclude that oxygen's vibrational quantum number has a large effect on whether oxygen dissociation will occur. This conclusion is, of course, well known in the literature. However, the basic principle, that the range in dissociation probability from a specific reactive state quantifies the effect of that reactive state on dissociation, forms the basis for our analysis in the rest of this paper.

The average probability of dissociation also varies substantially for different reactions, which makes it difficult to aggregate data for both nitrogen and oxygen dissociation. This issue is also apparent when attempting to aggregate data for different temperatures. We therefore normalize the probability of dissociation from a specific state $P_d(v)$ by the average

probability of dissociation P_d ,

$$S(v) \equiv \frac{P_d(v)}{P_d} \quad (3.2)$$

S is the support factor, and it quantifies the effect that a particular reactive state (v in this case) has on dissociation⁹. For example, $S(v=35) = 200$, which means a molecule with $v=35$ is 200 times more likely to dissociate, when compared to the average. Alternatively, vibrational quantum number *supports* dissociation, by a factor of 200 for $v = 35$.

The support factor may also be cast in terms of population densities, such as those shown previously in Figure 3.4. Equivalent to Equation 3.2, we can write

$$S(v) = \frac{f_d(v)}{f(v)} \quad (3.3)$$

in which $f(v)$ is the PDF of vibrational quantum number for all molecules and $f_d(v)$ is the PDF for molecules that go on to dissociate. Figure 3.25b shows both of these terms for the same condition as Figure 3.25a. High- v molecules are more likely to dissociate, and so (compared to the whole population) they make up a disproportionately large fraction of the population which goes on to dissociate. The difference between right-hand-side numerators in Equations (3.2) and (3.3) is subtle: $P_d(v)$ is the probability that a given v -level will dissociate, whereas $f_d(v)$ is the population distribution of particles which will dissociate. For both subfigures of 3.25, the support factor is equal to the ratio of solid to dashed lines. A wide range of values in the support factor indicates that the reactant state in question has a large effect on whether dissociation will occur.

A good way to illustrate the utility of the support factor is to investigate how the vibrational quantum number's effect on dissociation changes with temperature. Previous research on nitrogen dissociation [25, 84] has shown that, as temperature increases, vibrationally-excited molecules play a less dominant role in dissociation, because other energy modes are able to make up for the lack of vibrational energy. We find that oxygen dissociation in $O_2 + N_2$ behaves similarly; support for oxygen dissociation by vibrational quantum number v is shown in Figure 3.26. At conditions sampled from 5000 K, a high- v molecule is approximately 10^8 times more likely to dissociate than a low- v molecule. At 13,000 K, though, the range in S has decreased to approximately 10^3 , meaning that vibration has less of an effect on dissociation at high temperatures.

⁹The support factor was defined but not motivated in Section 2.3.4.

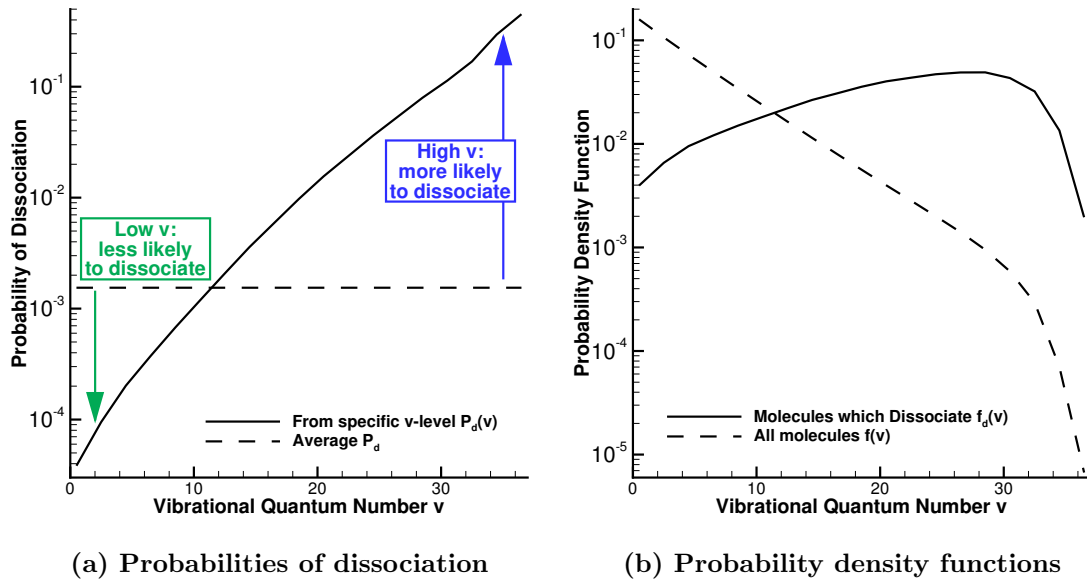


Figure 3.25: Conditional (solid) and unconditional (dashed) probabilities and PDFs for oxygen dissociation in $O_2 + N_2$, $T_{tr} = T_v = 10,000$ K.

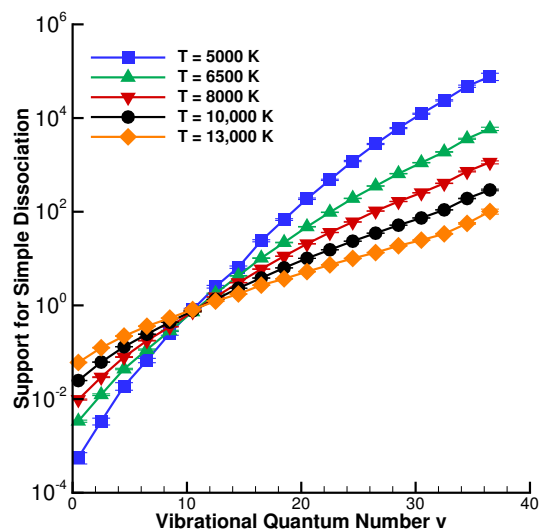


Figure 3.26: Support for simple oxygen dissociation by reactant oxygen's v -level in $O_2 + N_2$.

3.5.2 Simple Dissociation

In this Section, we examine the effect of each reactive state on simple dissociation when conditions are sampled from thermal equilibrium. Data for $T_{\text{tr}} = T_{\text{v}} = 10,000 \text{ K}$ are presented here, and other temperatures are qualitatively similar. The support factor is shown; as discussed, the range in S quantifies the effect of a particular reactive state on dissociation. Each reactive state is represented by energy, which is normalized by the corresponding dissociation energy D_0 . Note that the rotational (and thus internal) energy of a molecule can exceed its dissociation energy; these *quasi-bound* states are rare but make up a considerable portion of molecules which dissociate [25]. To most easily compare between reactive states, both axis ranges are held fixed for all plots in this Section.

Support for simple dissociation by the dissociating molecule's internal energy is shown in Figure 3.27a. For all simple dissociations, the support factor varies over a large range: a nitrogen molecule with no internal energy is approximately one million times less likely to dissociate than a nitrogen molecule with internal energy near the bond energy. This means that the dissociating molecule's internal energy has a large effect on dissociation. We also observe several other features in the data. Curves for nitrogen dissociation with each collision partner are similar, especially at relatively high energies where most of the dissociations actually occur. Therefore, in addition to rates for each partner being similar (as discussed in Section 3.1.1), these in-depth statistics are also independent of the partner species. Support for oxygen dissociation varies over a smaller range than for nitrogen dissociation; oxygen is a weaker bond than nitrogen, and so translational energy is more able to make up for a lack of internal energy. A similar trend is observed as temperature changes for a constant dissociating species [25, 84]. Finally, a discontinuity in slope exists at $\varepsilon_{\text{int}} = D_0$, the interface between bound and quasibound molecules. A bound molecule has one pathway to dissociation: its energy must increase. A quasibound molecule, however, has two pathways to dissociation: its energy can increase, or rotational energy can be transferred into vibrational energy. By definition, a quasibound molecule is prevented from dissociating by the centrifugal barrier; if rotation decreases while internal energy remains the same, dissociation can occur. This change in pathways for dissociation, we believe, is responsible for the discontinuity, although further research is needed. Ultimately though, the key conclusion from Figure 3.27a is that the dissociating molecule's internal energy has a substantial effect on whether or not dissociation will occur.

Figure 3.27b shows support for simple dissociation by the collision partner's internal energy, and it is starkly different. For all 4 applicable simple dissociations, the support factor is nearly constant at 1. (Note that $\text{A}_2 + \text{A}_2$ interactions do not appear here because atomic species have no vibrational or rotational energy.) When $S = 1$ everywhere, dissociation is formally statistically independent of the collision partner's internal energy. Conceptually,

if the probability of dissociation with a highly-energetic partner is the same as with a non-energetic partner, the collision partner's internal energy does not influence whether that dissociation occurs. For these cases, we find dissociation to be mostly independent of the collision partner's internal energy. The largest variation in support occurs for $\text{N}_2 + \text{N}_2$, where colliding with a partner with internal energy above the dissociation energy is approximately 3 times more likely to result in dissociation than colliding with a non-excited partner. This factor of 3 is much smaller than the factor of one million observed for the dissociating molecule's internal energy. Moreover, molecules with internal energy larger than the dissociation energy are rare (0.02% for N_2 at this condition), and they are not strongly selected in this case. Therefore, for the purposes of modeling chemical kinetics, simple dissociation is approximately independent of the collision partner's internal energy. This conclusion has important ramifications for model formulation, which are discussed at the end of this Section.

Figure 3.28 shows support for simple dissociation by the reactant relative translational energy E_r . As expected, this reactant quantity is important for determining whether dissociation will occur, although the range in support is not as large as the range in support for the dissociating molecule's internal energy. Unlike other reactant states, we observe different behavior for $\text{N}_2 + \text{N}$ and $\text{O}_2 + \text{O}$ interactions, compared with the others: relative translational energy is more effective at promoting dissociation in $\text{A}_2 + \text{A}$ reactions. This is the primary reason why $\text{N}_2 + \text{N}$ and $\text{O}_2 + \text{O}$ have a higher reaction rate constant in thermal nonequilibrium; when vibrational energy is depleted, translational energy is more relevant. Now, we have shown support for simple dissociation by the three independent reactive energies: the dissociating molecule's internal energy, the collision partner's internal energy (if it exists), and the relative translational energy. Of these, the dissociating molecule's internal energy has the largest effect on dissociation, relative translational energy has a moderate effect, and the collision partner's internal energy is likely negligible.

We can also separate internal energy into vibrational and rotational components, in order to further investigate the dependence of dissociation on the dissociating molecule's internal energy. Formally, this separation is ambiguously defined, because rotation and vibration are inherently coupled. However, when conditions are sampled from thermal equilibrium, as they are here, this separation is performed only as a postprocessing step. Furthermore, we find that the method of separation has a negligible effect on the results shown, as demonstrated in the next Section. Figure 3.29 shows support for simple dissociation by the dissociating molecule's vibrational and rotational energy. Both modes affect dissociation, but vibration's effect is particularly pronounced. First, the range of support by vibrational energy is larger than the range of support for rotational energy. Second, the maximum vibrational energy is less than the maximum rotational energy, because rotational energy

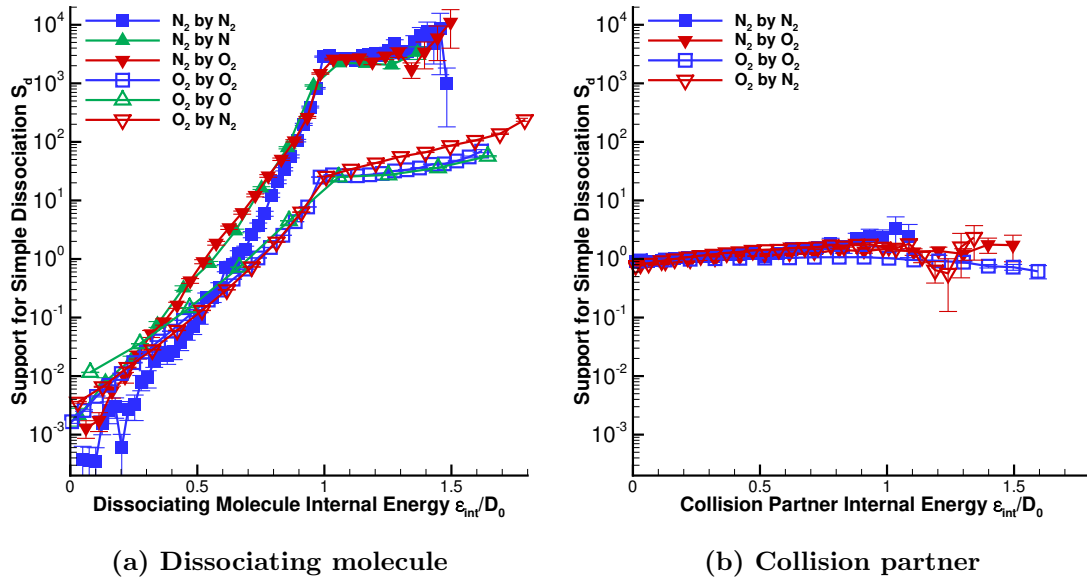


Figure 3.27: Support for simple dissociation by reactant internal energies, $T_{\text{tr}} = T_{\text{v}} = 10,000 \text{ K}$.

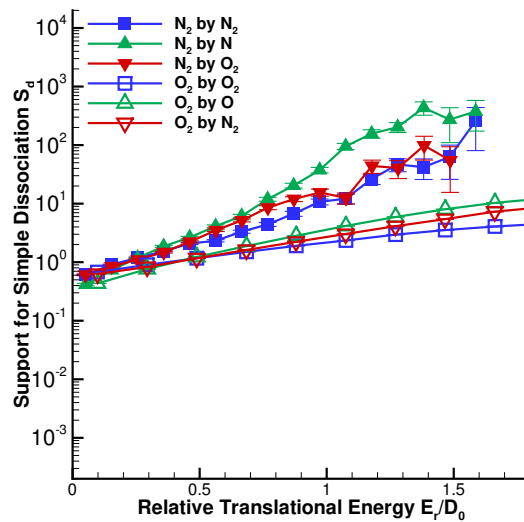


Figure 3.28: Support for simple dissociation by reactant relative translational energy, $T_{\text{tr}} = T_{\text{v}} = 10,000 \text{ K}$.

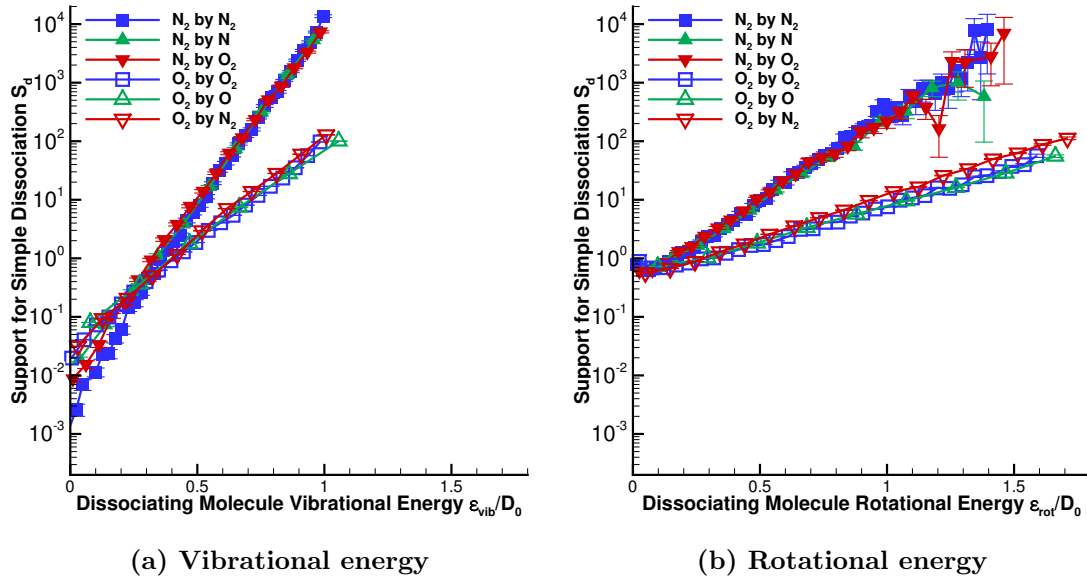


Figure 3.29: Support for simple dissociation by reactant energy modes of the dissociating molecule, $T_{\text{tr}} = T_{\text{v}} = 10,000 \text{ K}$.

can exceed the dissociation energy. (Rotational energy increases the centrifugal barrier, but vibrational energy does not.) The slope in support for simple dissociation is therefore much larger for vibration than rotation. This means that one unit of vibrational energy causes a larger increase in dissociation probability than one unit of rotational energy.

Vibrational energy's pronounced effect on dissociation is consistent with our discussion in Section 3.1.3 regarding the character of molecules that dissociate. When conditions are sampled from thermal equilibrium, vibrational and rotational energies are equally prevalent, and so most molecules that dissociate are vibrationally excited. There are therefore two reasons why vibrational and rotational energies evolve differently in a dissociating gas. First, rotation relaxes more quickly, and so a recently-shocked gas has more rotational than vibrational energy. Second, dissociation tends to draw more energy from vibration, and so a dissociating gas experiences more depletion of vibrationally-excited molecules than rotationally-excited molecules. Both of these differences are most pronounced at relatively low-to-moderate temperatures where the rovibrational coupling is weaker [10, 91]. The fact that vibrational and rotational energies evolve differently *and* that they affect dissociation differently means we should consider continuing to treat them separately in CFD for hypersonic applications.

For the purposes of modeling chemical kinetics, understanding the probability of dissociation P_d is critical. We have shown that the collision partner's internal energy is likely negligible, and that vibrational and rotational energies of the dissociating molecule have

distinct effects. It is therefore reasonable to represent the complete probability of simple dissociation, independent of all other variables, in terms of three reactant energies,

$$P_d(\varepsilon_{\text{vib}}, \varepsilon_{\text{rot}}, E_r) \quad (3.4)$$

in which ε_{vib} and ε_{rot} are the dissociating molecule's vibrational and rotational energy components, and E_r is the relative translational energy. This type of form has often been assumed in kinetic theory (see, for example, Jaffe [56] and Hansen *et al.* [125]), but here it has been demonstrated using statistical analysis of trajectory data. We also note that, for each of the simple dissociations examined so far, support for these reactant energies is roughly linear on a log-scale plot (Figures 3.28 and 3.29). Furthermore, the curves for vibrational and rotational energies are largely independent of collision partner species. Both of these observations may prove useful when attempting to fit a functional form to the full three-dimensional probability of dissociation, which we do not attempt here.

3.5.3 Thermal Nonequilibrium and Non-Simple Dissociations

We have found that, for simple dissociations at thermal equilibrium, the collision partner's internal energy does not greatly affect whether dissociation occurs. In this Section, we present two relatively minor caveats to this finding that we believe are worth noting. Figure 3.30 shows the support for simple dissociation by the collision partner's internal energy, with conditions sampled from varying degrees of thermal nonequilibrium in $O_2 + O_2$. As the vibrational temperature decreases, the range in support increases, meaning that the effect of collision partner's internal energy increases with increasing nonequilibrium. The effect is limited, however; even in the strongest nonequilibrium case ($T_{\text{tr}} = 10,000$ K, $T_v = 4000$ K), a high-energy partner is only about 2.2 times more likely to cause dissociation than a low-energy partner. (Note that the y -axis range here is much smaller than for other plots of support.) As we argued in the previous Section, this factor is small compared to other reactant effects. Nevertheless, the trend is clear, and the effect of the collision partner's internal energy on dissociation at conditions sampled from thermal nonequilibrium should continue to be examined.

More reactions than simple dissociation can result in the destruction of molecules. As discussed in Section 2.3.1, swap and double dissociations can occur in $N_2 + N_2$ and $N_2 + O_2$ collisions. For these events, there is no such thing as a collision partner: both reactant bonds break. It is therefore unreasonable to expect that any reactant energy state may be neglected. Figure 3.31 shows support for swap dissociation by the reactants' internal energy; the range in support is large for all cases. This means that Equation (3.4) is likely insufficient to model the probability of swap or double dissociation events. Non-simple dissociations

contribute to kinetics by varying degrees depending on the reaction and condition. As we have described, swap dissociations are relevant for both $\text{N}_2 + \text{N}_2$ and $\text{O}_2 + \text{O}_2$ reactions. In $\text{O}_2 + \text{O}_2$, swap dissociations account for at least 10 % of the effective dissociation rate for all temperatures. As we discuss in Section 3.7.1, dissociation and exchange in $\text{N}_2 + \text{O}_2$ is the dominant mechanism to destroy N_2 in that reaction for all conditions. Further research is needed to analyze these more complex reactions and determine the extent to which they must be captured in a chemical kinetics model for CFD.

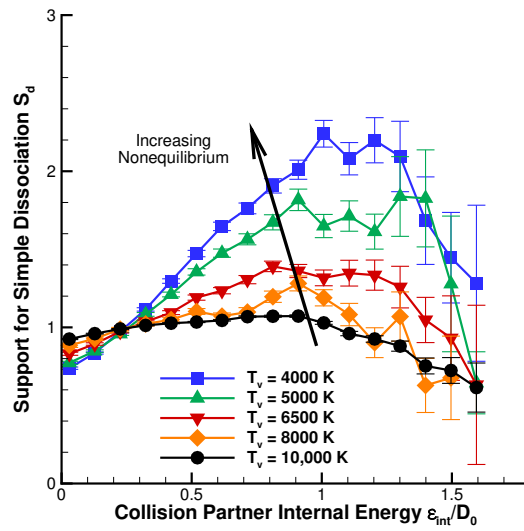


Figure 3.30: Support for simple dissociation by the collision partner's internal energy for $\text{O}_2 + \text{O}_2$ in the nonequilibrium test set, $T_{\text{tr}} = 10,000 \text{ K}$.

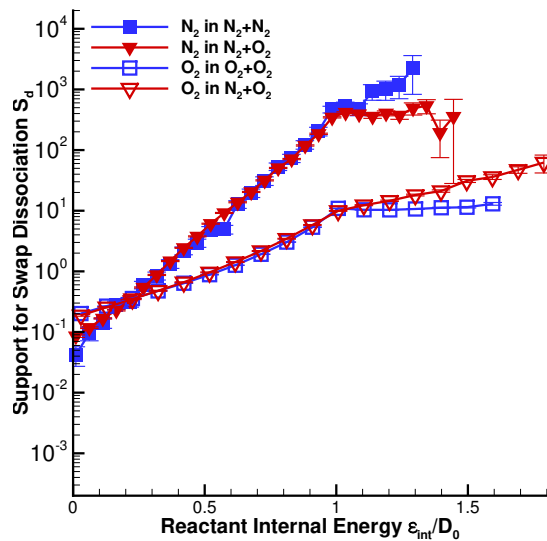


Figure 3.31: Support for swap dissociation by reactant energies for $T_{\text{tr}} = T_v = 10,000 \text{ K}$.

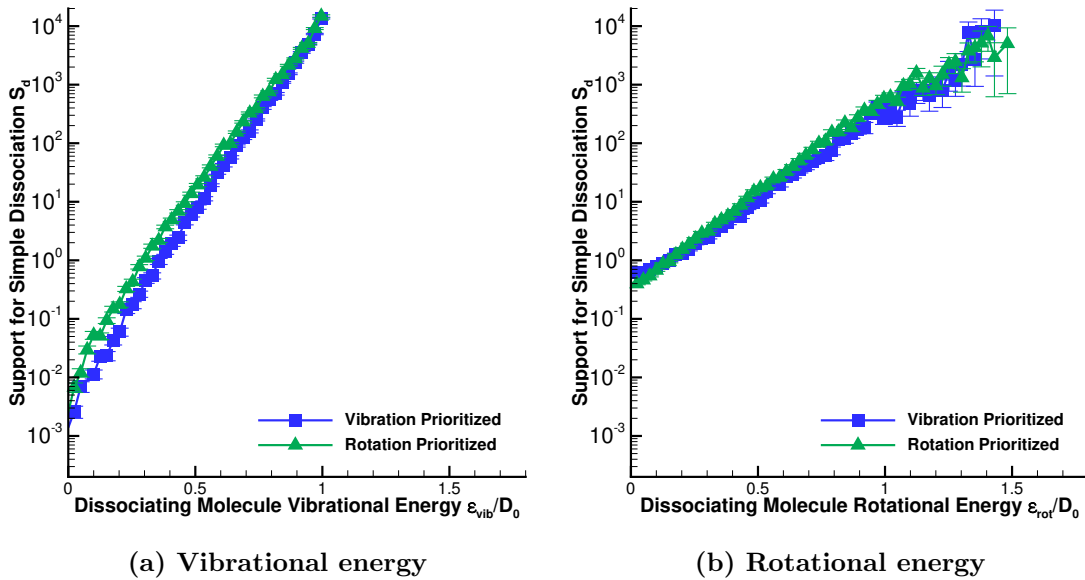


Figure 3.32: Support for simple dissociation by energy modes of the dissociating molecule, for both the vibration-prioritized and the rotation-prioritized energy separation framework; $\text{N}_2 + \text{N}_2$ interactions at $T_{\text{tr}} = T_{\text{v}} = 10,000$ K.

3.5.4 Comparison of Energy Separation Methodologies

We wish to briefly assess whether our choice of energy separation methodology is influencing the conclusion that rotational energy is less effective at promoting dissociation than vibrational energy. Recall that, consistent with other researchers and past work, we use the vibration-prioritized framework, as described in Section 2.1.2. For the case of $\text{N}_2 + \text{N}_2$ at $T_{\text{tr}} = T_{\text{v}} = 10,000$ K, we therefore recompute rovibrational energies using the rotation-prioritized framework. Because this case is sampled from a single rovibrational temperature, the separation methodology does not influence the preparation of particles. Figure 3.32 shows the support for simple dissociation by rotational and vibrational energies, with both frameworks. The results are only slightly different; for both frameworks, the range in support by vibrational energy is approximately 3 orders of magnitude larger than the range in support by rotational energy. Therefore, we conclude that the separation methodology is not a substantial contributor to the different effect observed for vibrational and rotational energy.

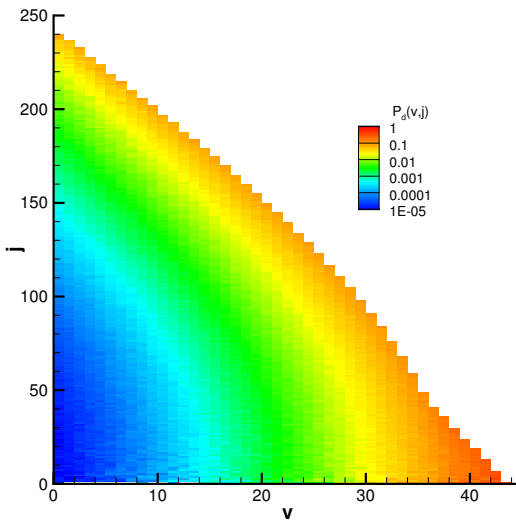


Figure 3.33: Probability of dissociation from each rovibrational level

3.5.5 Why Vibration?

In this Section, we investigate why vibrational energy has a stronger effect on dissociation than rotational energy does. Several of REAQCT’s updated postprocessor capabilities were designed with this goal in mind, specifically the multi-dimensional PDFs and expected values. Let us frame a central question: *what quantity is a good predictor of dissociation?* We will use the $\text{O}_2 + \text{O}$ reaction, averaged over all ground-electronic-state interaction states, at $T_{\text{tr}} = T_v = 10,000 \text{ K}$, which is a relatively simple reaction and has good statistical convergence. We first compute the probability of dissociation from each rovibrational level, $P_d(v, j)$. These data may be visualized as a contour plot, as in Figure 3.33, which gives a good sense for the overall trends but is not particularly useful for quantitative analysis.

A scatter plot compared to each component of energy, Figure 3.34, shows clearly that neither vibrational or rotational energy alone are good predictors of dissociation. Substantial vertical scatter in the data indicate that a specific value of the abscissa may result in a range of dissociation probabilities. Internal energy, too, is a poor predictor of dissociation because, as shown in Figure 3.35, there is also substantial scatter. For a given internal energy, molecules that are more vibrationally excited are found to be more likely to dissociate; this conclusion is consistent with our findings using the support factor. We identify two sample rovibrational levels with similar internal energy: one with small ε_{vib} and the other with large ε_{vib} . The state which has its internal energy in rotation is approximately 8.5 times less likely to dissociate than the state which has its internal energy in vibration.

The effective diatomic potentials for these two states are shown in Figure 3.36. Although neither of these molecules is quasibound, the molecule with mostly rotational energy requires

more energy to dissociate due to the centrifugal barrier, assuming its angular momentum remains constant. We quantify this by defining the *remainder energy*, ε_{rem} , which is the difference between the centrifugal barrier height and the internal energy,

$$\varepsilon_{\text{rem}}(v, j) = \max [V_{D,\text{eff}}(j)] - \varepsilon_{\text{int}}(v, j) \quad (3.5)$$

in which max refers to the local maximum¹⁰. Several analyses in the literature have used the barrier height in theoretical arguments, often as an effective dissociation energy [56, 60, 73]; this interpretation is similar. In this case, however, here we are directly evaluating its validity as a predictor for dissociation. We find that the barrier energy is a relatively good predictor of dissociation; the scatter in probability is approximately a factor of 2, a substantial portion of which is due to statistical uncertainty. This result indicates that the reason why rotational energy is less effective at promoting dissociation is because rotational energy also increases the centrifugal barrier. Adding one unit of rotational energy reduces ε_{rem} by an amount less than the energy added. This reduction does not occur for vibrational energy.

¹⁰The global maximum is at low r , due to the repulsive wall.

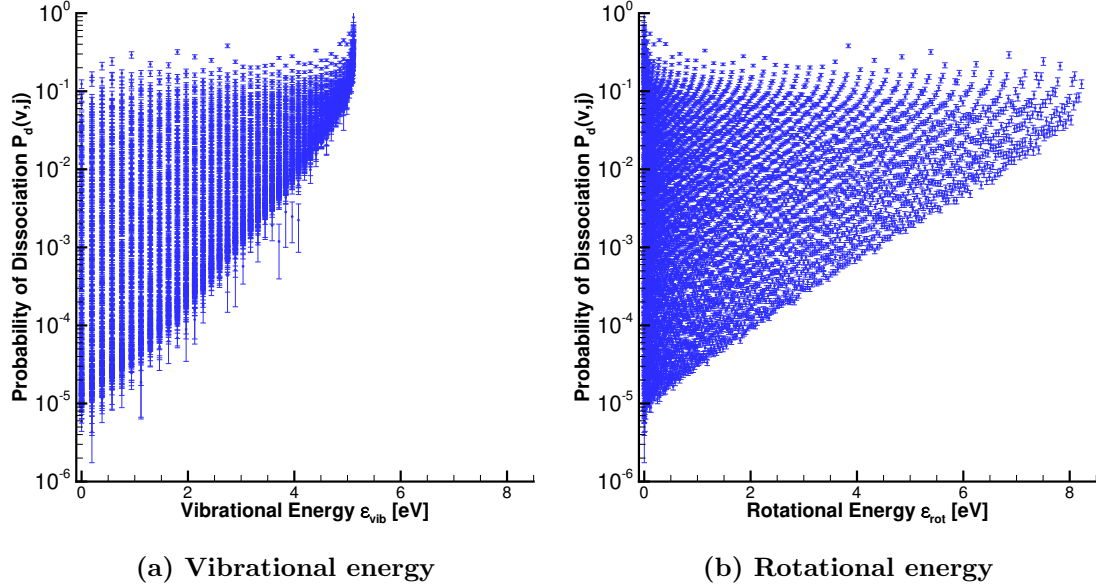


Figure 3.34: Probability of dissociation from each vibrational level, compared to vibrational and rotational energy.

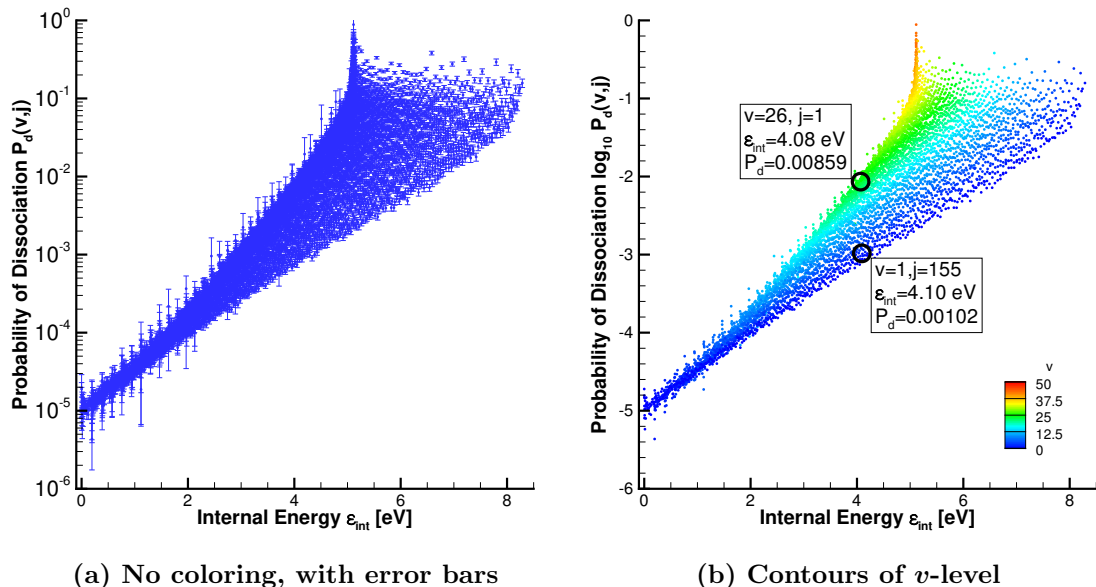


Figure 3.35: Probability of dissociation from each vibrational level, compared to internal energy. The trend in v -level is apparent, and two states with similar ε_{int} are displayed

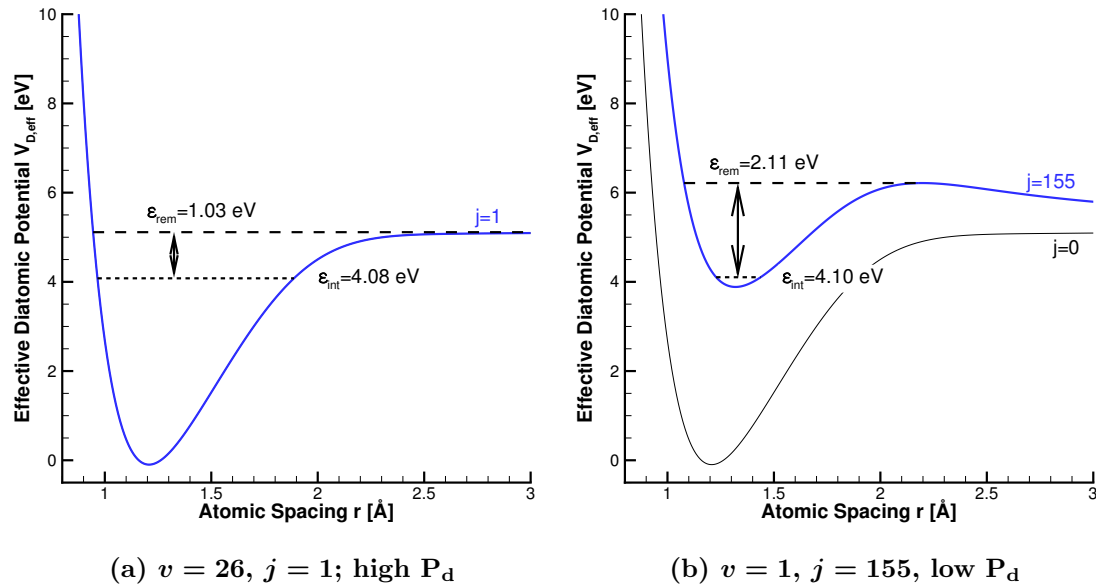


Figure 3.36: Effective diatomic potential for two rovibrational states with similar internal energies

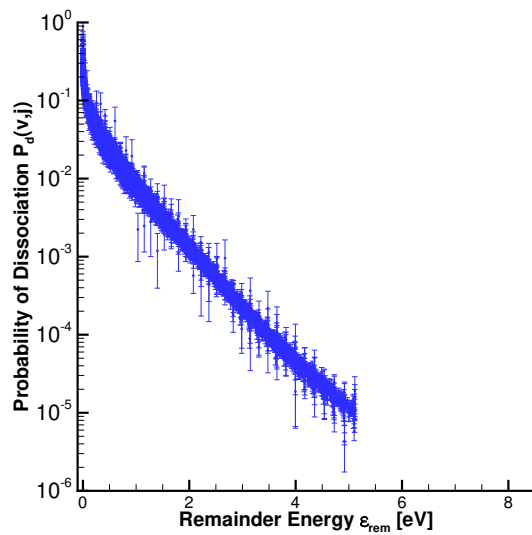


Figure 3.37: Probability of dissociation from a specific remainder energy ϵ_{rem}

3.6 Fitting QCT Data

In this Section, we describe the methodology and results for fitting aggregate quantities of interest from QCT to relatively simple analytic forms. When possible, functional forms that exist in the literature are used. Fits are considered for both the dissociation rate and change in vibrational energy per dissociation, for the equilibrium and nonequilibrium test sets. Each dissociation reaction with a specific collision partner (eg. O₂ dissociation with N₂ partner) is considered separately. Each dissociation type (eg. effective, simple, and so on) is also considered separately, but particular attention is paid to effective dissociation. When surfaces for multiple degenerate states are available (O₂ + O₂ and O₂ + O), quantities of interest are averaged over the relevant surfaces before any fitting is performed. When performing the fitting, we do not weight data based on uncertainty but any values with relative error greater than 10% are discarded¹¹. Oxygen dissociation results in O₂ + N₂ are restricted to the range 4000 K to 13,000 K, in order to be consistent with the temperature range for other oxygen dissociation collision partners.

We present this analysis for several reasons. First, we want to establish the validity of functional forms in the literature, such as an Arrhenius rate, to our results. Second, some fitting coefficients have physical meaning that we are interested in describing. Finally, if the fits are accurate, others may use them in-lieu of our specific data points. However, the creation of these fits is *not* an endorsement of their use directly in a chemical kinetics model in CFD. As we will describe later, see Section 4.2.1, simply applying QCT results directly to a chemical kinetics model neglects that non-Boltzmann distributions of internal energy exist in a dissociating and relaxing gas.

3.6.1 Equilibrium Dissociation Rate

We first fit dissociation rate data for the equilibrium test set ($T_{\text{tr}} = T_{\text{v}}$) to the generalized Arrhenius form, Equation (1.1). To fit coefficients, we cast the equation in terms of inverse temperature and the natural logarithm of the dissociation rate,

$$\ln(k_{\text{d}}) = \ln(C) - n \ln\left(\frac{1}{T}\right) - T_{\text{D}} \frac{1}{T} \quad (3.6)$$

We choose to use this form for several reasons. First, the equation is now linear in the coefficients we wish to determine, $\{\ln(C), -n, -T_{\text{D}}\}$. We can therefore use a standard least squares estimator to determine the coefficients (see, for example, Riley *et al.* [126, p. 1271–

¹¹Reaction rate and vibrational energy change per dissociation are converged to within 5 % uncertainty for effective dissociation events, except for N₂ + O₂ at 4000 K which is ongoing and currently at 8 %. This cutoff is therefore only relevant for non-effective dissociation events such as swap dissociations, which we analyze only for the equilibrium dissociation rate. The cutoff for double dissociation is further increased to 20 %.

1277]). Second, a least squares minimization in $\ln(k_d)$ corresponds to minimizing the relative error in k_d , which is desirable. For the conditions of interest, k_d varies by many orders of magnitude, so minimizing the absolute error would essentially neglect relative error in the small but important k_d values at low temperatures. We note that this transformation corresponds to the usual way reaction rates are visualized: inverse temperature on the abscissa and log-scale reaction rate on the ordinate.

Results for all dissociation reactions we have considered are shown in Tables 3.1 and 3.2. The data are found to be well-described by the Arrhenius form; the goodness-of-fit metric R^2 [computed in $\ln(k_d)$ space] is better than 0.9998 for all results shown. For all effective dissociation rates, the maximum deviation is less than 5%, and it is often better than the estimated statistical error for low-temperature conditions. The fitted values of n are typically between 0 and -1.5 , which is consistent with theoretical results (eg. Ref. [13]) and data available in the literature (eg. Ref. [127]).

In most cases, including all effective dissociation rates, the fitted dissociation temperature is within 5% of the dissociation temperature based on the diatomic PES's dissociation energy. In the experimental literature, it is common to fit Arrhenius coefficients with a fixed T_D ¹². Therefore, we fit with T_D fixed as well as T_D determined by best-fit. For nitrogen, 113,200 K is chosen based on consensus in the fitting literature [18, 43, 128]. For oxygen, there is more variation in the literature, but 59,380 K is chosen based on similarity to the PES's dissociation energy and a majority of the literature we have reviewed [12, 36, 39, 44, 45, 128, 129]. Some dissociation temperatures from the literature and the PESs we have used are collected in the Appendix, Tables C.2 and C.3. The generalized Arrhenius fits with fixed T_D are generally only slightly less accurate than those with fitted T_D . These generalized Arrhenius fits are used for the remainder of the Section on fitting as a required input to other models. The plots for Sections 3.6.2 to 3.6.4 use the fixed T_D fits, and this choice does not meaningfully change the conclusions.

In the Arrhenius formulation, T_D corresponds to reaction's activation energy. In $N_2 + N_2$, we observe that the fitted T_D for swap dissociation is approximately 40% higher than for simple dissociation. In $O_2 + O_2$, the difference is less than 1%. This result is consistent with our observation in Section 3.2 but the underlying reason is currently unknown. We also observe that the double dissociation rate fit for $N_2 + O_2$ has an activation energy of 173,649 K, which is within 1% of the combined activation energy for nitrogen and oxygen dissociation¹³.

Plots of the Arrhenius reaction rate fits compared to QCT data for nitrogen and oxygen dissociation are shown later in Figures 3.43a and 3.44a (pages 111 and 112).

¹²Fixing T_D is sometimes a necessity when data exhibit substantial scatter, as the fit yields absurd results otherwise [40].

¹³The fit for double dissociation in $N_2 + O_2$ is only valid for 10,000 K to 30,000 K

Table 3.1: Arrhenius fit to nitrogen dissociation rate with $T_{\text{tr}} = T_{\text{v}}$.

M	Dissoc type	Fixed T_{D}	Rate Parameters				Rel. Error [%]	
			C [$\text{cm}^3 \text{s}^{-1} \text{K}^{-n}$]	n	T_{D} [K]	R^2	Avg	Max
N_2	Effective	no	5.9725×10^{-6}	-0.7017	117,529	0.999,992	0.94	1.61
		yes	2.5256×10^{-7}	-0.4062	113,200	0.999,94	2.51	3.71
N_2	Simple	no	1.4887×10^{-3}	-1.2597	121,629	0.999,994	0.74	1.16
		yes	3.1458×10^{-6}	-0.6843	113,200	0.9998	4.77	6.08
N_2	Swap	no*	4.5533	-1.9632	171,812	0.999,993	0.88	1.33
N	Effective	no	1.3271×10^{-6}	-0.5625	113,957	0.999,98	1.25	2.32
		yes	7.6331×10^{-7}	-0.5108	113,200	0.999,98	1.38	2.16
O_2	Effective	no	8.3724×10^{-5}	-0.9991	116,892	0.999,996	0.53	1.10
		yes	5.6371×10^{-6}	-0.7470	113,200	0.999,95	2.00	3.60
O_2	Simple	no	1.3129×10^{-2}	-1.4969	121,583	0.999,998	0.37	0.79
		yes	2.8702×10^{-5}	-0.9247	113,200	0.9998	4.68	6.91
O_2	Double	no	4.0187×10^{-3}	-1.3414	173,649	0.999,999,1	0.33	0.50

* The swap dissociation data in $\text{N}_2 + \text{N}_2$ is not well described by a fit with fixed T_{D}

Table 3.2: Arrhenius fit to oxygen dissociation rate with $T_{\text{tr}} = T_{\text{v}}$.

M	Dissoc type	Fixed T_{D}	Rate Parameters				Rel. Error [%]	
			C [$\text{cm}^3 \text{s}^{-1} \text{K}^{-n}$]	n	T_{D} [K]	R^2	Avg	Max
O_2	Effective	no	6.1327×10^{-6}	-0.7695	60,540	0.999,995	0.69	0.95
		yes	1.1463×10^{-6}	-0.6003	59,380	0.999,98	1.24	2.21
O_2	Simple	no	1.4582×10^{-4}	-1.1366	61,623	0.999,996	0.65	0.93
		yes	5.6887×10^{-6}	-0.8093	59,380	0.999,95	2.11	3.62
O_2	Swap	no	2.0716×10^{-8}	-0.2785	62,082	0.999,97	1.93	2.28
		yes	4.1607×10^{-10}	0.1158	59,380	0.999,91	2.97	5.42
O_2	Double	no	1.8810×10^{-3}	-1.3506	119,732	0.9998	3.78	5.89
O	Effective	no	1.5295×10^{-6}	-0.6541	60,552	0.999,997	0.55	1.04
		yes	2.8084×10^{-7}	-0.4831	59,380	0.999,98	1.10	2.22
N_2	Effective*	no	5.3041×10^{-7}	-0.5430	62,949	0.999,996	0.58	1.47
		yes	3.0410×10^{-9}	-0.0223	59,380	0.999,89	3.38	5.81
N_2	Simple*	no	5.4570×10^{-7}	-0.5460	62,966	0.999,996	0.57	1.46
		yes	3.0546×10^{-9}	-0.0228	59,380	0.999,89	3.40	5.83

* The rate of oxygen dissociation with partner N_2 at $T = 4000$ K currently has 8% relative error. Further runs to better-converge this case are ongoing, and so this rate and others based on it, which are discussed later, are subject to change.

3.6.2 Nonequilibrium Dissociation Rate

Next, we consider the dissociation rate for the nonequilibrium test set ($T_{\text{tr}} = 20,000 \text{ K}$ for nitrogen and $T_{\text{tr}} = 10,000 \text{ K}$ for oxygen). The rate at thermal nonequilibrium is often considered relative to the rate at thermal equilibrium by defining and fitting to the nonequilibrium correction factor

$$Z(T_{\text{tr}}, T_{\text{v}}) = \frac{k_d(T_{\text{tr}}, T_{\text{v}})}{k_d(T_{\text{tr}}, T_{\text{tr}})} \quad (3.7)$$

The dissociation rates at equilibrium are defined by the Arrhenius form, with coefficients taken from the previous Section's fits. Similar to the equilibrium rate, we fit in terms of the natural logarithm $\ln(Z)$. A variety of nonequilibrium correction factors are defined in the literature; the book chapter by Losev *et al.* [128] provides a good summary. Here, we consider three models that have fittable coefficients.

1. The Losev β model [119] assumes that the threshold energy for dissociation is $(D_0 - \beta k_B T_{\text{tr}})$; the nonequilibrium correction factor is,¹⁴

$$\ln Z(T_{\text{tr}}, T_{\text{v}}) = \ln Q_v(T_{\text{v}}) - \ln Q_v(T_{\text{tr}}) - (T_D - \beta T_{\text{tr}}) \left(\frac{1}{T_{\text{v}}} - \frac{1}{T_{\text{tr}}} \right) \quad (3.8)$$

where β is the fitting parameter, which is typically between 1 and 2 [42]. The vibrational partition function Q_v defined at temperature T is approximated by

$$Q_v(T) = \frac{1 - \exp(-T_D/T)}{1 - \exp(-\Theta_v/T)} \quad (3.9)$$

2. The Marrone-Treanor preferential dissociation model [1] assumes that vibrationally-excited molecules are more likely to dissociate, with an exponential dependence determined by the model parameter U . For this model,

$$\ln Z(T_{\text{tr}}, T_{\text{v}}) = \ln Q_v(T_{\text{tr}}) + \ln Q_v(T_F) - \ln Q_v(T_{\text{v}}) - \ln Q_v(-U) \quad (3.10)$$

$$\frac{1}{T_F} = \frac{1}{T_{\text{v}}} - \frac{1}{T_{\text{tr}}} - \frac{1}{U} \quad (3.11)$$

In the original paper, a more accurate vibrational partition function was presented and used for oxygen. However, we choose to use the simple form shown in Equation (3.9), which has also been used by Losev [128] and Knab [58] for the Marrone-Treanor model.

¹⁴We have been unable to locate the English translation of the cited work; the information presented here is based on summary information provided by Shatalov [42] and Losev *et al.* [128].

3. The general form of the Park [16, 18] model defines the nonequilibrium dissociation rate as the equilibrium rate evaluated using a controlling temperature $T_a = T_{\text{tr}}^s T_{\text{v}}^{1-s}$. The parameter s is usually 0.5 (corresponding to $\sqrt{T_{\text{tr}} T_{\text{v}}}$), but it is also said to be in the range 0.5 to 0.7 [19]. The general form yields a nonequilibrium correction factor of

$$\ln Z(T_{\text{tr}}, T_{\text{v}}) = n(1-s)(\ln T_{\text{v}} - \ln T_{\text{tr}}) + \frac{T_{\text{D}}}{T_{\text{tr}}} - \frac{T_{\text{D}}}{T_{\text{tr}}^s T_{\text{v}}^{1-s}} \quad (3.12)$$

Of these three forms, only the Losev β model is linear in the model parameter. We therefore use MATLAB's commercially-available nonlinear least squares fitting capability [130] to determine the model parameters for nonequilibrium rates. For each model, the best-fit parameters were determined for all dissociation reactions. The results for effective oxygen dissociation with all collision partners are shown in Figure 3.38; we have chosen to show oxygen dissociation for brevity but nitrogen dissociation has been analyzed in the same fashion. Also shown is the recent model of Luo *et al.* [60], which does not include any fitting parameters besides the generalized Arrhenius rate. We note that, in the limit of thermal equilibrium, Z becomes 1 by construction; we are therefore primarily interested in the behavior for $T_{\text{tr}} > T_{\text{v}}$.

The Marrone-Treanor model is found to fit the data well: the maximum relative deviation is within 5% for nitrogen dissociation with partners N₂ and N and oxygen dissociation with partners O₂ and O, and within 7.5% for both dissociations in N₂ + O₂. We will describe why the Marrone-Treanor model matches the data well soon. The Park and Losev models both perform moderately well; the maximum relative deviations are between 20% and 35% but there is a strong trend in the deviation, and the limiting behavior does not appear to be correct. The best-fit value of β for the Losev model also deviates substantially from the expected theoretical range. All three of the fitted models capture the increased effect of translational energy for dissociation with partner O (see Section 3.5.2); each fitting parameter is larger. The Luo *et al.* model, however, predicts very similar nonequilibrium correction factors for partners O₂ and O: the model is based on the impulsive behavior of the colliding *atom*, regardless of whether it constitutes an atom or a molecule. Furthermore, the prediction for oxygen dissociation with partner N₂ is about a factor of 6 too large for the lowest T_{v} condition. The reason for this mismatch is unclear, but the Luo *et al.* model has not yet been compared against data for this reaction [60]. We also note a strong dependence of the Luo *et al.* model on whether T_{D} is fixed for this case; the deviation is approximately a factor of 2 instead when using the fitted T_{D} Arrhenius form, perhaps because n is near 0 for the fixed T_{D} case.

3.6.3 Nonequilibrium Vibrational Energy Change per Dissociation

We now consider the vibrational energy change per dissociation for the nonequilibrium test set. Based on our analysis of the literature, few models are able to capture the behavior we have observed at these conditions. As we have previously described, this term is a model for the mechanism by which dissociation affects the nonequilibrium thermodynamic state. This term's behavior in the limit of extreme thermal nonequilibrium has, in the past, prevented several preferential dissociation models from being successfully used in CFD (see Section 1.3). The models for vibrational energy change per dissociation that we have considered are:

1. The Losev β model [119] yields

$$-\langle \varepsilon_{\text{vib}} \rangle_d = D - \beta k_B T_{\text{tr}} \quad (3.13)$$

This model reduces to the one used by Park to reinterpret experimental data [16] for $\beta = 1$. The Losev model contains no dependence of the vibrational energy change per dissociation on the vibrational temperature, so we do not include it in the analysis of the nonequilibrium test set.

2. The Marrone-Treanor [1] model yields

$$-\langle \varepsilon_{\text{vib}} \rangle_d = \frac{1}{Q(T_F)} \sum_v \exp\left(-\frac{\varepsilon_{\text{vib}}(v)}{k_B T_F}\right) \quad (3.14)$$

where we approximate the sums using the form from Knab *et al.* [58],

$$-\langle \varepsilon_{\text{vib}} \rangle_d = \frac{k_B \Theta_v}{\exp(\Theta_v/T_F) - 1} - \frac{D}{\exp(T_D/T_F) - 1} \quad (3.15)$$

3. The Sharma *et al.* [55] model simply predicts

$$-\langle \varepsilon_{\text{vib}} \rangle_d = 0.3 D \quad (3.16)$$

This model was recommended by Park [18, p. 108],¹⁵ and it does not depend on the thermodynamic state at all. Therefore, we do not include it in our analysis of either the nonequilibrium or equilibrium test set.

4. We finally consider the model of Luo *et al.* [60], which is described in the cited paper and (as before) does not contain any fittable coefficients besides the Arrhenius terms.

¹⁵In his book, Park cites the conference paper (Ref. [131]) that later became the referenced journal paper

We therefore only fit the Marrone-Treanor model to QCT data for change in energy per dissociation in the nonequilibrium test set. As before, fitting is performed for each dissociation reaction and dissociation type, with both fixed and fitted dissociation temperature. The characteristic vibrational temperature Θ_v is defined using the corresponding diatomic PES (see Table 2.1) and the dissociation energy is described using the dissociation temperature, $D = k_B T_D$. The results for oxygen dissociation with all collision partners are shown in Figure 3.38; the results for nitrogen dissociation are similar.

The Marrone-Treanor model is found to accurately describe the data: the maximum error is 0.13 eV for oxygen dissociation and 0.49 eV for nitrogen dissociation. The best-fit model parameter U is also found to be similar when fitting to rate data and when fitting to change in energy data (within 7% for oxygen dissociation and 15% for nitrogen dissociation). The model parameter, for all of these cases, is between $\frac{1}{3.5}$ and $\frac{1}{2}$ of the dissociation temperature.

The model of Luo *et al.* [60] predicts the trends correctly, but the maximum error is large: approximately 1.8 eV for oxygen dissociation. In their recent paper, the model has not been compared to any data for the change in vibrational energy due to dissociation, perhaps because such data are not widely available in the literature. We again observe sensitivity to whether fixed or fitted T_D is used for the case of oxygen dissociation with N_2 partner, although neither yields a good match.

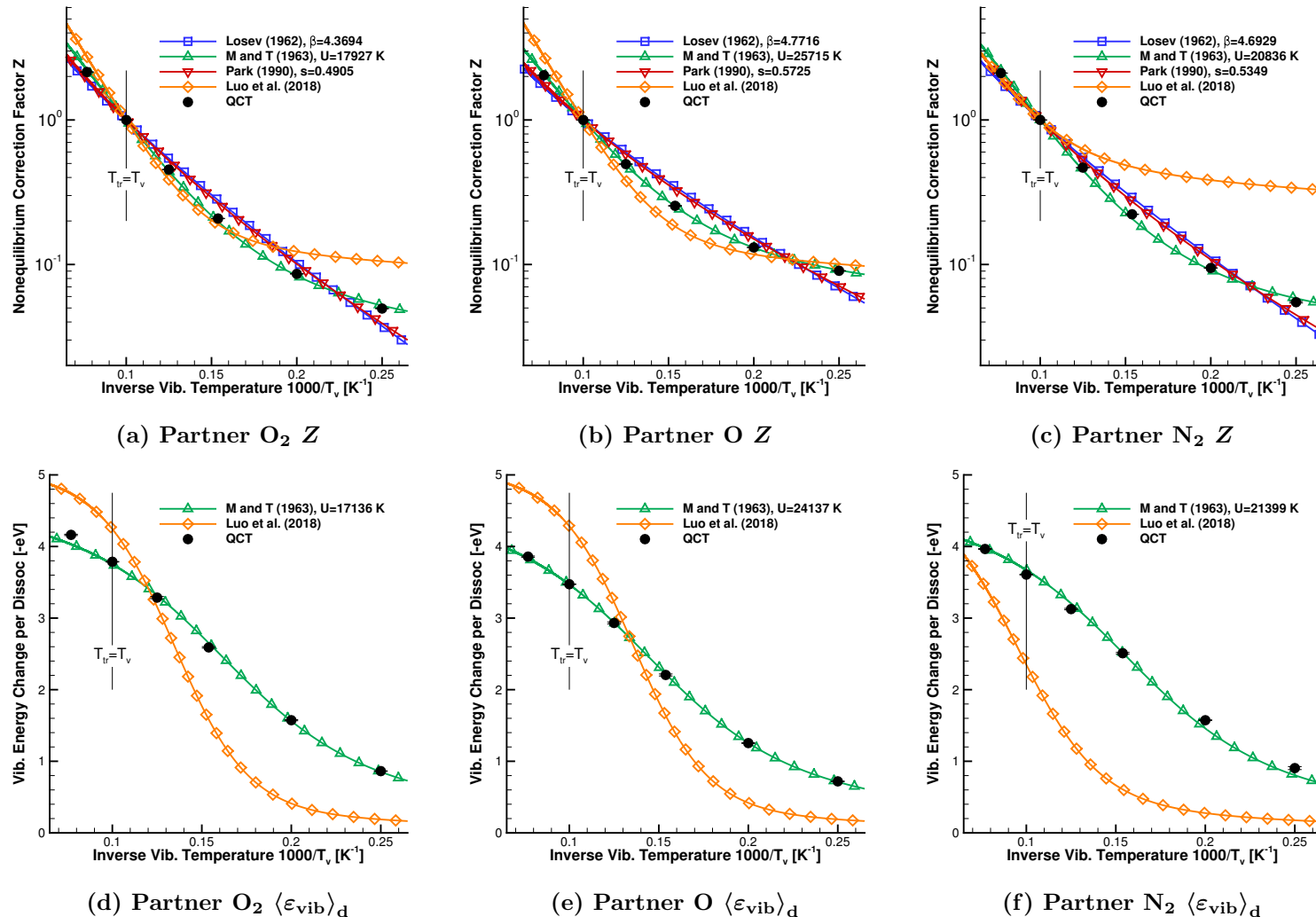


Figure 3.38: Nonequilibrium correction factor Z and average change in vibrational energy per dissociation $\langle \varepsilon_{\text{vib}} \rangle_d$ for effective oxygen dissociation in the nonequilibrium test set ($T_{\text{tr}} = 10,000$ K).

Based on the fitting results for the nonequilibrium test set, the Marrone-Treanor preferential dissociation model [1] is a strong candidate for describing the quantities of interest for dissociation from the QCT database. This is because the key assumption of their model is consistent with observations made from QCT data, which we will now discuss. In the Marrone-Treanor model, given that there is sufficient energy to dissociate, molecules with higher vibrational energy are more likely to dissociate. The distribution of vibrational levels that go on to dissociate, from their model, is

$$f_d(v) = C_{MT} f(v) M(v) F(v) \quad (3.17)$$

where C_{MT} is a normalization constant. Each of the remaining three terms have a physical meaning and are in the form of an exponential distribution in vibrational energy, characterized by some temperature. These temperatures may be positive or negative, and correspond respectively to a negative or positive slope on a log-scale plot. The terms are:

- $f(v) = \exp\left(-\frac{\varepsilon_{\text{vib}}(v)}{k_B T_v}\right)$ is a Boltzmann distribution of vibrational levels.
- $M(v) = \exp\left(-\frac{\varepsilon_{\text{vib}}(v)}{k_B (-T_t)}\right)$ is proportional to the number of collisions that have sufficient energy to dissociate. The temperature dependence is negative because high- v molecules experience more collisions that have sufficient energy to dissociate, and the translational energy is governed by T_t ¹⁶.
- $F(v) = \exp\left(-\frac{\varepsilon_{\text{vib}}(v)}{k_B (-U)}\right)$ captures the ‘preference’ that vibrationally-excited molecules have to dissociate. The characteristic temperature is the model parameter U . For small U , only the most vibrationally-energetic molecules may dissociate, and for large U a range of vibrational energies can lead to dissociation. In the limit of $U \rightarrow \infty$, there is no preference and the authors’ earlier Coupled Vibration-Dissociation-Vibration (CVDV) model is recovered [8]. The parameter U has dimensions of temperature, and has taken a range of values in the literature from $\frac{T_D}{6}$ to $\frac{T_D}{1.7}$ [1, 58, 128]. This range includes all values of U we have described so far.

When multiplied together, the inverse temperatures in each exponent add to yield an exponential of inverse T_F , which was defined in Equation (3.11).

We have already observed that vibrationally-excited molecules are more likely to dissociate, and that the dependence is roughly linear on a log-scale plot (see Section 3.5.2). The support factor may be computed for the Marrone-Treanor model by rearranging Equa-

¹⁶Rotational energy is neglected entirely for their analysis, which will be addressed in Section 3.6.4

tion (3.17),

$$S(v) = \frac{f_d(v)}{f(v)} \propto M(v) F(v) \quad (3.18)$$

$$S(v) \propto \exp\left[-\frac{\varepsilon_{\text{vib}}(v)}{k_B} \left(-\frac{1}{T_t} - \frac{1}{U}\right)\right] \quad (3.19)$$

Figure 3.39 compares support for simple oxygen dissociation by vibrational energy of the dissociating molecule with collision partner O₂ with the Marrone-Treanor model for $U = 17,927\text{ K}$. The parameter U was chosen based on the nonequilibrium rate best-fit and the constant of proportionality was adjusted roughly to align with the data. They match reasonably well, providing further indication that the preferential dissociation model is capturing physically relevant mechanisms for the nonequilibrium test set. We note that these type of specific data, such as dissociation rates from different v -levels, could have been used to fit model parameters. Instead, however, we chose to fit model parameters using primary quantities of interest (rate and change in energy), for both simplicity and to best fit the desired end result. Furthermore, if we were interested in this level of microscopic accuracy, other assumptions (such as the use of a simplified partition function) would have to be reevaluated. We are looking at these specific data only to qualitatively determine the validity of the model assumptions, and we have found that the model assumptions are consistent with the microscopic QCT results. This physical consistency is a major reason why the quantities of interest for the nonequilibrium test set are predicted accurately by the Marrone-Treanor preferential dissociation model.

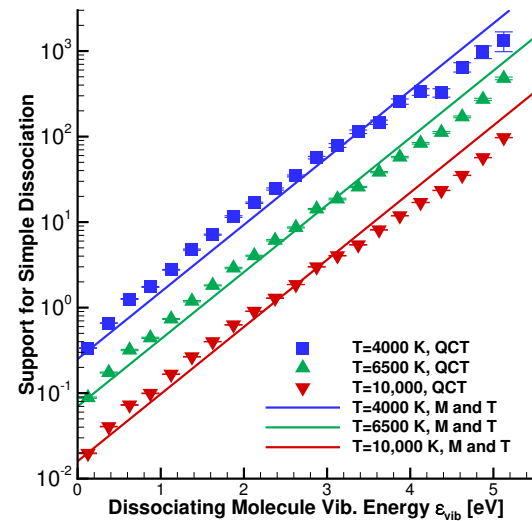


Figure 3.39: Support for oxygen dissociation compared to Marrone-Treanor [1] model; simple dissociation in $\text{O}_2 + \text{O}_2$, $T_{\text{tr}} = 10,000 \text{ K}$, $U = 17,927 \text{ K}$.

3.6.4 Equilibrium Vibrational Energy Change Per Dissociation

The final quantity of interest we fit is the vibrational energy change per dissociation for data in the equilibrium test set ($T_{\text{tr}} = T_v$). The models for vibrational energy change were described in the previous Section, and of those with fittable coefficients, only the Losev β model [119] form appears to be able to provide a reasonable fit to the data. Unfortunately, the Marrone and Treanor preferential dissociation model [1] yields a constant T_F in the limit of thermal equilibrium, which in turn yields a constant $\langle \varepsilon_{\text{vib}} \rangle_d$.

The results are shown in Figure 3.40, which shows the QCT data, the Losev *et al.* [119] model with a fitted value of β , the Luo *et al.* [60] model, and the Marrone-Treanor [1] model with the value of U fitted from the nonequilibrium vibrational energy change data. Again, the plots focus on oxygen dissociation but nitrogen dissociation has been analyzed as well and performs similarly. We find that none of the models predict the QCT results particularly well. The most accurate predictions are due to the Losev model, which captures the correct trend and also yields a model parameter β near or within the expected theoretical range of 1 to 2. The maximum deviation for the Losev model is 0.32 eV for oxygen dissociation, but recall that the Losev model predictions for the nonequilibrium dissociation rate exhibited the incorrect limiting behavior and also yielded a β value near 4.5. The correct trend is also predicted by the Luo *et al.* model, but the maximum error is above 1 eV, which is larger even than the variation in the data for this test set. For the Marrone-Treanor model, the U parameter was determined using data for $T_{\text{tr}} = 10,000$ K, so fit is accurate for that condition but nowhere else. Correctly predicting the vibrational energy change at and near equilibrium is crucial for CFD (see, eg. Park [16]), so the poor predictive capability of models available in the literature is problematic.

Let us consider the behavior of the Marrone-Treanor model for the case of $T_{\text{tr}} = T_v$, using the form shown in Equation (3.17). As the equilibrium temperature increases, the population of vibrationally-excited molecules increases via the Boltzmann distribution's dependence on T_v . Also as the equilibrium temperature increases, more collisions involving low- v molecules have enough energy to yield a dissociation, via the dependence of the function M on T_t . These two competing effects exactly cancel out, because the first includes $(+T_v)$ and the second includes $(-T_t)$. As a result, the population distribution of molecules that dissociate, as predicted by the Marrone-Treanor model, is independent of temperature when $T_{\text{tr}} = T_v$.

This aspect of the Marrone-Treanor model is inconsistent with observations from QCT, from both the present analysis and previous analyses [25, 84]. For example, Figure 3.41a shows the distribution of vibrational quantum number for molecules that undergo simple dissociation in $\text{O}_2 + \text{O}_2$, for a range of temperatures with $T_{\text{tr}} = T_v$. At low temperature thermal equilibrium, the character of molecules that dissociate is almost exclusively

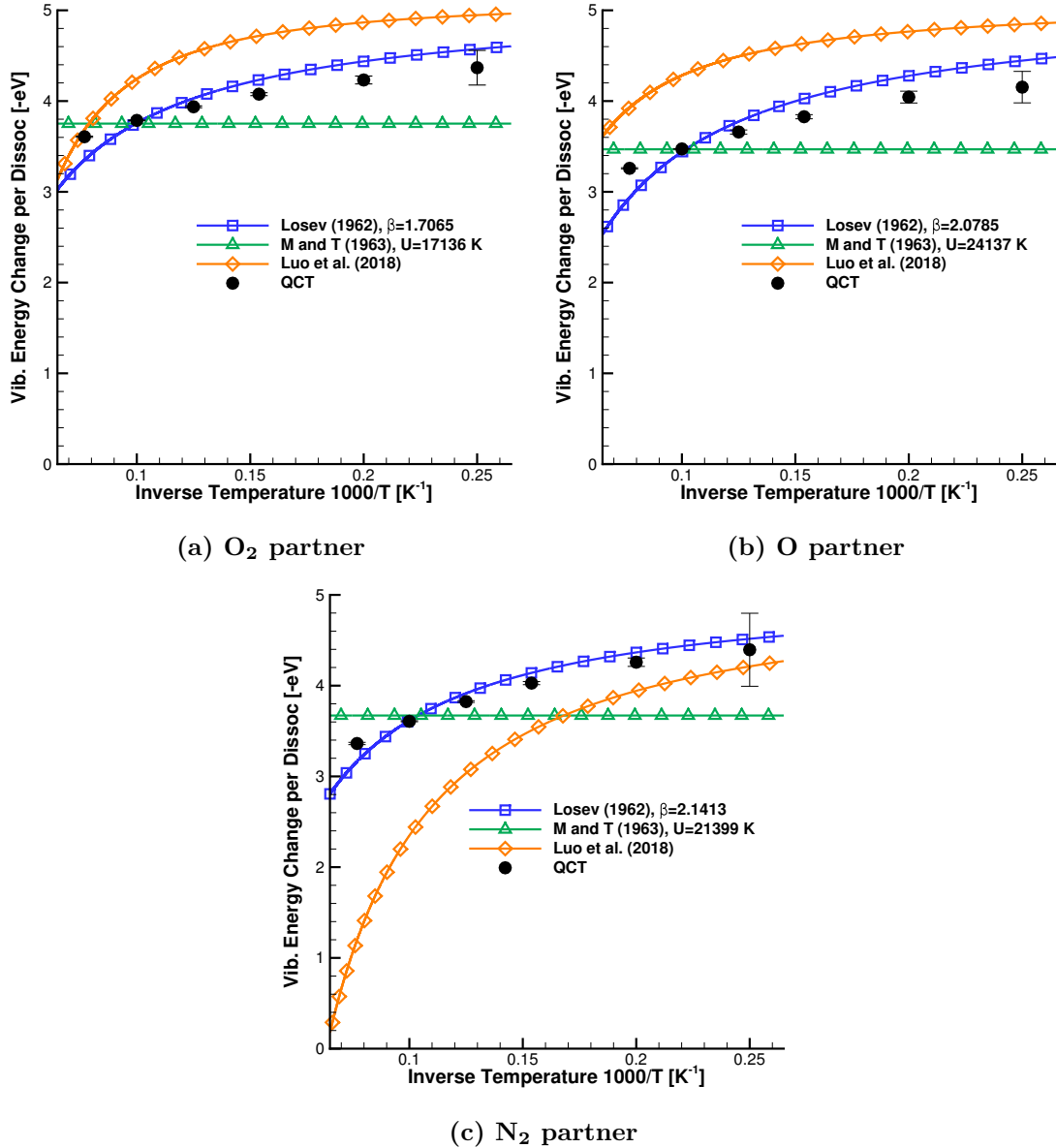


Figure 3.40: Change in vibrational energy per oxygen dissociation for the equilibrium test set.

vibrationally-excited. As all temperatures increase, this specificity weakens; other modes of energy are more able to make up for a deficit of vibrational energy. In this context, the other available modes of energy are rotation and translation.

At this point, a relevant question is: *what mechanism causes the PDF of v -levels to broaden as temperature increases?* If translational energy is the dominant mechanism, then the M function does not capture the effect of translational energy on dissociation, at least to the accuracy that we are interested in. Perhaps, for example, excess translational energy above the required energy to dissociate further increases the probability of dissociation; we do not observe a discontinuity in the effect of translational energy on dissociation based on Section 3.5.2. Alternatively, rotational energy could be causing this broadening. The original Marrone-Treanor model entirely neglects rotational energy, and we have demonstrated that it has an effect on dissociation in Section 3.5.2.. Of course, a combination of these mechanisms could also be present, each to a varying degree. Based on aggregate analyses of results in the QCT database, distinguishing between rotation and translation is difficult because trajectories are always sampled with $T_t = T_r$.

We address this question in two ways. First, as pointed out by Bender *et al.* [25] and observed in the present data, the average internal energy decrease per dissociation is roughly constant and equal to the dissociation energy. In other words, as temperature increases for $T_{tr} = T_v$, $\langle \varepsilon_{vib} \rangle_d$ decreases by the same amount that $\langle \varepsilon_{rot} \rangle_d$ increases, and the change in translational energy is small. This indicates that rotation is the primary contributor to the broadening of the PDF of dissociating molecule v as temperature increases. Second, we simulate a condition with trajectories sampled from $T_t \neq T_r$. Oxygen dissociation in $O_2 + O$ for the $1^5A'$ surface was chosen for simplicity and a lower computational expense, and the condition is $T_{tv} = 10,000\text{ K}$, $T_r = 5000\text{ K}$. By comparing to the existing cases with $T_{tr} = T_v$, we isolate the effect of rotational energy from translational energy. PDFs of vibrational quantum number for trajectories that dissociate, for these conditions, are shown in Figure 3.41b. The results for the two $T_r = 5000\text{ K}$ cases are found to be similar, whereas the $T_r = 10,000\text{ K}$ case is much broader. This result indicates that the PDF of dissociating v -levels depends on T_r and is mostly independent of T_t , so long as $T_t = T_v$. Our two methods of assessing this question are therefore consistent with each other, and so we conclude that the mechanism missing from the Marrone-Treanor preferential dissociation model [1] is the effect that rotation has on dissociation. As temperature increases, rotational energy promotes dissociation from a wider range of v -levels, reducing the average vibrational energy decrease per dissociation.

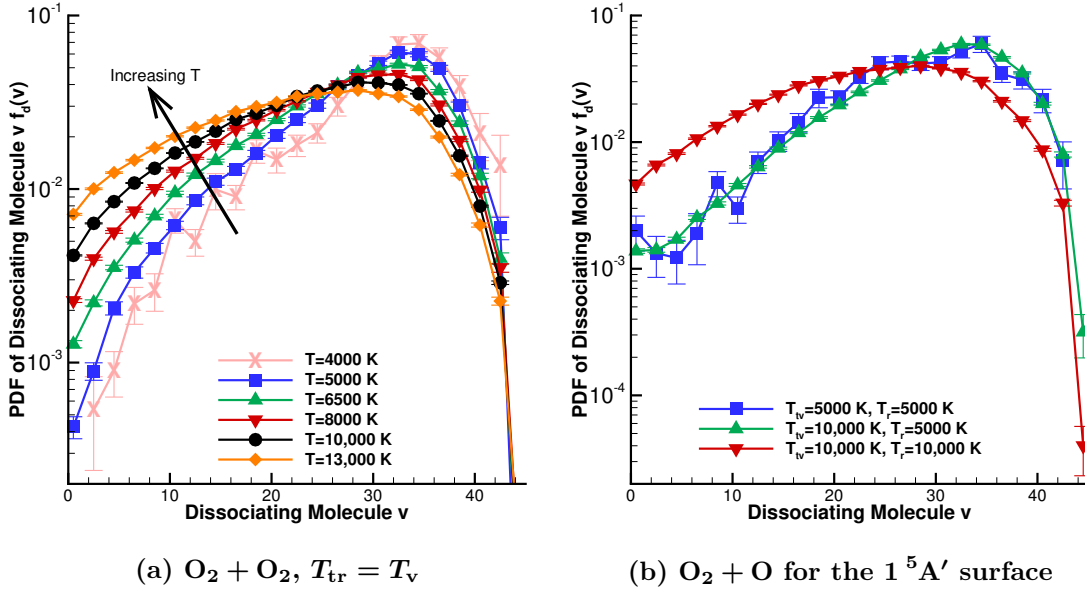


Figure 3.41: PDF of dissociating molecule v for oxygen dissociation, for assessing the assumptions in the Marrone-Treanor preferential dissociation model [1].

3.6.5 Fitting All Data in the QCT Database

Here, we propose a modification to the Marrone-Treanor preferential dissociation model [1] that yields a fit to both quantities of interest, in both the equilibrium and nonequilibrium test set, for all effective dissociation reactions that we have considered. As described in the previous Section, we believe this correction is necessary to account for the effect of rotational energy, which is neglected in the original Marrone-Treanor model. However, we note that the results presented in this Section are valid regardless of the physical nature of the missing mechanism.

Both the reaction rate and the change in vibrational energy per dissociation are well described by a single U , when T_{tr} is fixed. By construction, this value of U also fits $\langle \varepsilon_{\text{vib}} \rangle_d$ at thermal equilibrium for the single condition that matches the value of T_{tr} used for the nonequilibrium test set. Therefore, the value of U that describes the nonequilibrium behavior for a given T_{tr} may be determined by matching only the $\langle \varepsilon_{\text{vib}} \rangle_d$ value at the corresponding equilibrium condition.

For each condition in the equilibrium test set, we therefore determine the value of U that matches $\langle \varepsilon_{\text{vib}} \rangle_d$, via a Newton iteration on Equation (3.15). We now have the dependence of U on T_{tr} . This dependence is observed to be fit well by a linear relationship in inverse

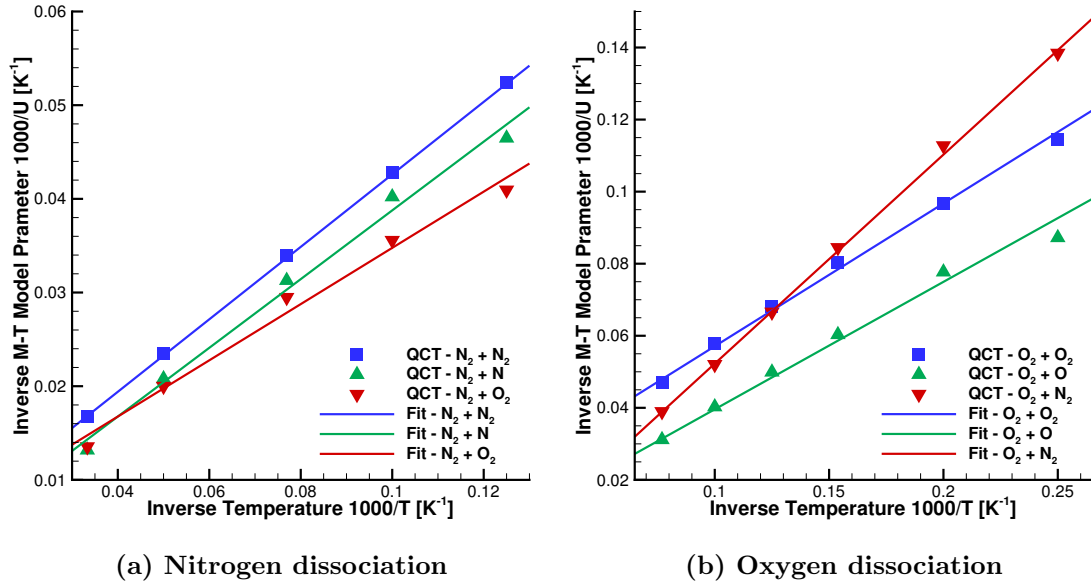


Figure 3.42: Dependence of Marrone-Treanor model parameter U on T , determined using the change in vibrational energy per dissociation in the equilibrium test set. The linear fit in inverse temperature space, Equation (3.20), is also shown.

temperature space,

$$\frac{1}{U} = \frac{a_U}{T_{\text{tr}}} + \frac{1}{U^*} \quad (3.20)$$

This form is based on intuition and trial-and-error, and, at this point, we are not assigning a physical meaning to each term. Nevertheless, the form is found to yield good agreement; the results are shown in Figure 3.42. Because we are interested in minimizing error in vibrational energy decrease per dissociation, the model parameters a_U and U^* are determined by fitting to $\langle \varepsilon_{\text{vib}} \rangle_d$ directly, by substituting Equation (3.20) into Equation (3.15). In this fashion, we have computed the dependence of U on T_{tr} based on the equilibrium vibrational energy change due to dissociation.

QCT data is compared to the model in Figure 3.43 for nitrogen dissociation and Figure 3.44 for oxygen dissociation; Tables 3.3 and 3.4 quantify the goodness of fit and describe the model parameters, a_U and U^* . The Arrhenius rate parameters are also required; those were shown in Tables 3.1 and 3.2. Now that we have a single model for all quantities of interest, we also assess whether a fixed or fitted T_D generalized Arrhenius form should be used; both are shown in the tables. Except for the case of oxygen dissociation with partner N_2 , the fitted T_D forms perform better. Therefore, we recommend and plot the fixed- T_D fit for oxygen dissociation with partner N_2 , and the fitted- T_D form elsewhere. The case of

oxygen dissociation with partner N₂ includes the $T_{\text{tr}} = T_{\text{v}} = 4000\text{ K}$ condition, which is not quite converged: the estimated uncertainty in rate is 8%. Perhaps the ongoing runs to reduce uncertainty for this condition will yield a better fitted T_{D} result.

This modified Marrone-Treanor model is found to accurately fit all quantities of interest for all effective dissociation reactions. Here, we highlight some statistics; full details are found in the tables as mentioned. The dissociation rate in the equilibrium test set, described using a generalized Arrhenius form, has a mean deviation at or below 1% for most cases; oxygen dissociation with partner N₂ is an outlier here with a maximum deviation of 5.8%. For all dissociation rates in the nonequilibrium test set, the model has a maximum deviation of 22% and the average deviation is below 5% for all oxygen dissociation cases. Vibrational energy per dissociation in the equilibrium test set is fit extremely well; the maximum error is 0.12 eV for nitrogen dissociation and 0.05 eV for oxygen dissociation. Finally, the vibrational energy change in the nonequilibrium test set has a maximum error of 0.24 eV. For reference, the dissociation energy of nitrogen is 9.8 eV and oxygen is 5.1 eV; these energy changes are therefore accurate to within 4% of the corresponding dissociation energy.

It is worth noting that all model parameters have been determined using data in the equilibrium test set only: dissociation rate to determine the generalized Arrhenius form, and average energy change per dissociation to determine the novel two-parameter fit to U . This means that the goodness of fit demonstrated for the nonequilibrium test set is predictive. Predictive capability of this accuracy is a strong indicator that we are capturing the dominant physical mechanisms instead of simply providing sufficient degrees of freedom to intersect the data. The Marrone-Treanor model is old and relatively simple, but it continues to be recommended for use by chemical kinetics authors [58, 128]. It has also been extended to exchange reactions by Knab *et al.* [58].

The modification we propose is consistent with qualitative and quantitative observations from QCT data. In order to further analyze the dependence on rotation, a suite of test cases with rotational nonequilibrium could be used. Voelkel *et al.* [104] has recently performed such an analysis for N₂ + N₂ interactions using the N₄ PES of Paukku *et al.* [25, 63, 64]. Future work could also better explore the functional form of U , perhaps providing a physical meaning to the proposed terms or proposing an alternate functional form. Regardless of the physical meaning, the modified Marrone-Treanor model that we propose is a simple, self-consistent description of dissociation at conditions characterized by T_{tr} and T_{v} .

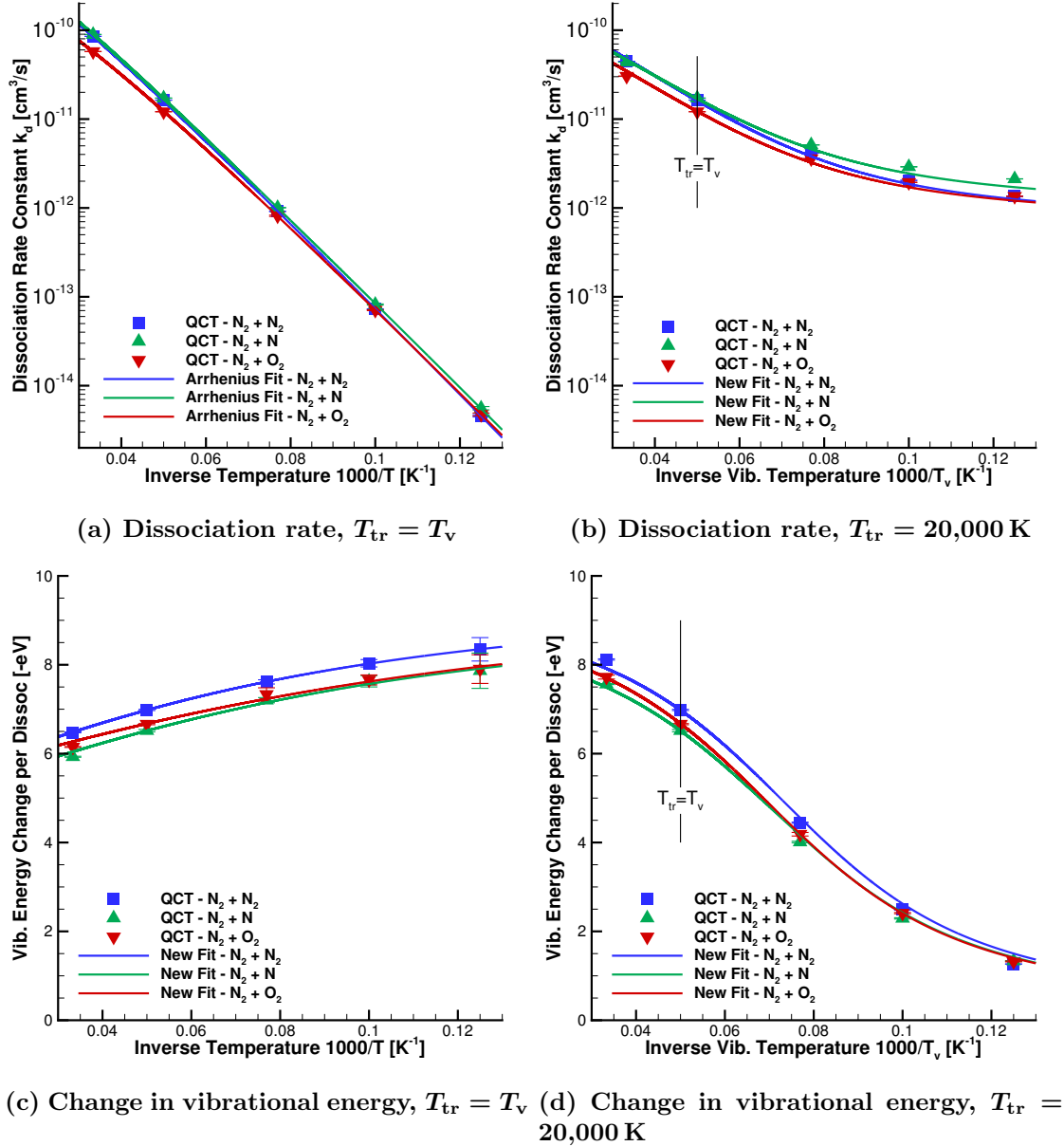


Figure 3.43: Fitting to all QCT data for nitrogen dissociation data with new model: the maximum relative error in rate is 22 % and the maximum error in vibrational energy change per dissociation is 0.24 eV.

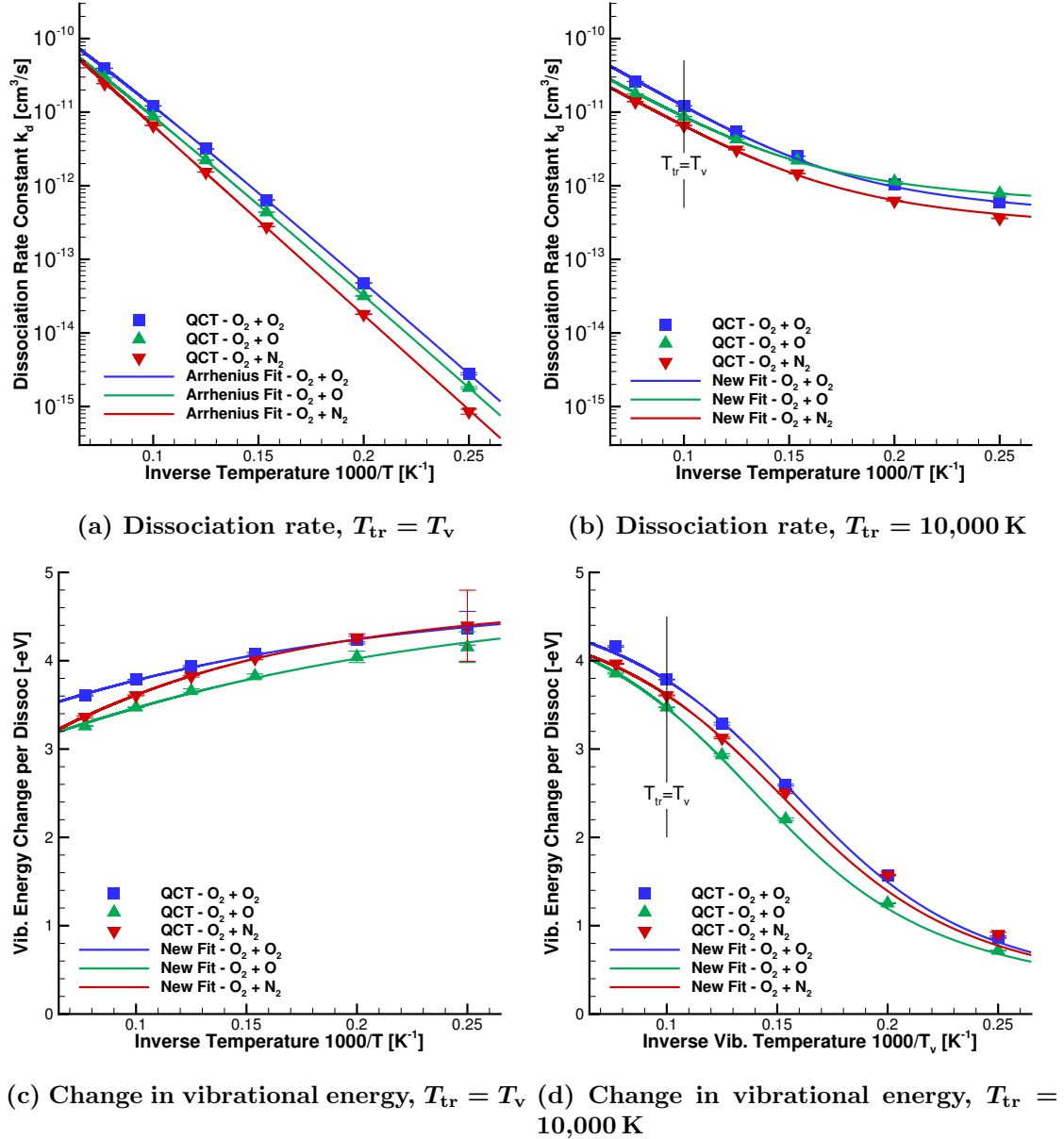


Figure 3.44: Fitting to all oxygen dissociation data with new model; effective dissociation with fixed T_D . The maximum relative error in rate is 15 % and the maximum error in energy change is 0.18 eV.

Table 3.3: New model parameters for effective nitrogen dissociation, showing goodness-of-fit for three sets of data: dissociation rate in the nonequilibrium test set, and vibrational energy change per dissociation in the equilibrium test set and nonequilibrium test set. AE is average error and ME is maximum error, which is computed relatively for rates and absolutely for energy change. Also requires the Arrhenius rate parameters shown in Table 3.1.

M	Fixed			U [K] at 20,000 K	Noneq. Set k_d			Eq. Set $\langle \varepsilon_{\text{vib}} \rangle_d$			Noneq. Set $\langle \varepsilon_{\text{vib}} \rangle_d$		
	T_D	a_U	U^* [K]		R^2	AE [%]	ME [%]	R^2	AE [eV]	ME [eV]	R^2	AE [eV]	ME [eV]
N_2	no	0.3868	254,556	42,973	0.997	6.0	8.7	0.999,92	0.006	0.009	0.996	0.138	0.236
	yes	0.5166	365,046	35,000	0.98	15.0	31.6	0.998	0.025	0.051	0.98	0.329	0.443
N	no	0.3668	478,708	48,952	0.988	10.8	21.9	0.992	0.056	0.113	0.998	0.088	0.154
	yes	0.3836	503,817	47,251	0.985	11.9	25.2	0.993	0.052	0.101	0.997	0.114	0.195
N_2	no	0.3001	210,253	50,604	0.991	10.3	14.5	0.986	0.065	0.121	0.9998	0.026	0.079
	yes	0.3664	192,401	42,523	0.98	16.4	30.5	0.992	0.050	0.088	0.995	0.154	0.233

Table 3.4: New model parameters for effective oxygen dissociation, showing goodness-of-fit for three sets of data: dissociation rate in the nonequilibrium test set, and vibrational energy change per dissociation in the equilibrium test set and nonequilibrium test set. AE is average error and ME is maximum error, which is computed relatively for rates and absolutely for energy change. Also requires the Arrhenius rate parameters shown in Table 3.2.

M	Fixed			U [K] at 10,000 K	Noneq. Set k_d			Eq. Set $\langle \varepsilon_{\text{vib}} \rangle_d$			Noneq. Set $\langle \varepsilon_{\text{vib}} \rangle_d$		
	T_D	a_U	U^* [K]		R^2	AE [%]	ME [%]	R^2	AE [eV]	ME [eV]	R^2	AE [eV]	ME [eV]
O_2	no	0.3965	57,343	17,517	0.998	4.6	8.5	0.998	0.012	0.017	0.998	0.040	0.080
	yes	0.4670	59,814	15,768	0.994	9.1	17.8	0.9993	0.007	0.009	0.996	0.057	0.112
O	no	0.3537	237,290	25,259	0.9995	2.1	4.3	0.990	0.027	0.053	0.9986	0.036	0.064
	yes	0.3761	137,160	22,270	0.995	6.5	12.8	0.990	0.027	0.054	0.9997	0.016	0.031
N_2	no	0.3620	385,466	25,777	0.98	13.3	52.4	0.989	0.032	0.071	0.96	0.189	0.376
	yes	0.5801	-174,299	19,131	0.998	4.6	15.0	0.9996	0.006	0.014	0.992	0.072	0.181

3.7 Miscellaneous QCT Results

3.7.1 All Reactions for $\text{N}_2 + \text{O}_2$

$\text{N}_2 + \text{O}_2$ interactions may yield a variety of outcomes, as described in Section 2.3.1. We have focused on the data for oxygen and nitrogen dissociation. In addition to these reactions, there are two exchange reactions that decompose N_2 and produce one or two NO molecules: ‘dissociation and exchange’ produces one NO, and ‘total exchange’ produces two. Neither of these exchange reactions are included in current chemical kinetics models for CFD.

Figure 3.45 shows the reaction rate constant for all reactions in $\text{N}_2 + \text{O}_2$. In this case, there are two nonequilibrium test sets: $T_{\text{tr}} = 20,000\text{ K}$, primarily to study nitrogen dissociation; and $T_{\text{tr}} = 10,000\text{ K}$, primarily to study oxygen dissociation. The temperature range for the equilibrium test set is also relatively large: 4000 K to 30,000 K. As expected, oxygen dissociation is the most common reaction. Dissociation and exchange is found to be the next most common reaction, for all conditions. It is at least 2 times more common than nitrogen dissociation. This means that exchange reactions are the dominant reaction to decompose molecular nitrogen in $\text{N}_2 + \text{O}_2$ interactions, and also the dominant reaction to produce atomic nitrogen.

The exchange reactions are found to occur from relatively low impact parameters, compared to dissociation reactions, as shown in Figure 3.46. A new molecule is formed during an exchange reaction; evidently this means that the collision must be more head-on. We also observe that the energy of product NO is strongly dependent on the exchange reaction that produced it. Figure 3.47 demonstrates that the population of NO produced via total exchange has many more high-energy molecules than the population produced via dissociation and exchange. This trend is particularly pronounced for vibrational energy; the product distribution is more different between the two exchange reactions than it is between cases sampled from 6500 K and 13,000 K. A similar dependence on reaction type for product NO was observed for the Zeldovich reactions by Bose and Candler [95–97].

Air is well known to decompose in several stages: oxygen dissociates first, and then the atomic oxygen decomposes nitrogen via the first Zeldovich reaction. The first Zeldovich reaction has a much higher rate than the dissociation and exchange reaction; for example, at 10,000 K, the rate constant is higher by a factor of 30 compared to the rate of Bose and Candler [96]. Therefore, the dissociation and exchange reaction is expected to be the dominant mechanism to decompose N, for this condition, only when the concentration of O is less than 30 times that of O_2 . Further analysis is necessary to determine the flows for which it is necessary to include these reactions. Also, the effect of vibrationally-excited NO was found to be important for predicting the BSUV experiments [99–103]. Investigation of these reactions is ongoing.

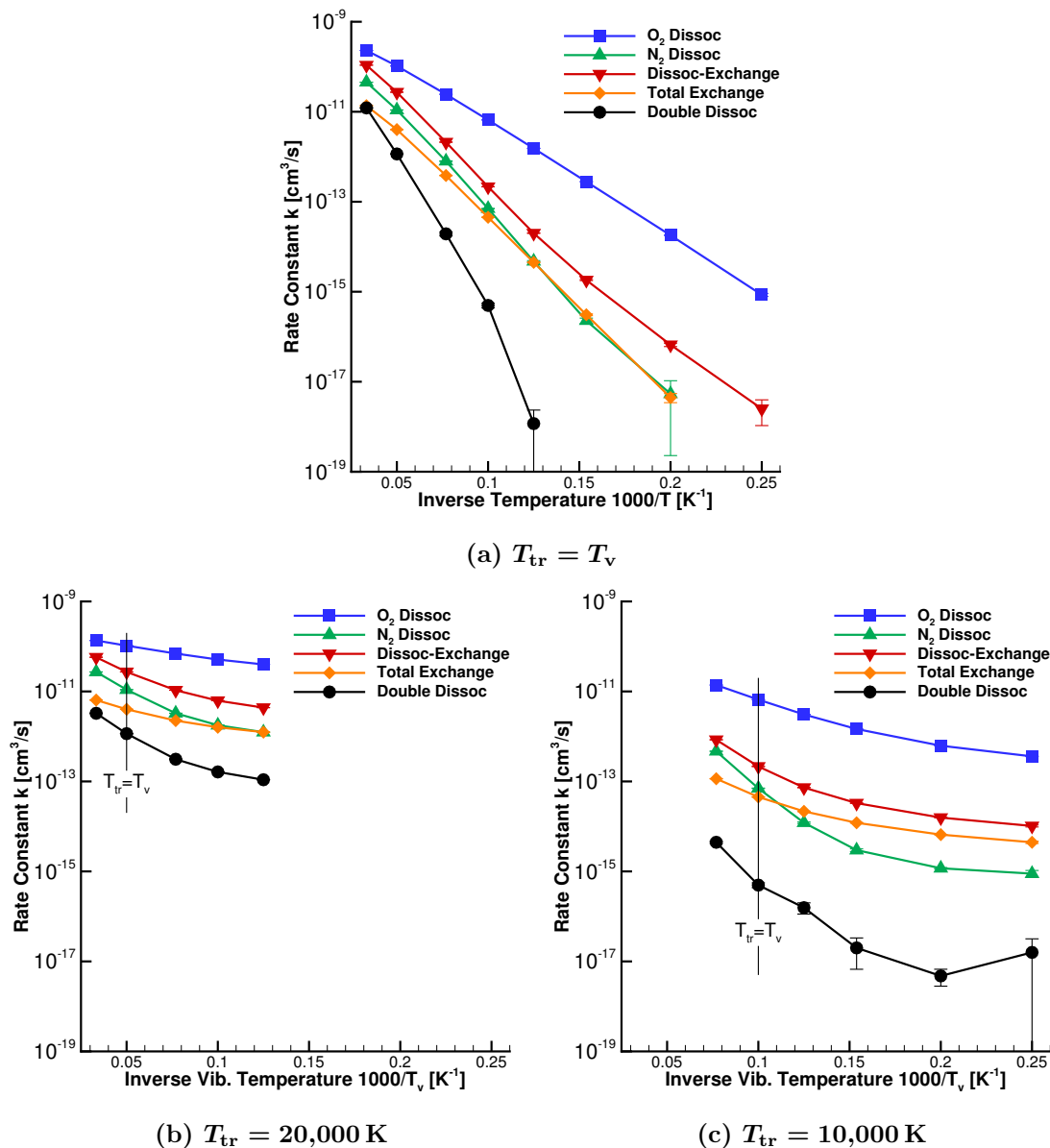


Figure 3.45: Rates for all reactions in $N_2 + O_2$, for the equilibrium and two nonequilibrium test sets.

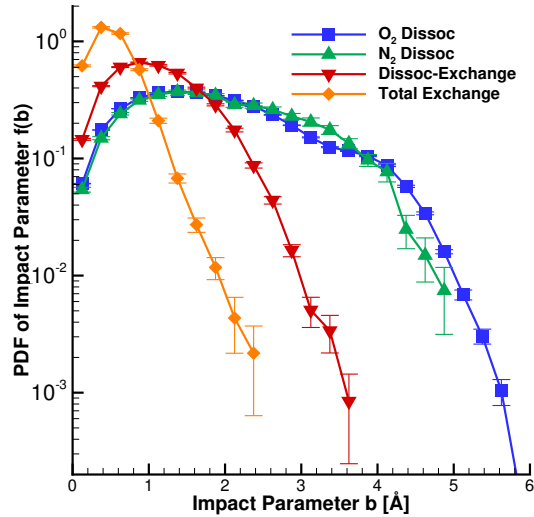


Figure 3.46: PDF of impact parameter for different events in $\text{N}_2 + \text{O}_2$ interactions, for conditions sampled with $T_{\text{tr}} = T_{\text{v}} = 10,000$ K.

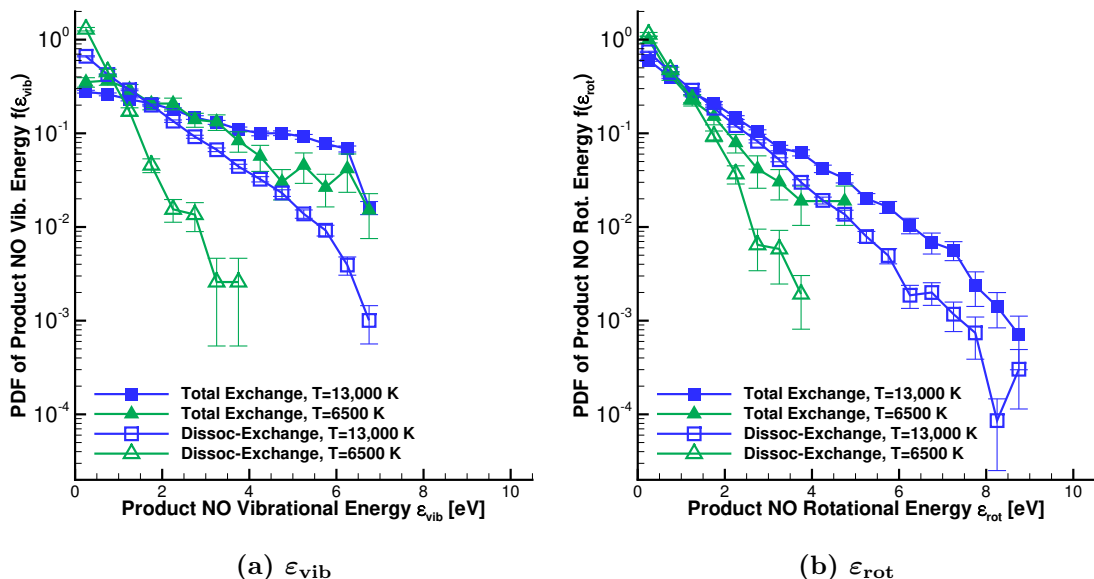


Figure 3.47: PDFs of rotational and vibrational energy of product NO for the two exchange reactions in $\text{N}_2 + \text{O}_2$ interactions; conditions are sampled from thermal equilibrium.

3.7.2 Degeneracy Error

An error in REAQCT was found to cause a slight error in the initial distribution of states; the issue was fixed in May 2018. The rotational degeneracy, which should be $(2j + 1)$, was computed using $(2j + 3)$ instead. Thanks to Dr. Erik Torres for first noticing the issue. We have determined that the effect of this error on preexisting trajectory data is minimal, as we describe in this Section.

PDFs of dissociating molecule v and j , with and without the error, are shown in Figure 3.48 for a sample case of oxygen dissociation with partner N₂ at 8000 K. The only statistically significant difference occurs at very low j , where the difference between incorrect and correct degeneracy is large. (For example, the degeneracy at $j = 0$ is 3 times higher with this error, but at $j = 50$ it is only 2 % higher.) For all conditions we have studied, the dynamics of very-low- j molecules are not critical.

For this sample case, the dissociation rate with the error is 1.4 % lower than without it. This difference is statistically significant (uncertainty is around 0.5 %), but less than the 5 % requirement for aggregate quantities of interest in the QCT database. The difference in average vibrational energy change per dissociation is 0.1 %. We have also examined the difference in dissociation rate for several other test cases: N₂ + N₂ at 10,000 K yielded a 2.3 % difference, and O₂ + O system at $T_{\text{tr}} = 10,000$ K, $T_v = 4000$ K yielded at 1 % difference. Other quantities have been checked, too, and no significant differences have been found.

All run folders in the QCT database include a DEGENERACY_BUG_STATUS file that de-

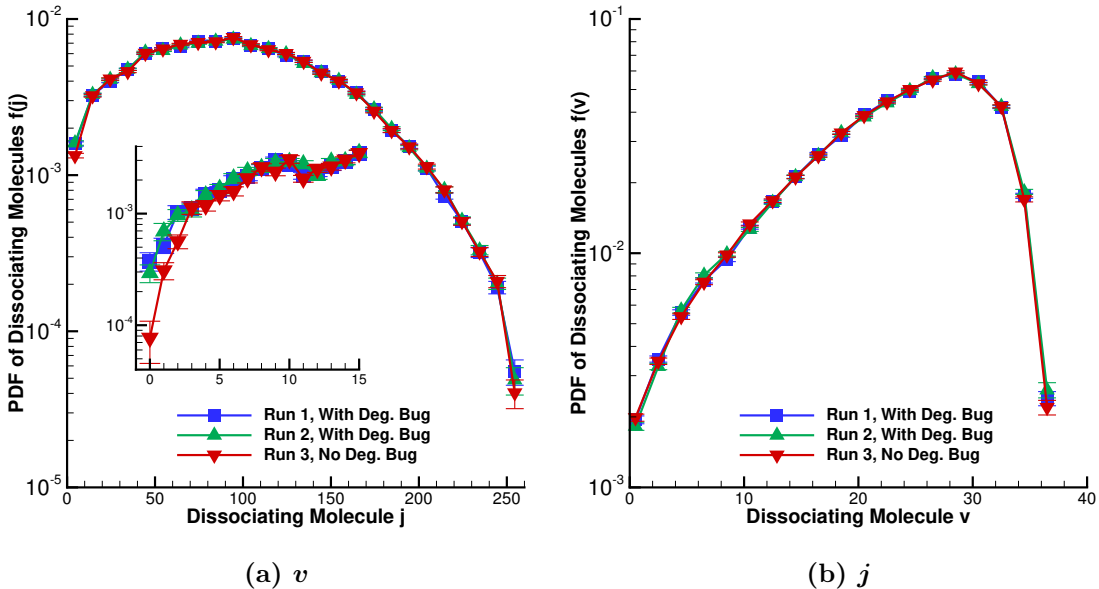


Figure 3.48: PDF of dissociating molecule quantum numbers oxygen dissociation with partner N₂ at 8000 K, with and without the degeneracy error.

scribes whether the trajectories were sampled from distributions with the error. All $N_2 + N_2$ trajectory runs include the error, and almost all $N_2 + N$ and $N_2 + O_2$ runs do too. None of the $O_2 + O_2$ or $O_2 + O$ results have the degeneracy error¹⁷.

The only situation where the degeneracy error was observed to meaningfully influence results is for calculating specific heat, which we discuss in Section 4.1.5. At temperatures below around 1000 K, the population of very-low- j molecules are important. The fits to specific heat that we describe all have this error fixed.

3.7.3 Atom-Diatom Interaction Times

We have briefly analyzed the time of $O_2 + O$ and $N_2 + N$ interactions, for the purposes of informing future studies on recombination. Two initially separated atoms cannot spontaneously form a diatom by themselves¹⁸, because they either have sufficient energy to be unbound or insufficient energy to cross the centrifugal barrier to become bound. Therefore, recombination must be accompanied by a third body which removes enough energy (or adds enough angular momentum) to leave the remaining two atoms bound. In a ‘direct’ three-body interaction, three colliding particles come together at approximately the same time¹⁹. An alternative mechanism for recombination is via an ‘indirect’ three-body interaction, where two particles collide and form a relatively long-lived metastable state, which is then struck by a third body. We are therefore interested in long-lived metastable states that could serve as catalysts for recombination.

These metastable states of interest must be formed from at least one atom collision partner, in order to potentially recombine into a diatom. The other partner may be either an atom or diatom. Atom-atom interactions may not form a metastable state, however, because there exist no complex structure in an effective diatomic potential. (Of course, two atoms moving extremely slowly toward each other will be in proximity of one another for a relatively long time, but this is not the type of interaction we are interested in isolating with this analysis.) Atom-diatom interactions, however, can plausibly admit metastable states that exist for a relatively long time. These interactions may be studied and isolated using our existing QCT tools, which is the preliminary analysis we present here.

One measure of collision time is simply the total time of the QCT integration, which we denote t_t . However, this time includes the reactants traveling toward each other, and the products traveling away from each other. These times are considerable, especially because our cutoff distances are chosen to be conservatively large, as described in Section 2.2:

¹⁷The results for oxygen dissociation presented at the 2018 AIAA winter conference [30] were computed with the error, but all new cases were run for the QCT database.

¹⁸Except due to quantum tunneling, which we do not expect to be important for N and O atoms.

¹⁹The relevant time scale is of molecular collisions, which are very short: the timestep used for this work is 0.05 fs. One example time scale is the vibrational period of rovibrational-ground-state O_2 , which is approximately 20 fs.

reactants are placed 15 Å apart and a trajectory is considered complete when their final spacing exceeds 15 Å. Furthermore, the total time also includes ‘flyby’ trajectories where no meaningful interaction took place, because the maximum impact parameter is 6 Å. For reference, the equilibrium bond length of N₂ is 1.1 Å and for O₂ it is 1.2 Å. These large distances mean that trajectories with long QCT integration times simply have very low relative velocities, regardless of whether an interaction occurs at all. The total QCT time, therefore, is a poor metric for interaction time, especially for the purpose of identifying long-lived metastable states.

We therefore modify the total collision time by subtracting the time taken for reactants to travel toward each other, and for products to travel away from each other. The travel time toward each other is defined using the initial reactant spacing, in the direction of the initial relative velocity, divided by the magnitude of initial relative velocity. The travel time away from each other is defined similarly using product quantities. This yields our definition of the interaction time,

$$t_i = t_t - \frac{\vec{r}_i \cdot (-\hat{\mathbf{v}}_i)}{|\vec{\mathbf{v}}_i|} - \frac{\vec{r}_f \cdot \hat{\mathbf{v}}_f}{|\vec{\mathbf{v}}_f|} \quad (3.21)$$

where \vec{r} and \vec{v} is the position and velocity of the atom, relative to the diatom. $\hat{\mathbf{v}}$ denotes the unit vector of velocity, which is multiplied by -1 when reactants are traveling toward each other. Subscript i denotes initial (reactant) and f denotes final (product), and this definition is only valid when there is a product diatom²⁰. This definition is similar to that used by Lin *et al.* [117], although we do not include any distance heuristics.

This interaction time is designed to identify long-lived collisions, because it is only positive and large when such an interaction has occurred. However, it can also be negative: consider, for example, two reactants traveling relatively slowly toward each other with low impact parameter. Before their centers of mass overlap, repulsive forces drive them apart; the distance traveled by reactants toward each other is less than the quantity $\vec{r}_i \cdot (-\hat{\mathbf{v}}_i)$. Similarly, the distance traveled by products away from each other is less than the quantity $\vec{r}_f \cdot \hat{\mathbf{v}}_f$. Thus, the final interaction time is negative. Several other definitions of interaction time have been considered, but no other metrics have been found to be suitable for identifying the interactions we wish to examine.

PDFs of interaction time are shown in Figure 3.49. Conditions are sampled from thermal equilibrium with 2000 K, for N₂ + N and O₂ + O interactions. 12 million trajectories were run for each surface; these trajectories are not in the main QCT database. Two PESs are used for the O₂ + O interactions: 1¹A' and 2⁵A', which exhibited relatively high and low exchange rates, respectively. For the O₂ + O interactions on the 1¹A' interaction state

²⁰Long-lived interactions are only found to occur with energies lower than the dissociation energy, so this is a reasonable restriction for our current purpose.

especially, long interactions are observed. The interatomic spacing over time, for two long interactions on the $1^1\text{A}'$ surface, is shown in Figure 3.50. Figure 3.50a is representative of long interactions: the reactants travel toward each other, and then form a metastable state that exists, in this case, for approximately 2500 fs²¹. Figure 3.50b is one of the longest interactions we have observed; the interaction is qualitatively similar, but the time spent with all three interatomic distances below 4 Å is approximately 200,000 fs.

The $1^1\text{A}'$ interaction state exhibits more long interactions than the $2^5\text{A}'$ interaction state, perhaps due to differences in the barrier for exchange. We do not observe any particularly long interactions for $\text{N}_2 + \text{N}$; the reason for this is currently unknown. This preliminary analysis is promising, and it indicates that long-lived $\text{O}_2 + \text{O}$ interactions may be candidates for recombination when struck by a fourth body.

3.7.4 Transition Probabilities

Postprocessing to yield PDFs in more than one variable enables the study of state transitions. This Section is inspired by the work of Grover [75], who examined the distribution of vibrational energy change for $\text{N}_2 + \text{N}$ and demonstrated shape similarity for no-reaction events. We will demonstrate that similar results may be obtained via postprocessing existing QCT data. Work is ongoing to demonstrate consistency between these methods for this type of result.

We first show joint PDFs of initial and final vibrational quantum number for a sample case of $\text{N}_2 + \text{N}$ sampled from thermal equilibrium at 20,000 K. The two events that yield a product molecule are shown: no reaction and exchange. As we described in Section 3.1.2, exchange reactions are much more likely to yield a large change in vibrational energy; these results are another way to qualitatively demonstrate the phenomenon. For no-reaction events, the population of trajectories is concentrated on the diagonal, which corresponds to no change in vibrational level. For exchange events, the distribution is much broader. Similar plots have been shown by other researchers, including Valentini *et al.* [11] and Grover [75].

From this joint PDF, the distribution of final states *given* an initial state and an event may be computed,

$$f_e(q_f|q_i) = \frac{f_e(q_i, q_f)}{f_e(q_i)} \quad (3.22)$$

in which q is an arbitrary quantity in either the initial or final state. The probability of obtaining a final state given an initial state is this PDF divided by the PDF spacing.

²¹The interaction time we have chosen may be interpreted using this figure as the time between x-axis intercepts of the initial downward slow and final upward slope.

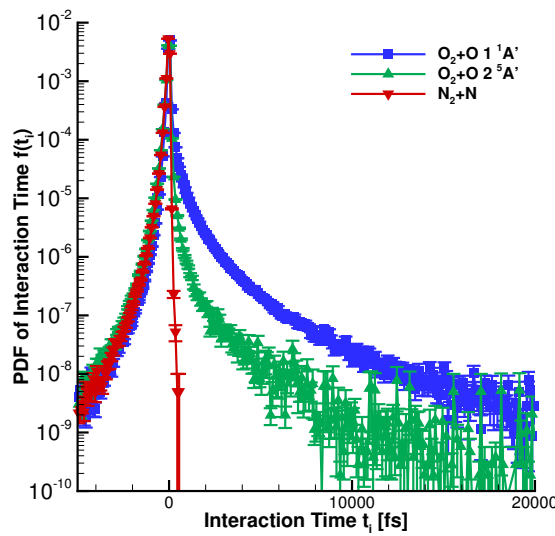


Figure 3.49: Distribution of interaction times for diatom-atom interactions, conditions sampled from equilibrium with $T_{\text{tr}} = T_{\text{v}} = 2000$ K.

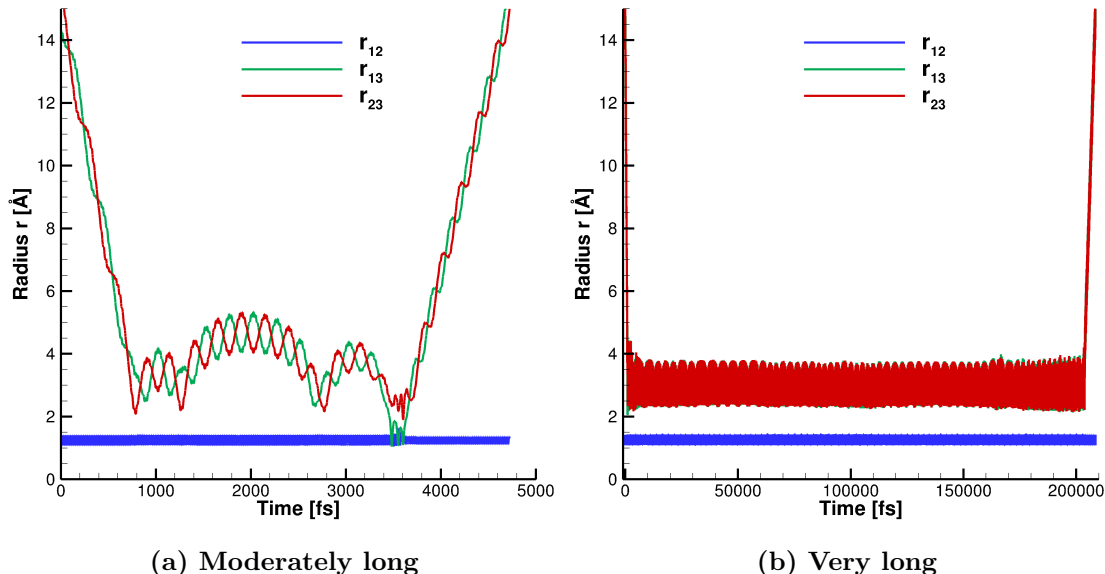


Figure 3.50: Interatomic distances as a function of time for two long-interaction events in $\text{O}_2 + \text{O}$ on the $1^1\text{A}'$ interaction state. Here, r is the interatomic distance between two atoms; atoms 1 and 2 form the reactant diatom.

Uncertainties are quantified using simple propagation of error [118, p. 73]; this derivation is similar to those discussed already in Section 2.3.4. In REAQCT, these quantities are computed from a variety of joint PDF using the `post_given_pre` utility. This feature is only implemented for $A_2 + A$ type reactions at the moment, although it could easily be extended to other reactions.

Transition probabilities given no-reaction events are shown in Figure 3.52. Two cases are shown, both sampled from thermal equilibrium: $N_2 + N$ at 20,000 K, and $O_2 + O$ system at 5000 K. For each of rotational and vibrational energy, the probability of a final energy is shown, given that a no-reaction event has occurred and that the initial energy is within some range. The distribution of final energies peaks sharply at the initial energy, as expected, because no energy change is the most likely outcome. The distribution is wider for rotational energy than vibrational energy, and also widens at higher temperatures. The difference between rotational and vibrational energy is most prevalent for molecules beginning at low energy (blue squares). Consistent with the results of Grover [75], the shapes are similar for all initial energies. These transition probabilities, along with similar data for exchange reactions, determine the relaxation of both rotational and vibrational energy. These data, therefore, may be used to describe the relaxation process for any distribution of internal energies, including QSS. Work to achieve this outcome, using both DMS and QCT data, is ongoing.

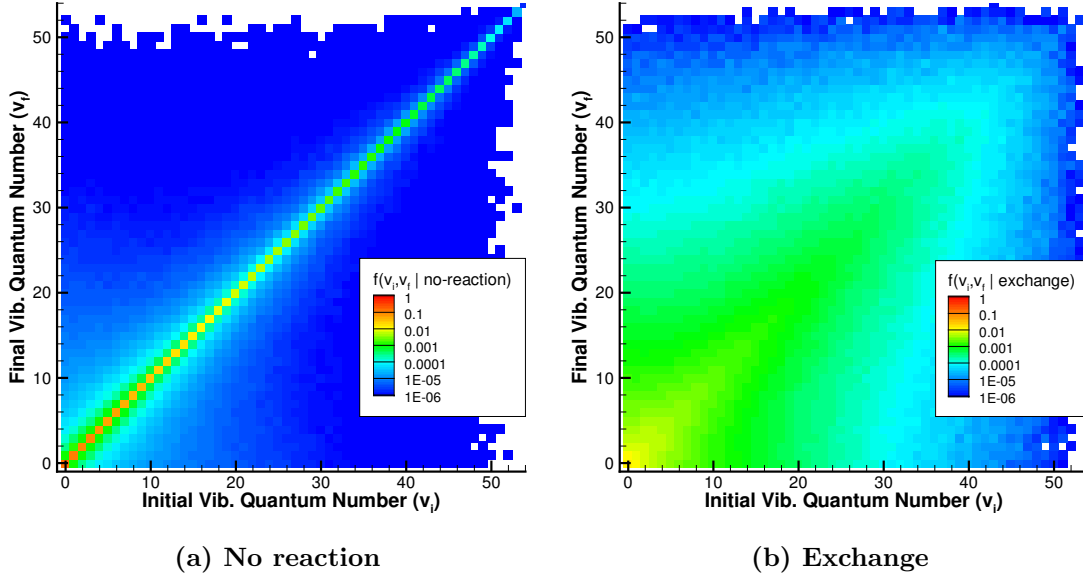


Figure 3.51: PDF of initial and final vibrational quantum number, for $\text{N}_2 + \text{N}$ interaction types that do not result in dissociation; $T_{\text{tr}} = T_{\text{v}} = 20,000$ K.

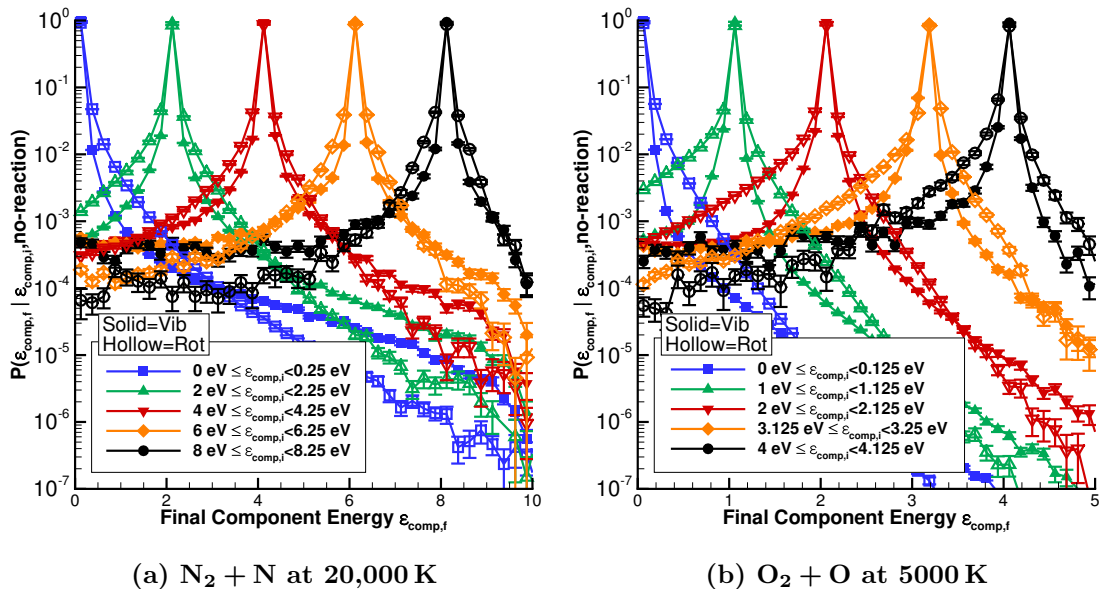


Figure 3.52: Probability of transition from an initial component energy to a final component energy, for no-reaction events sampled from thermal equilibrium.

Chapter 4

CFD Methodology and Results

4.1 Methodology

We first present the conservation equations of interest, and note the terms that must be described by a chemical kinetics model. Then, we describe the various chemical kinetics models we have examined. Finally, we note several modifications which we use to ensure consistency when comparing DMS and CFD results. We use the US3D code [21], an unstructured finite-volume solver which has been widely validated across a range of test cases.

4.1.1 Conservation Equations

We consider the Navier–Stokes equations that have been extended to include chemical reactions and vibrational relaxation. The equations presented here assume that rotational energy is in equilibrium with translation; for the conditions we present in the current work (10,000 K), rotational nonequilibrium does not play an important role [10]. A more complete description of these terms, presented in the context of US3D’s solution methodology, is given by Nompelis [132]. The mass conservation equation for species s is:

$$\frac{\partial \rho_s}{\partial t} + \nabla \cdot (\rho_s \vec{u}) = -\nabla \cdot (\rho_s \vec{v}_s) + w_s \quad (4.1)$$

in which ρ_s is the partial density of species s , \vec{u} is the bulk velocity, \vec{v}_s is the species diffusion velocity, and w_s is the rate of species formation. In this work, the only chemical reaction we consider is nitrogen dissociation,



where M is a generic collision partner, either N_2 or N in the present work. This reaction proceeds at a rate \mathcal{R} , which is negative for the forward reaction by convention. Nitrogen

dissociation results in the following species source terms:

$$w_{N2} = \mathcal{M}_{N2}(\mathcal{R}) \quad (4.3)$$

$$w_N = \mathcal{M}_N(-2\mathcal{R}) \quad (4.4)$$

where \mathcal{M}_s is the molar mass of species s . The reaction rate is described by the reaction rate constants and the molar concentrations,

$$\mathcal{R} = \sum_m \left(k_{b,m} \left(\frac{\rho_N}{\mathcal{M}_N} \right)^2 \frac{\rho_m}{\mathcal{M}_m} - k_{f,m} \frac{\rho_{N2}}{\mathcal{M}_{N2}} \frac{\rho_m}{\mathcal{M}_m} \right) \quad (4.5)$$

where k_m is the reaction rate constant for partner m , for either the forward f or backward b reaction. For the current work, the backward reaction is disabled in order to compare against DMS results; see Section 4.1.5. Therefore, in order to close the mass conservation equation, a chemical kinetics model must describe the reaction rate constant k_f .

The momentum equation is:

$$\frac{\partial (\rho \vec{u})}{\partial t} + \nabla \cdot (\rho \vec{u} \otimes \vec{u} + p \mathbf{I}) = \nabla \cdot \tilde{\tau} \quad (4.6)$$

in which ρ is the total density, p is pressure and $\tilde{\tau}$ is the shear stress tensor. No terms in the momentum equation require modeling by a chemical kinetics model. In US3D, the total energy (including any separately-treated components such as vibrational energy) is solved for:

$$\frac{\partial E}{\partial t} + \nabla \cdot [(E + p) \vec{u}] = \nabla \cdot (\tilde{\tau} \vec{u}) - \nabla \cdot (\vec{q}_t + \vec{q}_r + \vec{q}_v) - \nabla \sum_{s=1}^{ns} (\rho_s h_s \vec{v}_s) \quad (4.7)$$

in which E is the total energy per unit volume, \vec{q} is the heat flux vector for energy components, and h_s is the formation enthalpy of species s . No terms in the energy conservation equation require modeling by a chemical kinetics model.

Finally, we solve one vibrational energy equation, which is:

$$\frac{\partial E_v}{\partial t} + \nabla \cdot (E_v \vec{u}) = -\nabla \cdot \vec{q}_v - \nabla \cdot \sum_{s=1}^{ns} (\rho_s e_{v,s} \vec{v}_s) + w_v \quad (4.8)$$

in which $e_{v,s}$ is the average vibrational energy of species s per unit mass. The vibrational source term comprises two separate physical phenomena:

$$w_v = Q_{t-v} + \sum_s Q_{v,s} \quad (4.9)$$

in which Q_{t-v} is the vibrational energy change due to vibrational relaxation, and $Q_{v,s}$ is the vibrational energy change due to formation and destruction of chemical species. In order to better understand the evolution of vibrational energy, we sometimes split the vibrational energy change due to formation and destruction into two components: *nonpreferential* and *preferential*. We define,

$$Q_{v,s} = Q_{v,s,\text{non-pref}} + Q_{v,s,\text{pref}} \quad (4.10)$$

$$Q_{v,s,\text{non-pref}} = w_s \langle \varepsilon_{\text{vib},s} \rangle \quad (4.11)$$

The nonpreferential component of vibrational energy change due to dissociation is equal to the average vibrational energy of that species. This definition is chosen such that, if there is no preferential component, the destruction or formation of any chemical species does not directly yield a change in T_v . (If a population of diatoms has average vibrational energy $\langle \varepsilon_{\text{vib}} \rangle$, removing N diatoms and $N \langle \varepsilon_{\text{vib}} \rangle$ vibrational energy does not change the average energy per diatom.)

We must therefore model three terms: k_f , Q_{t-v} , and $Q_{v,s}$. These are the inputs required for a chemical kinetics model described in the introduction. In this work, we implement and examine 3 different models, which are described in the following sections.

4.1.2 Park Model

In this Section, we describe the Park model [18], which is used as a baseline point of comparison. The reaction rate constants are described in terms of a controlling temperature,

$$T_a = \sqrt{T_{\text{tr}} T_v} \quad (4.12)$$

and the forward rate constant is described by a modified Arrhenius form,

$$k_{f,m} = C_m T_a^n \exp\left(-\frac{\Theta_v}{T_a}\right) \quad (4.13)$$

The coefficients for nitrogen dissociation with partners N₂ and N are,

$$C_{N_2} = 7 \times 10^{21} \text{ cm}^3 \text{ mol}^{-1} \text{ s}^{-1} \quad (4.14)$$

$$C_N = 30 \times 10^{21} \text{ cm}^3 \text{ mol}^{-1} \text{ s}^{-1} \quad (4.15)$$

$$n = -1.6 \quad (4.16)$$

$$\Theta_v = 113,200 \text{ K} \quad (4.17)$$

Vibrational relaxation is described by vibrational relaxation times fit by Millikan and

White [54] with the Park high-temperature correction [20]. For complete details of computing Q_{t-v} from τ_v , see Nompelis [132]. The vibrational relaxation time for N₂ with collision partner m is described by,

$$p\tau_{v,m} = \exp \left[a_m \left(T_{\text{tr}}^{-1/3} - b_m \right) - 18.42 \right] \text{ atm s} \quad (4.18)$$

with the following parameters:

$$a_{N2} = 221 \quad (4.19)$$

$$a_N = 180 \quad (4.20)$$

$$b_{N2} = 0.0290 \quad (4.21)$$

$$b_N = 0.0262 \quad (4.22)$$

In typical implementations of the Park model in CFD, the change in vibrational energy due to dissociation is modeled as nonpreferential. Thus, for ‘standard Park’,

$$Q_{v,s} = w_s \langle \varepsilon_{\text{vib},s} \rangle \quad (4.23)$$

However, the Park model was originally developed with a different model for the change in vibrational energy due to dissociation [16],

$$Q_{v,s} = w_s (D_0 - k_B T_{\text{tr}}) \quad (4.24)$$

In this work, we refer to this as the ‘original Park’ model.

4.1.3 Park with New Parameters

In this Section, we describe a model which uses the form of the standard Park model, but with parameters derived from *ab-initio* data. Reaction rates and change in vibrational energy due to dissociation are taken from QCT, and relaxation times are taken from DMS¹. We are *not* endorsing this approach as the best way to improve predictive capability in CFD. As we have discussed previously [29, 30], these new data are an opportunity to improve the models themselves, not simply update the parameters. Nevertheless, this approach provides a useful point of comparison and analysis.

Reaction rate constants are described by the Park form [Eqns. (4.12) and (4.13)] with parameters from a fit due to Bender *et al.* [25]. The reaction rate constant for partner N is

¹This work was performed before the fitting results presented in Section 3.6.

the same as for partner N₂ based on later DMS [11] and the present QCT results,

$$C_{N2} = 2.71 \times 10^{18} \text{ cm}^3 \text{ mol}^{-1} \text{ s}^{-1} \quad (4.25)$$

$$C_N = C_{N2} \quad (4.26)$$

$$n = -0.675 \quad (4.27)$$

$$\Theta_v = 117,000 \text{ K} \quad (4.28)$$

Relaxation times are described by the Millikan and White form [Eqn. (4.18)] with parameters from a fit due to Valentini and Schwartzentruber [133],

$$a_{N2} = 128 \quad (4.29)$$

$$a_N = 102 \quad (4.30)$$

$$b_{N2} = 0.0145 \quad (4.31)$$

$$b_N = 0.0252 \quad (4.32)$$

Finally, we construct and fit by eye a simple model for the change in vibrational energy due to dissociation, based on QCT data,

$$\langle \varepsilon_{\text{vib}} \rangle_d = D_0 - \frac{3}{2} k_B T_{\text{tr}} - \frac{1}{15} \frac{D_0^2}{k_B} \left(\frac{1}{T_v} - \frac{1}{T_{\text{tr}}} \right) \quad (4.33)$$

$$Q_{v,s} = w_s \langle \varepsilon_{\text{vib}} \rangle_d \quad (4.34)$$

This form is based on Park's original preferential dissociation model and includes a nonequilibrium correction term which is linear in 1/T_v. $\langle \varepsilon_{\text{vib}} \rangle_d$ is bound to not exceed D_0 and to not be below the average vibrational energy. Importantly, the change in vibrational energy goes to 0 in the limit of $T_v \rightarrow 0$; the model is ill-conditioned for CFD otherwise. This fit was designed specifically for the conditions in this work, and is not intended for general use.

4.1.4 *ab-Initio* Model: Boltzmann

In this Section, we describe the microscopic to macroscopic model using Boltzmann distributions of vibrational energy. The key input to this model describes the probability of dissociation from a specific set of energies. So long as the collision energy is greater than D_0 , the probability of dissociation in N₂ + N₂ is [134],

$$P_d(E_r, \varepsilon_{\text{rot}}, \varepsilon_{\text{vib}}) = C_1 \left(\frac{E_r + \varepsilon_{\text{rot}} + \varepsilon_{\text{vib}} - D_0}{D_0} \right)^\alpha \frac{D_0}{E_r} \exp \left(\beta \frac{\varepsilon_{\text{rot}}}{D_0} \right) \exp \left(\gamma \frac{\varepsilon_{\text{vib}}}{D_0} \right) \quad (4.35)$$

with parameters,

$$C_1 = 7.5 \times 10^{-3} \quad (4.36)$$

$$\alpha = 1.80 \quad (4.37)$$

$$\beta = 0.50 \quad (4.38)$$

$$\gamma = 2.50 \quad (4.39)$$

The rate constant is derived by analytically integrating reaction probabilities with molecular energies distributed as Boltzmann. Note that, in order to achieve a closed form for the integration, one must describe a Boltzmann distribution to integrate over. In this work, similar to Ref. [134], a simple harmonic oscillator and a rigid rotor is assumed. We are in the process of moving beyond this assumption for future work. This yields,

$$k_{f,m}(T_t, T_r, T_v) = A_m T_t^\eta \exp\left[-\frac{D_0}{k_B T_t}\right] G_{\text{rot}} G_{\text{vib}} \quad (4.40)$$

$$(4.41)$$

with parameters,

$$\eta = \alpha - 0.5 = 1.30 \quad (4.42)$$

$$A_{N2} = 4.39 \times 10^{-17} \text{ cm}^3 \text{ s}^{-1} \quad (4.43)$$

where G_{rot} and G_{vib} are the functions that capture the dependence on rotational energy and vibrational energy. They have the following form,

$$G_{\text{rot}} = \begin{cases} \frac{\exp[j_{\max}(j_{\max} + 1)\delta_{\text{rot}}] - 1}{\delta_{\text{rot}}} \frac{\eta_{\text{rot}}\theta_r}{T_r} & \text{if } \delta_{\text{rot}} \neq 0 \\ j_{\max}(j_{\max} + 1) \frac{\eta_{\text{rot}}\theta_r}{T_r} & \text{if } \delta_{\text{rot}} = 0 \end{cases} \quad (4.44)$$

$$G_{\text{vib}} = \begin{cases} \exp\left(\frac{\delta_{\text{vib}}}{2}\right) \frac{1 - \exp(\delta_{\text{vib}}v_{\max})}{1 - \exp(\delta_{\text{vib}})} \frac{1 - \exp(-\theta_v/T_v)}{\exp[-\theta_v/(2T_v)]} & \text{if } \delta_{\text{vib}} \neq 0 \\ v_{\max} \frac{1 - \exp(-\theta_v/T_v)}{\exp[-\theta_v/(2T_v)]} & \text{if } \delta_{\text{vib}} = 0 \end{cases} \quad (4.45)$$

where δ_{rot} and δ_{vib} are measures of the degree of nonequilibrium relative to the dissociation energy in rotation and vibration, respectively, and j_{\max} and v_{\max} are the maximum quantum

numbers,

$$\delta_{\text{rot}} = \eta_{\text{rot}} \theta_r k_B \left(-\frac{1}{k_B T_r} + \frac{\beta}{D_0} + \frac{1}{k_B T_t} \right) \quad (4.46)$$

$$\delta_{\text{vib}} = \theta_v k_B \left(-\frac{1}{k_B T_v} + \frac{\gamma}{D_0} + \frac{1}{k_B T_t} \right) \quad (4.47)$$

$$j_{\max} = \sqrt{\frac{\varepsilon_{\text{rot}}^{\max}}{k_B \theta_r \eta_{\text{rot}}}} \quad (4.48)$$

$$v_{\max} = \frac{D_0}{k_B \theta_v} \quad (4.49)$$

$$\eta_{\text{rot}} = 0.75 \quad (4.50)$$

For N₂, the maximum rotational energy $\varepsilon_{\text{rot}}^{\max}$ is approximately 14 eV. As discussed, our current implementation assumes $T_t = T_r$, but the full form is shown here for completeness.

In order to determine the average vibrational energy decrease due to dissociation we assume it is equal to the average vibrational energy of molecules which dissociate. Note that these quantities are not identical for N₂ + N₂ interactions: the collision partner's vibrational energy tends to decrease slightly, and swap and double dissociations also contribute. The average vibrational energy of molecules that dissociate, computed using an expected value and simplifying, is

$$\langle \varepsilon_{\text{vib}}^d \rangle = \frac{1}{P_d} \sum_j \sum_v \int_{E_r} \varepsilon_{\text{vib}} P_d(E_r, \varepsilon_{\text{rot}}, \varepsilon_{\text{vib}}) f(E_r, \varepsilon_{\text{rot}}, \varepsilon_{\text{vib}}) dE_r \quad (4.51)$$

$$\langle \varepsilon_{\text{vib}}^d \rangle = \frac{\sum_j \sum_v \int_{E_r} \varepsilon_{\text{vib}} P_d(E_r, \varepsilon_{\text{rot}}, \varepsilon_{\text{vib}}) f(E_r, \varepsilon_{\text{rot}}, \varepsilon_{\text{vib}}) dE_r}{\sum_j \sum_v \int_{E_r} P_d(E_r, \varepsilon_{\text{rot}}, \varepsilon_{\text{vib}}) f(E_r, \varepsilon_{\text{rot}}, \varepsilon_{\text{vib}}) dE_r} \quad (4.52)$$

$$\langle \varepsilon_{\text{vib}}^d \rangle = \frac{k_B \theta_v}{G_{\text{vib}} Q_v} \frac{\partial (G_{\text{vib}} Q_v)}{\partial \delta_{\text{vib}}} \quad (4.53)$$

where Q_v is the vibrational partition function, which is currently modeled using a simple harmonic oscillator. We finally obtain,

$$\langle \varepsilon_{\text{vib}}^d \rangle = \begin{cases} k_B \theta_v \left[\frac{1}{2} - \frac{v_{\max} \exp(\delta_{\text{vib}} v_{\max})}{1 - \exp(\delta_{\text{vib}} v_{\max})} + \frac{\exp(\delta_{\text{vib}})}{1 - \exp(\delta_{\text{vib}})} \right] & \text{if } \delta_{\text{vib}} \neq 0 \\ k_B \theta_v \left(1 + \frac{v_{\max}}{2} \right) & \text{if } \delta_{\text{vib}} = 0 \end{cases} \quad (4.54)$$

which yields the source term for vibrational energy change due to formation and destruction,

$$Q_{v,s} = w_s \left\langle \varepsilon_{\text{vib}}^{\text{d}} \right\rangle \quad (4.55)$$

The reaction rate and energy change per dissociation for N partner is taken to be the same as for partner N_2 . The change in vibrational energy due to relaxation is not currently treated by our *ab-initio* model. We therefore use the Valentini and Schwartzentruber [133] fits to a typical vibrational relaxation time, Eqns. (4.29)–(4.32). Finally, several expressions in this Section have limiting behavior when $\delta = 0$. The implementation of this limiting, in the context of finite-precision arithmetic, is described in Section C.5.

4.1.5 Consistency with DMS

For the bulk of the results in this work (Section 4.2), CFD results are compared with DMS. We therefore make several modifications to the typical CFD paradigm in order to make this comparison as consistent as reasonably possible. Some of these modifications will be relaxed in Section 4.3, and further analysis will be addressed in future studies. In this Section, we describe these modifications.

First, CFD calculations are performed for a single cell with symmetry boundary conditions and a fixed volume. This mimics the typical 0-dimensional simulation performed in DMS.

Second, translational temperature T_t is held fixed, mimicking a translationally-isothermal reactor. The DMS simulations we compare with resample translational energy from a Maxwell-Boltzmann distribution each timestep. Note that we are treating rotational energy in a manner inconsistent with DMS. Rotational energy is assumed to be equilibrated with translational energy in our current implementation, whereas DMS allows the rotational energy distribution to evolve via the outcome of trajectories. For the temperatures considered in the present work (around 10000 K), we do not expect rotational nonequilibrium to be important in nitrogen [10]. However, assuming rotational equilibrium at T_t is a simplifying assumption of the current CFD implementation and we may relax it in the future.

Third, we choose to initialize CFD with $T_{\text{tr}} = T_v$. DMS typically begins with $T_r = T_v$ because generating a distribution with different internal temperatures requires specifying a method of separating vibrational and rotational energy. Furthermore, we are approximating $T_t = T_r$ in CFD, thus $T_t = T_r = T_v$ is the only initial condition which is consistent between CFD and DMS. We assess the impact of this choice in Section 4.2.1

Vibrational Energy and Temperature

The final modification we make is to treat vibrational energy and temperature consistently between CFD and DMS. Without modification, they would be inconsistent in two ways. First, vibrational energy at high temperatures is typically defined using the NASA Lewis database [135, 136], which includes electronic energy. At the temperatures of interest (around 10000 K), electronic energy is non-negligible for N₂ and N. In contrast, the PESs in the DMS calculations are for ground electronic state interactions only. Second, vibrational temperature in DMS results in the literature has previously been defined as $\langle \varepsilon_{\text{vib}} \rangle / k_B$. This definition is inconsistent with CFD because it does not include the vibrational degrees of freedom typically used to define a temperature. All of these issues are solved by consistently defining the relationship between average vibrational energy and vibrational temperature, via the following procedure.

For a range of temperatures ($T_r = T_v$), a Boltzmann distribution of nitrogen molecules is generated using the diatomic potential used for QCT [63]. The average internal energy ($\varepsilon_{\text{int}} = \varepsilon_{\text{rot}} + \varepsilon_{\text{vib}}$) of the Boltzmann distribution is then computed for each temperature. This results in a table of temperatures and the corresponding average internal energy.

For CFD, $5/2 RT$ is added to the average internal energy to yield enthalpy, which is fit to the NASA Lewis form [135, 136]. This fit is used in place of the typical N₂ enthalpy fit, and it excludes electronic energy. An electronically-excluded fit for the enthalpy of N, equal to $5/2 RT$, is also constructed. The fitting parameters are shown in the Appendix, Section C.4, and Figure 4.1 shows specific heat at constant pressure for the electronically-excluded fits, the typical NASA Lewis fits, and vibrational energy using the Simple Harmonic Oscillator (SHO) assumption.

For DMS, we subtract $k_B T$ from the table of average internal energy, approximately removing rotational energy. (In CFD, rotational energy is typically treated as $k_B T$). Then, we interpolate the average vibrational energy from DMS on this table to find the corresponding temperature, which is T_v . In this manner, we define T_v from $\langle \varepsilon_{\text{vib}} \rangle$ in DMS the same way it is done in CFD. This postprocessing is used to define T_v for the DMS data presented in this work.

In the future, we will have to describe the evolution of electronic energy as a gas relaxes and dissociates. However, the current DMS and QCT calculations exclude electronic energy and we therefore do not have models based on *ab-initio* data. Therefore, our approach is to neglect them for the time being.

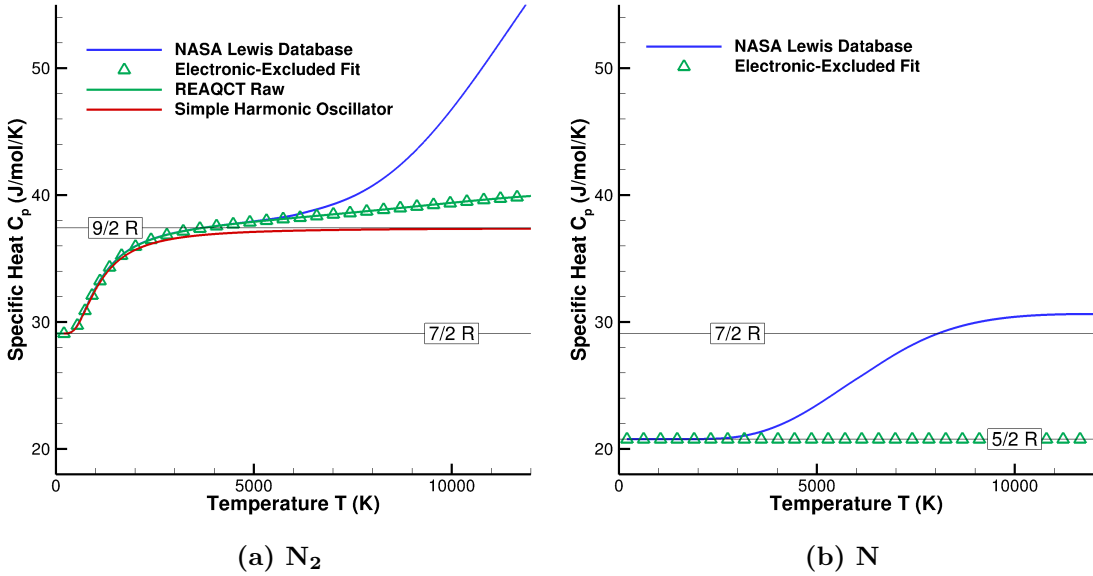


Figure 4.1: Specific heat at constant pressure (C_p) for N_2 and N , new fits constructed to exclude electronic energy to ensure a consistent comparison with DMS.

4.2 Zero-Dimensional Isothermal Results

In this Section, we present CFD simulations run in a manner to be consistent with DMS (see Section 4.1.5). We are interested in comparing results with DMS data from Valentini *et al.* [11]. In order to better understand the effect of each parameter, we first examine several specific effects. Because these simulations are isothermal, the system’s total energy increases as dissociation occurs. We therefore focus on the initial dissociation period, before the energy becomes unrealistically high. An initial density of 1.2824 kg/m^3 is used to match the reference DMS data. Because all processes are bimolecular, decreasing the density only results in a corresponding increase in the time scales.

4.2.1 Individual Comparisons

We first compare results for the standard Park model to DMS, shown in Figure 4.2. The standard Park model results in significantly faster dissociation compared to the DMS calculation; the time for $1/3$ of the initial N_2 to be dissociated is approximately 4 times longer for DMS than for the standard Park model. One important reason for this difference is the evolution of vibrational temperature. In standard Park, the vibrational energy decrease per dissociation is equal to the average vibrational energy of that species: nonpreferential energy decrease due to dissociation. As a result, the T_v remains equal to T_{tr} throughout the

simulation. The source terms of vibrational energy are also shown; the relaxation term is zero because $T_v = T_{tr}$ and the preferential component of energy change due to dissociation is also zero.

Next, we examine the effect of initial condition, in order to defend our choice of temperature initialization ($T_{v,0} = T_{tr,0}$). Figure 4.3 compares results for $T_{v,0} = 300$ K to $T_{v,0} = T_{tr,0}$. The gas initialized as vibrationally-cold relaxes quickly compared to the time-scales of dissociation, and dissociation for this case lags behind dissociation for the initially-equilibrated case. This lag time is small, however, and the time-histories are very similar. This weak dependence on initialization is also observed for the other chemical kinetics models we have tested. As expected, the vibrational relaxation source term is large initially, then drops to 0 as T_v approaches T_{tr} .

The effect of vibrational energy decrease due to dissociation is shown next; Figure 4.4 compares standard Park to Park's original preferential dissociation model. As dissociation occurs, the vibrational temperature decreases, especially at first when the dissociation rate is the largest. Eventually, the vibrational energy increase due to relaxation balances the vibrational energy decrease due to dissociation, resulting in a roughly-constant T_v . This balance is QSS modeled in CFD: the two terms are both large, but opposite sign and roughly equal magnitude, as seen by the vibrational source terms plotted in Figure 4.4b. The dissociation rate is reduced by approximately a factor of 2 because the vibrational temperature is depressed due to dissociation. The preferential dissociation model for vibrational energy decrease due to dissociation has a pronounced effect on dissociation rate for all isothermal cases we have studied.

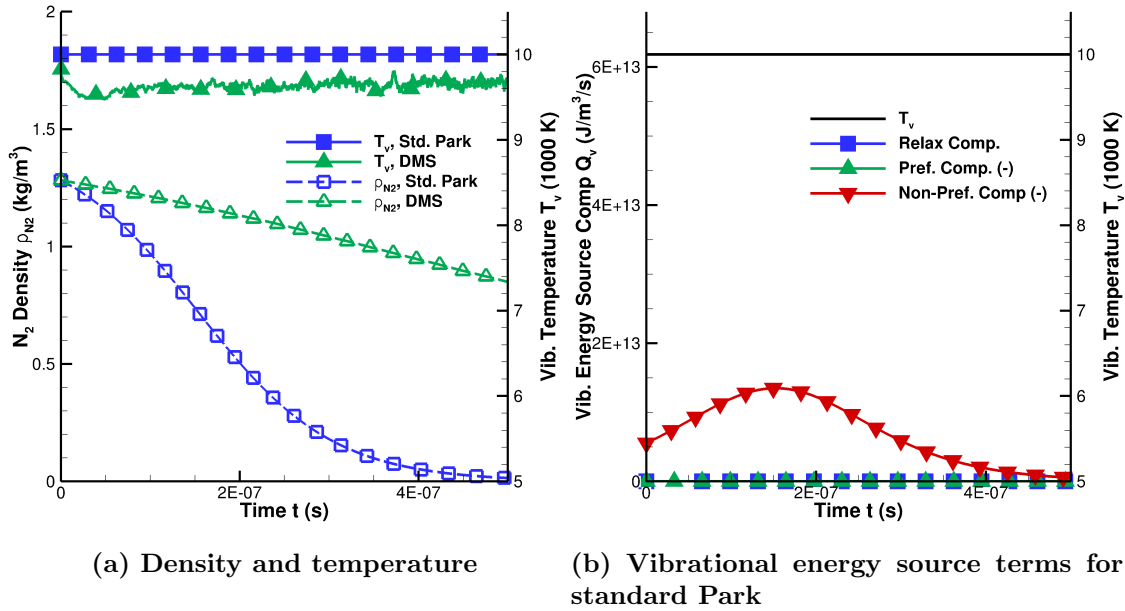
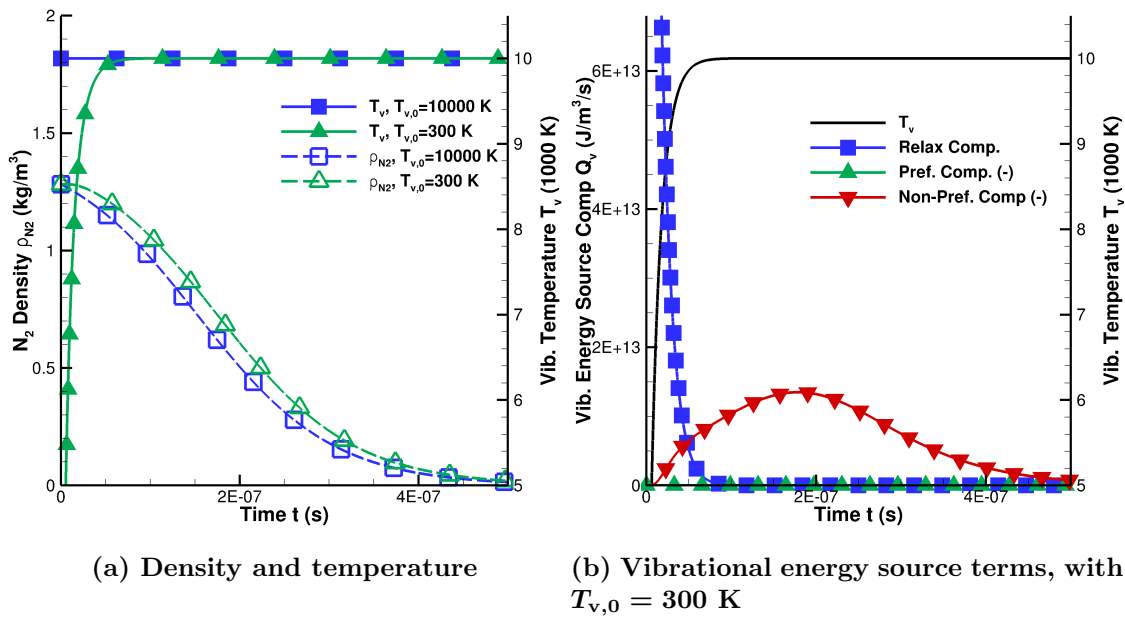
Incorporating electronic energy complicates the previous conclusions about vibrational energy, because electronic energy is considered together with vibrational energy in our CFD implementation. We must first define the electronic energy change due to formation/destruction of species; in the absence of better information, we choose the average electronic energy of that species (nonpreferential). Figure 4.5 compares the Park original model with and without electronic energy. Electronic energy has two important effects. First, the vibrational-electronic energy decrease per to dissociation is lessened, because forming atomic nitrogen around 10000 K *increases* electronic energy: N is formed at its average electronic energy which is appreciable, see Figure 4.1b. Second, including electronic energy increases the overall vibrational-electronic energy density, so a given decrease in vibrational energy yields less decrease in vibrational temperature. Together, these two effects substantially mitigate the dissociation-rate decrease caused by a preferential dissociation model. Unfortunately, we do not have *ab-initio* data to inform our treatment of electronic energy, and there are several unknowns. What is the average electronic energy of nitrogen molecules which dissociate? What is the average electronic energy of nitrogen

atoms formed via dissociation? The second question especially has important ramifications for our understanding of recombination. Therefore, we neglect electronic energy to ensure a well-posed comparison between CFD and DMS.

Park's rates describe N as a relatively effective collision partner for dissociating N_2 , compared to partner N_2 . QCT and DMS data have shown that the dissociation rates for $N_2 + N_2$ and $N_2 + N$ are similar, however. Instead, N promotes vibrational relaxation via exchange reactions in $N_2 + N$ [84, 85]. Previous works [11] and our present work have argued that these effects yield the same outcome: nitrogen dissociation progresses faster in the presence of atomic nitrogen. Figure 4.6 attempts to evaluate these conclusions in a CFD context: Park's original model is compared to the Park with new parameters model modified to use Park's original decrease in vibrational energy due to dissociation. We are therefore modifying the reaction rate and vibrational relaxation time. The dissociation rates are found to be very similar. In the Park original model, the vibrational temperature is lowered substantially, slowing the otherwise rapid dissociation of N_2 via N. In the other case, the T_v relaxes toward T_{tr} more rapidly. This result is a reminder that the thermal and chemical evolution of a gas is coupled, and different model parameters may have a similar effect on quantities of interest.

4.2.2 Comparison Between Models

A comparison between each chemical kinetics model presented is shown in Figure 4.7. As discussed earlier, the standard Park model yields dissociation that is too fast. Dissociation in the 'Park with new parameters' formulation is slower than standard Park by approximately a factor of 2. The dissociation rate is still approximately twice as fast as DMS, however. This is an important conclusion: simply using QCT rates sampled from a Boltzmann gas does not yield the same result as DMS. Depletion of high-energy molecules, especially vibrationally-excited ones, decreases the dissociation rate by approximately a factor of 2 [11]. This depletion is nonequilibrium *within* the vibrational mode, which is not captured by a multi-temperature model that assumes Boltzmann distributions of separate internal energy modes.

Figure 4.2: Standard Park compared to DMS, $T_{v,0} = T_{tr,0}$ Figure 4.3: Effect of initial T_v , with standard Park

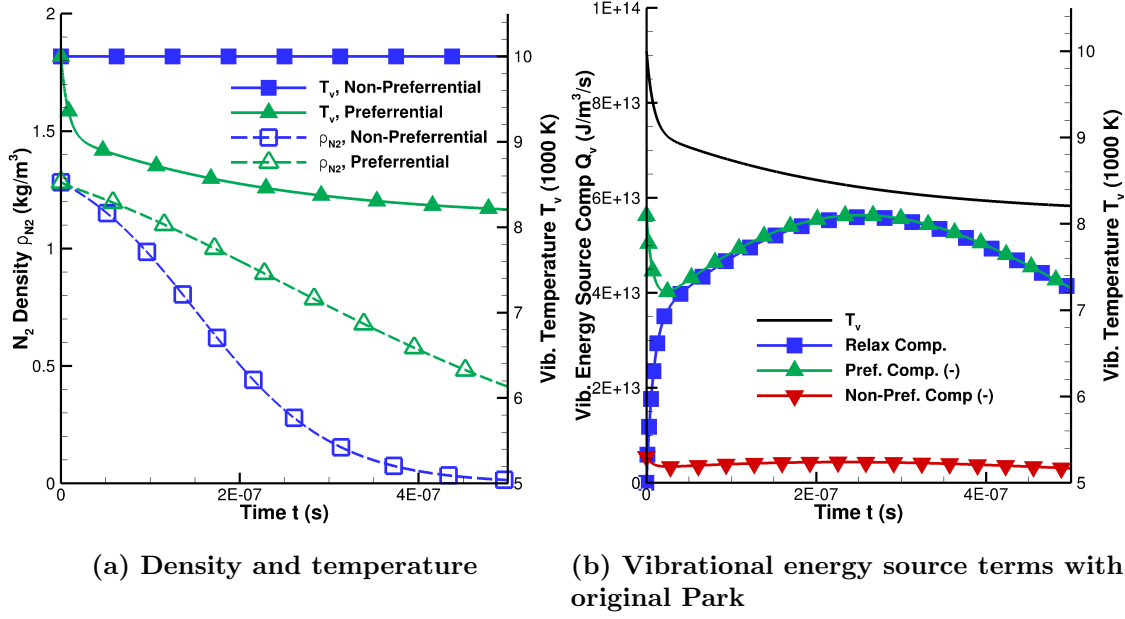


Figure 4.4: Effect of a preferential dissociation for change in vibrational energy, using Park's original model compared to standard Park

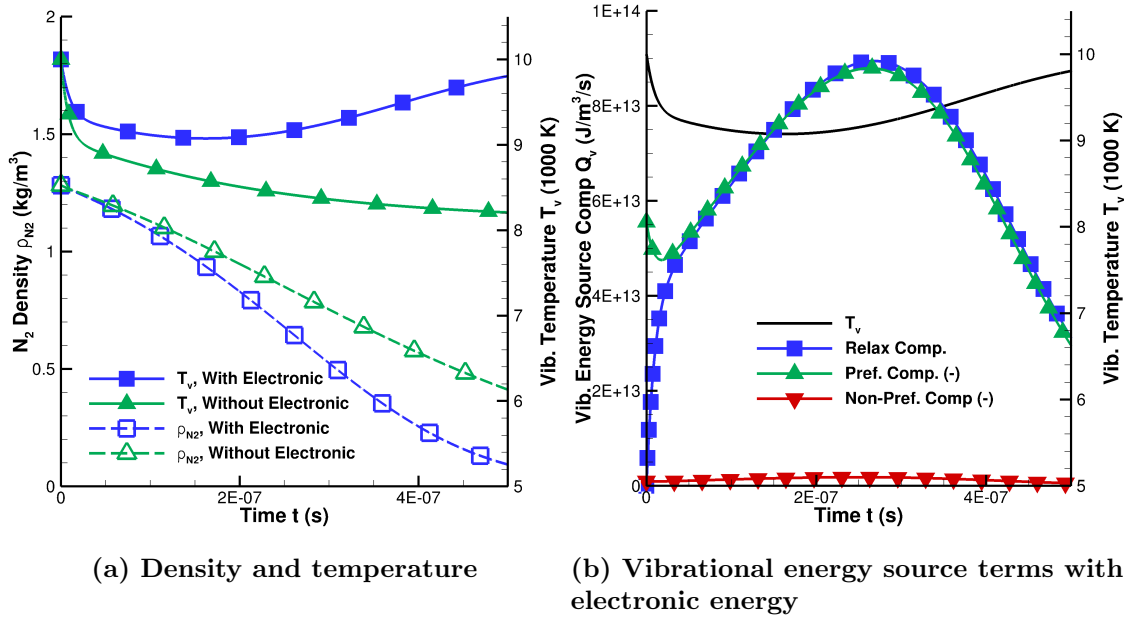


Figure 4.5: Effect of electronic energy, Park original model

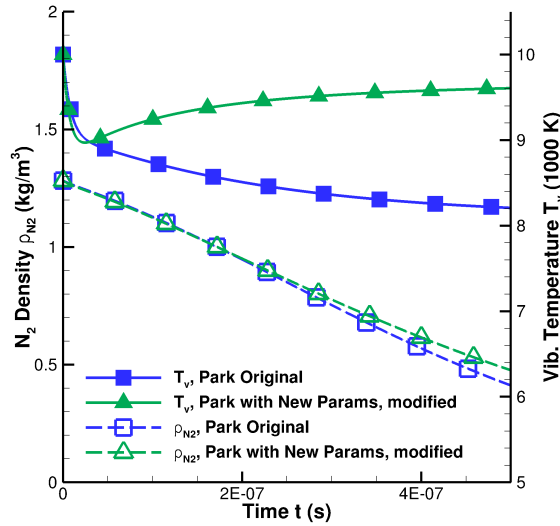
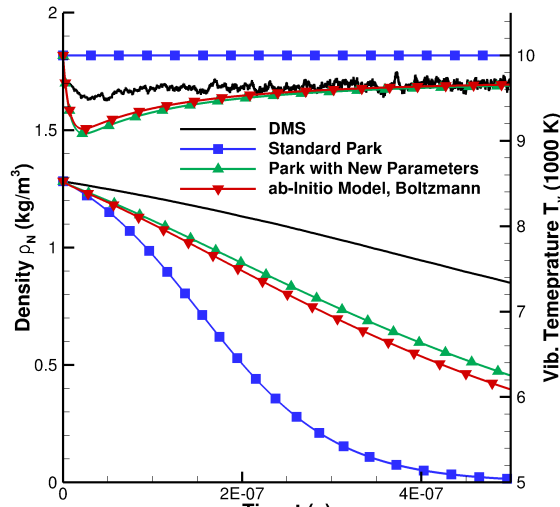


Figure 4.6: Park's original model compared to 'Park with new parameters' model modified to use Park's original decrease in vibrational energy due to dissociation.



(a) Main Models

Figure 4.7: Standard Park, Park with new parameters, and the *ab-initio* model with Boltzmann distributions.

The *ab-initio* model with Boltzmann distributions yields a similar result to the ‘Park with new parameters’ model. This result is expected: the model should reproduce Boltzmann fits if a Boltzmann is input. We believe that this approach, when modified to incorporate the non-Boltzmann distributions which exist during QSS [137], will be able to capture the depletion of vibrationally-excited molecules.

4.3 Other Conditions

4.3.1 Adiabatic Single-Cell

In this Section, we examine cases run in an adiabatic manner, rather than isothermal. All other modifications for consistency with DMS (see Section 4.1.5) are used: single-cell constant volume, electronically-excluded internal energy, and recombination off.

Two effects are examined: initial condition and change in vibrational energy due to dissociation. We choose two initial conditions, which define $T_{\text{tr},0}$ and $T_{\text{v},0}$ in this case. The first initial condition has $T_{\text{tr},0} = T_{\text{v},0}$, with the temperatures set such that the initial total enthalpy is $h_{t,0} = 20 \text{ MJ/kg}$. The second initial condition has $T_{\text{v},0} = 300 \text{ K}$, with T_{tr} set to yield the same total energy density as the first case. We are therefore able to examine the effect of starting in thermal equilibrium or nonequilibrium, but the final state is similar. Total energy is set equal because it is the conserved quantity for this constant volume reactor. The gas is initially all N₂ with a density of 1.2824 kg/m³, as in the previous Section. The initial conditions for the adiabatic runs are shown in Table 4.1.

Table 4.1: Initial conditions for adiabatic simulations

	$T_{\text{v},0} = T_{\text{tr},0}$	$T_{\text{v}} = 300 \text{ K}$
N ₂ Density ρ_{N_2} (kg/m ³)	1.2824	1.2824
Translational-Rotational Temperature $T_{\text{tr},0}$ (K)	14778 K	21043
Vibrational Temperature $T_{\text{v},0}$ (K)	14778 K	300
Total enthalpy h_t (MJ/kg)	20.0	21.9
Total energy e (MJ/kg)	15.6	15.6

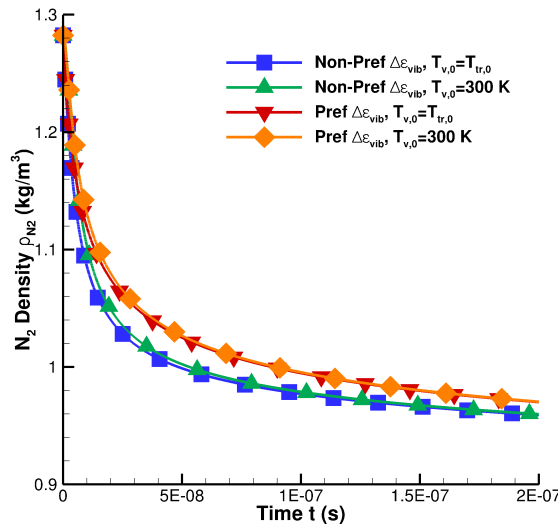
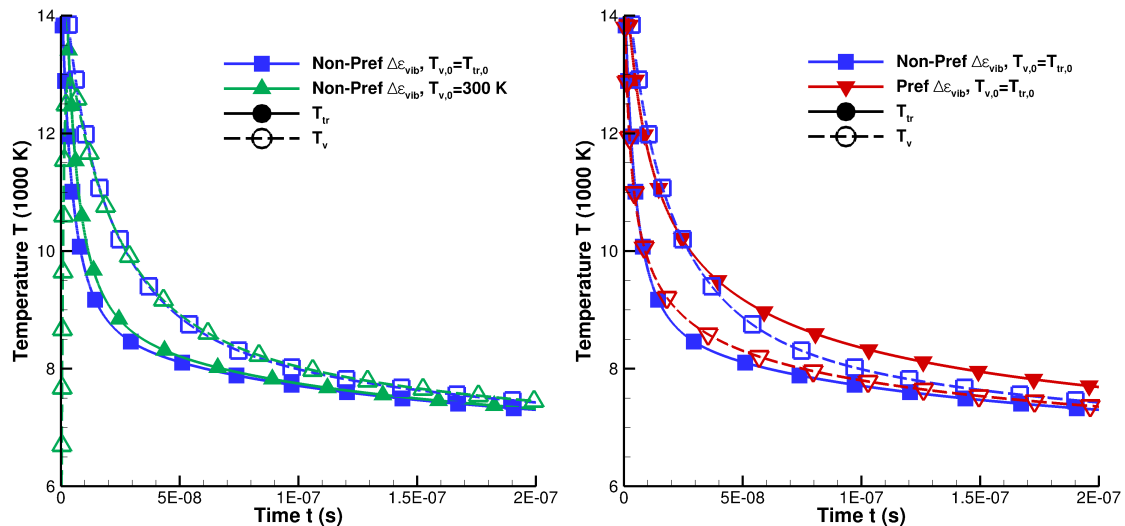
We also choose two slightly different chemical kinetics models to examine the effect of preferential vibrational energy change due to dissociation. Both models use standard Park reaction rates with relaxation times due to Millikan and White, as outlined in Section 4.1.2. For vibrational energy change due to dissociation, we use either nonpreferential or Park’s original preferential model. We therefore have four total simulations: each initial condition and each chemical kinetic model. These basic models allow us to explain the trends more easily, and therefore help understand the limitations of conclusions made using isothermal results. Results for the four simulations are shown in Figure 4.8 and are discussed herein.

Broadly speaking, the adiabatic results differ from the isothermal results in several ways. Obviously, all temperatures decrease substantially as the simulation progresses, as energy is expended to form N. This means that most dissociations occur relatively early, while the gas is hottest. In contrast, the isothermal reactors with the Park dissociation rates experience an acceleration in dissociation as N initially forms and provides a more efficient collision partner than N₂. Also, the net amount of destruction of N₂ is less; even an initial 20 MJ/kg is not enough to dissociate the majority of N₂. This is a reminder of the vast energy source provided by an isothermal reactor, and it is why we have chosen to focus on the initial dissociation period for the entire present work.

The initial condition does not have a substantial effect on the net dissociation rate or the temperature timetraces. As with the isothermal case, relaxation occurs relatively quickly compared to dissociation. Furthermore, the dissociation rate in an adiabatic system is self-stabilizing: less dissociation leaves more energy, resulting in more dissociation. This means that initial condition has even less of an effect in the adiabatic case than the isothermal case (shown previously in Figure 4.3).

The model for vibrational energy change due to dissociation has a moderate effect on the dissociation rate, and a strong effect on the temperature evolution. We explain why by looking first at the temperature profiles (Figure 4.8c). If the change in vibrational energy is nonpreferential, then dissociation causes no decrease in T_v and a large decrease in T_{tr}. In this case, T_{tr} decreases first, and T_v decreases only due to vibrational relaxation. T_{tr} remains below T_v for the entire simulation. In contrast, a preferential vibrational energy change due to dissociation causes a large decrease in T_v due to dissociation, and so energy relaxes into the vibrational mode. This difference is further demonstrated by examining the source terms for vibrational energy between these two cases, shown in Figure 4.9. (Note that the relaxation term is negative for the nonpreferential case.)

Although T_{tr} and T_v evolve differently in these two cases, their geometric mean $\sqrt{T_{tr}T_v}$ is not as different. Thus, the dissociation rate using Park's rates are only moderately different: approximately 10%. The specifics will obviously depend on the dissociation model, but the overall point is clear: the model for change in vibrational energy due to dissociation has a more pronounced effect on the overall dissociation rate in the case of an isothermal reactor, compared to an adiabatic reactor.

(a) N_2 density

(b) Temperature, effect of initial condition (c) Temperature, effect of energy change due to dissociation

Figure 4.8: Adiabatic results

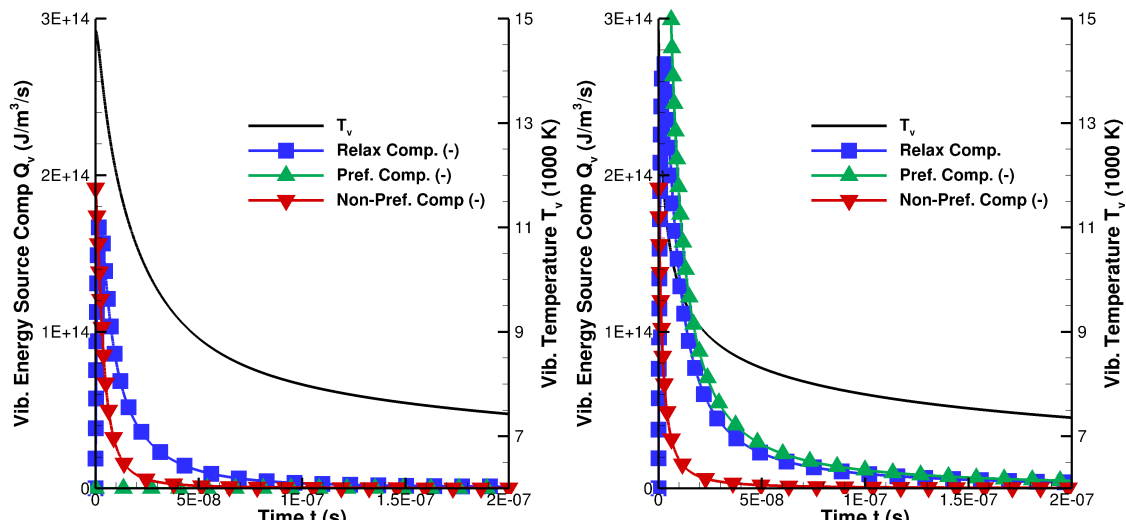


Figure 4.9: Vibrational energy source term for adiabatic simulations, $T_{v,0} = T_{\text{tr},0}$

Chapter 5

Conclusions

A database of quasiclassical trajectories for air species reactions is generated and systematically analyzed. The conditions and primary quantities of interest are chosen to focus on modeling chemical kinetics for CFD at hypersonic conditions. The work builds on that of Bender [25, 113], who studied $\text{N}_2 + \text{N}_2$ reactions and some $\text{N}_2 + \text{N}$ reactions [11]. $\text{N}_2 + \text{O}_2$, $\text{O}_2 + \text{O}_2$, and $\text{O}_2 + \text{O}$ interactions are added, for a total of 6 dissociation reactions: nitrogen dissociation with 3 collision partners and oxygen dissociation with 3 collision partners. Trajectories are sampled from Boltzmann or approximately-Boltzmann distributions characterized by two temperatures: T_{tr} and T_v . The two primary quantities of interest, the dissociation rate and average vibrational energy change per dissociation, are statistically converged to within 5 % relative error. The temperature range of interest is 8000 K to 30,000 K for nitrogen dissociation and 4000 K to 13,000 K for oxygen dissociation. For each reaction, an equilibrium test set and a nonequilibrium test set is considered. These initial conditions allow one to study the coupled vibration-dissociation process and compare to existing chemical kinetics models for CFD.

Nitrogen dissociation is considered first; for all partners, the results are described in the context of the 3 inputs required for a chemical kinetics model in CFD. The dissociation rate for nitrogen is found to be similar for all collision partner species studied, when conditions are sampled from the same thermal environment. The thermal environment will depend strongly on species, though, because atomic nitrogen promotes vibrational relaxation via exchange reactions. Thus, the current results are consistent with shock tube data that show nitrogen dissociates more readily in the presence of atomic nitrogen. Park's rates [18], however, were determined using Millikan and White's vibrational relaxation times, which do not correctly capture the effect of exchange in $\text{N}_2 + \text{N}$. The role that atomic nitrogen plays in promoting nitrogen dissociation, therefore, is incorrectly modeled by using different reaction rate constants for collision partners N_2 and N .

In addition to reaction rates and vibrational relaxation times, a two-temperature chem-

ical kinetics model also requires the vibrational energy change due to reaction. This is a model for the mechanism by which chemical reactions affect the thermodynamic state. For the equilibrium test set, the majority of dissociation energy comes from vibration at all conditions. As the equilibrium temperature decreases, even more energy comes from vibration: more than 75% for all nitrogen dissociation reactions below 10,000 K. When conditions are sampled from low-vibrational-energy conditions, most of the energy comes from rotation instead. At $T_{\text{tr}} = 20000$ K, $T_v = 8000$ K, less than 15% of the nitrogen dissociation energy comes from vibration, again for all collision partners studied. The stark difference between behavior at equilibrium and nonequilibrium is not captured by current models in CFD.

Interactions of electronically ground-state $\text{O}_2 + \text{O}_2$ may occur on one of three degenerate states, and $\text{O}_2 + \text{O}$ interactions may occur on one of nine. PESs are available for each state [66–68], and QCT calculations are performed for each one, at all conditions considered. The interaction state is found to have a moderate effect on the dissociation rate: in $\text{O}_2 + \text{O}_2$ the triplet surface is about 60 % more reactive than the other surfaces and in $\text{O}_2 + \text{O}$ the surfaces varied meaningfully only when conditions were sampled from thermal nonequilibrium. In contrast, mechanisms of vibrational relaxation in $\text{O}_2 + \text{O}$ are found to be extremely dependent on the interaction state, due to three competing mechanisms. The exchange rate is found to vary by up to 4 orders of magnitude between surfaces, and the exchange rate is negatively correlated to the average vibrational energy change per exchange, because the energy barrier for exchange depends on the interaction state. Additionally, the energy change per no-reaction event depends on the interaction state. The $1^1\text{A}'$ surface, which admits ozone and has been the focus of past analyses [74, 80, 122–124], is found to be particularly unique because it corresponds to ozone. Based on these results, and the results of the complementary DMS [78, 79], considering all interaction states for $\text{O}_2 + \text{O}$ is found to be critical.

Results for oxygen dissociation with collision partners O_2 , O , and N_2 are compared with previous results and the available data in the literature. In general, the character of molecules that dissociate is found to be similar for all dissociation reactions; vibrationally-excited molecules dissociate from thermal equilibrium, and when T_v is suppressed rotation compensates for vibration. The dissociation rate of oxygen with collision partner N_2 is found to be much lower than predicted by the popular Park [18] model. The present result agrees reasonably well with the limited data available in the literature; the Park rate is too high based on the experimental data also. A specific rate is not suggested, however, because the present work does not account for the non-Boltzmann distributions of internal energy that exist in a real gas as it dissociates. Nevertheless, the result is clear that the Park rate for N_2 partner should be lower.

A variety of analyses are also performed on the QCT database as a whole, with par-

ticular focus on aggregating multiple reactions together and finding common elements in the dissociation process. The support factor, S , is defined to quantify the effect that each reactive state has on dissociation, for a number of reactions or conditions. In simple dissociation events, which account for the majority of dissociations for all conditions and reactions considered, the collision partner's internal energy has only a small effect on dissociation, and may be neglected for the purposes of modeling. Vibrational energy is found to have a larger effect on dissociation than rotational energy, and this effect is demonstrated to be due to the centrifugal barrier. Therefore, vibrational energy does indeed behave differently than rotational energy, and it should continue to be treated separately from other components (translation and rotation) in chemical kinetics models for CFD. We note that this does not preclude rotational energy also being treated separately.

Quantities of interest from the database are also fit to various chemical kinetics models in the literature, for the purposes of drawing conclusions about the dominant behaviors in the data. This is *not* designed to be used directly in CFD, because the present QCT data do not include the effect of non-Boltzmann distributions of energy. The classic Marrone and Treanor preferential dissociation model [1] is found to fit all data in the nonequilibrium test sets well, with a maximum relative error of approximately 20 % for all cases. However, the Marrone-Treanor model does not accurately predict the change in vibrational energy per dissociation when conditions are sampled from thermal equilibrium. This mismatch is found to be due to their neglect of rotational energy, and a modification is proposed that matches all data in the QCT database to within 22 %. The vast majority of conditions and reactions are described to within 5 %. The two parameters in this modified form may be fit using only the data in the equilibrium test set, but it has predictive capability for the nonequilibrium test set also. This indicates that the dominant physical mechanisms are being correctly captured, instead of simply providing sufficient degrees of freedom to match the data. These findings should help inform future models based on *ab-initio* data that incorporate the effect of non-Boltzmann distributions of internal energy.

Finally, several chemical kinetics models were implemented into a production CFD code designed for hypersonic applications. At this stage, the focus is on understanding the effect of each component of a chemical kinetics model, especially in the context of what has been learned from the QCT results. Implementations of the Park [18] model in current CFD use a nonpreferential vibrational energy change per dissociation, which means that dissociation does not directly reduce the vibrational temperature. This result is inconsistent with the observed behavior of a dissociating gas ensemble, and correcting this component of the model is found to have a large effect on the CFD results. In order to validate a new CFD model, a self-consistent comparison between CFD and DMS is required; several steps are taken to achieve this goal. CFD and DMS results are compared using a chemical kinetics

model based on Boltzmann distributions, and the dissociation rate from CFD is found to be too fast. This is an expected result: the vibrational energy distribution of a dissociating gas has a depleted tail, which results in a lower-than-Boltzmann dissociation rate. In order to capture this effect in CFD, a new chemical kinetics model based on non-Boltzmann distributions is necessary. The QCT database, the accurate fits to Boltzmann data we present, and the insight gained about the dissociation process itself should form the basis of these next-generation models.

Bibliography

- [1] Marrone, P. V., and Treanor, C. E., “Chemical Relaxation with Preferential Dissociation from Excited Vibrational Levels,” *The Physics of Fluids*, Vol. 6, No. 9, 1963, pp. 1215–1221. doi:10.1063/1.1706888.
- [2] Gnoffo, P. A., “Planetary-Entry Gas Dynamics,” *Annual Review of Fluid Mechanics*, Vol. 31, No. 1, 1999, pp. 459–494. doi:10.1146/annurev.fluid.31.1.459.
- [3] Candler, G. V., “Rate Effects in Hypersonic Flows,” *Annual Review of Fluid Mechanics*, Vol. 51, No. 1, 2019, p. null. doi:10.1146/annurev-fluid-010518-040258.
- [4] Poovathingal, S., Schwartzentruber, T. E., Murray, V. J., Minton, T. K., and Candler, G. V., “Finite-Rate Oxidation Model for Carbon Surfaces from Molecular Beam Experiments,” *AIAA Journal*, Vol. 55, No. 5, 2017, pp. 1644–1658. doi:10.2514/1.J055371.
- [5] Wray, K. L., “Shock-Tube Study of the Coupling of the O₂-Ar Rates of Dissociation and Vibrational Relaxation,” *The Journal of Chemical Physics*, Vol. 37, No. 6, 1962, pp. 1254–1263. doi:10.1063/1.1733273.
- [6] Park, C., “Problems of Rate Chemistry in the Flight Regimes of Aeroassisted Orbital Transfer Vehicles,” *Thermal Design of Aeroassisted Orbital Transfer Vehicles*, Progress in Astronautics and Aeronautics, Vol. 96, edited by H. F. Nelson, AIAA, New York, 1985, pp. 511–537. doi:10.2514/5.9781600865718.0511.0537.
- [7] Hammerling, P., Teare, J. D., and Kivel, B., “Theory of Radiation from Luminous Shock Waves in Nitrogen,” *The Physics of Fluids*, Vol. 2, No. 4, 1959, pp. 422–426. doi:10.1063/1.1724413.
- [8] Treanor, C. E., and Marrone, P. V., “Effect of Dissociation on the Rate of Vibrational Relaxation,” *The Physics of Fluids*, Vol. 5, No. 9, 1962, pp. 1022–1026. doi:10.1063/1.1724467.
- [9] Park, C., “Assessment of a Two-Temperature Kinetic Model for Dissociating and Weakly Ionizing Nitrogen,” *Journal of Thermophysics and Heat Transfer*, Vol. 2, No. 1, 1988, pp. 8–16. doi:10.2514/3.55.
- [10] Valentini, P., Schwartzentruber, T. E., Bender, J. D., Nompelis, I., and Candler, G. V., “Direct Molecular Simulation of Nitrogen Dissociation Based on an *ab initio*

- Potential Energy Surface," *Physics of Fluids*, Vol. 27, No. 8, 2015, p. 086102. doi: 10.1063/1.4929394.
- [11] Valentini, P., Schwartzenruber, T. E., Bender, J. D., and Candler, G. V., "Dynamics of Nitrogen Dissociation from Direct Molecular Simulation," *Physical Review Fluids*, Vol. 1, No. 4, 2016, p. 043402. doi:10.1103/PhysRevFluids.1.043402.
- [12] Matthews, D. L., "Interferometric Measurement in the Shock Tube of the Dissociation Rate of Oxygen," *The Physics of Fluids*, Vol. 2, No. 2, 1959, pp. 170–178. doi: 10.1063/1.1705908.
- [13] Byron, S. R., "Measurement of the Rate of Dissociation of Oxygen," *The Journal of Chemical Physics*, Vol. 30, No. 6, 1959, pp. 1380–1392. doi:10.1063/1.1730209.
- [14] Rink, J. P., Knight, H. T., and Duff, R. E., "Shock Tube Determination of Dissociation Rates of Oxygen," *The Journal of Chemical Physics*, Vol. 34, No. 6, 1961, pp. 1942–1947. doi:10.1063/1.1731797.
- [15] Jerig, L., Thielen, K., and Roth, P., "High-Temperature Dissociation of Oxygen Diluted in Argon or Nitrogen," *AIAA Journal*, Vol. 29, No. 7, 1991, pp. 1136–1139. doi:10.2514/3.10714.
- [16] Park, C., "Two-Temperature Interpretation of Dissociation Rate Data for N₂ and O₂," *26th Aerospace Sciences Meeting*, AIAA Paper 1988-458, 1988. doi:10.2514/6.1988-458.
- [17] Park, C., "Assessment of Two-Temperature Kinetic Model for Ionizing Air," *Journal of Thermophysics and Heat Transfer*, Vol. 3, No. 3, 1989, pp. 233–244. doi:10.2514/3.28771.
- [18] Park, C., *Nonequilibrium Hypersonic Aerothermodynamics*, John Wiley & Sons, Inc., New York, 1990.
- [19] Park, C., "Review of Chemical-Kinetic Problems of Future NASA Missions, I: Earth Entries," *Journal of Thermophysics and Heat Transfer*, Vol. 7, No. 3, 1993, pp. 385–398. doi:10.2514/3.431.
- [20] Park, C., Howe, J. T., Jaffe, R. L., and Candler, G. V., "Review of Chemical-Kinetic Problems of Future NASA Missions, II: Mars Entries," *Journal of Thermophysics and Heat Transfer*, Vol. 8, No. 1, 1994, pp. 9–23. doi:10.2514/3.496.
- [21] Candler, G. V., Johnson, H. B., Nompelis, I., Subbareddy, P. K., Drayna, T. W., Gidzak, V., and Barnhardt, M. D., "Development of the US3D Code for Advanced Compressible and Reacting Flow Simulations," *53rd AIAA Aerospace Sciences Meeting*, AIAA Paper 2015-1893, 2015. doi:10.2514/6.2015-1893.
- [22] Wright, M. J., White, T., and Mangini, N., "Data Parallel Line Relaxation (DPLR) Code User Manual: Acadia - Version 4.01.1," Tech. Rep. TM-2009-215388, NASA, October 2009.

- [23] Mazaheri, A., Gnoffo, P. A., Johnston, C. O., and Kleb, W. L., "LAURA Users Manual: 5.5-65135," Tech. Rep. TM-2013-217800, NASA, February 2013.
- [24] Truhlar, D. G., and Muckerman, J. T., "Reactive Scattering Cross Sections III: Quasiclassical and Semiclassical Methods," *Atom-Molecule Collision Theory: A Guide for the Experimentalist*, edited by R. B. Bernstein, Plenum Press, New York, 1979, Chap. 16, pp. 505 – 566.
- [25] Bender, J. D., Valentini, P., Nompelis, I., Paukku, Y., Varga, Z., Truhlar, D. G., Schwartzentruber, T., and Candler, G. V., "An Improved Potential Energy Surface and Multi-Temperature Quasiclassical Trajectory Calculations of $N_2 + N_2$ Dissociation Reactions," *The Journal of Chemical Physics*, Vol. 143, No. 5, 2015, p. 054304. doi:10.1063/1.4927571.
- [26] Richard L. Jaffe, M. P., David W. Schwenke, "First Principles Calculation of Heavy Particle Rate Coefficients," *Hypersonic Nonequilibrium Flows: Fundamentals and Recent Advances*, Vol. 247, edited by E. Josyula, Progress in Aerospace Sciences, AIAA, New York, 2015, pp. 103–158. doi:10.2514/5.9781624103292.0103.0158.
- [27] Schwartzentruber, T. E., Grover, M. S., and Valentini, P., "Direct Molecular Simulation of Nonequilibrium Dilute Gases," *Journal of Thermophysics and Heat Transfer*, Vol. 32, No. 4, 2017, pp. 892–903. doi:10.2514/1.T5188.
- [28] Chaudhry, R. S., Bender, J. D., Schwartzentruber, T. E., and Candler, G. V., "Quasiclassical Trajectory Analysis of Nitrogen for High-Temperature Chemical Kinetics," *Journal of Thermophysics and Heat Transfer*, Vol. 32, No. 4, 2018, pp. 833–845. doi:10.2514/1.T5484.
- [29] Chaudhry, R. S., Bender, J. D., Schwartzentruber, T. E., and Candler, G. V., "Quasiclassical Trajectory Analysis of N_2+O_2 and Implications for Hypersonic CFD," *47th AIAA Thermophysics Conference*, AIAA Paper 2017-3167, 2017. doi:10.2514/6.2017-3167.
- [30] Chaudhry, R. S., Grover, M. S., Bender, J. D., Schwartzentruber, T. E., and Candler, G. V., "Quasiclassical Trajectory Analysis of Oxygen Dissociation via O_2 , O, and N_2 ," *2018 AIAA Aerospace Sciences Meeting*, AIAA Paper 2018-0237, 2018. doi:10.2514/6.2018-0237.
- [31] Chaudhry, R. S., Bender, J. D., Valentini, P., Schwartzentruber, T. E., and Candler, G. V., "Analysis of Dissociation and Internal Energy Transfer in High-Energy N_2+O_2 Collisions using the Quasiclassical Trajectory Method," *46th AIAA Thermophysics Conference*, AIAA Paper 2016-4319, 2016. doi:10.2514/6.2016-4319.
- [32] Chaudhry, R. S., Singh, N., Grover, M. S., Schwartzentruber, T. E., and Candler, G. V., "Implementation of a Nitrogen Chemical Kinetics Model Based on ab-Initio Data for Hypersonic CFD," *2018 Joint Thermophysics and Heat Transfer Conference*, AIAA Paper 2018-3439, 2018. doi:10.2514/6.2018-3439.

- [33] Chaudhry, R. S., and Candler, G. V., "Statistical Analyses of Quasiclassical Trajectory Data for Air Dissociation," *2019 AIAA Aerospace Sciences Meeting*, AIAA Paper, 2019.
- [34] Eckerman, J., "The Measurement of the Rate of Dissociation of Oxygen at High Temperature," Ph.D. thesis, The Catholic University of America, Washington, DC, 1958.
- [35] Boyd, I. D., and Schwartzentruber, T. E., *Nonequilibrium Gas Dynamics and Molecular Simulation*, Cambridge Aerospace Series, Vol. 42, Cambridge University Press, Cambridge, UK, 2017.
- [36] Ibragimova, L. B., Sergievskaya, A. L., Levashov, V. Y., Shatalov, O. P., Tunik, Y. V., and Zabelinskii, I. E., "Investigation of Oxygen Dissociation and Vibrational Relaxation at Temperatures 4000–10800 K," *The Journal of Chemical Physics*, Vol. 139, No. 3, 2013, p. 034317. doi:10.1063/1.4813070.
- [37] Camac, M., and Vaughan, A., "O₂ Dissociation Rates in O₂-Ar Mixtures," *The Journal of Chemical Physics*, Vol. 34, No. 2, 1961, pp. 460–470. doi:10.1063/1.4757209.
- [38] Schexnayder, C. J., Jr., and Evans, J. S., "Measurements of the Dissociation Rate of Molecular Oxygen," Tech. Rep. TR R-108, NASA, 1961.
- [39] Generalov, N. A., and Losev, S. A., "Vibration, Excitation, and Molecular Dissociation of Gaseous Oxygen and Carbon Dioxide in a Shock Wave," *Journal of Quantitative Spectroscopy and Radiative Transfer*, Vol. 6, No. 1, 1966, pp. 101–125. doi: 10.1016/0022-4073(66)90066-5.
- [40] Johnston, H. S., "Gas Phase Reaction Kinetics of Neutral Oxygen Species," Tech. Rep. 20, National Standard Reference Data Series – National Bureau of Standards, September 1968.
- [41] Byron, S. R., "Interferometric Measurement of the Rate of Dissociation of Oxygen Heated by Strong Shock Waves," Ph.D. thesis, Cornell University, New York, February 1959.
- [42] Shatalov, O. P., "Molecular Dissociation of Oxygen in the Absence of Vibrational Equilibrium," *Combustion, Explosion and Shock Waves*, Vol. 9, No. 5, 1973, pp. 610–613. doi:10.1007/BF00742888.
- [43] Bortner, M. H., "A Review of Rate Constants of Selected Reactions of Interest in Re-Entry Flow Fields in the Atmosphere," Tech. Rep. NBTNA-484, National Bureau of Standards, May 1969.
- [44] Wray, K. L., "Chemical Kinetics of High Temperature Air," *Hypersonic Flow Research*, edited by F. R. Riddell, AIAA, New York, 1962, pp. 181–204. doi: 10.2514/5.9781600864810.0181.0204.
- [45] Ibragimova, L. B., Smekhov, G. D., and Shatalov, O. P., "Dissociation Rate Constants of Diatomic Molecules under Thermal Equilibrium Conditions," *Fluid Dynamics*, Vol. 34, No. 1, 1999, pp. 153 – 157. doi:10.1007/BF02698767.

- [46] Cary, B., "Shock-Tube Study of the Termal Dissociation of Nitrogen," *The Physics of Fluids*, Vol. 8, No. 1, 1965, pp. 26–35. doi:10.1063/1.1761099.
- [47] Byron, S., "Shock-Tube Measurement of the Rate of Dissociation of Nitrogen," *The Journal of Chemical Physics*, Vol. 44, No. 4, 1966, pp. 1378–1388. doi:10.1063/1.1726870.
- [48] Appleton, J. P., Steinberg, M., and Liquornik, D. J., "Shock-Tube Study of Nitrogen Dissociation using Vacuum-Ultraviolet Light Absorption," *The Journal of Chemical Physics*, Vol. 48, No. 2, 1968, pp. 599–608. doi:10.1063/1.1668690.
- [49] Hanson, R. K., and Baganoff, D., "Shock-Tube Study of Nitrogen Dissociation Rates Using Pressure Measurements," *AIAA Journal*, Vol. 10, No. 2, 1972, pp. 211–215. doi:10.2514/3.50082.
- [50] Roth, P., and Thielen, K., "Measurements of N Atom Concentrations in Dissociation of N₂ by Shock Waves," *Shock Waves and Shock Tubes: Proceedings of the 15th International Symposium on Shock Waves and Shock Tubes, 1985*, edited by D. Bershader and R. Hanson, Stanford University Press, 1986, pp. 245–252.
- [51] Owen, K. G., Davidson, D. F., and Hanson, R. K., "Measurements of Oxygen Dissociation Using Laser Absorption," *Journal of Thermophysics and Heat Transfer*, Vol. 30, No. 2, 2016, pp. 274–278. doi:10.2514/1.T4506.
- [52] "JANAF Thermochemical Data," The Dow Chemical Co., Midland, Michigan, 1961.
- [53] Blackman, V., "Vibrational Relaxation in Oxygen and Nitrogen," *Journal of Fluid Mechanics*, Vol. 1, No. 1, 1956, pp. 61 – 85. doi:10.1017/S0022112056000056.
- [54] Millikan, R. C., and White, D. R., "Systematics of Vibrational Relaxation," *The Journal of Chemical Physics*, Vol. 39, No. 12, 1963, pp. 3209–3213. doi:10.1063/1.1734182.
- [55] Sharma, S. P., Huo, W. M., and Park, C., "Rate Parameters for Coupled Vibration-Dissociation in a Generalized SSH Approximation," *Journal of Thermophysics and Heat Transfer*, Vol. 6, No. 1, 1992, pp. 9–21. doi:10.2514/3.312.
- [56] Jaffe, R. L., "Rate Constants for Chemical Reactions in High-Temperature Nonequilibrium Air," *Thermophysical Aspects of Re-Entry Flows*, Vol. 103, edited by J. N. Moss and C. D. Scott, Progress in Aerospace Sciences, AIAA, New York, 1986, pp. 123–151. doi:10.2514/5.9781600865770.0123.0151.
- [57] Olynick, D. P., and Hassan, H. A., "New Two-Temperature Dissociation Model for Reacting Flows," *Journal of Thermophysics and Heat Transfer*, Vol. 7, No. 4, 1993, pp. 687–696. doi:10.2514/3.478.
- [58] Knab, O., Fruehauf, H. H., and Messerschmid, E. W., "Theory and Validation of the Physically Consistent Coupled Vibration-Chemistry-Vibration Model," *Journal of Thermophysics and Heat Transfer*, Vol. 9, No. 2, 1995, pp. 219–226. doi:10.2514/3.649.

- [59] Macheret, S. O., and Rich, J. W., “Nonequilibrium Dissociation Rates Behind Strong Shock Waves: Classical Model,” *Chemical Physics*, Vol. 174, No. 1, 1993, pp. 25–43. doi:10.1016/0301-0104(93)80049-F.
- [60] Luo, H., Alexeenko, A. A., and Macheret, S. O., “Assessment of Classical Impulsive Models of Dissociation in Thermochemical Nonequilibrium,” *Journal of Thermophysics and Heat Transfer*, Vol. 32, No. 4, 2018, pp. 861–868. doi:10.2514/1.T5375.
- [61] Macheret, S. O., and Adamovich, I. V., “Semiclassical Modeling of State-Specific Dissociation Rates in Diatomic Gases,” *The Journal of Chemical Physics*, Vol. 113, No. 17, 2000, pp. 7351–7361. doi:10.1063/1.1313386.
- [62] Bender, J. D., Doraiswamy, S., Truhlar, D. G., and Candler, G. V., “Potential Energy Surface Fitting by a Statistically Localized, Permutationally Invariant, Local Interpolating Moving Least Squares Method for the Many-Body Potential: Method and Application to N₄,” *The Journal of Chemical Physics*, Vol. 140, No. 5, 2014, p. 054302. doi:10.1063/1.4862157.
- [63] Paukku, Y., Yang, K. R., Varga, Z., and Truhlar, D. G., “Global *ab initio* Ground-State Potential Energy Surface of N₄,” *The Journal of Chemical Physics*, Vol. 139, No. 4, 2013, p. 044309. doi:10.1063/1.4811653.
- [64] Paukku, Y., Yang, K. R., Varga, Z., and Truhlar, D. G., “Erratum: ‘Global *ab initio* Ground-State Potential Energy Surface of N₄’ [J. Chem. Phys. 139, 044309 (2013)],” *The Journal of Chemical Physics*, Vol. 140, No. 1, 2014, p. 019903. doi:10.1063/1.4861562.
- [65] Varga, Z., Meana-Pañeda, R., Song, G., Paukku, Y., and Truhlar, D. G., “Potential Energy Surface of Triplet N₂O₂,” *The Journal of Chemical Physics*, Vol. 144, No. 2, 2016, p. 024310. doi:10.1063/1.4939008.
- [66] Paukku, Y., Yang, K. R., Varga, Z., Song, G., Bender, J. D., and Truhlar, D. G., “Potential Energy Surfaces of Quintet and Singlet O₄,” *The Journal of Chemical Physics*, Vol. 147, No. 3, 2017, p. 034301. doi:10.1063/1.4993624.
- [67] Paukku, Y., Varga, Z., and Truhlar, D. G., “Potential Energy Surface of Triplet O₄,” *The Journal of Chemical Physics*, Vol. 148, No. 12, 2018, p. 124314. doi:10.1063/1.5017489.
- [68] Varga, Z., Paukku, Y., and Truhlar, D. G., “Potential Energy Surfaces for O + O₂ Collisions,” *The Journal of Chemical Physics*, Vol. 147, No. 15, 2017, p. 154312. doi:10.1063/1.4997169.
- [69] Duchovic, R. J., Volobuev, Y. L., Lynch, G. C., Truhlar, D. G., Allison, T. C., Wagner, A. F., Garrett, B. C., and Corchado, J. C., “POTLIB 2001: A Potential Energy Surface Library for Chemical Systems,” *Computer Physics Communications*, Vol. 144, No. 2, 2002, pp. 169–187. doi:10.1016/S0010-4655(01)00437-4, URL <http://comp.chem.umn.edu/potlib>.

- [70] Duchovic, R. J., Volobuev, Y. L., Lynch, G. C., Truhlar, D. G., Allison, T. C., Wagner, A. F., Garrett, B. C., and Corchado, J. C., “A Correction to the POTLIB Library described in “POTLIB 2001: A Potential Energy Surface Library for Chemical Systems”: [Comput. Phys. Comm. 144 (2002) 169-187],” *Computer Physics Communications*, Vol. 156, No. 3, 2004, pp. 319–322. doi:10.1016/S0010-4655(03)00434-X.
- [71] Andersson, K., Malmqvist, P.-Å., and Roos, B. O., “Second-Order Perturbation Theory with a Complete Active Space Self-Consistent Field Reference Function,” *The Journal of Chemical Physics*, Vol. 96, No. 2, 1992, pp. 1218–1226. doi:10.1063/1.462209.
- [72] Werner, H.-J., “Third-Order Multireference Perturbation Theory The CASPT3 Method,” *Molecular Physics*, Vol. 89, No. 2, 1996, pp. 645–661. doi:10.1080/002689796173967.
- [73] Nikitin, E., *Theory of Elementary Atomic and Molecular Processes in Gases*, Clarendon Press, Oxford, 1974.
- [74] Andrienko, D. A., and Boyd, I. D., “Rovibrational Energy Transfer and Dissociation in O₂-O Collisions,” *The Journal of Chemical Physics*, Vol. 144, No. 10, 2016, p. 104301. doi:10.1063/1.4943114.
- [75] Grover, M. S., “Direct Molecular Simulation of Nitrogen and Oxygen at Hypersonic Conditions,” Ph.D. thesis, University of Minnesota, Minneapolis, MN, February 2018.
- [76] Lin, W., Varga, Z., Song, G., Paukku, Y., and Truhlar, D. G., “Global Triplet Potential Energy Surfaces for the N₂(X¹Σ) + O(³P) → NO(X²Π) + N(⁴S) Reaction,” *The Journal of Chemical Physics*, Vol. 144, No. 2, 2016, p. 024309. doi:10.1063/1.4938241.
- [77] “NIST Computational Chemistry Comparison and Benchmark Database,” Tech. Rep. Standard Reference Database 101, NIST, April 2018. URL <http://cccbdb.nist.gov>.
- [78] Grover, M. S., Schwartzentruber, T. E., Varga, Z., and Truhlar, D. G., “Dynamics of Vibrational Energy Excitation and Dissociation in Oxygen from Direct Molecular Simulation,” *2018 AIAA Aerospace Sciences Meeting*, AIAA Paper 2018-0238, 2018. doi:10.2514/6.2018-0238.
- [79] Grover, M. S., Schwartzentruber, T. E., Varga, Z., and Truhlar, D. G., “Vibrational Energy Transfer and Collision Induced Dissociation in O + O₂ Collisions,” (Submitted for publication).
- [80] Varandas, A., and Pais, A., “A Realistic Double Many-Body Expansion (DMBE) Potential Energy Surface for Ground-State O₃ from a Multiproperty Fit to ab initio Calculations, and to Experimental Spectroscopic, Inelastic Scattering, and Kinetic Isotope Thermal Rate Data,” *Molecular Physics*, Vol. 65, No. 4, 1988, pp. 843–860. doi:10.1080/00268978800101451.
- [81] Varandas, A., and Pais, A., “Double Many-Body Expansion Potential Energy Surface for O₄(³A), Dynamics of the O(³P) + O₃(¹A₁) Reaction, and Second Virial Coefficients of Molecular Oxygen,” *Theoretical and Computational Models for Organic*

- Chemistry*, edited by S. J. Formosinho, I. G. Csizmadia, and L. G. Arnaut, Springer Netherlands, Dordrecht, 1991, pp. 55–78. doi:10.1007/978-94-011-3584-9_4.
- [82] Chaban, G., Jaffe, R., Schwenke, D., and Huo, W., “Dissociation Cross Sections and Rate Coefficients for Nitrogen from Accurate Theoretical Calculations,” *46th AIAA Aerospace Sciences Meeting and Exhibit*, AIAA Paper 2008-1209, 2008. doi:10.2514/6.2008-1209.
- [83] Jaffe, R., Schwenke, D., and Chaban, G., “Theoretical Analysis of N₂ Collisional Dissociation and Rotation–Vibration Energy Transfer,” *47th AIAA Aerospace Sciences Meeting including The New Horizons Forum and Aerospace Exposition*, AIAA Paper 2009-1569, 2009. doi:10.2514/6.2009-1569.
- [84] Panesi, M., Jaffe, R. L., Schwenke, D. W., and Magin, T. E., “Rovibrational Internal Energy Transfer and Dissociation of N₂(¹Σ_g⁺) – N(⁴S_u) System in Hypersonic Flows,” *The Journal of Chemical Physics*, Vol. 138, No. 4, 2013, p. 044312. doi:10.1063/1.4774412.
- [85] Kim, J. G., and Boyd, I. D., “State-Resolved Master Equation Analysis of Thermochemical Nonequilibrium of Nitrogen,” *Chemical Physics*, Vol. 415, 2013, pp. 237–246. doi:10.1016/j.chemphys.2013.01.027.
- [86] Panesi, M., Munafò, A., Magin, T. E., and Jaffe, R. L., “Nonequilibrium Shock-Heated Nitrogen Flows Using a Rovibrational State-to-State Method,” *Physical Review E*, Vol. 90, No. 1, 2014, p. 013009. doi:10.1103/PhysRevE.90.013009.
- [87] Andrienko, D., and Boyd, I. D., “Investigation of Oxygen Vibrational Relaxation by Quasi-Classical Trajectory Method,” *Chemical Physics*, Vol. 459, 2015, pp. 1–13. doi:10.1016/j.chemphys.2015.07.023.
- [88] Andrienko, D. A., and Boyd, I. D., “High Fidelity Modeling of Thermal Relaxation and Dissociation of Oxygen,” *Physics of Fluids*, Vol. 27, No. 11, 2015, p. 116101. doi:10.1063/1.4935241.
- [89] Andrienko, D. A., and Boyd, I. D., “Master Equation Study of Vibrational and Rotational Relaxations of Oxygen,” *Journal of Thermophysics and Heat Transfer*, Vol. 30, No. 3, 2016, pp. 533–552. doi:10.2514/1.T4769.
- [90] Andrienko, D. A., and Boyd, I. D., “Kinetic Models of Oxygen Thermochemistry Based on Quasi-Classical Trajectory Analysis,” *Journal of Thermophysics and Heat Transfer*, Vol. 32, No. 4, 2018, pp. 904–916. doi:10.2514/1.T4968.
- [91] Macdonald, R. L., Jaffe, R. L., Schwenke, D. W., and Panesi, M., “Construction of a Coarse-Grain Quasi-Classical Trajectory Method. I. Theory and Application to N₂+N₂ System,” *The Journal of Chemical Physics*, Vol. 148, No. 5, 2018, p. 054309. doi:10.1063/1.5011331.
- [92] Andrienko, D. A., and Boyd, I. D., “State-Specific Dissociation in O₂-O₂ Collisions by Quasiclassical Trajectory Method,” *Chemical Physics*, Vol. 491, 2017, pp. 74 – 81. doi:10.1016/j.chemphys.2017.05.005.

- [93] Torres, E., and Magin, T. E., “Coupling of State-Resolved Rovibrational Coarse-Grain Model for Nitrogen to Stochastic Particle Method for Simulating Internal Energy Excitation and Dissociation,” *The Journal of Chemical Physics*, Vol. 149, No. 17, 2018, p. 174106. doi:10.1063/1.5030211.
- [94] Sahai, A., Lopez, B., Johnston, C. O., and Panesi, M., “Adaptive Coarse Graining Method for Energy Transfer and Dissociation Kinetics of Polyatomic Species,” *The Journal of Chemical Physics*, Vol. 147, No. 5, 2017, p. 054107. doi:10.1063/1.4996654.
- [95] Bose, D., and Candler, G. V., “Thermal Rate Constants of the $\text{N}_2 + \text{O} \rightarrow \text{NO} + \text{N}$ Reaction using *ab initio* $^3\text{A''}$ and $^3\text{A'}$ Potential Energy Surfaces,” *The Journal of Chemical Physics*, Vol. 104, No. 8, 1996, pp. 2825–2833. doi:10.1063/1.471106.
- [96] Bose, D., and Candler, G. V., “Kinetics of the $\text{N}_2 + \text{O} \rightarrow \text{NO} + \text{N}$ Reaction under Thermodynamic Nonequilibrium,” *Journal of Thermophysics and Heat Transfer*, Vol. 10, No. 1, 1996, pp. 148–154. doi:10.2514/3.765.
- [97] Bose, D., and Candler, G. V., “Thermal Rate Constants of the $\text{O}_2 + \text{N} \rightarrow \text{NO} + \text{O}$ Reaction Based on the $^2\text{A'}$ and $^4\text{A'}$ Potential-Energy Surfaces,” *The Journal of Chemical Physics*, Vol. 107, No. 16, 1997, pp. 6136–6145. doi:10.1063/1.475132.
- [98] Boyd, I. D., Candler, G. V., and Levin, D. A., “Dissociation Modeling in Low Density Hypersonic Flows of Air,” *Physics of Fluids*, Vol. 7, No. 7, 1995, pp. 1757–1763. doi:10.1063/1.868490.
- [99] Bose, D., and Candler, G. V., “Simulation of Hypersonic Flows using a Detailed Nitric Oxide Formation Model,” *Physics of Fluids*, Vol. 9, No. 4, 1997, pp. 1171–1181. doi:10.1063/1.869205.
- [100] Erdman, P. W., Zipf, E. C., Espy, P., Howlett, C., Levin, D. A., Loda, R., Collins, R. J., and Candler, G. V., “Flight Measurements of Low-Velocity Bow Shock Ultraviolet Radiation,” *Journal of Thermophysics and Heat Transfer*, Vol. 7, No. 1, 1993, pp. 37–41. doi:10.2514/3.11566.
- [101] Levin, D. A., Candler, G. V., Collins, R. J., Erdman, P. W., Zipf, E., Espy, P., and Howlett, C., “Comparison of Theory with Experiment for the Bow Shock Ultraviolet Rocket Flight,” *Journal of Thermophysics and Heat Transfer*, Vol. 7, No. 1, 1993, pp. 30–36. doi:10.2514/3.11565.
- [102] Levin, D. A., Candler, G. V., Collins, R. J., Erdman, P. W., Zipf, E. C., and Howlett, C. L., “Examination of Theory for Bow Shock Ultraviolet Rocket Experiments – I,” *Journal of Thermophysics and Heat Transfer*, Vol. 8, No. 3, 1994, pp. 447–452. doi:10.2514/3.563.
- [103] Levin, D. A., Braunstein, M., Candler, G. V., Collins, R. J., and Smith, G. P., “Examination of Theory for Bow Shock Ultraviolet Rocket Experiments – II,” *Journal of Thermophysics and Heat Transfer*, Vol. 8, No. 3, 1994, pp. 453–459. doi:10.2514/3.564.

- [104] Voelkel, S., Varghese, P. L., and Raman, V., "Multitemperature Dissociation Rate of $N_2+N_2 \rightarrow N_2+N+N$ Calculated Using Selective Sampling Quasi-Classical Trajectory Analysis," *Journal of Thermophysics and Heat Transfer*, Vol. 31, No. 4, 2017, pp. 965–975. doi:10.2514/1.T5103.
- [105] Koura, K., "Monte Carlo Direct Simulation of Rotational Relaxation of Diatomic Molecules using Classical Trajectory Calculations: Nitrogen Shock Wave," *Physics of Fluids*, Vol. 9, No. 11, 1997, pp. 3543–3549. doi:10.1063/1.869462.
- [106] Koura, K., "Monte Carlo Direct Simulation of Rotational Relaxation of Nitrogen through High Total Temperature Shock Waves using Classical Trajectory Calculations," *Physics of Fluids*, Vol. 10, No. 10, 1998, pp. 2689–2691. doi:10.1063/1.869782.
- [107] Norman, P., Valentini, P., and Schwartzentruber, T., "GPU-Accelerated Classical Trajectory Calculation Direct Simulation Monte Carlo Applied to Shock Waves," *Journal of Computational Physics*, Vol. 247, 2013, pp. 153–167. doi:10.1016/j.jcp.2013.03.060.
- [108] Valentini, P., Norman, P., Zhang, C., and Schwartzentruber, T. E., "Rovibrational Coupling in Molecular Nitrogen at High Temperature: An Atomic-Level Study," *Physics of Fluids*, Vol. 26, No. 5, 2014, p. 056103. doi:10.1063/1.4875279.
- [109] Macdonald, R. L., Grover, M. S., Schwartzentruber, T. E., and Panesi, M., "State-to-State and Direct Molecular Simulation Study of Energy Transfer and Dissociation in Nitrogen Mixtures," *2018 AIAA Aerospace Sciences Meeting*, AIAA Paper 2018-0239, 2018. doi:10.2514/6.2018-0239.
- [110] Macdonald, R. L., Grover, M. S., Schwartzentruber, T. E., and Panesi, M., "Construction of a Coarse-Grain Quasi-Classical Trajectory Method. II. Comparison Against the Direct Molecular Simulation Method," *The Journal of Chemical Physics*, Vol. 148, No. 5, 2018, p. 054310. doi:10.1063/1.5011332.
- [111] Jaffe, R. L., Grover, M., Venturi, S., Schwenke, D. W., Valentini, P., Schwartzentruber, T. E., and Panesi, M., "Comparison of Potential Energy Surface and Computed Rate Coefficients for N₂ Dissociation," *Journal of Thermophysics and Heat Transfer*, Vol. 32, No. 4, 2018, pp. 869–881. doi:10.2514/1.T5417.
- [112] Grover, M. S., and Schwartzentruber, T. E., "Internal Energy Relaxation and Dissociation in Molecular Oxygen using Direct Molecular Simulation," *47th AIAA Thermophysics Conference*, AIAA Paper 2017-3488, 2017. doi:10.2514/6.2017-3488.
- [113] Bender, J. D., "Multiscale Computational Analysis of Nitrogen and Oxygen Gas-Phase Thermochemistry in Hypersonic Flows," Ph.D. thesis, University of Minnesota, Minneapolis, MN, February 2016.
- [114] Zheng, J., Li, Z. H., Jasper, A. W., Bonhommeau, D. A., Valero, R., Meana-Pañeda, R., Mielke, S. L., and Truhlar, D. G., *A Molecular Dynamics Program for Performing Classical and Semiclassical Trajectory Simulations for Electronically Adiabatic*

- and Nonadiabatic Processes for Gas-Phase and Materials Systems*, University of Minnesota Department of Chemistry and Supercomputing Institute, Minneapolis, Minnesota, July 2017. URL <https://comp.chem.umn.edu/ant/>, accessed November 19, 2018.
- [115] Vincenti, W. G., and Kruger, C. H., Jr., *Introduction to Physical Gas Dynamics*, John Wiley & Sons, Inc., New York, 1965.
 - [116] Jaffe, R. L., “The Calculation of High-Temperature Equilibrium and Nonequilibrium Specific Heat Data for N₂, O₂, and NO,” *22nd Thermophysics Conference*, AIAA Paper 1987-1633, 1987. doi:10.2514/6.1987-1633.
 - [117] Lin, W., Meana-Pañeda, R., Varga, Z., and Truhlar, D. G., “A Quasiclassical Trajectory Study of the N₂(X¹Σ) + O(³P) → NO(X²Π) + N(⁴S) Reaction,” *The Journal of Chemical Physics*, Vol. 144, No. 23, 2016, p. 234314. doi:10.1063/1.4954042.
 - [118] Taylor, J. R., *An Introduction to Error Analysis*, University Science Books, Mill Valley, CA, 1982.
 - [119] Losev, S. A., and Generalov, N. A., “A Study of the Excitation of Vibrations and Dissociation of Oxygen Molecules at High Temperatures,” *Soviet Physics Doklady*, Vol. 6, 1962, p. 1081.
 - [120] Mankodi, T. K., Bhandarkar, U. V., and Puranik, B. P., “Dissociation Cross Sections for N₂ + N → 3N and O₂ + O → 3O Using the QCT Method,” *The Journal of Chemical Physics*, Vol. 146, No. 20, 2017, p. 204307. doi:10.1063/1.4983813.
 - [121] Kiefer, J. H., and Lutz, R. W., “The Effect of Oxygen Atoms on the Vibrational Relaxation of Oxygen,” *Symposium (International) on Combustion*, Vol. 11, No. 1, 1967, pp. 67–76. doi:10.1016/S0082-0784(67)80134-6.
 - [122] Esposito, F., Armenise, I., Capitta, G., and Capitelli, M., “O–O₂ State-to-State Vibrational Relaxation and Dissociation Rates Based on Quasiclassical Calculations,” *Chemical Physics*, Vol. 351, No. 1, 2008, pp. 91–98. doi:10.1016/j.chemphys.2008.04.004.
 - [123] Kulakhmetov, M., Gallis, M., and Alexeenko, A., “Ab Initio-Informed Maximum Entropy Modeling of Rovibrational Relaxation and State-Specific Dissociation with Application to the O₂ + O System,” *The Journal of Chemical Physics*, Vol. 144, No. 17, 2016, p. 174302. doi:10.1063/1.4947590.
 - [124] Wilson, T. J., Pan, T.-J., and Stephani, K. A., “State-to-State Dissociation and Recombination Modeling in DSMC using Quasi-classical Trajectory Calculations for O + O₂,” *2018 AIAA Aerospace Sciences Meeting*, AIAA Paper 2018-1487, 2018. doi:10.2514/6.2018-1487.
 - [125] Hansen, C. F., “Dissociation of Diatomic Gases,” *The Journal of Chemical Physics*, Vol. 95, No. 10, 1991, pp. 7226–7233. doi:10.1063/1.461400.

- [126] Riley, K. F., Hobson, M. P., and Bence, S. J., *Mathematical Methods for Physics and Engineering*, 3rd ed., Cambridge University Press, Cambridge, UK, 2006.
- [127] Park, C., “Review of Finite-Rate Chemistry Models for Air Dissociation and Ionization,” *Molecular Physics and Hypersonic Flows*, NATO ASI Series (Series C: Mathematical and Physical Sciences), Vol. 482, edited by M. Capitelli, Kluwer Academic Publishers, Dordrecht, 1996, pp. 581–596. doi:10.1007/978-94-009-0267-1_39.
- [128] Losev, S., Kovach, E., Makarov, V., Pogosbekjan, M., and Sergievskaya, A., “Chemistry Models for Air Dissociation,” *Molecular Physics and Hypersonic Flows*, NATO ASI Series (Series C: Mathematical and Physical Sciences), Vol. 482, edited by M. Capitelli, Kluwer Academic Publishers, Dordrecht, 1996, pp. 581–596. doi:10.1007/978-94-009-0267-1_40.
- [129] Andrienko, D. A., and Boyd, I. D., “Kinetic Models of Oxygen Thermochemistry Based on Quasi-Classical Trajectory Analysis,” *Journal of Thermophysics and Heat Transfer*, 2018. doi:10.2514/1.T4968.
- [130] “MATLAB Release 2018a,” The MathWorks, Inc., Natick, Massachusetts, United States, 2018.
- [131] Sharma, S. P., Huo, W. M., and Park, C., “The Rate Parameters for Coupled Vibration-Dissociation in a Generalized SSH Approximation,” *23rd Thermophysics, Plasmadynamics and Lasers Conference*, AIAA Paper 1988-2714, 1988. doi:10.2514/6.1988-2714.
- [132] Nompelis, I., “Computational Study of Hypersonic Double-Cone Experiments for Code Validation,” Ph.D. thesis, University of Minnesota, Minneapolis, MN, May 2004.
- [133] Valentini, P., and Schwartzentruber, T. E., “Ab Initio Based Model for High Temperature Nitrogen Rovibrational Excitation and Dissociation,” *54th AIAA Aerospace Sciences Meeting*, AIAA Paper 2016-0500, 2016. doi:10.2514/6.2016-0500.
- [134] Singh, N., and Schwartzentruber, T. E., “Coupled Vibration-Rotation Dissociation Model for Nitrogen from Direct Molecular Simulations,” *47th AIAA Thermophysics Conference*, AIAA Paper 2017-3490, 2017. doi:10.2514/6.2017-3490.
- [135] Gordon, S., and McBride, B. J., “Computer Program for Calculation of Complex Chemical Equilibrium Compositions and Applications, 1. Analysis,” Tech. Rep. RP-1331, NASA, October 1994.
- [136] McBride, B. J., and Gordon, S., “Computer Program for Calculation of Complex Chemical Equilibrium Compositions and Applications, 2. Users Manual and Program Description,” Tech. Rep. RP-1331-2, NASA, June 1996.
- [137] Singh, N., and Schwartzentruber, T. E., “Nonequilibrium Internal Energy Distributions during Dissociation,” *Proceedings of the National Academy of Sciences*, Vol. 115, No. 1, 2018, pp. 47–52. doi:10.1073/pnas.1713840115.

- [138] Mohr, P. J., Newell, D. B., and Taylor, B. N., “CODATA Recommended Values of the Fundamental Physical Constants: 2014,” *Journal of Physical and Chemical Reference Data*, Vol. 45, No. 4, 2016, p. 043102. doi:10.1063/1.4954402.

Appendix A

Glossary

A.1 Nomenclature

Latin

a_U	Model parameter for modified Marrone-Treanor form	Equation (3.20)
b	Impact parameter, Å	
C	Coefficient in generalized Arrhenius form, $\text{cm}^3\text{s}^{-1}\text{K}^{-n}$	Equation (1.1)
D_0	Ground-state dissociation energy, eV	Equation (2.4)
E	Expected value	Section 2.3.5
E_r	Relative translational energy, eV	
f_e	Probability distribution function (PDF) of event e	Equation (2.35)
g	Relative contribution from trajectory subset	Equation (2.50)
h	Planck constant, $6.626,070,040(81) \times 10^{-34} \text{ J sec}$	Table C.1
\hbar	Reduced Planck constant, $\hbar = \frac{h}{2\pi}$	
j	Rotational quantum number	
k	Rate constant, cm^3/sec	Equation (2.20)
k_B	Boltzmann constant, $1.380,648,52(79) \times 10^{-23} \text{ J/K}$	Table C.1
\ln	Natural logarithm	
M	Generic collision partner	
$M^{(n)}$	n -th Moment	Equation (2.46)
\mathcal{M}	Molar mass, g mol^{-1}	
n	Temperature exponent in generalized Arrhenius form	Equation (1.1)
\mathcal{N}_{rv}	Number of rovibrational states	Section 2.1.1
\mathcal{N}	Number of trajectories satisfying some condition	
P_e	Probability of event e	Equation (2.39)
q	Arbitrary quantity	

Q	Partition function	Section 2.1.3
r	Interatomic spacing, Å	
s	Model parameter for generalized Park form [18]	Equation (3.12)
S_e	Support factor for event e	Section 3.5.1
\mathcal{S}	Symmetry factor	Equation (2.20)
t_i	Interaction Time, fs	Equation (3.21)
T	Temperature, K	
T_D	Characteristic temperature of dissociation, K	Section 2.1.1
U	Model parameter for Marrone-Treanor model [1], K	Equation (3.11)
U^*	Model parameter for modified Marrone-Treanor form, K	Equation (3.20)
v	Vibrational quantum number	
V_D	Diatom Potential, eV	
$V_{D,\text{eff}}$	Effective diatomic potential, eV	Equation (2.1)
\mathcal{V}	Volume of strata	Section 2.3.2
w	Weight of individual trajectory, OR	Equation (2.29)
	Source term in conservation equations	
Z	Nonequilibrium correction factor for dissociation rate	Equation (3.7)

Greek

ε_{GS}	Ground-state energy, eV	Equation (2.2)
ε_{int}	Internal energy, eV	Section 2.1.1
ε_{rem}	Remainder energy, eV	Equation (3.5)
ε_{rot}	Rotational energy, eV	Section 2.1.2
ε_{vib}	Vibrational energy, eV	Section 2.1.2
η	Multisurface correction factor for oxygen dissociation, $\frac{16}{3}$	Section 1.4.1
Θ_v	Characteristic temperature of vibration, K	Equation (2.3)
μ	Reduced mass	
ρ	Density, kg m ⁻³	

Subscripts

d	Dissociation	
d	Index for dimension of stratified sampling	Section 2.3.2
e	Exchange	
e	Generic event	
k	Index for stratified sampling	Section 2.3.2
s	Species	
t	Translational	
r	Rotational	

v	Vibrational	
0	Initial condition	
$\langle \varepsilon_{\text{vib}} \rangle_d$	Change in system vibrational energy per dissociation	Equation (2.44)

A.2 Acronyms

AEM	Aerospace Engineering and Mechanics
AIAA	American Institute of Aeronautics and Astronautics
DMS	Direct Molecular Simulation
DSMC	Direct Simulation Monte Carlo
GCC	GNU Compiler Collection
GNU	GNU's Not Unix!
GPU	Graphical Processing Unit
MPI	Message Passing Interface
MSI	Minnesota Supercomputing Institute
MUE	Mean Unsigned Error
NASA	National Aeronautics and Space Administration
PDF	Probability Density Function
PES	Potential Energy Surface
PGI	The Portland Group
QCT	Quasiclassical Trajectory
QSS	Quasi-Steady State
REAQCT	Rovibrational Energetics and Analysis of QuasiClassical Trajectories
SHO	Simple Harmonic Oscillator
UV	Ultraviolet

Appendix B

Tables of QCT Data

This Chapter contains summary tables for all trajectories in the QCT database. Almost all of the $\text{N}_2 + \text{N}_2$ results were generated by Bender *et al.* [25], and some of the $\text{N}_2 + \text{N}$ results first appeared in Valentini *et al.* [11]. Except for $\text{N}_2 + \text{N}_2$, all trajectories use $b_{\max} = 6 \text{ \AA}$.

Reported uncertainties are one-sigma-deviation statistical error, as described in Section 2.3. In our notation, the number in parenthesis indicates the magnitude of uncertainty in the last digit of the reported value. For example, $1.23(4) \times 10^{10} \text{ cm}^3/\text{sec}$ is equivalent to $1.23 \pm 0.04 \times 10^{10} \text{ cm}^3/\text{sec}$. Similar to the recommendation of Taylor [118, p. 16], if the leading digit in the uncertainty is 1, then two digits are retained for the uncertainty. (This also adds an extra significant figure to reported value.) For example, $1.234(12) \times 10^{10} \text{ cm}^3/\text{sec}$ is correct and equivalent to $1.234 \pm 0.012 \times 10^{10} \text{ cm}^3/\text{sec}$.

Table B.1: Summary statistics for $\text{N}_2 + \text{N}_2$, equilibrium test set ($T_{\text{tr}} = T_{\text{v}}$). Run and analyzed by Bender *et al.* [25, 113], included here for completeness.

T [K]	\mathcal{N} [10^6]	b_{max} [\AA]	$k_{\text{d}}^{(\text{eff})}$ [cm^3/sec]	$\langle \Delta\varepsilon_{\text{vib}} \rangle_{\text{d}}^{(\text{eff})}$ [eV]	$\langle \Delta\varepsilon_{\text{rot}} \rangle_{\text{d}}^{(\text{eff})}$ [eV]	$k_{\text{d}}^{(\text{event})}/k_{\text{d}}^{(\text{eff})}$ [%]			
						<i>simple</i>	<i>swap</i>	<i>double</i>	k_{m} [cm^3/sec]
8000	400	8	$4.58(13) \times 10^{-15}$	-8.3(3)	-1.69(7)	99.08(18)	0.92(18)	0(0)	$5.0(6) \times 10^{-17}$
10,000	256	8	$7.25(7) \times 10^{-14}$	-8.03(8)	-2.04(3)	96.94(10)	3.06(10)	0(0)	$1.54(4) \times 10^{-15}$
13,000	56	8	$9.13(5) \times 10^{-13}$	-7.61(5)	-2.56(2)	92.45(11)	7.51(11)	0.033(9)	$3.02(5) \times 10^{-14}$
20,000	40	8	$1.633(3) \times 10^{-11}$	-6.984(13)	-3.399(8)	80.52(5)	18.88(5)	0.600(12)	$8.96(3) \times 10^{-13}$
30,000	16	8	$8.513(10) \times 10^{-11}$	-6.478(9)	-4.118(7)	69.18(5)	28.17(5)	2.647(19)	$5.529(15) \times 10^{-12}$

Table B.2: Summary statistics for $\text{N}_2 + \text{N}_2$, nonequilibrium test set ($T_{\text{tr}} = 20,000$ K). Run and analyzed by Bender *et al.* [25, 113], included here for completeness.

T_{v} [K]	\mathcal{N} [10^6]	b_{max} [\AA]	$k_{\text{d}}^{(\text{eff})}$ [cm^3/sec]	$\langle \Delta\varepsilon_{\text{vib}} \rangle_{\text{d}}^{(\text{eff})}$ [eV]	$\langle \Delta\varepsilon_{\text{rot}} \rangle_{\text{d}}^{(\text{eff})}$ [eV]	$k_{\text{d}}^{(\text{event})}/k_{\text{d}}^{(\text{eff})}$ [%]			
						<i>simple</i>	<i>swap</i>	<i>double</i>	k_{m} [cm^3/sec]
8000	240	6	$1.352(2) \times 10^{-12}$	-1.265(5)	-9.093(19)	80.03(6)	19.74(6)	0.237(8)	$2.183(6) \times 10^{-13}$
10,000	96	8	$2.043(5) \times 10^{-12}$	-2.488(11)	-7.90(2)	80.33(8)	19.40(8)	0.262(12)	$2.749(12) \times 10^{-13}$
13,000	70	7	$4.160(9) \times 10^{-12}$	-4.446(13)	-5.950(16)	81.24(7)	18.46(7)	0.300(11)	$3.971(16) \times 10^{-13}$
20,000	40	8	$1.633(3) \times 10^{-11}$	-6.984(13)	-3.399(8)	80.52(5)	18.88(5)	0.600(12)	$8.96(3) \times 10^{-13}$
30,000	16	8	$4.457(7) \times 10^{-11}$	-8.119(15)	-2.317(6)	76.96(6)	21.73(6)	1.312(18)	$1.838(8) \times 10^{-12}$

Table B.3: Summary statistics for $\text{N}_2 + \text{N}_2$, all conditions. Run and analyzed by Bender *et al.* [25, 113], included here for completeness.

T [1000 K]			$k_d^{(event)}/k_d^{(eff)} [\%]$							
tr	v	\mathcal{N} [10^6]	b_{\max} [Å]	$k_d^{(eff)}$ [cm^3/sec]	$\langle \Delta\varepsilon_{\text{vib}} \rangle_d^{(eff)}$ [eV]	$\langle \Delta\varepsilon_{\text{rot}} \rangle_d^{(eff)}$ [eV]	simple	swap	double	k_m [cm^3/sec]
8	8	400	8	$4.58(13) \times 10^{-15}$	-8.3(3)	-1.69(7)	99.08(18)	0(0)	5.0(6)	$\times 10^{-17}$
8	10	105	7	$4.53(7) \times 10^{-14}$	-8.77(17)	-1.17(3)	98.77(12)	1.23(12)	0(0)	$1.8(2) \times 10^{-16}$
8	13	60	6	$3.72(3) \times 10^{-13}$	-9.03(8)	-0.901(11)	98.19(7)	1.81(7)	0.006(4)	$1.22(8) \times 10^{-15}$
8	20	28	7	$4.231(14) \times 10^{-12}$	-9.27(4)	-0.693(4)	95.35(6)	4.46(5)	0.188(13)	$1.50(4) \times 10^{-14}$
8	30	24	8	$1.650(3) \times 10^{-11}$	-9.45(2)	-0.586(2)	90.50(5)	8.78(4)	0.720(16)	$8.26(12) \times 10^{-14}$
10	8	320	8	$1.00(2) \times 10^{-14}$	-6.65(15)	-3.60(9)	96.4(2)	3.6(2)	0(0)	$6.3(3) \times 10^{-16}$
10	10	256	8	$7.25(7) \times 10^{-14}$	-8.03(8)	-2.04(3)	96.94(10)	3.06(10)	0(0)	$1.54(4) \times 10^{-15}$
10	13	70	7	$5.26(3) \times 10^{-13}$	-8.62(6)	-1.401(13)	96.28(8)	3.69(8)	0.025(12)	$5.32(15) \times 10^{-15}$
10	20	28	7	$5.367(17) \times 10^{-12}$	-9.06(3)	-0.978(5)	93.30(6)	6.49(6)	0.209(14)	$4.51(8) \times 10^{-14}$
10	30	24	8	$2.016(4) \times 10^{-11}$	-9.321(19)	-0.793(2)	88.22(5)	10.98(5)	0.801(16)	$1.822(19) \times 10^{-13}$
13	8	240	6	$5.30(5) \times 10^{-14}$	-3.80(5)	-6.56(7)	88.96(19)	11.04(19)	0(0)	$8.13(10) \times 10^{-15}$
13	10	96	8	$1.855(16) \times 10^{-13}$	-6.01(7)	-4.27(5)	91.58(17)	8.42(17)	0(0)	$1.34(2) \times 10^{-14}$
13	13	56	8	$9.13(5) \times 10^{-13}$	-7.61(5)	-2.56(2)	92.45(11)	7.51(11)	0.033(9)	$3.02(5) \times 10^{-14}$
13	20	24	8	$7.47(2) \times 10^{-12}$	-8.63(3)	-1.532(7)	89.57(7)	10.17(7)	0.257(15)	$1.408(16) \times 10^{-13}$
13	30	16	8	$2.621(5) \times 10^{-11}$	-9.06(2)	-1.162(4)	84.57(6)	14.53(6)	0.900(19)	$4.48(4) \times 10^{-13}$
20	8	240	6	$1.352(2) \times 10^{-12}$	-1.265(5)	-9.093(19)	80.03(6)	19.74(6)	0.237(8)	$2.183(6) \times 10^{-13}$
20	10	96	8	$2.043(5) \times 10^{-12}$	-2.488(11)	-7.90(2)	80.33(8)	19.40(8)	0.262(12)	$2.749(12) \times 10^{-13}$
20	13	70	7	$4.160(9) \times 10^{-12}$	-4.446(13)	-5.950(16)	81.24(7)	18.46(7)	0.300(11)	$3.971(16) \times 10^{-13}$
20	20	40	8	$1.633(3) \times 10^{-11}$	-6.984(13)	-3.399(8)	80.52(5)	18.88(5)	0.600(12)	$8.96(3) \times 10^{-13}$
20	30	16	8	$4.457(7) \times 10^{-11}$	-8.119(15)	-2.317(6)	76.96(6)	21.73(6)	1.312(18)	$1.838(8) \times 10^{-12}$
30	8	180	6	$1.4089(10) \times 10^{-11}$	-0.4139(14)	-10.051(8)	73.75(3)	24.94(3)	1.315(7)	$1.825(2) \times 10^{-12}$
30	10	96	8	$1.6722(16) \times 10^{-11}$	-1.049(3)	-9.438(11)	73.10(4)	25.53(4)	1.369(10)	$2.058(4) \times 10^{-12}$
30	13	70	7	$2.247(2) \times 10^{-11}$	-2.208(4)	-8.313(10)	72.63(4)	25.94(4)	1.425(11)	$2.477(4) \times 10^{-12}$
30	20	24	8	$4.445(6) \times 10^{-11}$	-4.672(8)	-5.891(10)	71.33(5)	26.84(5)	1.828(17)	$3.729(10) \times 10^{-12}$
30	30	16	8	$8.513(10) \times 10^{-11}$	-6.478(9)	-4.118(7)	69.18(5)	28.17(5)	2.647(19)	$5.529(15) \times 10^{-12}$

Table B.4: Summary statistics for $\text{N}_2 + \text{N}$, equilibrium test set ($T_{\text{tr}} = T_{\text{v}}$).

T [K]	\mathcal{N} [10^6]	k_d [cm^3/sec]	$\langle \Delta\varepsilon_{\text{vib}} \rangle_d$ [eV]	$\langle \Delta\varepsilon_{\text{rot}} \rangle_d$ [eV]	k_e [cm^3/sec]	$\langle \Delta\varepsilon_{\text{vib}} \rangle_e$ [eV]	$\langle \Delta\varepsilon_{\text{rot}} \rangle_e$ [eV]
8000	240	$5.6(2) \times 10^{-15}$	-7.9(4)	-1.60(9)	$7.718(5) \times 10^{-12}$	$-3.0(7) \times 10^{-3}$	$2.1(8) \times 10^{-3}$
10,000	150	$8.20(12) \times 10^{-14}$	-7.63(13)	-1.82(4)	$2.0638(11) \times 10^{-11}$	$-4.6(7) \times 10^{-3}$	$8.8(9) \times 10^{-3}$
13,000	60	$1.006(7) \times 10^{-12}$	-7.20(6)	-2.20(2)	$5.528(3) \times 10^{-11}$	$-5.2(10) \times 10^{-3}$	0.0104(13)
20,000	18	$1.722(6) \times 10^{-11}$	-6.52(3)	-2.896(13)	$1.8377(12) \times 10^{-10}$	$-4.9(16) \times 10^{-3}$	0.014(2)
30,000	18	$8.939(14) \times 10^{-11}$	-5.930(11)	-3.490(7)	$3.6133(19) \times 10^{-10}$	$-4.9(15) \times 10^{-3}$	0.018(2)

Table B.5: Summary statistics for $\text{N}_2 + \text{N}$, nonequilibrium test set ($T_{\text{tr}} = 20,000$ K).

T_{v} [K]	\mathcal{N} [10^6]	k_d [cm^3/sec]	$\langle \Delta\varepsilon_{\text{vib}} \rangle_d$ [eV]	$\langle \Delta\varepsilon_{\text{rot}} \rangle_d$ [eV]	k_e [cm^3/sec]	$\langle \Delta\varepsilon_{\text{vib}} \rangle_e$ [eV]	$\langle \Delta\varepsilon_{\text{rot}} \rangle_e$ [eV]
8000	90	$2.122(7) \times 10^{-12}$	-1.333(8)	-6.71(3)	$1.1541(4) \times 10^{-10}$	0.9139(7)	-0.5638(11)
10,000	60	$2.903(11) \times 10^{-12}$	-2.292(14)	-6.11(3)	$1.2434(5) \times 10^{-10}$	0.7583(9)	-0.4785(13)
13,000	60	$5.118(15) \times 10^{-12}$	-4.011(17)	-4.878(19)	$1.4031(6) \times 10^{-10}$	0.5136(9)	-0.3338(13)
20,000	18	$1.722(6) \times 10^{-11}$	-6.52(3)	-2.896(13)	$1.8377(12) \times 10^{-10}$	-0.0049(16)	0.014(2)
30,000	60	$4.371(5) \times 10^{-11}$	-7.565(10)	-2.017(3)	$2.3971(8) \times 10^{-10}$	-0.4721(9)	0.3574(11)

Table B.6: Summary statistics for $\text{N}_2 + \text{O}_2$, equilibrium test set ($T_{\text{tr}} = T_v$).

T [K]	\mathcal{N} [10^6]	$k_{\text{O2-d}}$ [cm^3/sec]	$\langle \Delta\varepsilon_{\text{vib}} \rangle_{\text{O2-d}}$ [eV]	$\langle \Delta\varepsilon_{\text{rot}} \rangle_{\text{O2-d}}$ [eV]	$k_{\text{N2-d}}$ [cm^3/sec]	$\langle \Delta\varepsilon_{\text{vib}} \rangle_{\text{N2-d}}$ [eV]	$\langle \Delta\varepsilon_{\text{rot}} \rangle_{\text{N2-d}}$ [eV]
4000	360	$8.5(6) \times 10^{-16}$	-4.4(4)	-0.91(10)	0(0)	-	-
5000	1440	$1.797(16) \times 10^{-14}$	-4.26(5)	-1.112(15)	$5(5) \times 10^{-18}$	-10(13)	-0.1(3)
6500	660	$2.789(10) \times 10^{-13}$	-4.028(17)	-1.443(7)	$2.3(3) \times 10^{-16}$	-8.3(13)	-1.6(2)
8000	363	$1.536(3) \times 10^{-12}$	-3.824(10)	-1.738(5)	$4.75(17) \times 10^{-15}$	-7.9(3)	-1.92(9)
10,000	240	$6.577(8) \times 10^{-12}$	-3.607(6)	-2.057(4)	$7.03(9) \times 10^{-14}$	-7.66(11)	-2.22(4)
13,000	12	$2.446(8) \times 10^{-11}$	-3.363(13)	-2.441(10)	$7.96(14) \times 10^{-13}$	-7.33(15)	-2.63(6)
20,000	120	$1.0410(5) \times 10^{-10}$	-3.067(2)	-2.963(2)	$1.0949(18) \times 10^{-11}$	-6.663(13)	-3.488(8)
30,000	60	$2.3000(12) \times 10^{-10}$	-2.868(2)	-3.354(2)	$4.533(6) \times 10^{-11}$	-6.149(10)	-4.168(7)

Table B.7: Summary statistics for $\text{N}_2 + \text{O}_2$, nonequilibrium test set targeted at oxygen dissociation ($T_{\text{tr}} = 10,000$ K).

T_v [K]	\mathcal{N} [10^6]	$k_{\text{O2-d}}$ [cm^3/sec]	$\langle \Delta\varepsilon_{\text{vib}} \rangle_{\text{O2-d}}$ [eV]	$\langle \Delta\varepsilon_{\text{rot}} \rangle_{\text{O2-d}}$ [eV]	$k_{\text{N2-d}}$ [cm^3/sec]	$\langle \Delta\varepsilon_{\text{vib}} \rangle_{\text{N2-d}}$ [eV]	$\langle \Delta\varepsilon_{\text{rot}} \rangle_{\text{N2-d}}$ [eV]
4000	30	$3.61(5) \times 10^{-13}$	-0.90(2)	-5.36(8)	$8.9(16) \times 10^{-16}$	-0.7(3)	-7.6(14)
5000	600	$6.220(14) \times 10^{-13}$	-1.573(5)	-4.572(13)	$1.17(5) \times 10^{-15}$	-1.30(10)	-7.4(3)
6500	120	$1.463(5) \times 10^{-12}$	-2.509(12)	-3.423(15)	$3.0(2) \times 10^{-15}$	-3.3(4)	-5.6(4)
8000	120	$3.079(8) \times 10^{-12}$	-3.125(10)	-2.655(9)	$1.21(5) \times 10^{-14}$	-6.1(3)	-3.58(17)
10,000	240	$6.577(8) \times 10^{-12}$	-3.607(6)	-2.057(4)	$7.03(9) \times 10^{-14}$	-7.66(11)	-2.22(4)
13,000	120	$1.3877(18) \times 10^{-11}$	-3.965(6)	-1.634(3)	$4.69(3) \times 10^{-13}$	-8.50(7)	-1.457(15)

Table B.8: Summary statistics for $\text{N}_2 + \text{O}_2$, nonequilibrium test set targeted at nitrogen dissociation ($T_{\text{tr}} = 20,000$ K).

T_v [K]	\mathcal{N} [10^6]	$k_{\text{O2-d}}$ [cm^3/sec]	$\langle \Delta\varepsilon_{\text{vib}} \rangle_{\text{O2-d}}$ [eV]	$\langle \Delta\varepsilon_{\text{rot}} \rangle_{\text{O2-d}}$ [eV]	$k_{\text{N2-d}}$ [cm^3/sec]	$\langle \Delta\varepsilon_{\text{vib}} \rangle_{\text{N2-d}}$ [eV]	$\langle \Delta\varepsilon_{\text{rot}} \rangle_{\text{N2-d}}$ [eV]
8000	120	$3.986(3) \times 10^{-11}$	-1.2798(16)	-5.042(5)	$1.243(5) \times 10^{-12}$	-1.324(10)	-8.76(4)
10,000	120	$5.118(3) \times 10^{-11}$	-1.7615(18)	-4.465(4)	$1.776(6) \times 10^{-12}$	-2.411(13)	-7.71(3)
13,000	18	$6.949(11) \times 10^{-11}$	-2.306(5)	-3.830(8)	$3.27(2) \times 10^{-12}$	-4.19(4)	-5.96(5)
20,000	120	$1.0410(5) \times 10^{-10}$	-3.067(2)	-2.963(2)	$1.0949(18) \times 10^{-11}$	-6.663(13)	-3.488(8)
30,000	6	$1.354(3) \times 10^{-10}$	-3.564(9)	-2.474(7)	$2.711(13) \times 10^{-11}$	-7.72(4)	-2.438(17)

Table B.9: Summary statistics for $\text{O}_2 + \text{O}_2$ system, equilibrium test set ($T_{\text{tr}} = T_{\text{v}}$).

T [K]	\mathcal{N} [10^6]	$k_{\text{d}}^{(\text{eff})}$ [cm^3/sec]	$\langle \Delta\varepsilon_{\text{vib}} \rangle_{\text{d}}^{(\text{eff})}$ [eV]	$\langle \Delta\varepsilon_{\text{rot}} \rangle_{\text{d}}^{(\text{eff})}$ [eV]	$k_{\text{d}}^{(\text{event})}/k_{\text{d}}^{(\text{eff})}$ [%]			k_{m} [cm^3/sec]
					<i>simple</i>	<i>swap</i>	<i>double</i>	
4000	360	$2.79(10) \times 10^{-15}$	-4.37(19)	-0.69(3)	86.4(8)	13.6(8)	0(0)	$7.3(19) \times 10^{-18}$
5000	360	$4.78(4) \times 10^{-14}$	-4.23(4)	-0.915(11)	84.0(2)	16.0(2)	0(0)	$3.35(14) \times 10^{-16}$
6500	180	$6.40(2) \times 10^{-13}$	-4.076(16)	-1.150(5)	80.38(10)	19.60(10)	0.021(4)	$6.81(10) \times 10^{-15}$
8000	90	$3.163(7) \times 10^{-12}$	-3.937(10)	-1.369(4)	76.59(7)	23.32(7)	0.095(6)	$4.26(4) \times 10^{-14}$
10,000	180	$1.2147(10) \times 10^{-11}$	-3.787(4)	-1.6104(18)	72.59(3)	27.00(3)	0.409(5)	$2.109(6) \times 10^{-13}$
13,000	18	$3.948(6) \times 10^{-11}$	-3.607(7)	-1.896(4)	67.63(6)	31.07(6)	1.301(16)	$8.56(4) \times 10^{-13}$

Table B.10: Summary statistics for $\text{O}_2 + \text{O}_2$ system, nonequilibrium test set ($T_{\text{tr}} = 10,000$ K).

T_{v} [K]	\mathcal{N} [10^6]	$k_{\text{d}}^{(\text{eff})}$ [cm^3/sec]	$\langle \Delta\varepsilon_{\text{vib}} \rangle_{\text{d}}^{(\text{eff})}$ [eV]	$\langle \Delta\varepsilon_{\text{rot}} \rangle_{\text{d}}^{(\text{eff})}$ [eV]	$k_{\text{d}}^{(\text{event})}/k_{\text{d}}^{(\text{eff})}$ [%]			k_{m} [cm^3/sec]
					<i>simple</i>	<i>swap</i>	<i>double</i>	
4000	180	$6.019(17) \times 10^{-13}$	-0.862(5)	-4.730(17)	75.82(10)	24.03(10)	0.144(9)	$1.333(13) \times 10^{-14}$
5000	90	$1.046(3) \times 10^{-12}$	-1.574(8)	-3.929(16)	74.31(12)	25.53(12)	0.160(12)	$2.21(2) \times 10^{-14}$
6500	54	$2.527(7) \times 10^{-12}$	-2.590(10)	-2.838(11)	73.36(11)	26.48(11)	0.162(10)	$4.99(5) \times 10^{-14}$
8000	18	$5.51(2) \times 10^{-12}$	-3.286(15)	-2.107(10)	73.13(14)	26.62(13)	0.243(15)	$1.005(13) \times 10^{-13}$
10,000	180	$1.2147(10) \times 10^{-11}$	-3.787(4)	-1.6104(18)	72.59(3)	27.00(3)	0.409(5)	$2.109(6) \times 10^{-13}$
13,000	18	$2.608(5) \times 10^{-11}$	-4.162(9)	-1.249(3)	71.50(7)	27.76(7)	0.741(15)	$4.41(3) \times 10^{-13}$

Table B.11: Summary statistics for $\text{O}_2 + \text{O}_2$, for all surfaces with $T_{\text{tr}} = T_{\text{v}} = 10,000 \text{ K}$.

Surface	$\mathcal{N} [10^6]$	$k_{\text{d}}^{(\text{eff})} [\text{cm}^3/\text{sec}]$	$\langle \Delta\varepsilon_{\text{vib}} \rangle_{\text{d}}^{(\text{eff})} [\text{eV}]$	$\langle \Delta\varepsilon_{\text{rot}} \rangle_{\text{d}}^{(\text{eff})} [\text{eV}]$	$k_{\text{d}}^{(\text{event})}/k_{\text{d}}^{(\text{eff})} [\%]$			$k_{\text{m}} [\text{cm}^3/\text{sec}]$
					simple	swap	double	
Singlet	60	$1.0884(14) \times 10^{-11}$	-3.787(6)	-1.672(3)	69.11(5)	30.68(5)	0.206(6)	$3.087(13) \times 10^{-13}$
Triplet	60	$1.6168(18) \times 10^{-11}$	-3.766(5)	-1.595(2)	67.60(5)	32.04(5)	0.360(6)	$3.882(15) \times 10^{-13}$
Quintet	60	$9.987(14) \times 10^{-12}$	-3.807(6)	-1.612(3)	78.19(5)	21.31(5)	0.500(9)	$8.50(7) \times 10^{-14}$
SYS	180	$1.2147(10) \times 10^{-11}$	-3.787(4)	-1.6104(18)	72.59(3)	27.00(3)	0.409(5)	$2.109(6) \times 10^{-13}$

Table B.12: Summary statistics for $\text{O}_2 + \text{O}_2$, for all surfaces with $T_{\text{tr}} = T_{\text{v}} = 5000 \text{ K}$.

Surface	$\mathcal{N} [10^6]$	$k_{\text{d}}^{(\text{eff})} [\text{cm}^3/\text{sec}]$	$\langle \Delta\varepsilon_{\text{vib}} \rangle_{\text{d}}^{(\text{eff})} [\text{eV}]$	$\langle \Delta\varepsilon_{\text{rot}} \rangle_{\text{d}}^{(\text{eff})} [\text{eV}]$	$k_{\text{d}}^{(\text{event})}/k_{\text{d}}^{(\text{eff})} [\%]$			$k_{\text{m}} [\text{cm}^3/\text{sec}]$
					simple	swap	double	
Singlet	120	$3.67(5) \times 10^{-14}$	-4.29(8)	-0.933(19)	85.8(4)	14.2(4)	0(0)	$5.0(3) \times 10^{-16}$
Triplet	120	$7.29(8) \times 10^{-14}$	-4.11(5)	-0.933(12)	77.8(3)	22.2(3)	0(0)	$6.9(4) \times 10^{-16}$
Quintet	120	$3.49(5) \times 10^{-14}$	-4.37(8)	-0.89(2)	91.3(3)	8.7(3)	0(0)	$8.7(13) \times 10^{-17}$
SYS	360	$4.78(4) \times 10^{-14}$	-4.23(4)	-0.915(11)	84.0(2)	16.0(2)	0(0)	$3.35(14) \times 10^{-16}$

Table B.13: Summary statistics for $\text{O}_2 + \text{O}_2$, for all surfaces with $T_{\text{tr}} = 10,000 \text{ K}$, $T_{\text{v}} = 4000 \text{ K}$.

Surface	$\mathcal{N} [10^6]$	$k_{\text{d}}^{(\text{eff})} [\text{cm}^3/\text{sec}]$	$\langle \Delta\varepsilon_{\text{vib}} \rangle_{\text{d}}^{(\text{eff})} [\text{eV}]$	$\langle \Delta\varepsilon_{\text{rot}} \rangle_{\text{d}}^{(\text{eff})} [\text{eV}]$	$k_{\text{d}}^{(\text{event})}/k_{\text{d}}^{(\text{eff})} [\%]$			$k_{\text{m}} [\text{cm}^3/\text{sec}]$
					simple	swap	double	
Singlet	60	$6.12(3) \times 10^{-13}$	-0.703(6)	-4.44(2)	72.78(16)	27.13(16)	0.097(12)	$2.48(3) \times 10^{-14}$
Triplet	60	$8.82(3) \times 10^{-13}$	-0.875(6)	-4.343(19)	68.95(14)	30.90(14)	0.146(13)	$2.97(4) \times 10^{-14}$
Quintet	60	$4.32(2) \times 10^{-13}$	-0.893(9)	-5.29(4)	85.10(16)	14.74(16)	0.155(17)	$1.23(7) \times 10^{-15}$
SYS	180	$6.019(17) \times 10^{-13}$	-0.862(5)	-4.730(17)	75.82(10)	24.03(10)	0.144(9)	$1.333(13) \times 10^{-14}$

Table B.14: Summary statistics for O₂ + O system, equilibrium test set ($T_{\text{tr}} = T_{\text{v}}$).

T [K]	\mathcal{N} [10^6]	k_d [cm^3/sec]	$\langle \Delta\varepsilon_{\text{vib}} \rangle_d$ [eV]	$\langle \Delta\varepsilon_{\text{rot}} \rangle_d$ [eV]	k_e [cm^3/sec]	$\langle \Delta\varepsilon_{\text{vib}} \rangle_e$ [eV]	$\langle \Delta\varepsilon_{\text{rot}} \rangle_e$ [eV]
4000	1080	$1.80(6) \times 10^{-15}$	-4.15(17)	-0.80(4)	$3.0373(4) \times 10^{-11}$	-4.72(6) $\times 10^{-3}$	$1.34(7) \times 10^{-3}$
5000	540	$3.18(4) \times 10^{-14}$	-4.04(6)	-0.902(16)	$4.1316(7) \times 10^{-11}$	-3.73(10) $\times 10^{-3}$	$1.07(12) \times 10^{-3}$
6500	270	$4.38(2) \times 10^{-13}$	-3.83(2)	-1.120(7)	$6.1080(12) \times 10^{-11}$	-2.85(17) $\times 10^{-3}$	$1.2(2) \times 10^{-3}$
8000	54	$2.233(11) \times 10^{-12}$	-3.66(2)	-1.311(9)	$8.568(4) \times 10^{-11}$	-1.3(4) $\times 10^{-3}$	-1(6) $\times 10^{-4}$
10,000	540	$8.695(7) \times 10^{-12}$	-3.473(4)	-1.5207(17)	$1.245,08(16) \times 10^{-10}$	-1.22(15) $\times 10^{-3}$	$7(2) \times 10^{-4}$
13,000	54	$2.945(4) \times 10^{-11}$	-3.259(6)	-1.763(3)	$1.8576(7) \times 10^{-10}$	-7(5) $\times 10^{-4}$	$5(8) \times 10^{-4}$

Table B.15: Summary statistics for O₂ + O system, nonequilibrium test set ($T_{\text{tr}} = 10,000$ K).

T_{v} [K]	\mathcal{N} [10^6]	k_d [cm^3/sec]	$\langle \Delta\varepsilon_{\text{vib}} \rangle_d$ [eV]	$\langle \Delta\varepsilon_{\text{rot}} \rangle_d$ [eV]	k_e [cm^3/sec]	$\langle \Delta\varepsilon_{\text{vib}} \rangle_e$ [eV]	$\langle \Delta\varepsilon_{\text{rot}} \rangle_e$ [eV]
4000	540	$7.864(16) \times 10^{-13}$	-0.719(3)	-3.589(10)	$8.1618(11) \times 10^{-11}$	0.389,15(14)	-0.2402(2)
5000	270	$1.140(3) \times 10^{-12}$	-1.254(5)	-3.255(11)	$8.7201(16) \times 10^{-11}$	0.327,35(19)	-0.2066(3)
6500	54	$2.214(10) \times 10^{-12}$	-2.206(14)	-2.558(15)	$9.703(4) \times 10^{-11}$	0.2264(4)	-0.1477(7)
8000	54	$4.304(15) \times 10^{-12}$	-2.932(14)	-1.982(9)	$1.0839(4) \times 10^{-10}$	0.1241(5)	-0.0836(7)
10,000	540	$8.695(7) \times 10^{-12}$	-3.473(4)	-1.5207(17)	$1.245,08(16) \times 10^{-10}$	-1.22(15) $\times 10^{-3}$	$7(2) \times 10^{-4}$
13,000	54	$1.772(3) \times 10^{-11}$	-3.858(9)	-1.183(3)	$1.4793(6) \times 10^{-10}$	-0.1517(5)	0.1050(7)

Table B.16: Summary statistics for O₂ + O at $T = 10,000$ K.

Surface	\mathcal{N} [10^6]	k_d [cm^3/sec]	$\langle \Delta\varepsilon_{\text{vib}} \rangle_d$ [eV]	$\langle \Delta\varepsilon_{\text{rot}} \rangle_d$ [eV]	k_e [cm^3/sec]	$\langle \Delta\varepsilon_{\text{vib}} \rangle_e$ [eV]	$\langle \Delta\varepsilon_{\text{rot}} \rangle_e$ [eV]
1 ¹ A'	60	$9.244(19) \times 10^{-12}$	-3.214(9)	-1.688(5)	$3.4031(9) \times 10^{-10}$	-1.3(3) $\times 10^{-3}$	$1.3(4) \times 10^{-3}$
1 ¹ A''	60	$9.59(2) \times 10^{-12}$	-3.241(9)	-1.650(5)	$2.7076(7) \times 10^{-10}$	-1.9(3) $\times 10^{-3}$	$4(4) \times 10^{-4}$
2 ¹ A'	60	$8.275(18) \times 10^{-12}$	-3.552(10)	-1.486(4)	$6.717(3) \times 10^{-11}$	-7(6) $\times 10^{-4}$	$-2(9) \times 10^{-4}$
1 ³ A'	60	$9.87(2) \times 10^{-12}$	-3.187(9)	-1.667(5)	$3.0655(7) \times 10^{-10}$	-6(3) $\times 10^{-4}$	$6(4) \times 10^{-4}$
1 ³ A''	60	$9.92(2) \times 10^{-12}$	-3.139(8)	-1.696(5)	$3.2128(7) \times 10^{-10}$	-2.5(3) $\times 10^{-3}$	$1.2(4) \times 10^{-3}$
2 ³ A'	60	$9.120(19) \times 10^{-12}$	-3.454(9)	-1.533(4)	$8.170(4) \times 10^{-11}$	-1.2(5) $\times 10^{-3}$	$1.9(8) \times 10^{-3}$
1 ⁵ A'	60	$8.131(18) \times 10^{-12}$	-3.624(10)	-1.448(5)	$4.468(3) \times 10^{-11}$	4(8) $\times 10^{-4}$	$-4(12) \times 10^{-4}$
1 ⁵ A''	60	$8.059(18) \times 10^{-12}$	-3.715(10)	-1.380(4)	$3.774(3) \times 10^{-11}$	2(8) $\times 10^{-4}$	$-1.0(14) \times 10^{-3}$
2 ⁵ A'	60	$7.992(18) \times 10^{-12}$	-3.646(10)	-1.426(4)	$2.856(3) \times 10^{-11}$	5(10) $\times 10^{-4}$	$-1(16) \times 10^{-4}$
SYS	540	$8.695(7) \times 10^{-12}$	-3.473(4)	-1.5207(17)	$1.245,08(16) \times 10^{-10}$	-1.22(15) $\times 10^{-3}$	$7(2) \times 10^{-4}$

Table B.17: Summary statistics for $\text{O}_2 + \text{O}$ at $T = 5000\text{ K}$.

Surface	$\mathcal{N} [10^6]$	$k_d [\text{cm}^3/\text{sec}]$	$\langle \Delta\varepsilon_{\text{vib}} \rangle_d [\text{eV}]$	$\langle \Delta\varepsilon_{\text{rot}} \rangle_d [\text{eV}]$	$k_e [\text{cm}^3/\text{sec}]$	$\langle \Delta\varepsilon_{\text{vib}} \rangle_e [\text{eV}]$	$\langle \Delta\varepsilon_{\text{rot}} \rangle_e [\text{eV}]$
$1^1\text{A}'$	60	$3.37(11) \times 10^{-14}$	-3.72(15)	-1.11(5)	$1.9618(6) \times 10^{-10}$	$-3.15(17) \times 10^{-3}$	$1.16(18) \times 10^{-3}$
$1^1\text{A}''$	60	$3.39(11) \times 10^{-14}$	-3.75(15)	-1.06(4)	$8.616(3) \times 10^{-11}$	$-1.5(2) \times 10^{-3}$	$-1(3) \times 10^{-4}$
$2^1\text{A}'$	60	$2.79(9) \times 10^{-14}$	-4.19(17)	-0.83(4)	$3.019(6) \times 10^{-12}$	$-1.5(13) \times 10^{-3}$	$3(16) \times 10^{-4}$
$1^3\text{A}'$	60	$3.74(12) \times 10^{-14}$	-3.76(15)	-1.05(5)	$1.2873(4) \times 10^{-10}$	$-1.56(17) \times 10^{-3}$	$4(2) \times 10^{-4}$
$1^3\text{A}''$	60	$3.48(10) \times 10^{-14}$	-3.64(13)	-1.13(4)	$1.4043(4) \times 10^{-10}$	$-6.62(18) \times 10^{-3}$	$1.9(2) \times 10^{-3}$
$2^3\text{A}'$	60	$3.27(10) \times 10^{-14}$	-4.09(16)	-0.86(4)	$3.788(7) \times 10^{-12}$	$-8(12) \times 10^{-4}$	$1.0(16) \times 10^{-3}$
$1^5\text{A}'$	60	$3.01(10) \times 10^{-14}$	-4.20(18)	-0.84(4)	$1.020(4) \times 10^{-12}$	$3(3) \times 10^{-3}$	$-2(4) \times 10^{-3}$
$1^5\text{A}''$	60	$3.02(10) \times 10^{-14}$	-4.27(18)	-0.75(3)	$8.80(4) \times 10^{-13}$	$-3(3) \times 10^{-3}$	$3(4) \times 10^{-3}$
$2^5\text{A}'$	60	$2.97(12) \times 10^{-14}$	-4.2(2)	-0.81(5)	$3.66(2) \times 10^{-13}$	$-2(5) \times 10^{-3}$	$-5(7) \times 10^{-3}$
SYS	540	$3.18(4) \times 10^{-14}$	-4.04(6)	-0.902(16)	$4.1316(7) \times 10^{-11}$	$-3.73(10) \times 10^{-3}$	$1.07(12) \times 10^{-3}$

Table B.18: Summary statistics for $\text{O}_2 + \text{O}$ at $T_{\text{tr}} = 10,000\text{ K}$, $T_v = 4000\text{ K}$.

Surface	$\mathcal{N} [10^6]$	$k_d [\text{cm}^3/\text{sec}]$	$\langle \Delta\varepsilon_{\text{vib}} \rangle_d [\text{eV}]$	$\langle \Delta\varepsilon_{\text{rot}} \rangle_d [\text{eV}]$	$k_e [\text{cm}^3/\text{sec}]$	$\langle \Delta\varepsilon_{\text{vib}} \rangle_e [\text{eV}]$	$\langle \Delta\varepsilon_{\text{rot}} \rangle_e [\text{eV}]$
$1^1\text{A}'$	60	$1.240(6) \times 10^{-12}$	-0.637(5)	-3.79(2)	$2.8281(8) \times 10^{-10}$	0.3479(2)	-0.2120(4)
$1^1\text{A}''$	60	$1.273(6) \times 10^{-12}$	-0.635(5)	-3.40(2)	$1.9739(5) \times 10^{-10}$	0.3610(3)	-0.2066(4)
$2^1\text{A}'$	60	$7.42(4) \times 10^{-13}$	-0.683(7)	-3.50(3)	$3.960(2) \times 10^{-11}$	0.4665(6)	-0.2629(10)
$1^3\text{A}'$	60	$1.457(6) \times 10^{-12}$	-0.602(5)	-3.274(18)	$2.2963(6) \times 10^{-10}$	0.3475(2)	-0.2084(4)
$1^3\text{A}''$	60	$1.486(6) \times 10^{-12}$	-0.617(5)	-3.464(19)	$2.5629(6) \times 10^{-10}$	0.3712(2)	-0.2057(4)
$2^3\text{A}'$	60	$8.33(5) \times 10^{-13}$	-0.723(7)	-3.47(3)	$4.059(2) \times 10^{-11}$	0.4497(6)	-0.3165(10)
$1^5\text{A}'$	60	$4.85(4) \times 10^{-13}$	-0.893(12)	-4.06(4)	$1.0742(13) \times 10^{-11}$	0.9233(17)	-0.587(2)
$1^5\text{A}''$	60	$3.59(3) \times 10^{-13}$	-0.992(14)	-4.12(5)	$6.342(11) \times 10^{-12}$	0.665(2)	-0.876(4)
$2^5\text{A}'$	60	$4.86(3) \times 10^{-13}$	-0.837(10)	-3.66(4)	$3.789(8) \times 10^{-12}$	1.014(3)	-0.980(5)
SYS	540	$7.864(16) \times 10^{-13}$	-0.719(3)	-3.589(10)	$8.1618(11) \times 10^{-11}$	0.389,15(14)	-0.2402(2)

Appendix C

Miscellaneous

C.1 PES Source Wishlist

This whitepaper was written by Ross S. Chaudhry and Erik Torres. It was sent to Prof. Truhlar on February 13, 2018. The proposed changes were implemented by Zoltan Varga.

We are working on incorporating multiple PESs at the same time into our QCT and DMS codes. Our main design goals are:

- Minimal modification of PES source. Ideally, the PES should be downloaded and used directly, without modification. Unit conversion, iteration tolerances, and other PES-specific usage should be in interface files.
- Speed. If possible, we should avoid branching (if-statements) every time a PES call needs to be made.
- Flexibility. Adding new PESs and species should be relatively easy. No change should preclude us from running electronically non-adiabatic trajectories.

C.1.1 Problem

Currently, we are unable to compile multiple unmodified PESs into the same program. The primary reason for this problem is common blocks, a legacy Fortran construct to store global variables. In the PESs, a variety of variables are declared as a part of common blocks, such as:

```
common /msprmt/    a,ab,ra,rb
```

Multiple PESs have common blocks with the same name (`msprmt`) containing a variety of variable names and values. During compilation, as far as we can tell, routines containing these conflicting common blocks may never be linked together. By design, common blocks are global and referenced only by their name.

Separately, multiple PESs have subroutines with the same name, such as `pot`, which results in subroutine name conflicts. We can probably circumvent the subroutine name conflict, but not the common block name conflict.

In the past, we have gotten around these issues by renaming *every* conflicting object (subroutine names and common blocks) to something specific for each PES. However, this solution is intrusive, error prone, and inflexible.

C.1.2 Proposed Solution

As of the Fortran 90 standard, the preferred way to encapsulate something like a PES is a *module*. Modules are objects which may contain subroutines and variables. Variables declared by the module itself are accessible by subroutines in that module; this specific functionality was intended to replace common blocks. Modules have a variety of other features which would be beneficial, including name association, implicit interfaces, and procedure pointers.

Modifying the existing PESs to be a module is relatively easy. The important modifications are:

- Declare each PES file to be a module by wrapping the entire file in

```
module my_name ... end module my_name
```
- Remove all common blocks. For each variable defined in the common block, declare it at the beginning of the module. These variables are now accessible by every subroutine inside the module.
- Variable initializations, set using `DATA` statements, should be moved to after their declaration at the beginning of the module. We should test whether flagging these as `parameter` results in a speedup.

All existing subroutines are unmodified, except for the removal of their declared common block. They are now encapsulated in the PES module. Each PES would be one module, and it would have a specific name.

In order to call subroutines from the PES, the calling routine must `use` the PES module. The simplest example is:

```
program main
```

```

use pes_o4_singlet      ! This allows us to call routines from the pes
implicit none

<Declare X,Y,Z,...>

call pot(X,Y,Z,E,dEdX,dEdY,dEdZ)

end program main

```

When inheriting variables or subroutines with `use`, they can be renamed in the current scope with `=>`. This allows us to call routines from more than one PES:

```

program main
use pes_o4_singlet, only : pot_o4_singlet => pot
use pes_o4_quintet, only : pot_o4_quintet => pot
implicit none

<Declare X,Y,Z,...>

call pot_o4_singlet(X,Y,Z,E,dEdX,dEdY,dEdZ)

call pot_o4_quintet(X,Y,Z,E,dEdX,dEdY,dEdZ)

end program main

```

This simple example of calling two PESs in the same program is, as far as we know, impossible without modifying the current PES source.

C.1.3 Other Changes

If the PES source is changed to be a module, we have thought of several other minor changes which would be nice. In roughly the order of importance:

1. Incorporate a standardized diatomic potential. Several components of preprocessing and postprocessing use diatomic potentials: enumerating the rovibrational levels; ‘drifting’ molecules to randomize their vibrational phase; determining rovibrational quantum numbers from a product molecule. We get a considerable speedup by avoiding a call to the complete multibody PES.

In the past, the diatomic potential was simply EV2GM2. However, the recently-added dispersion term also includes diatomic terms and is a separate multibody routine,

`d3disp`. This caused problems because we didn't recognize that `EV2GM2` was not the complete diatomic potential. Relying on the users to determine the diatomic PES is error-prone.

Separately, the `d3disp` term is really a series of diatomic terms, so perhaps it should be broken into its diatomic components and merged with existing terms to yield a speedup.

2. Incorporate various modern Fortran keywords which allow for optimizations and make development/use less error prone:

- `intent` should be given to subroutine arguments. For example, `X` is an input to `pot`, so it should be flagged as `intent(IN)`. The compiler is then allowed to optimize such that `X` will never change within the subroutine. Also, this helps ensure that the interface typed by calling routines matches the PES itself.
- Remove implicit typing. Each variable should be declared explicitly, and `implicit none` should appear at the top of the module.
- Declare most components of the PES module as `private`, which makes them inaccessible to everybody except the PES itself. This prevents accidental usage of the `P` array by the calling routine, for example. Subroutines which are meant to be used, such as `pot`, are declared `public`. If parameters such as `re` should be accessible, declare them as `public` also.

This doesn't prevent an experienced user from calling PES internals; I have done this to debug, for example. In this case, the one-line `private` keyword, at the top of the module, would be temporarily commented out.

3. Migrate the PES to 'free form' from the current 'fixed form'. Fixed form source (`*.f`) begins on (at least) column 7 and has various legacy restrictions. Free form source (typically `*.f90`) is more flexible.

Note that this is *different* than including features such as modules. Modern Fortran with modules can be written in fixed form.

We envision these changes would be made to all PESs in the air series while separately retaining the existing legacy source for backwards-compatibility.

C.2 Sample Results File

```

REAQCT results file
tt [K]:      5000.000
numtemps, ediarvflag :
            3           1
tr, tv :
      5000.000      5000.000
Total trajectories:      360000000

Reactants: O2 + O2
PES System Name: 04_system_umn_latest
Number of surfaces:      3
      1 04_singlet_umn_v1
      2 04_triplet_umn_v2
      3 04_quintet_umn_v1

-- Collision Rate Components
Average reactant vrel [cm/s]
  from ensemble statistics : 3.0304766899520764E+05
  from theory : 3.0304102883857599E+05

Average reactant Erel [eV]
  from ensemble statistics : 8.6178494227792635E-01
  from theory : 8.6173323849609551E-01

Relative reduced mass [amu] : 1.5999400000000001E+01
Symmetry factor: : 2
Maximum impact parameter [A] : 6.00000

-- Counts
NOTE: A double-dissoc trajectory contributes 2 to "ne" counts.
NOTE: Each trajectory contributes exactly 1 to "nt" counts.
[To verify, the following should hold:
  nt-samples= (ne-noevent+ ne-dissoc+ ne-methathesis)- (ne-double-dissoc/2)]
For all strata:
  nt-samples = 360000000
  ne-noevent = 359957608
  ne-dissoc = 41551
  ne-simple-dissoc = 31080
  ne-single-dissoc-swap = 10471
  ne-double-dissoc = 0
  ne-methathesis = 841
  ne-dissoc-reac-b-b = 27544
  ne-dissoc-reac-b-q = 14005
  ne-dissoc-reac-q-q = 2

Counts summed over all strata except impact parameter:
Impact parameter stratum # 1:
  bmin [A] = 0.00000
  bmax [A] = 1.00000
  normalized vol. [%] = 2.77778
  nt-samples = 89492799
  ne-noevent = 89468301
  ne-dissoc = 23707
  ne-simple-dissoc = 16438

```

```

    ne-single-dissoc-swap =          7269
    ne-double-dissoc      =           0
    ne-metathesis        =          791
    ne-dissoc-reac-b-b   =         18037
    ne-dissoc-reac-b-q   =         5670
    ne-dissoc-reac-q-q   =           0
Impact parameter stratum #  2:
    bmin [A]                =     1.00000
    bmax [A]                =     2.00000
    normalized vol. [%]    =     8.33333
    nt-samples              =    88452896
    ne-noevent               =    88440523
    ne-dissoc                =     12324
        ne-simple-dissoc     =     9445
        ne-single-dissoc-swap =     2879
        ne-double-dissoc     =           0
    ne-metathesis            =          49
    ne-dissoc-reac-b-b     =     7656
    ne-dissoc-reac-b-q     =     4667
    ne-dissoc-reac-q-q     =           1
Impact parameter stratum #  3:
    bmin [A]                =     2.00000
    bmax [A]                =     3.00000
    normalized vol. [%]    =    13.88889
    nt-samples              =    72408157
    ne-noevent               =    72404116
    ne-dissoc                =     4040
        ne-simple-dissoc     =     3723
        ne-single-dissoc-swap =     317
        ne-double-dissoc     =           0
    ne-metathesis            =           1
    ne-dissoc-reac-b-b     =     1533
    ne-dissoc-reac-b-q     =     2506
    ne-dissoc-reac-q-q     =           1
Impact parameter stratum #  4:
    bmin [A]                =     3.00000
    bmax [A]                =     4.00000
    normalized vol. [%]    =    19.44444
    nt-samples              =    54717035
    ne-noevent               =    54715819
    ne-dissoc                =     1216
        ne-simple-dissoc     =     1210
        ne-single-dissoc-swap =       6
        ne-double-dissoc     =           0
    ne-metathesis            =           0
    ne-dissoc-reac-b-b     =     281
    ne-dissoc-reac-b-q     =     935
    ne-dissoc-reac-q-q     =           0
Impact parameter stratum #  5:
    bmin [A]                =     4.00000
    bmax [A]                =     5.00000
    normalized vol. [%]    =    25.00000
    nt-samples              =    36597131
    ne-noevent               =    36596894
    ne-dissoc                =     237
        ne-simple-dissoc     =     237

```

```

ne-single-dissoc-swap = 0
ne-double-dissoc = 0
ne-metathesis = 0
ne-dissoc-reac-b-b = 36
ne-dissoc-reac-b-q = 201
ne-dissoc-reac-q-q = 0
Impact parameter stratum # 6:
bmin [A] = 5.00000
bmax [A] = 6.00000
normalized vol. [%] = 30.55556
nt-samples = 18331982
ne-noevent = 18331955
ne-dissoc = 27
    ne-simple-dissoc = 27
    ne-single-dissoc-swap = 0
    ne-double-dissoc = 0
ne-metathesis = 0
ne-dissoc-reac-b-b = 1
ne-dissoc-reac-b-q = 26
ne-dissoc-reac-q-q = 0

Counts summed over all strata except ground-state degeneracy:
Ground-state degeneracy stratum # 1:
Surface name = 04_singlet_umn_v1
normalized vol. [%] = 11.11111
nt-samples = 120000000
ne-noevent = 119989139
ne-dissoc = 10519
    ne-simple-dissoc = 8272
    ne-single-dissoc-swap = 2247
    ne-double-dissoc = 0
ne-metathesis = 342
ne-dissoc-reac-b-b = 6480
ne-dissoc-reac-b-q = 4039
ne-dissoc-reac-q-q = 0
Ground-state degeneracy stratum # 2:
Surface name = 04_triplet_umn_v2
normalized vol. [%] = 33.33333
nt-samples = 120000000
ne-noevent = 119977630
ne-dissoc = 21927
    ne-simple-dissoc = 14946
    ne-single-dissoc-swap = 6981
    ne-double-dissoc = 0
ne-metathesis = 443
ne-dissoc-reac-b-b = 16132
ne-dissoc-reac-b-q = 5794
ne-dissoc-reac-q-q = 1
Ground-state degeneracy stratum # 3:
Surface name = 04_quintet_umn_v1
normalized vol. [%] = 55.55556
nt-samples = 120000000
ne-noevent = 119990839
ne-dissoc = 9105
    ne-simple-dissoc = 7862
    ne-single-dissoc-swap = 1243

```

```

ne-double-dissoc      =          0
ne-metathesis        =         56
ne-dissoc-reac-b-b   =        4932
ne-dissoc-reac-b-q   =        4172
ne-dissoc-reac-q-q   =          1

-- Rates and error

Overall statistics on "dissoc" events:
Dissociation probability       : 3.2845904138107327E-05
One-sigma deviation            : 2.7579081445045800E-07

Dissociation cross section [cm^3] : 3.7147842410687780E-19
One-sigma deviation             : 3.1191206277785826E-21

Dissociation rate constant [cm^3/s]: 4.7777551599097377E-14
One-sigma deviation              : 4.0116447434541898E-16 ( 0.83965 %)

Contributions from impact params:
Integration stratum # 1       : 1.0316980298726357E-14 ( 21.59378 +- 0.21544 %)
Integration stratum # 2       : 1.6656162737365651E-14 ( 34.86190 +- 0.34967 %)
Integration stratum # 3       : 1.1483908261806476E-14 ( 24.03620 +- 0.36384 %)
Integration stratum # 4       : 6.3581592080926165E-15 ( 13.30784 +- 0.37882 %)
Integration stratum # 5       : 2.2754443671565771E-15 ( 4.76258 +- 0.32530 %)
Integration stratum # 6       : 6.8689672594970647E-16 ( 1.43770 +- 0.29610 %)

Contributions from surfaces :
04_singlet_umn_v1           : 4.0733068532930798E-15 ( 8.52557 +- 0.13445 %)
04_triplet_umn_v2           : 2.4292846740454931E-14 ( 50.84573 +- 0.42113 %)
04_quintet_umn_v1           : 1.9411398005349373E-14 ( 40.62870 +- 0.43718 %)

Contributions from events :
simple-dissoc                : 4.0111224644457032E-14 ( 83.95412 +- 0.21871 %)
single-dissoc-swap            : 7.6663269546403503E-15 ( 16.04588 +- 0.21871 %)
double-dissoc                 : 0.0000000000000000E+00 ( 0.00000 +- 0.00000 %)

Contributions from reac states:
dissoc-reac-b-b               : 2.4135558953453388E-14 ( 50.51653 +- 0.42157 %)
dissoc-reac-b-q               : 2.3636918253579225E-14 ( 49.47285 +- 0.42161 %)
dissoc-reac-q-q               : 5.0743920647648207E-18 ( 0.01062 +- 0.00755 %)

Overall statistics on "metathesis" events:
[FOR COMPARISON ONLY. Percentage is of the dissociation rate constant.]
Metathesis rate constant [cm^3/s] : 3.3513422536493639E-16 ( 0.70145 %)

```

C.3 Physical Constants

Table C.1: Some physical constants used in the work; these quantities are assumed to be exact

Quantity	Value	Reference
Avogadro Constant N_A , mol $^{-1}$	6.022,140,857(74) $\times 10^{23}$	CODATA 2014 [138]
Bohr radius a_0 , Å	0.529,177,210,67(12) $\times 10^{-10}$	CODATA 2014 [138]
Boltzmann Constant k_B , J/K	1.380,648,52(79) $\times 10^{-23}$	CODATA 2014 [138]
Boltzmann Constant k_B , eV/K	8.617,330,3(50) $\times 10^{-5}$	CODATA 2014 [138]
Electron Volt eV, J	1.602,176,620,8(98) $\times 10^{-19}$	CODATA 2014 [138]
Hartree energy E_h , J	4.359,744,650(54) $\times 10^{-18}$	CODATA 2014 [138]
Hartree energy E_h , eV	27.211,386,02(17)	CODATA 2014 [138]
Molar Mass N, g mol $^{-1}$	14.0067	NASA Lewis [135, 136]
Molar Mass O, g mol $^{-1}$	15.9994	NASA Lewis [135, 136]
Planck's Constant h , J sec	6.626,070,040(81) $\times 10^{-34}$	CODATA 2014 [138]

Table C.2: Dissociation temperature of N₂ from various sources.

Source	T_D
Vincenti and Kruger [115]	113,000
Bortner [43]	113,200
Park [16, 18]	113,200
Losev <i>et al.</i> [128]	113,200
N ₄ Surface [62–64]	113,381
N ₂ O ₂ Surface [65]	113,228

Table C.3: Dissociation temperature of O₂ from various sources.

Source	T_D
Vincenti and Kruger [115]	59,500
Bortner [43]	59,400
Park [16, 18]	59,500
Losev <i>et al.</i> [128]	59,380
N ₂ O ₂ Surface [65]	59,377
O ₄ and O ₃ Surfaces [66–68]	59,334

C.4 Enthalpy Fits

The electronically-excluded fits for enthalpy are, using the NASA Lewis format for thermodynamic data (Ref. [136], Appendix A),

```

N          RSC ee nitrogen sys, AIAA 2018 Summer, mod from NASA Lewis
3 N-ee   N   1.00    0.00    0.00    0.00    0.00 0  14.0067000    472680.000
      200.000  1000.0007 -2.0 -1.0  0.0  1.0  2.0  3.0  4.0  0.0       6197.428
0.000000000D+00 0.000000000D+00 2.500000000D+00 0.000000000D+00 0.000000000D+00
0.000000000D+00 0.000000000D+00                           5.610463780D+04 4.193905036D+00
      1000.000 6000.0007 -2.0 -1.0  0.0  1.0  2.0  3.0  4.0  0.0       6197.428
0.000000000D+00 0.000000000D+00 2.500000000D+00 0.000000000D+00 0.000000000D+00
0.000000000D+00 0.000000000D+00                           5.610463780D+04 4.193905036D+00
      6000.000 20000.0007 -2.0 -1.0  0.0  1.0  2.0  3.0  4.0  0.0       6197.428
0.000000000D+00 0.000000000D+00 2.500000000D+00 0.000000000D+00 0.000000000D+00
0.000000000D+00 0.000000000D+00                           5.610463780D+04 4.193905036D+00
N2         RSC ee nitrogen sys, AIAA 2018 Summer, fit by IN using REAQCT
3 N2-ee   N   2.00    0.00    0.00    0.00    0.00 0  28.0134000    0.000
      200.000  1000.0007 -2.0 -1.0  0.0  1.0  2.0  3.0  4.0  0.0       8670.104
2.358578210E+04-4.023531477E+02 6.190065510E+00-8.792960519E-03 1.416083864E-05
-9.832860368E-09 2.580457541E-12                           8.099079480E+02-1.136612340E+01
      1000.000 6000.0007 -2.0 -1.0  0.0  1.0  2.0  3.0  4.0  0.0       8670.104
4.642520858E+05-1.884678905E+03 5.661145607E+00-3.867340642E-04 8.104962789E-08
-8.651140666E-12 3.902231052E-16                           1.056914866E+04-1.297051828E+01
      6000.000 20000.0007 -2.0 -1.0  0.0  1.0  2.0  3.0  4.0  0.0       8670.104
-1.072969016E+07 5.136553660E+02 6.145132857E+00-4.778523180E-04 5.741317120E-08
-2.757392534E-12 4.439407604E-17                           -1.309456388E+04-1.627685706E+01

```

C.5 Evaluating Near $\delta = 0$

Although G_{rot} and G_{vib} are continuous, their numerical evaluation near $\delta = 0$ must be considered due to precision loss that is discussed in this section. This occurs because their numerator and denominator are both 0 when $\delta = 0$. (Analytically, these functions are evaluated exactly at $\delta = 0$ in Eqns. (4.44) and (4.45).) First, consider the relevant component of G_{rot} , which we denote as \mathcal{G}_1 ,

$$\mathcal{G}_1 \equiv \frac{\exp[j_{\max}(j_{\max} + 1)\delta_{\text{rot}}] - 1}{\delta_{\text{rot}}} \quad (\text{C.1})$$

Near $\delta_{\text{rot}} = 0$, this expression behaves as $[(1 + \epsilon) - 1]$, where ϵ is small. Because $(1 + \epsilon)$ is evaluated first and cast into the working numerical precision, $[(1 + \epsilon) - 1]$ deviates from ϵ . This deviation increases as ϵ approaches machine epsilon for the floating point representation

used. The solution for this precision loss, which we present and evaluate in this section, is to approximate these functions near $\delta = 0$ and analytically simplify.

We first examine \mathcal{G}_1 . Expanding about $\delta_{\text{rot}} = 0$ and simplifying yields,

$$\mathcal{G}_1 = \sum_{n=1}^{\infty} \frac{[j_{\max}(j_{\max} + 1)]^n \delta_{\text{rot}}^{n-1}}{n!} \quad (\text{C.2})$$

If δ_{rot} is smaller than some threshold value, some number of terms from this equation must be used to evaluate \mathcal{G}_1 , instead of the typical evaluation using Eq. (C.1). In order to determine the threshold value and the sufficient number of terms, we evaluate various representations of \mathcal{G}_1 and compare to a benchmark value computed using higher-precision arithmetic. Figure C.1a shows the relative error in \mathcal{G}_1 computed with Eq. C.1, and the first one, two, or three terms from Eq. C.2. A nominal value of $j_{\max} = 300$ is used, and the limit is approached from the negative and positive direction. Based on the results, a threshold value of 10^{-10} with two terms is sufficient to maintain a relative error below 10^{-10} . \mathcal{G}_1 is therefore evaluated numerically using

$$\mathcal{G}_1 \approx \begin{cases} [j_{\max}(j_{\max} + 1)] + \frac{\delta_{\text{rot}}}{2} [j_{\max}(j_{\max} + 1)]^2 & \text{if } |\delta_{\text{rot}}| < 10^{-10} \\ \frac{\exp[j_{\max}(j_{\max} + 1)\delta_{\text{rot}}] - 1}{\delta_{\text{rot}}} & \text{otherwise.} \end{cases} \quad (\text{C.3})$$

We consider G_{vib} next, which is defined earlier in Eqn. (4.45). The relevant component is denoted \mathcal{G}_2 , and we expand about $\delta_{\text{vib}} = 0$ and simplify,

$$\mathcal{G}_2 \equiv \frac{1 - \exp(\delta_{\text{vib}} v_{\max})}{1 - \exp(\delta_{\text{vib}})} \quad (\text{C.4})$$

$$\mathcal{G}_2 = \frac{\sum_{n=1}^{\infty} \frac{\delta_{\text{vib}}^{n-1} v_{\max}}{n!}}{\sum_{n=1}^{\infty} \frac{\delta_{\text{vib}}^{n-1}}{n!}} \quad (\text{C.5})$$

In this case, we have Taylor series in both the numerator and the denominator. However, the results are similar, as shown in Figure C.1b. As before, the unmodified form (Eq. C.4) is compared to the first one, two, or three terms in each sum from Eq. C.5. A nominal value of $v_{\max} = 35$ is used. Here, a threshold value of 10^{-6} with two terms in each sum yields a

relative error below 10^{-9} . \mathcal{G}_2 is therefore evaluated numerically using

$$\mathcal{G}_2 \approx \begin{cases} \frac{2v_{\max} + \delta_{\text{vib}} v_{\max}^2}{2 + \delta_{\text{vib}}} & \text{if } |\delta_{\text{vib}}| < 10^{-6} \\ \frac{1 - \exp(\delta_{\text{vib}} v_{\max})}{1 - \exp(\delta_{\text{vib}})} & \text{otherwise.} \end{cases} \quad (\text{C.6})$$

Finally, the expression for change in vibrational energy due to dissociation, Eq. (4.54) contains,

$$\mathcal{G}_3 \equiv -\frac{v_{\max} \exp(\delta_{\text{vib}} v_{\max})}{1 - \exp(\delta_{\text{vib}} v_{\max})} + \frac{\exp(\delta_{\text{vib}})}{1 - \exp(\delta_{\text{vib}})} \quad (\text{C.7})$$

Performing a Taylor-series expansion for each \exp and simplifying yields,

$$\mathcal{G}_3 = \frac{\sum_{n=2}^{\infty} \frac{\delta_{\text{vib}}^{n-2}}{n!} [(v_{\max} - 1)(v_{\max} + 1)^n - v_{\max}^{n+1} + 1]}{\sum_{n=2}^{\infty} \frac{\delta_{\text{vib}}^{n-2}}{n!} [(v_{\max} + 1)^n - v_{\max}^n - 1]} \quad (\text{C.8})$$

The results are shown in Figure C.1c. In this case, the unmodified expression diverges more rapidly from the correct value in the limit of $\delta_{\text{vib}} \rightarrow 0$, compared to \mathcal{G}_1 and \mathcal{G}_2 . This rapid divergence occurs because the first derivative of the numerator and denominator of Eq.(C.7) are also 0. In this case, we choose a threshold value of 10^{-5} with two terms in each sum, which yields a relative error below 10^{-7} . \mathcal{G}_3 is therefore evaluated numerically using

$$\mathcal{G}_3 \approx \begin{cases} \frac{3v_{\max} - 3 + 2\delta_{\text{vib}}(v_{\max} + 1)}{6 + 3\delta_{\text{vib}}(v_{\max} + 1)} & \text{if } |\delta_{\text{vib}}| < 10^{-5} \\ -\frac{v_{\max} \exp(\delta_{\text{vib}} v_{\max})}{1 - \exp(\delta_{\text{vib}} v_{\max})} + \frac{\exp(\delta_{\text{vib}})}{1 - \exp(\delta_{\text{vib}})} & \text{otherwise.} \end{cases} \quad (\text{C.9})$$

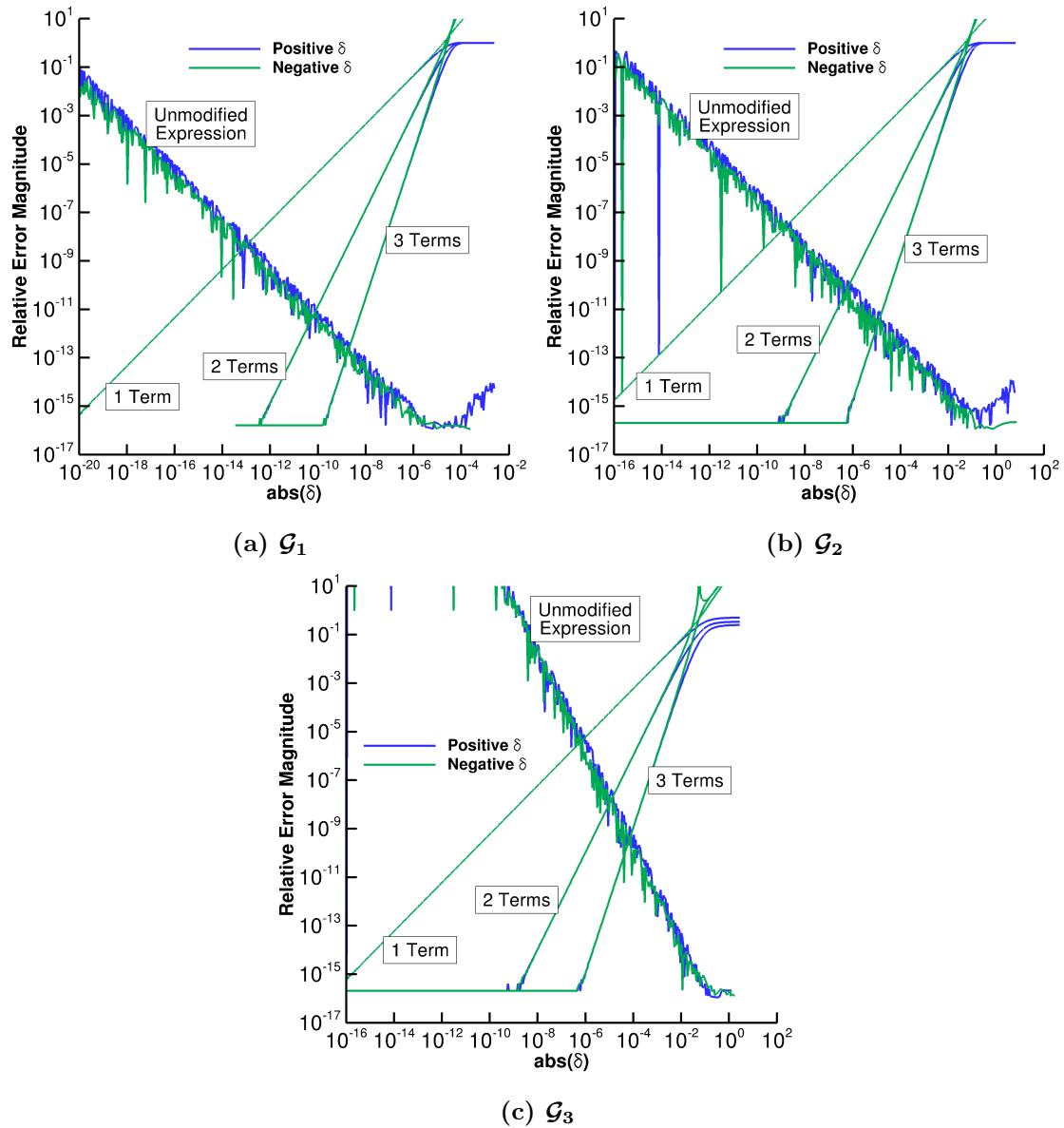


Figure C.1: Relative error magnitude when computing expressions near $\delta = 0$